Determination of the CKM phase γ at LHCb using the decay mode $B^{\pm} \to DK^{\pm}$ and a study of the decays $D^0 \to K^0_S K^{\pm}\pi^{\mp}$ using data from the CLEO experiment

Daniel Johnson
Merton College, Oxford

Thesis submitted in fulfilment of the requirements for the degree of Doctor of Philosophy at the University of Oxford

Trinity Term, 2013

Abstract

This thesis documents studies of CP violation in $B^{\pm} \to [K^0_S h^+ h^-]_D K^{\pm}$, $(h = \pi/K)$ decays using data taken by the LHCb experiment during 2011, and the first measurement of γ to be made at the Large Hadron Collider (LHC),

$$\gamma = (45^{+43}_{-38})^{\circ}. \tag{1}$$

Also included is a study of $D^0 \to K^0_S K^{\mp}\pi^{\pm}$ decays using CLEO III and CLEO-c data, resulting in the first amplitude models to be published for these decays and a measurement of the ratio of their branching fractions.

Acknowledgements

This thesis is the product of four years' study in Oxford and Geneva. The number of people who have played a part in supporting me through that period is large, and the task of listing them all nigh-on impossible. Nevertheless, I will try to highlight a few people to whom my debt of thanks is very great.

The most significant role played in my academic experience at Oxford University, stretching back eight years to my first undergraduate days, is that of Professor Guy Wilkinson. I am deeply grateful to him for his diligent teaching, dedicated supervision and consistent encouragement. It was he who first introduced me to the world of experimental particle physics and led me on my first steps through it. Dr Sneha Malde deserves a heartfelt thanks for her first class guidance whilst she supervised a portion of my DPhil, and it is my privilege to count her as a friend too. During my DPhil, I have been grateful for opportunities to work with Tim Gershon, Malcolm John and Jonas Rademacker, and I am thankful to them for their advice. It has been a delight to work with the Oxford LHCb group and to form many friendships with its current and former members: Faye Cheung, Denis Derkach, Paolo Gandini, Rhorry Gauld, Hamish Gordon, Ed Greening, Neville Harnew, Donal Hill, Philip Hunt, Nazim Hussain, Olli Lupton, Andrew Powell, Ed Smith, Patrick Spradlin, Chris Thomas and Nick Torr.

Thanks are due to the Science and Technology Facilities Council (STFC) for sponsoring my research, to Merton College for hosting me so comfortably during my time in Oxford, and to the European Centre for Nuclear Research (CERN) where I spent two enjoyable and productive years working on long term attachment.

Navigating the sea of necessary administration accompanying a course of study in three countries has been as straightforward as could be hoped, thanks to the commitment of Sue Geddes and Kim Proudfoot in Oxford and Lalaine Barbon Strebel at CERN. Lalaine's provision of cake in the secretariat was always perfectly timed.

This thesis, and the work documented therein, is, in no small part, the product of an upbringing and education provided and supported by my parents. I am grateful for the love and energy which they poured into raising me. Like them, my brother Tom is, though living

far away, rarely forgotten.

My stays in Oxford and Geneva have been the source of a number of invaluable friendships, greatly enriching my experience of work and life in both places. Amongst them I am grateful to Allan Beckett, for his faithful friendship; Daniel Teuber, for his steady support; Sam Allberry, for his dependable companionship; and Vaughan Roberts, for his wise counsel and generous grace. Finally, I am overwhelmingly thankful for my best friend, Mary-Anne, whose support has already been without equal. It is an honour to face the future with such a talented, devoted and joyful wife.

May the truth of the words shared by the Oxford crest and Psalm 27, "God is my light", continue to encompass my endeavours, within and without the academy. I am deeply thankful to have had these few years to gaze, in some detail, at one aspect of the marvellous work of his hands.

Contents

Introduction

Precise measurements of the Standard Model (SM) of particle physics provide an excellent means not only to place tight constraints on the self-consistency of the SM but also to search indirectly for New Physics (NP). One of the least well measured SM parameters is the complex phase γ in the CKM quark mixing matrix, responsible in the SM for violation of the combined charge-parity (CP) symmetry. Measurements of this phase can be made directly by studying relevant tree- or loop-level interactions. Alternatively, a measurement of γ can be made indirectly by assuming SM self-consistency and performing a global fit to measurements of other parameters. Both categories of γ measurement have potential to reveal SM inconsistencies and to search for new particles or effects.

The technique of measuring γ by studying the decays of B mesons finds its origins in papers by Gronau, London and Wyler in 1991. The LHCb experiment on the Large Hadron Collider (LHC) operated by the *Organisation Européene pour la Recherche Nucléaire* (CERN) is fast acquiring data to allow high precision measurement of γ to be made using this and other, related techniques. This thesis describes the first constraints to be placed on the CKM phase γ using data from the LHCb experiment in studying tree-level $B^{\pm} \to [K^0_S h^+ h^-]_D K^{\pm}$ decays, where the subscript D denotes a neutral D meson of unknown flavour. This analysis has been published [1].

This thesis also contains studies using the full data sets collected by the CLEO III and CLEO-c detectors, situated on the Cornell Electron Storage Ring (CESR), NY. Studies

were carried out of different D^0 meson final states, $D^0 \to K^0_S K^\mp \pi^\pm$ [1], which have potential to increase the sensitivity of γ measurement in $B^\pm \to \tilde{D} K^\pm$ decays. The intermediate resonances formed in each of these D^0 decays are of significant interest in their own right as a means to test flavour SU(3) symmetry in the charm system. The analysis has also been published [2] and contains the first amplitude models to be published in these modes.

Chapter 1 introduces the two analyses and describes the techniques used for each. The LHCb, CLEO III and CLEO-c detectors are detailed in Chapter 2, as are the facilities for data processing and production of simulated samples of decays. The analysis of the decays $D^0 \to K^0_S K^\mp \pi^\pm$ using CLEO data is presented in Chapter 3 as well as a measurement of the ratio of the branching fractions for $D^0 \to K^0_S K^+ \pi^-$ and $D^0 \to K^0_S K^- \pi^+$ decay processes, which will form an input to a future γ measurement. Chapters 4 and 5 contain the first measurement of γ carried out using LHCb data where $B^\pm \to [K^0_S \pi^+ \pi^-]_D K^\pm$ and $B^\pm \to [K^0_S K^+ K^-]_D K^\pm$ decays have been used. The results are summarised, and their context is discussed, in Chapter 6.

The selection of the CLEO III and CLEO-c data was carried out by other members of the CLEO collaboration but, since a description of the selection is necessary, it is included in Chapter 3. For the analysis of LHCb data, described in Chapters 4 and 5, the selection of the data and the evaluation of the experimental systematic uncertainties were performed in collaboration with another member of the Oxford LHCb group.

[1] Charge conjugation is implied throughout this introductory chapter and the whole of Chapter 3.

1 CP violation and Dalitz analysis techniques

Standard Model CP violation is introduced, particularly as manifested in the decays of B mesons. The rich Dalitz structure present in n-body ($n > 2$) decays is considered and the isobar modelling technique to describe n-body resonant structure is outlined. Understanding Dalitz structure is useful and interesting in its own right, but also allows the formalism for charge-parity violation studies to be extended to Dalitz analyses, as shown at the end of the chapter.

1.1 Introduction

The Standard Model of particle physics has been shown over many years to describe nature with remarkable accuracy. Recent, high profile examples of this success include the discovery of a resonance whose properties are consistent with those of the long-awaited Higgs boson [3, 4] and the recent observation of charm mixing [5, 6]. However, a number of observational and phenomenological issues remain unexplained, for example the observed hierarchy of particle masses, the interaction between particle physics and cosmology in explaining the nature of Dark Matter, the apparent absence of strong CP violation, and the cause of the enormous preponderance of matter and relative scarcity of its counterpart, anti-matter. At a most basic, theoretical level, there is a failure to reconcile a quantum description of the gravitational interaction with the Standard Model theory of the electroweak and strong forces.

There are two broad methods of further investigation: precise measurements of Standard Model observables to distinguish areas of weakness and searches for effects beyond the

Standard Model using direct and indirect probes. The study of flavour physics is a powerful tool for measurements in both categories, providing opportunities for increased precision measurements, such as that presented in this thesis, and a means to make indirect searches for New Physics.

Within the flavour physics sector, much attention in recent years has centred on the study of D and B mesons, quark-antiquark bound states containing a charm (c) or beauty (b) quark, respectively, and of which large data samples are now available. This thesis describes an exploration of the resonant content of a little-studied charm decay and, secondly, an analysis of CP violation in $B^{\pm}$ meson decays via a D^0 or $\bar{D}^0$ meson. Throughout this thesis, where reference is made to the intermediate neutral D meson whose flavour could be D^0 or $\bar{D}^0$, the generic label $\tilde{D}$ is used. Besides being of intrinsic interest, the results of the former charm study have potential to complement the latter B CP violation study by providing a $B^{\pm}$ CP violation measurement via a different charmed decay route.

1.2 CP violation and its study in $B^{\pm} \to \tilde{D}K^{\pm}$ decays

In an attempt to understand the imbalance between the observed quantities of matter and anti-matter in the universe, the hypothesis of baryogenesis was introduced in which a baryon-antibaryon production asymmetry is generated very early in the history of the universe. In 1967, Andrei Sakharov proposed three criteria as essential for this baryogenesis, the so-called 'Sakharov Conditions' [7]. Firstly, baryon number non-conservation must be possible. Secondly, breaking of charge (C) and combined charge-parity (CP) symmetry must take place. Thirdly, interactions are required to take place outside thermal equilibrium. The study of the second of these conditions has assumed great importance in flavour physics in recent decades in the K and D systems and, as for this thesis, in the B system.

An interaction breaks the combined charge (C) and parity (P) symmetries when a process occurs differently after charge conjugation, exchanging all particles for anti-particles, and parity transformation, inverting the coordinate system used to describe the interaction. The

breaking of CP symmetry in the decays of kaons [8] had recently been observed at the time of Sakharov's work. Not until over three decades later was evidence for CP violation in the B system uncovered [9, 10] and not until the following year did such evidence finally reach the level of observation [11, 12]. Although the combined CP symmetry is broken, there exists a third symmetry, time inversion 'T', and it is thought that the combined symmetry CPT is conserved in all physical processes.

CP-violating processes are divided into three categories. The first, known as 'direct', comprises CP violation resulting from a difference between the amplitudes for a process and its CP-conjugate decay. The second category involves 'indirect' CP violation arising as a consequence of mixing in neutral meson systems, and the third arises from interference between contributing amplitudes with and without mixing. Only CP violation arising from the first, direct, category is relevant for the studies described in this thesis, and the other two categories are not discussed further here.

For the decay from an initial state i to a final state f in a process governed by the weak interaction hamiltonian, $\mathcal{H}$, direct CP violation causes a difference in the magnitude for the two amplitudes $\langle f|\mathcal{H}|i\rangle$ and $\left\langle \bar{f}|\mathcal{H}|\bar{i}\right\rangle$ where $\bar{i}$ represents the CP-conjugate state of the initial state i. In that case, $\frac{\left|\left\langle \bar{f}|\mathcal{H}|\bar{i}\right\rangle\right|}{|\langle f|\mathcal{H}|i\rangle|} \neq 1$. For decays of charged hadrons and of baryons where there is no possibility for mixing, this is the only way in which CP violation can be manifested.

1.2.1 CP violation in the Standard Model

The couplings of charged-current weak interactions in the SM Lagrangian between the up-type (u, c, t, charge $+2/3$) and down-type (d, s, b, charge $-1/3$) quark flavours are

$$-\frac{g}{\sqrt{2}}(\bar{u}_L, \bar{c}_L, \bar{t}_L)\gamma^\mu W_\mu^+ V_{CKM} \begin{pmatrix} d_L \\ s_L \\ b_L \end{pmatrix} + \text{higher order terms}, \tag{1.1}$$

where g is a coupling constant, γ^μ are the Dirac matrices and $W_\mu^\pm$ is the charged current operator. The vectors of physical up-type and down-type quark states enclose the operator term and the Cabibbo Kobayashi Maskawa (CKM) quark-mixing matrix, V_{ij}, contains vertex factors for a transition from a down-type flavour j to an up-type flavour i. The corresponding transition from an up-type i to a down-type j is V_{ij}^*. The set of vertex factors for the possible quark transitions is represented in the 3×3 matrix

$$V_{\mathrm{CKM}} = \begin{pmatrix} V_{ud} & V_{us} & V_{ub} \\ V_{cd} & V_{cs} & V_{cb} \\ V_{td} & V_{ts} & V_{tb} \end{pmatrix}. \tag{1.2}$$

In order to conserve probability in quark transitions, it is required that the matrix V_{CKM} be unitary, which implies that $\sum_j V_{ij} V_{kj}^* = \delta_{ik}$. These relations correspond to a set of constraints upon combinations of the CKM matrix elements, three of which sum three pairs of matrix element products to unity and six such sums which vanish. Of these nine relations, the most frequently discussed is

$$V_{ud}V_{ub}^* + V_{cd}V_{cb}^* + V_{td}V_{tb}^* = 0, \tag{1.3}$$

because all the phases and magnitudes of the complex terms are of a similar size and are therefore more readily accessible to measurement in experiments.

Parameterising the CKM matrix

A general 3×3 matrix with complex elements has eighteen parameters. The imposition of the requirement that the matrix be unitary halves the number of free parameters to nine. A phase transformation can be applied to each of the six quark fields, $q_i \to q_i e^{\theta_i}$, leaving the Lagrangian unchanged, allowing five relative phases in the CKM matrix to be removed. The sixth is physically irrelevant, corresponding to an overall phase in the CKM matrix which has no impact on the transition probabilities determined from it. Of the four parameters which remain, unitarity constraints and phase transformations leave just one complex phase,

which gives rise to CP violation, and three amplitudes.

CP violation is seen by differences in the decay amplitude for a weak decay process, $\mathcal{A}(i \to j)$, and the amplitude for its conjugate decay, $\mathcal{A}(\bar{i} \to \bar{j})$. In the CKM paradigm, the only means for CP violation to occur is through a difference in the CKM matrix elements for the decay and its conjugate amplitude. This can only occur if the CKM matrix is complex. One helpful parameterisation of the CKM matrix encapsulates an experimental understanding of the relative magnitudes and complexity of the matrix elements in an expansion in the small parameter λ, which is the sine of the Cabibbo angle and has a value of approximately 0.2. The following parameterisation is named after its author, Lincoln Wolfenstein [13], and allows simple, approximate, expression of the CKM matrix up to terms of order λ^4:

$$V_{\mathrm{CKM}} = \begin{pmatrix} 1-\frac{\lambda^2}{2} & \lambda & A\lambda^3(\rho - i\eta) \\ -\lambda & 1-\frac{\lambda^2}{2} & A\lambda^2 \\ A\lambda^3(1-\rho-i\eta) & -A\lambda^2 & 1 \end{pmatrix} + \mathcal{O}(\lambda^4), \tag{1.4}$$

where $A\lambda^2 = \lambda \left|\frac{V_{cb}}{V_{us}}\right|$ and $A\lambda^3(\rho - i\eta) = V_{ub}$. Expanding to all orders in λ allows the unitarity of the CKM matrix to be restored precisely and the matrix can then be described in terms of the set of parameters $\lambda, A, \bar{\rho}$ and $\bar{\eta}$, where $\bar{\rho} = [\rho(1-\lambda^2/2)+...]$ and $\bar{\eta} = [\eta(1-\lambda^2/2)+...]$. The unitarity constraints can then be represented in an illuminating way. The sums of products of matrix elements are simply sums of three complex numbers and can be expressed by a sum of three vectors in the complex plane. The vectors must form a vanishing sum and so produce closed 'Unitarity Triangles' (UTs). The most frequently discussed of these triangles, referred to earlier in Equation 1.3, can helpfully be represented in the complex plane. Dividing the three terms by the second gives

$$\frac{V_{ud}V_{ub}^*}{V_{cd}V_{cb}^*} + 1 + \frac{V_{td}V_{tb}^*}{V_{cd}V_{cb}^*} = 0. \tag{1.5}$$

The three complex terms describe a closed triangle in the complex plane, shown in Figure 1.1, where the magnitudes of the terms form the sides and their phases determine the three angles. Of the two notations in circulation, (α, β, γ) and (ϕ_2, ϕ_1, ϕ_3), the former is employed

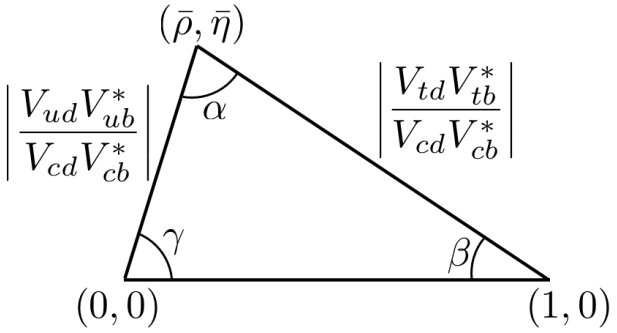

Figure 1.1: The most commonly referred to unitarity triangle (UT).

throughout this thesis, where

$$\begin{aligned}
\gamma &= \arg\left(-\frac{V_{ud}V_{ub}^*}{V_{cd}V_{cb}^*}\right), \\
\beta &= 180^\circ - \arg\left(\frac{V_{td}V_{tb}^*}{V_{cd}V_{cb}^*}\right), \text{ and} \\
\alpha &= 180^\circ - \arg\left(\frac{V_{ud}V_{ub}^*}{V_{td}V_{tb}^*}\right).
\end{aligned}$$

Although it is possible to construct five more such triangles, each corresponding to a different unitarity constraint, only this one will be considered in this thesis. This triangle will henceforth be referred to as 'the unitarity triangle' (UT).

1.2.2 Measuring the parameters of the Unitarity Triangle

Non-unitarity of the CKM matrix would indicate the presence of physics beyond the SM, such as the existence of a fourth generation of quarks or the existence of new particles. In order to test the unitarity of the CKM matrix, it is desirable to determine as many of its properties as possible precisely and to over-constrain the triangle. A number of measurements of processes with dependence upon the values of CKM elements are used to measure the UT parameters, and these are summarised here with the exception of the angle γ which will be discussed in more detail later:

- The length of the left-hand side of the triangle shown in Figure 1.1 is given by $\left|\frac{V_{ud}V_{ub}^*}{V_{cd}V_{cb}^*}\right|$ which can be written more simply with reference to the Wolfenstein parameterisation

of Equation 1.4, neglecting terms of order λ^4 or higher, as $\frac{|V_{ub}|}{|V_{us}||V_{cb}|}$. The magnitudes of these matrix elements can be determined using semileptonic decays. The magnitude of V_{us} is determined in decays of charged or neutral kaons to a $\pi^{0,\pm}\ell(e,\mu)^{\mp}\nu$ final state. It can also be measured relative to V_{ud}, itself measured precisely in nuclear beta decays, through a comparison of $K \to \mu\nu(\gamma)$ and $\pi \to \mu\nu(\gamma)$ processes. Studies of semileptonic B meson decays to charmed final states $X_c\ell\bar{\nu}$ allow measurement of V_{cb}. Similarly, studies of decays to charmless final states $X_u\ell\bar{\nu}$ allow measurement of V_{ub}. Measurements of these quantities yield an annulus in the $\bar{\rho},\bar{\eta}$ plane on which the apex of the unitarity triangle of Figure 1.1 must lie.

- Given that, to $\mathcal{O}(\lambda^4)$, the length of the right hand side of the unitarity triangle is given by $\frac{1}{\lambda}\left|\frac{V_{td}}{V_{cb}}\right|$, where the measurement of V_{cb} has been considered earlier, it is found that the side can be measured by studying oscillations of neutral B mesons where t quarks enter in the relevant box diagram. For each system, the rate of the oscillations is governed by the difference in the masses, Δm of the mass eigenstates, and the most precise determination of the length of the UT side is made by measuring the ratio $\left|\frac{V_{td}}{V_{ts}}\right|$ using the ratio of the B_d and B_s mass differences, $\frac{\Delta m_d}{\Delta m_s}$.

- The angle α is measured by studying $b \to u\bar{u}d$ processes. The most sensitive measurements so far have been made using time-dependent CP violation analyses of $B^0 \to \rho^+\rho^-$ decays where the amplitude of oscillations is sensitive to the phase α [14]. The fact that the branching fraction for $B^0 \to \rho^0\rho^0$ is small [15], where the process is sensitive to contributions from diagrams containing loops, leads to a strong constraint on the low level of contamination from diagrams containing loops in $B^0 \to \rho^+\rho^-$.

- The angle β is determined in a time-dependent analysis of CP asymmetries in neutral B decays to $c\bar{c}s$ final states, of which decays to CP eigenstates such as $B^0 \to J/\psi K^0_{\rm S}$ incur the smallest theoretical uncertainties. The time dependent CP asymmetry is given by $\frac{\Gamma(\bar{B}^0(t)\to f)-\Gamma(B^0(t)\to f)}{\Gamma(\bar{B}^0(t)\to f)+\Gamma(B^0(t)\to f)} = -\eta_f \sin 2\beta \sin(\Delta m_d t)$.

- Other constraints come from kaon decays, the most important currently being measurements of CP violation in neutral kaon mixing, forming a parabolic band in the

$(\bar{\rho}, \bar{\eta})$ plane.

The current status of these various experimental constraints is illustrated in Figure 1.2. The angle γ is still very poorly constrained, as can be seen in the Figure, as a consequence of the low yields of the processes in which it can be measured. The measurement of this angle is now considered in more detail.

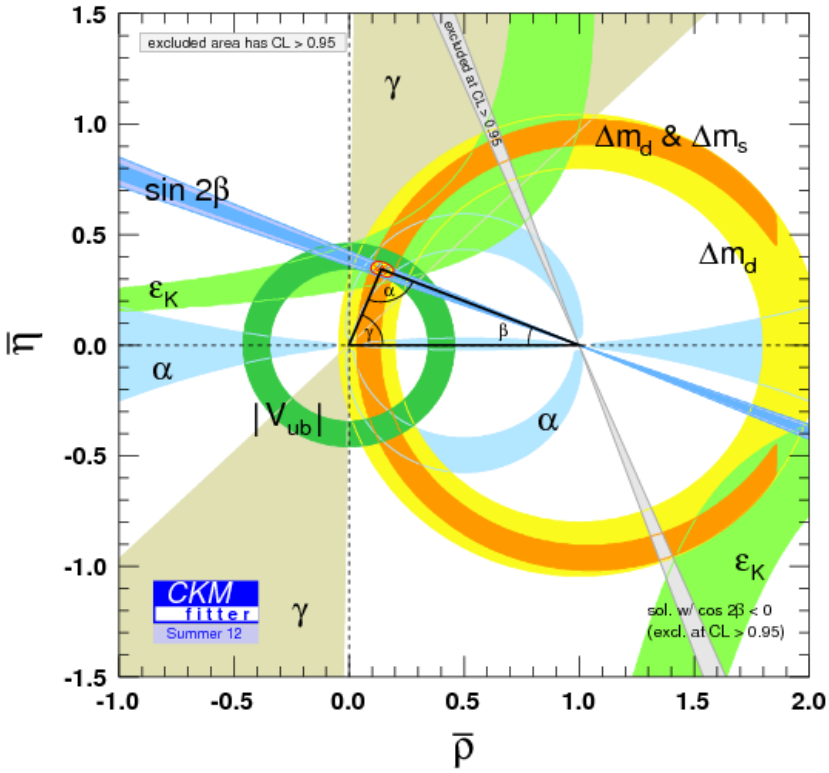

Figure 1.2: Most recent results [16], presented at ICHEP 2012, for global fit to the unitarity triangle containing the various measurements discussed as inputs.

1.2.3 Measuring the UT angle γ

The angle γ can be measured directly in 'tree-level processes', which involve Feynman diagrams with no loops at first order, providing a standard candle measurement of an SM parameter. This direct measurement, which currently has an uncertainty of around 12° [16], can be compared with indirect measurements of γ made by performing a global fit, which

assumes CKM unitarity, to other measurements relating to UT parameters, where the uncertainty is currently around 4.5° [16]. This would allow a stringent test of CKM unitarity. Finally, measurements of γ are possible using 'loop-level processes' where loop diagrams enter the decay amplitudes at leading order. Comparing measurements in tree- and loop-level processes has potential to uncover new particles or effects which enter the loop in the latter category.

This thesis culminates in a direct measurement of the CKM phase γ in tree-level $B^{\pm} \to \tilde{D}K^{\pm}$ decays in Chapters 4 and 5. Though no loop-level measurements of γ are made in this thesis, the technique is summarised in Appendix B.

Measurement of γ in tree-level decays

A powerful channel for measurement of γ at tree-level is the decay of a charged B meson via a D^0 or $\bar{D}^0$ meson, generically referred to by the symbol $\tilde{D}$, and a kaon. Sensitivity to γ arises as a result of interference between the amplitudes for $B^- \to D^0 K^-$ and $B^- \to \bar{D}^0 K^-$ decays. In the case of a B^- decay, the interfering processes are shown in Figure 1.3 where 1.3(a) and 1.3(b) differ by a weak vertex factor $\frac{V_{cb}V_{us}^*}{V_{ub}V_{cs}^*}$ and by the fact that the latter is colour-suppressed. Topologically and kinematically the B decays are identical, so the differences in the amplitudes for the decays only arise as a result of the stated difference in the weak vertex factors and a difference in the strong interactions. The amplitudes $\mathcal{A}_{B^- \to D^0 K^-}$ and $\mathcal{A}_{B^- \to \bar{D}^0 K^-}$ are related as follows:

$$\begin{aligned} \mathcal{A}_{B^- \to \bar{D}^0 K^-} &= \mathcal{A}_{B^- \to D^0 K^-} \times r_B e^{\left(i \arg\left[\frac{V_{ub}V_{cs}^*}{V_{cb}V_{us}^*}\right]\right)} e^{i\delta_B} \\ &\approx \mathcal{A}_{B^- \to D^0 K^-} \times r_B e^{-i\gamma} e^{i\delta_B}. \end{aligned} \tag{1.6}$$

Considering the Wolfenstein parameterisation of the CKM matrix in Equation 1.4, it can be seen that V_{cs} and V_{us} can only have a very small imaginary component, as is also the case for V_{cd} and V_{ud}, so that the term $e^{i \arg\left(\frac{V_{ub}V_{cs}^*}{V_{cb}V_{us}^*}\right)}$ is simply equal to $e^{-i\gamma}$. Whilst γ parameterises the weak part of the interaction, the phase δ_B is the strong, CP-conserving phase difference

between the $B^- \to \bar{D}^0 K^-$ and $B^- \to D^0 K^-$ decays. The quantity r_B is the ratio of the magnitudes of the amplitudes, $r_B = \left|\frac{\mathcal{A}_{B^- \to \bar{D}^0 K^-}}{\mathcal{A}_{B^- \to D^0 K^-}}\right|$. Consideration of the values of the CKM matrix elements and anticipated colour suppression between the diagrams leads to an expected value of r_B around 0.1.

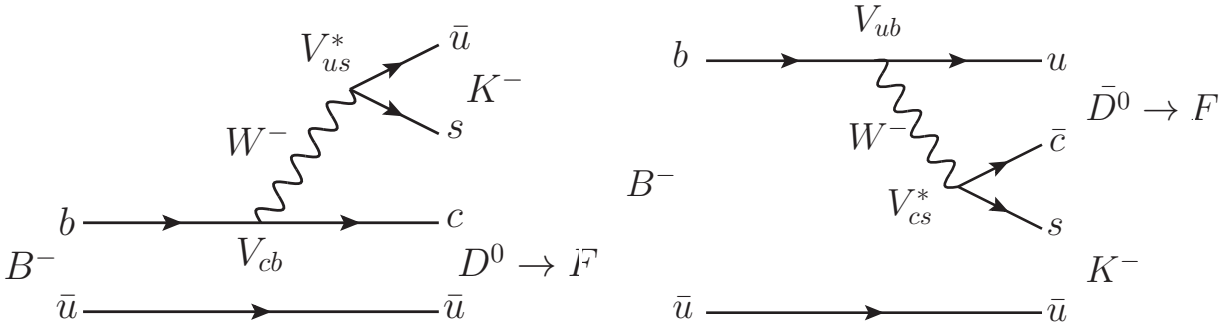

(a) Decay via D^0 (b) Decay via $\bar{D}^0$

Figure 1.3: Feynman diagrams for tree-level $B^- \to \tilde{D} K^-$ decays.

Measurement of the phase γ is possible by exploiting interference in the decay to a final state, F, which is accessible to both D^0 and $\bar{D}^0$ mesons, generically labelled by $\tilde{D}$. Such a scenario is illustrated in Figure 1.4 where, as well as the strong and weak phase differences between the two $B^\pm \to \tilde{D} K^\pm$ amplitudes, there is also a factor between the $D^0 \to F$ and $\bar{D}^0 \to F$ amplitudes, characterised by an amplitude ratio, r_D, and strong phase difference, δ_D. The D^0 and $\bar{D}^0$ decay amplitudes can be related:

$$\mathcal{A}_{\bar{D}^0 \to F} = \mathcal{A}_{D^0 \to F} \times r_D e^{-i\delta_D}. \tag{1.7}$$

The method assumes that CP violation in the D decay is small enough to be neglected, an assumption supported by current limits on CP violation in $D^0 \to K^0_S \pi^+ \pi^-$ decays.

The amplitude for the decay $B^- \to [F]_D K^-$ is given by

$$\begin{aligned}
\mathcal{A}_{B^- \to [F]_D K^-} &= \mathcal{A}_{B^- \to D^0 K^-} \times \mathcal{A}_{D^0 \to F} + \mathcal{A}_{B^- \to \bar{D}^0 K^-} \times \mathcal{A}_{\bar{D}^0 \to F} \\
&= \mathcal{A}_{B^- \to D^0 K^-} \times (\mathcal{A}_{D^0 \to F} + r_B e^{i(\delta_B - \gamma)} \times \mathcal{A}_{\bar{D}^0 \to F}) \\
&= \mathcal{A}_{B^- \to D^0 K^-} \times \mathcal{A}_{D^0 \to F} \times (1 + r_B r_D e^{i(\delta_B - \gamma - \delta_D)}),
\end{aligned} \tag{1.8}$$

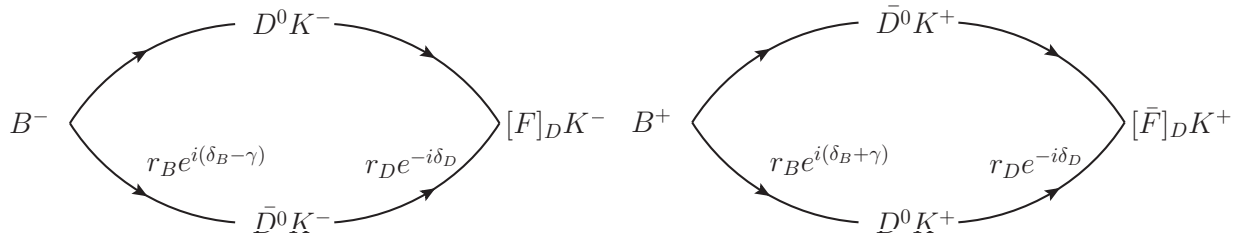

(a) B^- decay (b) B^+ decay

Figure 1.4: Diagram of interference between decay amplitudes for the decays $B^- \to [F]_D K^-$ and $B^+ \to [F]_D K^+$ where the decay to the F final state can take place via a D^0 or $\bar{D}^0$ meson.

where the relation in Equation 1.6 has been used for the first step and that in Equation 1.7 for the second. Following a similar argument, with reference to Figure 1.4(b), the equation for $\mathcal{A}_{B^+\to[\bar{F}]_DK^+}$ is given by

$$\mathcal{A}_{B^+\to[\bar{F}]_DK^+} = \mathcal{A}_{B^+\to\bar{D}^0K^+} \times \mathcal{A}_{\bar{D}^0\to\bar{F}} \times (1 + r_B r_D e^{i(\delta_B+\gamma-\delta_D)}), \tag{1.9}$$

where the sign of the CP-violating phase, γ, is reversed.

All the tools are now in place for the dependence of the $B^\pm$ decay rates upon the quantities $r_B, \delta_B, \gamma, r_D$ and δ_D to be written:

$$\begin{aligned} N(B^- \to [F]_D K^-) &\propto 1 + r_B^2 r_D^2 + 2 r_B r_D \cos(\delta_B - \gamma - \delta_D), \\ N(B^+ \to [\bar{F}]_D K^+) &\propto 1 + r_B^2 r_D^2 + 2 r_B r_D \cos(\delta_B + \gamma - \delta_D). \end{aligned} \tag{1.10}$$

Similar equations can be written for the CP-conjugate processes. The diagrams in Figure 1.4 are the same after the factor $r_D e^{-i\delta_D}$ is moved from the lower to the upper decay in both cases, giving

$$\begin{aligned} N(B^- \to [\bar{F}]_D K^-) &\propto r_B^2 + r_D^2 + 2 r_B r_D \cos(\delta_B - \gamma + \delta_D), \\ N(B^+ \to [F]_D K^+) &\propto r_B^2 + r_D^2 + 2 r_B r_D \cos(\delta_B + \gamma + \delta_D). \end{aligned} \tag{1.11}$$

By measuring the relative yields in each of these channels, γ can be determined.

The use of $B^{\pm} \to \tilde{D}K^{\pm}$ decays with the D^0 or $\bar{D}^0$ decaying to a common final state to determine the phase γ was first proposed with a $\tilde{D}$ decay to the CP eigenstates K^+K^- and $\pi^+\pi^-$ (a 'GLW' analysis, after its proponents [17, 18]) for which $r_D = 1$ and $\delta_D = 0°$ and 180° respectively. However, the small value for r_B means that interference is small, limiting the sensitivity for a measurement of γ. It was later realised that non-CP eigenstates could also be used, such as the two-body $K^{\pm}\pi^{\mp}$ final state where the favoured decay $D^0 \to K^-\pi^+$ and the suppressed $\bar{D}^0 \to K^-\pi^+$ form the two $\tilde{D}$ decay routes which interfere (an 'ADS' analysis, again so named after its proponents [19, 20]). In this case, the small value of r_B around 0.1 is balanced by a small value of r_D between Cabibbo-favoured and doubly Cabibbo-suppressed decays of around 0.06, leading to a relatively large interference term. In exactly the same way, an 'ADS-like' analysis could be carried out using singly Cabibbo suppressed final states which are not CP eigenstates, such as $\tilde{D} \to K^0_S K^{\pm}\pi^{\mp}$. Such an analysis is discussed further in Section 6.1.4. These $\tilde{D}$ final states have been exploited in a number of analyses in recent years, first the GLW analyses for the CP eigenstates [21, 22, 23, 24] and, later, by adding ADS analyses of the $K^{\pm}\pi^{\mp}$ final state [25, 26, 27, 24] and, analogously, the $K^{\pm}\pi^{\mp}\pi^+\pi^-$ final state [28].

In addition to these GLW and ADS analyses of two- and multi-body final states, a further class of $B^{\pm} \to \tilde{D}K^{\pm}$ analyses exists, involving Dalitz analysis of self-conjugate, multi-body final states such as $K^0_S\pi^+\pi^-$ and $K^0_S K^+K^-$ [29]. Chapters 4 and 5 of this thesis describe an analysis of the $K^0_S h^+h^-$ final states using LHCb data [1], the theoretical background for which is given in Section 1.5. The multi-body final state is particularly interesting given the possibility for resonances to enter in the D decay depending on the kinematics of the D final state. The presence of resonances causes the strong phase, δ_D, to vary depending on the kinematics of the final state. This can be exploited, as will be described in Section 1.5, but first of all the description of multi-body D decays is discussed.

1.3 Multi-body D^0 decays

Decays of a D^0 meson to final states containing three (or more) particles are of great interest to study because of the possibility for the formation of intermediate states which then decay to pairs (or sets) of the final particles. The resulting decay structure is of intrinsic interest since the relations between intermediate states with known flavour content can be measured and used to test predictions of SM flavour symmetries (see Section 3.1). Understanding the intermediate structure provides an insight into the behaviour of the strong phase of the decay. The focus of this section will be three-body decays of D mesons since these are the category of multi-body D decays analysed in this thesis.

1.3.1 The use of Dalitz plots to visualise resonant structure

The decay structure of three-body D^0 meson decays can be described in terms of a combination of a simple $1 \to 3$ 'non-resonant' decay amplitude and other amplitudes where a short-lived, strongly decaying 'resonant' intermediate state is formed and which decays to pairs of the three decay products, shown in Figure 1.5.

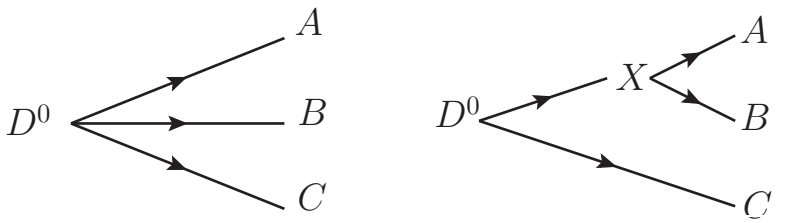

(a) Non-resonant (b) Via $X \to AB$ resonance

Figure 1.5: 3-body D^0 decays to stable pseudoscalars A, B and C.

Resonances between particular pairs of the three final-state particles are more likely to be formed in particular kinematic arrangements of the three four-vectors. The twelve degrees of freedom in the arrangement of the three final four-vectors are reduced to nine by constraining their invariant masses to each daughter mass. Conserving energy and momentum removes a further four degrees of freedom and, finally, rotating the coordinate system such that two four-vectors are contained in the $x - y$ plane with one directed along the x-axis removes

three more. It is therefore possible to uniquely represent the kinematic space of possible four-vector arrangements for a three-body D^0 decay, known as the D^0 meson's phase space, in two dimensions. Resonances between different pairs of the final particles in particular spatial arrangements dominate different parts of the three-body phase space.

Dalitz plots

The three-body phase space can be illustrated using a plot of the invariant mass squared of one pair of particles against that for another pair, known as a Dalitz plot [30]. In this Lorentz invariant representation, the density of states in the D^0 kinematic phase space is distributed uniformly across the plot and the variation in point-density is therefore proportional to the variation in the square of the overall matrix element, $\mathcal{M}$, of the decay:

$$d\Gamma = \frac{1}{(2\pi)^3}\frac{1}{32M_{D^0}^3}|\mathcal{M}|^2 dm_{AB}^2 dm_{BC}^2. \tag{1.12}$$

In this equation, M_{D^0} is the D^0 mass and m_{AB} and m_{BC} are the invariant masses of the AB or BC pairs of particles. Resonances appear as straight bands horizontally, vertically or diagonally, depending on the pair of particles between which the resonance forms. A non-resonant decay populates the Dalitz plot uniformly. The form of a Dalitz plot can be seen in Figure 1.6 where extrema and points of intuitive kinematic interest are noted.

Understanding the structure in a Dalitz plot

The structure appearing in the D^0 Dalitz plot is complicated by the interference between resonances. In the simple case where interference is neglected, a number of basic features of the structure arising from an individual resonance can be explained simply. For example, though a resonance itself produces a dense, linear band across a Dalitz plot, the spin of the resonance determines the density of points as a function of position along the band. This can be seen in Figure 1.7, where $D^0 \to K^0_S\pi^+\pi^-$ simulated data have been generated for three resonances independently and the resulting distributions superimposed. A spin 0

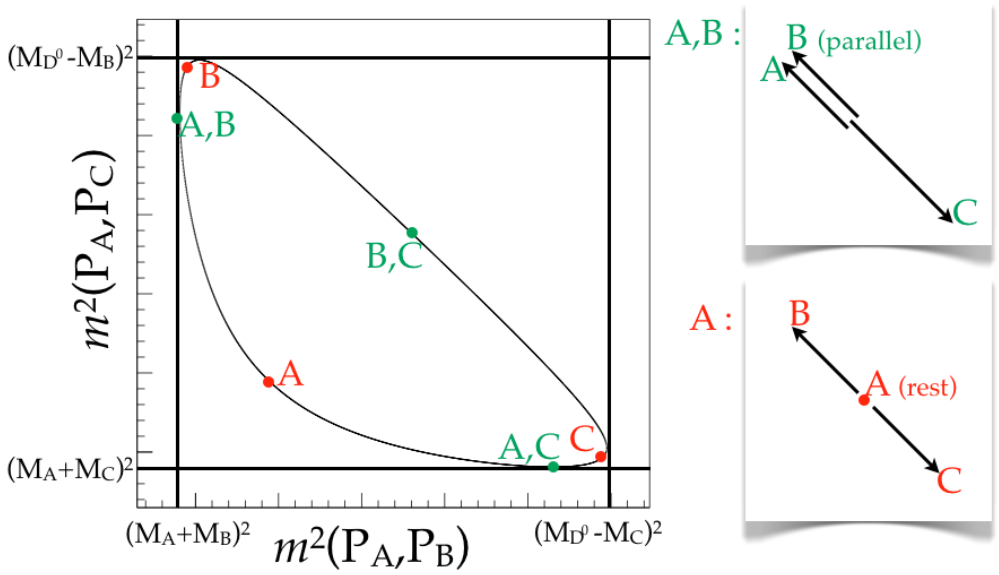

Figure 1.6: General form of a Dalitz plot, showing extrema and points where the four-vector arrangement is symmetric, for points where one of the final three particles, A, B or C, is at rest (red) or where two travel in the same direction (green).

resonance has a uniform distribution of points along the band (blue points, Figure 1.7); a spin 1 resonance has a marked point-density depletion around the centre of the band (red points, Figure 1.7); a spin 2 resonance has two such regions of depletion (magenta points, Figure 1.7), and so on. Form factors of the resonance and D^0 meson have a role to play in shaping the resonance, but are not considered in more detail until Section 1.4.3.

1.4 Describing resonant structure in D^0 decays

An 'isobar' modelling technique [31] is commonly employed as a means of developing a physically intuitive description of resonant structure in the Dalitz plot. The technique is employed in Chapter 3 to produce models of the decays $D^0 \to K^0_S K^- \pi^+$ and $D^0 \to K^0_S K^+ \pi^-$.

In the isobar formalism, an amplitude is assigned to each contributing resonant or non-resonant component and these resonances are then combined coherently to form an overall quantum amplitude for the decay. The non-resonant decay proceeds irrespective of the final point in the Dalitz plot and the magnitude and phase of its quantum amplitude are therefore constant over the plot. Conversely, the quantum amplitude associated with a resonance does

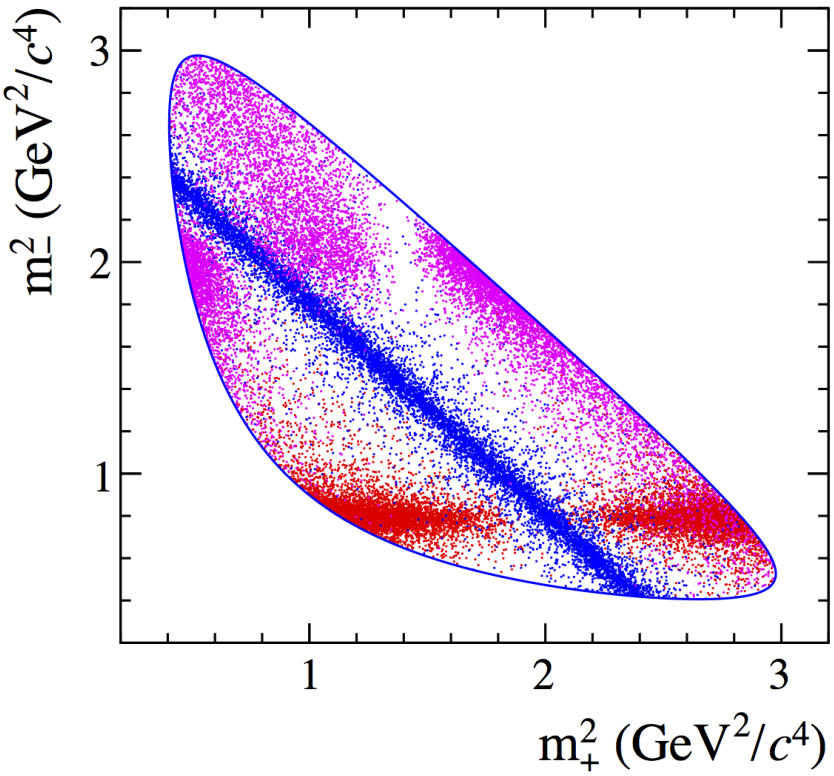

Figure 1.7: Simulated $D^0 \to K^0_S\pi^+\pi^-$ Dalitz structure corresponding to three incoherent resonances, a scalar $f_0(980) \to \pi^+\pi^-$ resonance (blue points), a vector $K^{*-} \to K^0_S\pi^-$ (red points) and a tensor $K^*_2(1430)^- \to K^0_S\pi^-$ (magenta points). The axis labels correspond to the invariant mass squared for the K^0_S meson and a pion, the charge of which is denoted by the sign subscript.

vary over the phase space and can interfere with those of other resonances where they overlap in the D^0 meson phase space.

The quantum amplitude for each resonance between two daughters (A, B) in the decay of a D^0 meson contains a lineshape, $L(M_{AB})$, which is a function of the reconstructed mass of the resonance, M_{AB}; form factors for the D^0 and resonance decay vertices, F_{D^0} and F_r respectively; and a sum, Ω_i, over the spins of the parent particle and resonance. The amplitude is given by

$$\mathcal{A}_i = F_{D^0} L(M_{AB}) \Omega_i F_r. \tag{1.13}$$

1.4.1 Resonance lineshapes: $L(M_{AB})$

The most commonly used function to describe a resonant lineshape is the relativistic Breit-Wigner function:

$$L(M_{AB}) = \frac{1}{M_r^2 - M_{AB}^2 - iM_r\Gamma_{AB}}, \tag{1.14}$$

which depends upon M_r, the pole mass of the resonance, and Γ_{AB}, its full width. The lineshape provides a relativistic description with intuitively clear parameters. There is a subtlety in the definition of the width Γ_{AB}, known as the 'running width', which is conventionally related to the intrinsic full width of the resonance, Γ_r, as follows:

$$\Gamma_{AB} = \Gamma_r \left(\frac{p_{AB}}{p_r}\right)^{2J+1} \frac{M_r}{M_{AB}} F_r^2, \tag{1.15}$$

where p_{AB} is the momentum of A or B in the AB rest frame, p_r the momentum of either in the resonance rest frame and J is the spin of the resonance. An example of the lineshape is given for a $K^*(892)^\pm \to K^0_S\pi^\pm$ resonance in Figure 1.8(a). The relativistic Breit-Wigner is used as the default lineshape and is suitable in most cases. For resonances where the pole mass is very close to threshold (such as the $a_0(980)^\pm \to K^0_S K^\pm$), it is found to be preferable to use an alternative description which accounts for the threshold effect, known as a Flatté

lineshape [32]. This lineshape is given by

$$L(M_{AB}) = \frac{1}{M_r^2 - M_{AB}^2 - i(\rho_{\eta\pi} g_{\eta\pi}^2 + \rho_{\bar{K}K} g_{\bar{K}K}^2)}, \tag{1.16}$$

where $\rho_{AB} = 2p_{AB}/M_{AB}$, and $g_{\bar{K}K}$ and $g_{\eta\pi}$ are the $a_0(980)$ couplings to the $\bar{K}K$ and $\eta\pi$ systems respectively. In this thesis, the values for the couplings are taken to be $g_{\bar{K}K} = (329 \pm 27)\,\mathrm{MeV}/c^2$ and $g_{\eta\pi} = (324 \pm 15)\ \mathrm{MeV}/c^2$ [33]. An example of this lineshape is given for an $a_0(980)^{\pm} \to K^0_{\mathrm{S}} K^{\pm}$ resonance in Figure 1.8(b), though it is worth noting that the sharp spike in the distribution lies outside the kinematic region in the $D^0 \to K^0_{\mathrm{S}} K^{\mp}\pi^{\pm}$ Dalitz plot.

Another case in which an alternative lineshape is preferable is that used to describe the $K_0^*(1430) \to K\pi$ resonance where, in past analyses of the $K\pi$ spectrum, a different parameterisation has been used to account for the significant phase variation below the resonant pole mass and the nearby $K\eta'$ threshold. In the amplitude model studies presented in this thesis, the contribution from this resonance is combined coherently with that of a $K\pi$ S-wave, an approach adopted in many other studies. This parameterisation is similar to that employed by the LASS collaboration to describe $K\pi$ scattering data [34]. However, the exact form of the resonance lineshape used is that employed by the *BABAR* collaboration (see supplementary material in the e-print version of [35]):

$$L(M_{AB}) = T_{K\pi L=0}(M_{AB})/\rho(M_{AB}). \tag{1.17}$$

The quantities $\rho(M_{AB})$ and $T_{K\pi L=0}(M_{AB})$ are defined as

$$\begin{aligned}
\rho(s) &= p_{AB}/\sqrt{s}, \\
T_{K\pi L=0}(M_{AB}) &= F\sin(\delta_F + \phi_F)e^{i(\delta_F+\phi_F)} + R\sin\delta_R e^{i(\delta_R+\phi_R)}e^{i2(\delta_F+\phi_F)}, \\
\tan\delta_R &= M_{K_0^*(1430)}\Gamma_{K_0^*(1430)}(M_{AB})/(M^2_{K_0^*(1430)} - M^2_{AB}), \\
\text{and } \cot\delta_F &= 1/(ap_{AB}) + rp_{AB}/2,
\end{aligned} \tag{1.18}$$

where M_{AB} and p_{AB} are defined as previously and the values of the other fixed parameters are given in Table 1.1 [35]. Of the fixed parameters, F and R determine the proportions of resonant and non-resonant contributions to the lineshape, whilst ϕ_F and ϕ_R are the phases for the two parts. The phase δ_R contains the Breit-Wigner contribution. The parameter a acts as a scattering length, and r as an effective interaction length. An example of the lineshape is shown for the $K^*(1430)^{\pm}$ resonance in Figure 1.8(c).

Table 1.1: Parameters used in the $K\pi$ S-wave parameterisation [35].

Parameter	Value
F	0.62 ± 0.04
ϕ_F (rad)	-0.100 ± 0.010
R	1
ϕ_R (rad)	1.10 ± 0.02
a $(\text{GeV})^{-1}$	0.224 ± 0.003
r $(\text{GeV})^{-1}$	-15.01 ± 0.13

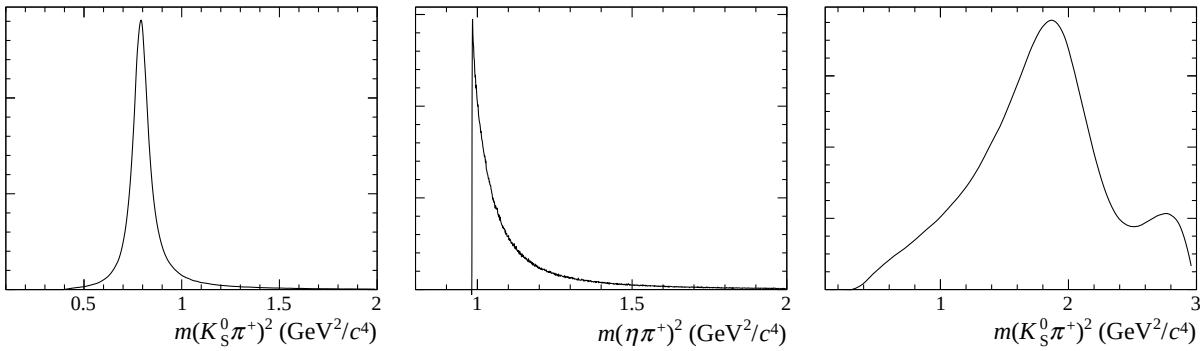

(a) Breit-Wigner $K^*(892)^{\pm} \to K^0_S\pi^{\pm}$

(b) Flatté $a_0(980)^{\pm} \to \eta\pi^{\pm}$

(c) LASS $K^*_0(1430)^{\pm} \to K^0_S\pi^{\pm}$

Figure 1.8: Examples of resonant lineshapes referred to in the main text, shown as a function of invariant mass squared.

1.4.2 Resonance spin factors: Ω_i

The spin of a resonance has a dramatic effect on the population of points in the Dalitz plot, as already shown in Figure 1.7. There is a spin factor, ϵ^{μ}_{λ}, associated with the vertex at which the resonance is produced and at which it decays. For an intermediate resonance with non-zero spin, there are multiple helicity states, labelled by λ, in which the resonance could

exist. In the matrix element for the resonant decay, an incoherent sum is included over the various helicity states which results in a factor in the matrix element corresponding to the angular distribution of the final-state particles. This factor is evaluated using the 'helicity formalism' and the resulting spin sums for scalar, vector and tensor resonances are given in Table 1.2.

Table 1.2: Spin Factors, Ω_i where i labels the spin of the resonance. The p_X^μ are the four-vectors for the particle labelled by X.

Spin factor	Definition			
Ω_0:		1		
Ω_1:	$(p_{D^0}^\mu + p_C^\mu)$	$T_{\mu\alpha}$	$(p_B^\alpha - p_A^\alpha)$	$/(\mathrm{GeV})^2$
Ω_2:	$(p_{D^0}^\mu + p_C^\mu)(p_D^\nu + p_C^\nu)$	$T_{\mu\nu\alpha\beta}$	$(p_B^\alpha - p_A^\alpha)(p_B^\beta - p_A^\beta)$	$/(\mathrm{GeV})^4$

For a spin 1 resonance the $T_{\mu\alpha}$ factor can be calculated and is given exactly by

$$T_{\mu\alpha} = \sum \varepsilon_\mu^* \varepsilon_\alpha = -g_{\mu\alpha} + \frac{p_\mu p_\alpha}{M_{AB}^2}, \tag{1.19}$$

where p_μ denotes the resonance's four-momentum, M_{AB} is defined as previously and $g_{\mu\alpha}$ is the metric tensor. $T_{\mu\alpha}$ is conventionally determined [31] by replacing M_{AB}^2 with the pole mass, M_r, of the resonance, giving

$$T_{\mu\alpha} \equiv -g_{\mu\alpha} + \frac{p_\mu p_\alpha}{M_r^2}. \tag{1.20}$$

For a spin 2 resonance, the evaluation is more complicated [36]:

$$T_{\mu\nu\alpha\beta} = \frac{1}{2}\left(T_{\mu\alpha}T_{\nu\beta} + T_{\mu\beta}T_{\nu\alpha}\right) - \frac{1}{3}T_{\mu\nu}T_{\alpha\beta}, \tag{1.21}$$

where the M_{AB} factor is again replaced by M_r, and $T_{\mu\alpha}$ are the spin 1 factors. The order in which the decay products are considered is significant and care is taken to define the ordering clearly for the analysis presented in Chapter 3.

1.4.3 Decay vertex form factors: F_X

The form factors assigned to the D^0 decay vertex and to the decay vertex of the resonance are dependent upon the momentum of the daughters in the resonance rest frame. Intuitively, this is understood by the need to conserve angular momentum in the decay to two spin 0 particles with a given impact parameter, leading to a preference for particular values of daughter momentum. The factors typically chosen are known as Blatt-Weisskopf penetration factors and contain an explicit dependence upon the daughter momentum as described and the 'radius' of the parent, R. The factors as published in [31] are given in Table 1.3.

Table 1.3: Blatt-Weisskopf penetration factors.

Spin	Factor
0	1
1	$\sqrt{\frac{1+R^2p_r^2}{1+R^2p_{AB}^2}}$
2	$\sqrt{\frac{9+3R^2p_r^2+R^4p_r^4}{9+3R^2p_{AB}^2+R^4p_{AB}^4}}$

1.4.4 Combining resonances to form a signal model

The combination of resonant contributions is achieved by adding the individual amplitudes together with a complex coefficient multiplying each contributing resonance. When fitting the model to data, the coefficients can vary and thus regulate the contribution each resonance makes to the fit probability density function (PDF). For a model containing N resonances, the combination is made as follows:

$$\mathcal{A}_{\text{total}} = \mathcal{A}_1 + C_2 \times \mathcal{A}_2 + \ldots + C_N \times \mathcal{A}_N, \tag{1.22}$$

where C_i are the complex coefficients and the $\mathcal{A}_i$ are the amplitudes for each resonance.

1.5 CP violation in $B^{\pm} \to (K^0_S h^+ h^-)_D K^{\pm}$ and sensitivity to γ

The use of interference between $B^{\pm} \to D^0 K^{\pm}$ and $B^{\pm} \to \bar{D}^0 K^{\pm}$ decays as a means to measure the CKM phase γ has been discussed in Section 1.2 and attention now turns to the case where the intermediate $\tilde{D}$ meson decays to the three body final state $K^0_S\pi^+\pi^-$ or $K^0_S K^+ K^-$. Although the experimental details involved in using both final states differ, much of their theoretical treatment is identical and, for the rest of this chapter, details given for the $K^0_S\pi^+\pi^-$ final state should be taken to apply to the $K^0_S K^+ K^-$ state as well, unless otherwise stated. For the $D^0 \to K^0_S h^+ h^-$ final state, there is an important extension to the formalism presented in Section 1.2.3 relating to the strong phase in the D decay. The presence of resonances in the D phase space causes the D strong phase to vary across the Dalitz plot. Figure 1.9 illustrates the interfering processes, making explicit their dependence upon the position in the Dalitz plot, (m^2_+, m^2_-).

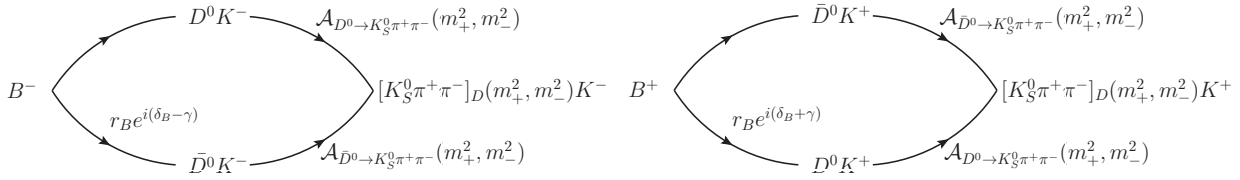

(a) B^- decay (b) B^+ decay

Figure 1.9: Diagram of interference between decay amplitudes for the decays $B^- \to [K^0_S\pi^+\pi^-]_D K^-$ and $B^+ \to [K^0_S\pi^+\pi^-]_D K^+$ where the decay to the $\tilde{D}$ final state could take place via a D^0 or $\bar{D}^0$ meson.

The amplitude for the decay $D^0 \to K^0_S\pi^+\pi^-$ is written as a function of position in the D^0 meson Dalitz plane whose axes are chosen to be $m^2_+ = m(K^0_S\pi^+)^2$ and $m^2_- = m(K^0_S\pi^-)^2$:

$$\mathcal{A}_{D^0}(m^2_+, m^2_-) = |\mathcal{A}_{D^0}(m^2_+, m^2_-)| e^{i\delta_{D^0}(m^2_+, m^2_-)}, \tag{1.23}$$

where $\delta_{D^0}(m^2_+, m^2_-)$ is the strong phase of the D^0 amplitude at the (m^2_+, m^2_-) coordinate in the Dalitz plot. In the limit that charm CP violation can be neglected, the symmetry of the

final state under CP conjugation and inversion of the π^+, π^- pair results in

$$\mathcal{A}_{D^0\to K^0_S\pi^+\pi^-}(m^2_+, m^2_-) = \mathcal{A}_{\bar{D}^0\to K^0_S\pi^+\pi^-}(m^2_-, m^2_+). \tag{1.24}$$

A similar equation for the $\bar{D}^0$ decay is given by

$$\mathcal{A}_{\bar{D}^0\to K^0_S\pi^+\pi^-}(m^2_+, m^2_-) = |\mathcal{A}_{D^0\to K^0_S\pi^+\pi^-}(m^2_-, m^2_+)|e^{i\delta_{D^0}(m^2_-, m^2_+)}, \tag{1.25}$$

analogous to that given in Equation 1.23. In the case that $F = K^0_S\pi^+\pi^-$, the equations for $\mathcal{A}_{B^-\to[F]_D K^-}$ and $\mathcal{A}_{B^+\to[F]_D K^+}$ found earlier (Equations 1.8 and 1.9) are rewritten:

$$\begin{aligned}
\mathcal{A}_{B^-\to[K^0_S\pi^+\pi^-]K^-}(m^2_+, m^2_-) &= \mathcal{A}_{B^-\to D^0K^-} \times (\mathcal{A}_{D^0\to K^0_S\pi^+\pi^-}(m^2_+, m^2_-) \\
&\quad + r_B e^{i(\delta_B-\gamma)}\mathcal{A}_{\bar{D}^0\to K^0_S\pi^+\pi^-}(m^2_+, m^2_-)) \qquad (1.26)\\
\mathcal{A}_{B^+\to[K^0_S\pi^+\pi^-]K^+}(m^2_+, m^2_-) &= \mathcal{A}_{B^+\to \bar{D}^0K^+} \times (\mathcal{A}_{\bar{D}^0\to K^0_S\pi^+\pi^-}(m^2_+, m^2_-) \\
&\quad + r_B e^{(i\delta_B+\gamma)}\mathcal{A}_{D^0\to K^0_S\pi^+\pi^-}(m^2_+, m^2_-)). \qquad (1.27)
\end{aligned}$$

Using the relation given in Equation 1.25, these equations can be simplified:

$$\begin{aligned}
\mathcal{A}_{B^-\to[K^0_S\pi^+\pi^-]K^-}(m^2_+, m^2_-) &= e^{i\theta_1}\mathcal{A}_{B^-\to D^0K^-} \times (|\mathcal{A}_{D^0\to K^0_S\pi^+\pi^-}(m^2_+, m^2_-)| \\
&\quad + r_B e^{i(\delta_B-\gamma)}|\mathcal{A}_{D^0\to K^0_S\pi^+\pi^-}(m^2_-, m^2_+)|e^{-i\Delta\delta_D}) \\
&= e^{i\theta_1}\mathcal{A}_{B^-\to D^0K^-} \times (|\mathcal{A}_{D^0\to K^0_S\pi^+\pi^-}(m^2_+, m^2_-)| \\
&\quad + r_B e^{i(\delta_B-\gamma-\Delta\delta_D)}|\mathcal{A}_{D^0\to K^0_S\pi^+\pi^-}(m^2_-, m^2_+)|), \text{ and} \qquad (1.28)\\
\mathcal{A}_{B^+\to[K^0_S\pi^+\pi^-]K^+}(m^2_+, m^2_-) &= e^{i\theta_2}\mathcal{A}_{B^+\to \bar{D}^0K^+} \times (|\mathcal{A}_{D^0\to K^0_S\pi^+\pi^-}(m^2_-, m^2_+)|e^{-i\Delta\delta_D} \\
&\quad + r_B e^{i(\delta_B+\gamma)}|\mathcal{A}_{D^0\to K^0_S\pi^+\pi^-}(m^2_+, m^2_-)|)) \\
&= e^{i\theta_2}\mathcal{A}_{B^+\to \bar{D}^0K^+} \times (|\mathcal{A}_{D^0\to K^0_S\pi^+\pi^-}(m^2_-, m^2_+)| \\
&\quad + r_B e^{i(\delta_B+\gamma+\Delta\delta_D)}|\mathcal{A}_{D^0\to K^0_S\pi^+\pi^-}(m^2_+, m^2_-)|)), \qquad (1.29)
\end{aligned}$$

where the θ phases are irrelevant overall phases for the two equations which will disappear when the decay rate, instead of the decay amplitude, is considered. In these equations, the

quantity $\Delta\delta_D$ is defined by convention to be the difference in strong phase between the D^0 and $\bar{D}^0$ decays to the same Dalitz coordinate:

$$\begin{aligned}\Delta\delta_D(m_+^2, m_-^2) &\equiv \delta_{\bar{D}^0}(m_+^2, m_-^2) - \delta_{D^0}(m_+^2, m_-^2) \\ &= \delta_{D^0}(m_-^2, m_+^2) - \delta_{D^0}(m_+^2, m_-^2). \end{aligned} \tag{1.30}$$

This quantity is expected to vary significantly given the presence of numerous intermediate resonances in the $\tilde{D}$ decay. It is clear from Equations 1.28 and 1.29 that the presence of the CP-violating phase γ will not only cause a difference in the yield of B^+ and B^- candidates overall, but, by governing interference between $B^- \to D^0 K^-$ and $B^- \to \bar{D}^0 K^-$ decays which have different Dalitz distributions, will affect the distribution of $B^\pm$ candidates around the (m_+^2, m_-^2) Dalitz plot. It is the latter effect which is more significant and provides essentially all the sensitivity to γ in an analysis. In order to extract γ by studying the $B^\pm$ (m_+^2, m_-^2) Dalitz distributions, it is of course necessary to have an understanding of the behaviour of the strong phase difference $\Delta\delta_D$ in the Dalitz plot. This can be extracted from an amplitude model, similar to that proposed in Section 1.4. However, such an approach incurs significant systematic uncertainty on the extraction of γ as a result of modelling assumptions and is not the method employed in this thesis.

1.5.1 Dividing the Dalitz plot in order to make a model-independent determination of γ

Dividing the Dalitz plot into regions, as illustrated in Figure 1.10, increases the number of observables which can be measured in the analysis and therefore allows for the determination of γ as well as the other hadronic parameters without resorting to the use of an amplitude model. Each of the regions in the (m_+^2, m_-^2) plane is labelled arbitrarily by the index i. The decay rate in region i is then found by integrating the expressions for $|\mathcal{A}|^2$ using Equations

1.28 and 1.29 over that portion of the (m_+^2, m_-^2) plane:

$$N^i_{B^-\to[K^0_S\pi^+\pi^-]K^-} \propto \int_i d\vec{x}|\mathcal{A}_{D^0\to K^0_S\pi^+\pi^-}(m_+^2,m_-^2)|^2 + r_B^2\int_i d\vec{x}|\mathcal{A}_{D^0\to K^0_S\pi^+\pi^-}(m_-^2,m_+^2)|^2$$
$$+2r_B\int_i d\vec{x}|\mathcal{A}_{D^0\to K^0_S\pi^+\pi^-}(m_+^2,m_-^2)||\mathcal{A}_{D^0\to K^0_S\pi^+\pi^-}(m_-^2,m_+^2)|\cos(\delta_B-\gamma-\Delta\delta_D), \text{ and} \quad (1.31)$$
$$N^i_{B^+\to[K^0_S\pi^+\pi^-]K^+} \propto r_B^2\int_i d\vec{x}|\mathcal{A}_{D^0\to K^0_S\pi^+\pi^-}(m_+^2,m_-^2)|^2 + \int_i d\vec{x}|\mathcal{A}_{D^0\to K^0_S\pi^+\pi^-}(m_-^2,m_+^2)|^2$$
$$+2r_B\int_i d\vec{x}|\mathcal{A}_{D^0\to K^0_S\pi^+\pi^-}(m_+^2,m_-^2)||\mathcal{A}_{D^0\to K^0_S\pi^+\pi^-}(m_-^2,m_+^2)|\cos(\delta_B+\gamma+\Delta\delta_D). \quad (1.32)$$

In these expressions, $\int_i d\vec{x}$ is an integration in the (m_+^2, m_-^2) plane over the region labelled by i. By convention, regions with a positive value of i are chosen to lie in the region where $m_-^2 > m_+^2$, and negative i are defined in the opposite regions. These equations are simplified by means of the following relations and substitutions:

$$\cos(\delta_B-\gamma-\Delta\delta_D) = \cos(\delta_B-\gamma)\cos(\Delta\delta_D)+\sin(\delta_B-\gamma)\sin(\Delta\delta_D), \quad (1.33)$$
$$\cos(\delta_B+\gamma+\Delta\delta_D) = \cos(\delta_B+\gamma)\cos(\Delta\delta_D)-\sin(\delta_B+\gamma)\sin(\Delta\delta_D), \quad (1.34)$$
$$x_- \equiv r_B\cos(\delta_B-\gamma), \quad (1.35)$$
$$y_- \equiv r_B\sin(\delta_B-\gamma), \quad (1.36)$$
$$x_+ \equiv r_B\cos(\delta_B+\gamma), \quad (1.37)$$
$$y_+ \equiv r_B\sin(\delta_B+\gamma), \quad (1.38)$$
$$A_{+,-} \equiv |\mathcal{A}_{D^0\to K^0_S\pi^+\pi^-}(m_+^2,m_-^2)|, \text{ and} \quad (1.39)$$
$$r_B^2 = x_\pm^2+y_\pm^2, \quad (1.40)$$

to give

$$N^i_{B^-\to[K^0_S\pi^+\pi^-]K^-} \propto \int_i d\vec{x}A^2_{+,-} + (x_-^2+y_-^2)\int_i d\vec{x}A^2_{-,+}$$
$$+2x_-\int_i d\vec{x}A_{+,-}A_{-,+}\cos(\Delta\delta_D) + 2y_-\int_i d\vec{x}A_{+,-}A_{-,+}\sin(\Delta\delta_D), \text{and} \quad (1.41)$$
$$N^i_{B^+\to[K^0_S\pi^+\pi^-]K^+} \propto (x_+^2+y_+^2)\int_i d\vec{x}A^2_{+,-} + \int_i d\vec{x}A^2_{-,+}$$
$$+2x_+\int_i d\vec{x}A_{+,-}A_{-,+}\cos(\Delta\delta_D) - 2y_+\int_i d\vec{x}A_{+,-}A_{-,+}\sin(\Delta\delta_D). \quad (1.42)$$

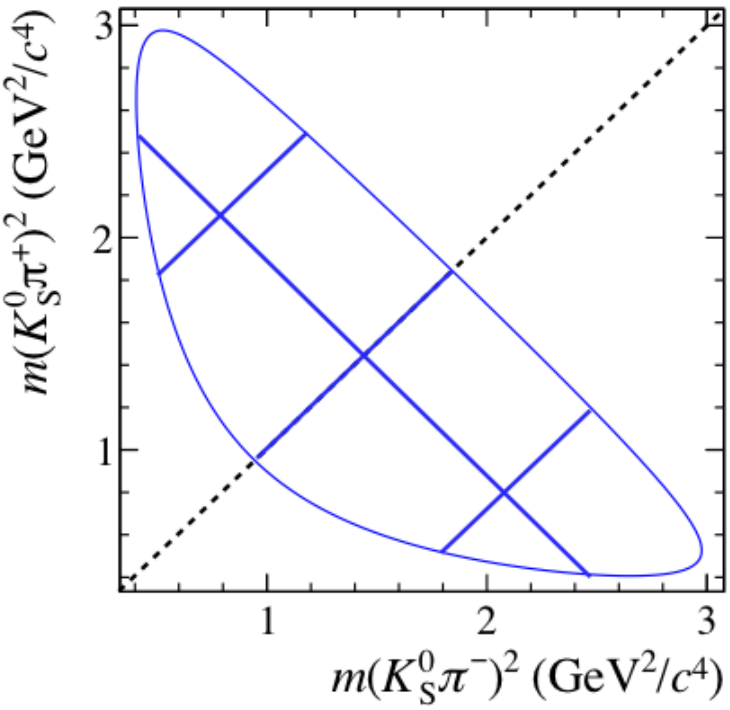

Figure 1.10: Simple division of the Dalitz plot according to a rectangular grid as first proposed in [29].

Choosing a Dalitz binning scheme

The symmetry of the final state under exchange of the $\pi^+\pi^-$ pair makes it sensible to choose bins which are symmetric about the diagonal symmetry axis in the (m^2_+, m^2_-) Dalitz plot. Bin i and bin $-i$ then lie in symmetrically opposing regions of the plot. The integrals are then replaced by the following:

$$K_i \equiv \int_i d\vec{x} A^2_{+,-}, \tag{1.43}$$

$$K_{-i} \equiv \int_i d\vec{x} A^2_{-,+}, \tag{1.44}$$

$$c_i \equiv \frac{\int_i d\vec{x} A_{+,-} A_{-,+} \cos(\Delta\delta_D)}{\int_i d\vec{x} A_{+,-} A_{-,+}}, \text{ and} \tag{1.45}$$

$$s_i \equiv \frac{\int_i d\vec{x} A_{+,-} A_{-,+} \sin(\Delta\delta_D)}{\int_i d\vec{x} A_{+,-} A_{-,+}}, \tag{1.46}$$

where the c_i and s_i are the amplitude weighted averages of the cosine or sine, respectively, of the strong phase difference $\Delta\delta_D = \delta_{D^0}(m_-^2, m_+^2) - \delta_{D^0}(m_+^2, m_-^2)$. It is clear by symmetry that, $c_{-i} = c_i$ and $s_{-i} = -s_i$. The K_i terms can be determined by measuring the yield of a flavour tagged $D^0 \to K^0_S\pi^+\pi^-$ decay in the region i and, since only relative values are needed, the K_i are often presented normalised to unity. The final equations are

$$\begin{aligned} N^{\pm i}_{B^- \to [K^0_S\pi^+\pi^-]K^-} &= h_- \left[K_{\pm i} + (x_-^2 + y_-^2)K_{\mp i} + 2\sqrt{K_i K_{-i}}(x_- c_{\pm i} \pm y_- s_{\pm i})\right] \\ N^{\pm i}_{B^+ \to [K^0_S\pi^+\pi^-]K^+} &= h_+ \left[(x_+^2 + y_+^2)K_{\pm i} + K_{\mp i} + 2\sqrt{K_i K_{-i}}(x_+ c_{\pm i} \mp y_+ s_{\pm i})\right], \end{aligned} \quad (1.47)$$

where the $h_\pm$ are normalisation factors such that the sum of all the $N^{\pm i}$ yields in the regions across the Dalitz plot is equal to the total $B^\pm$ yield.

Required number of Dalitz regions

Given the symmetry of the Dalitz plot about the $m_+^2 = m_-^2$ axis, N regions are chosen, symmetrically, on each side of the plot. There are therefore $4N$ observables: a B^+ and a B^- yield in each region on each side of the plot. There are $2N + 5$ unknowns: c_i and s_i in each bin on one side of the plot as well as r_B, δ_B, γ and the normalisation factors $h_\pm$. For $N > 2$, the system of equations is solvable. In fact, knowledge of the c_i and s_i parameters can be gained from quantum correlated D decays in data from the CLEO-c experiment, as described in Chapter 4, reducing the number of parameters measured, giving greater fit stability and more precise measurement of γ. The CLEO analysis used a division of the Dalitz plot into non-rectangular regions, unlike those in Figure 1.10, and the motivation for this choice of binning is discussed in Section 4.2. It is unfeasible to carry out the analysis at LHCb with the limited data samples currently available without exploiting the CLEO-c data in this way and doing so further improves the sensitivity to γ, r_B and δ_B in this analysis. Use of the CLEO-c data avoids the need for an amplitude model to describe the behaviour of the D strong phase in the Dalitz plot. A model-independent measurement of γ in $B^\pm \to \tilde{D}K^\pm$ decays is presented in Chapters 4 and 5.

2 The CLEO and LHCb Experiments

This thesis presents analyses of data from two experiments: a charm analysis using data from the CLEO III and CLEO-c experiments and a study of CP violation in B meson decays using LHCb data. This chapter describes the detector apparatus for each analysis.

2.1 The CLEO III and CLEO-c experiments

2.1.1 The Cornell Electron Storage Ring (CESR)

The CLEO III and CLEO-c detectors were situated on the Cornell Electron Storage Ring, pictured in Figure 2.1, which was an e^+e^- collider at Cornell University, Ithaca, NY. Electrons were accelerated by means of a linear accelerator (LINAC), and the electron beam impinged upon a tungsten target to produce positrons. The resulting electron/positron beams were inserted into the synchrotron, circulating just within the main storage ring, and accelerated further. The beams were then transferred to the storage ring where, after more acceleration and focussing, the instantaneous luminosity reached $2 \times 10^{33}\,\mathrm{cm}^{-2}\,\mathrm{s}^{-1}$.

2.1.2 The CLEO III and CLEO-c detectors

The hermetic detector for the CLEO experiment passed through a number of distinct phases during the operating period of the experiment from 1979 until 2008, but only the final two, 'CLEO III' (1999 to 2003) and 'CLEO-c' (2003 to 2008), are relevant to this thesis. The

Figure 2.1: Aerial view of the Cornell University campus with the position of CESR indicated in white [37].

data set collected during the CLEO III phase of operation amounted to $15\,\text{fb}^{-1}$, for which the centre-of-mass energy was set at the $\Upsilon(4S)$ resonance for much of the period. This energy scale was chosen primarily to allow b-physics studies but the large numbers of charm mesons produced promptly under the resonance makes the data set suitable for charm physics studies also. In 2003, following the advent of the asymmetric B factories providing much larger b-physics data sets than those available to CLEO, the CESR centre-of-mass energy was reduced to values in the range of 3 GeV to 4.2 GeV to facilitate precise measurements in the charm system. A data set corresponding to an integrated luminosity of $818\,\text{pb}^{-1}$ was then collected using the CLEO-c detector configuration.

A diagram of the CLEO-c detector is shown in Figure 2.2, differing only from the CLEO III configuration by the replacement of the CLEO III silicon detector with a drift chamber, reducing the detector material in this region, and the reduction of the magnetic field to improve the momentum determination for low energy particles.

The major components of the CLEO III and CLEO-c detectors are now described in order, from the $\sim$ 5 cm-diameter beryllium beam-pipe through the tracking system and particle identification (PID) system to the calorimeters beyond. The muon chambers, which are the final layer of the detector, are not used in the current analysis and are therefore

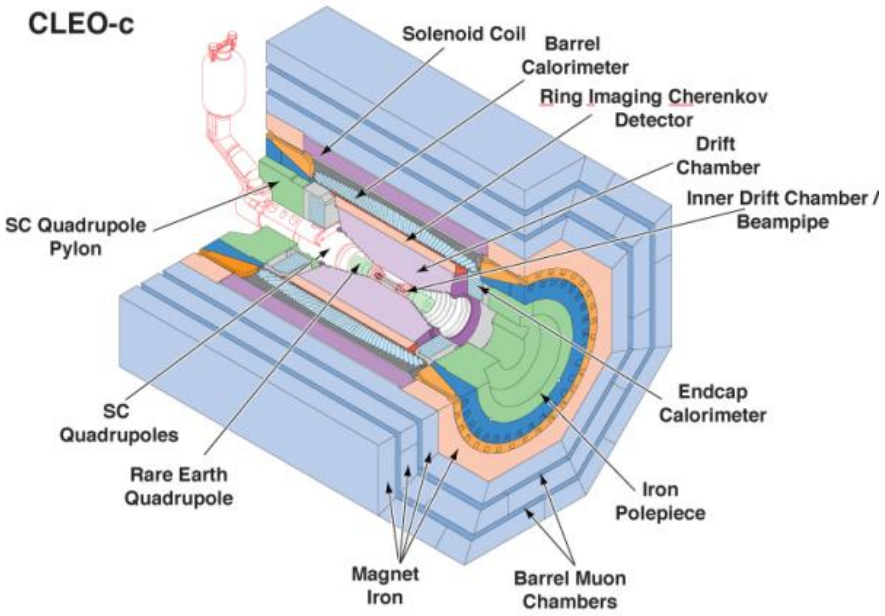

Figure 2.2: Diagram of the CLEO-c detector [37].

omitted from the discussion.

2.1.3 Magnet assembly

The CLEO II.V solenoid magnet [38], enclosing the ECAL, was retained in the CLEO III data-taking period and achieved a 1.5 T field strength with a high uniformity. The superconducting coil had an inner diameter of 2.9 m, was 3.5 m in length and operated at a current of 3300 A. The flux return was provided by three layers of steel interleaved between the muon detectors. A sheet of steel with a 2.5 cm thickness enclosed the outermost muon chamber to provide radiation shielding. Thermal isolation of the coil was achieved using a radiation screen built from panels of honeycomb aluminium and cooled using liquid nitrogen.

The field uniformity obtained was high: a variation of 0.1% over the full 2 m long by 1 m radius drift chamber. When converting the CLEO III detector to the CLEO-c configuration, the average track momenta decreased due to the decreased centre-of-mass energy and a lower field strength of 1.0 T was chosen in order to allow better measurement of low momentum tracks.

2.1.4 Tracking: drift chambers and silicon detector

Outside the beam-pipe, with a radial distance from the beam axis between 3 cm and 10 cm, the CLEO III detector contained a silicon-strip vertex detector with four double-sided layers comprising a total of around 125,000 strips. In the transition from CLEO III to CLEO-c, this silicon detector was replaced by a drift chamber spanning a radial interval of 5 cm to 11 cm, filled with a 60:40 mixture of helium-propane. The new collision energy meant that the ability to vertex B decays was no longer required and a reduction in the detector material in this region could instead be attained. The CLEO-c inner drift chamber is shown in two orientations in Figure 2.3. The main drift chamber occupied the space from 13 cm to 80 cm from the beam axis with 16 axial layers and a further 31 layers, with a small stereo angle of approximately 25 mrad. The spatial resolution achieved by the tracking system was 88 μm [39] and the relative momentum resolution was 0.6% for tracks with $p = 1.0\,\text{GeV}/c$ [40]. The main drift chamber is shown in Figure 2.4. An example event display is given in Figure 2.5, where the low multiplicity of the collisions, a consequence of the fact that no fragmentation particles are produced, is evident.

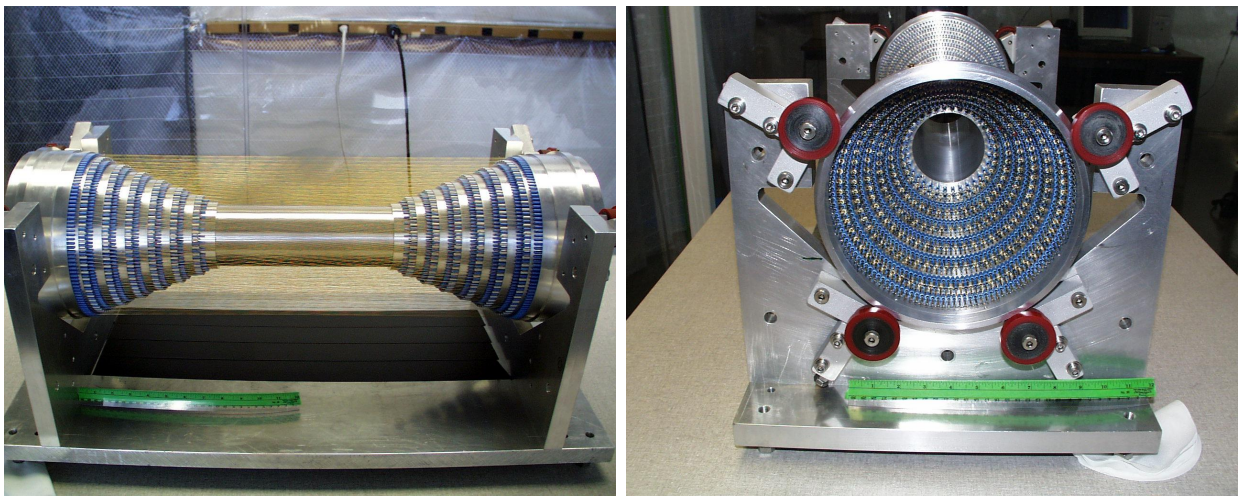

Figure 2.3: Photograph of the CLEO-c inner drift chamber [41].

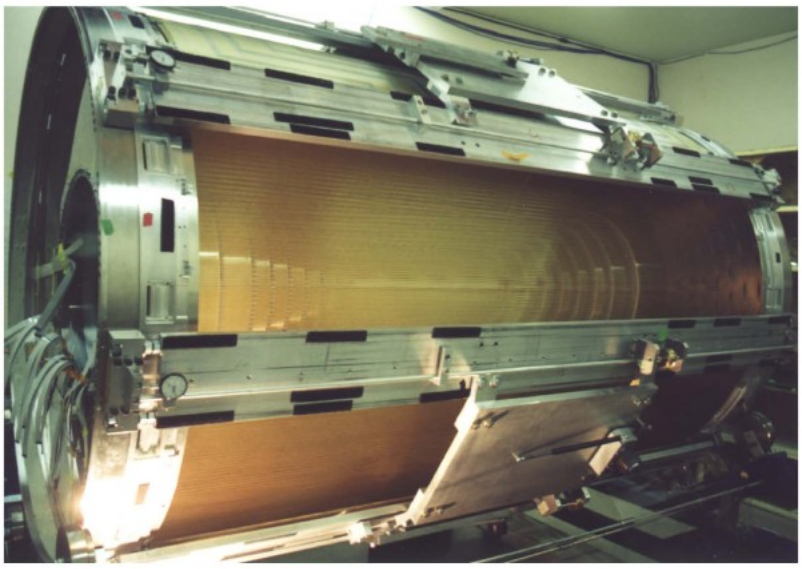

Figure 2.4: Photograph of the main CLEO drift chamber [37].

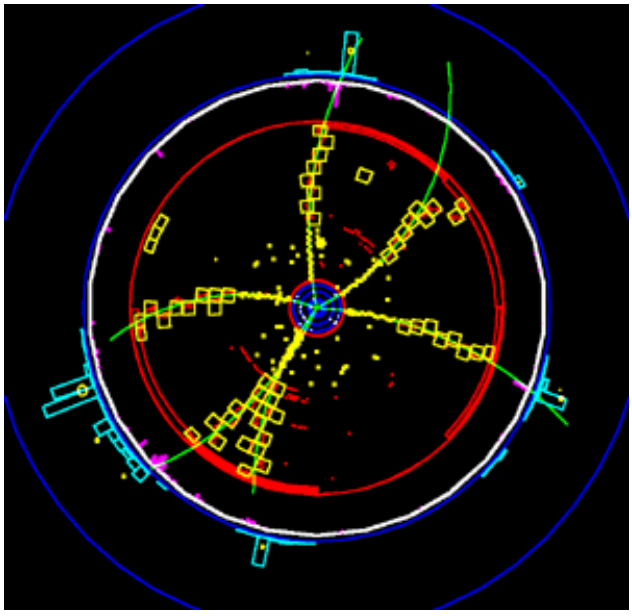

Figure 2.5: An example $D\bar{D}$ event, recorded by the CLEO-c detector [37].

2.1.5 Particle identification: $\frac{dE}{dx}$ and Ring Imaging Cherenkov (RICH) detector

The energy deposits in the sense wires of the drift chamber were used to measure the energy loss for a particle as a function of distance along its path. With reference to the Bethe-Bloch formula [42], the rate of energy deposit as a function of distance in a material was related to the speed of the ionising particle. Combined with a determination of the particle's momentum through its track curvature in a known magnetic field, the mass of the particle was then determined.

Above track momenta of around 700 MeV/c, measurements of $\frac{dE}{dx}$ cease to provide significant discrimination between particle masses, and a RICH detector is used to measure the particle's speed instead. A RICH detector provides a means to measure a particle's velocity which, through its relation to the particle's momentum, can be used to determine its mass and thus provide particle identification. A RICH works by exploiting Cherenkov emission by which coherent radiation is emitted in a cone around a charged particle's track when it traverses a medium with refractive index n at a speed greater than the speed of light in that medium, c/n. The angle, θ_c, at which the Cherenkov light is emitted depends upon the speed of the particle, v:

$$\cos\theta_c = \frac{c}{nv}, \tag{2.1}$$

where c is the speed of light. The usefulness of a RICH detector is limited at very high momenta where particles with different, high values of momentum have almost identical speed ($\sim c$) and hence almost identical Cherenkov angle ($\cos^{-1}\frac{1}{n}$). This makes it harder to distinguish particles with a different mass.

In order to minimise scattering before the CsI crystal calorimeter and to avoid imposing on the space reserved for this or the drift chamber, the CLEO RICH was allocated a radial space of 20 cm, with material occupying 12% of a radiation length [43]. A diagram of the detector is given in Figure 2.6. In order to fit the RICH in the available space, a thin, 1 cm-thick LiF crystal radiator was inserted by the inner surface, generating photons in the

135 – 165 nm wavelength range. Allowing a distance between the radiator and detector to enable proximity focussing of the generated Cherenkov light, the thin detector chosen was a multi-wire chamber filled with methane (CH_4, 93%) and photo-sensitive triethylamine (TEA, 7%) vapour [44].

The Cherenkov angle resolution per track, measured at CLEO III, was between 3.7 and 4.9 mrad. Studies using CLEO-c data, where the maximum particle momentum was between 1 GeV/c and 1.5 GeV/c demonstrated that the kaon-pion separation achieved was high: a typical $\pi \to K$ fake rate of $(1.10 \pm 0.37)\%$ for a pion efficiency of $(94.5 \pm 0.4)\%$. In the same data, the $K \to \pi$ fake rate was $(2.47 \pm 0.38)\%$ for a kaon efficiency of $(88.4 \pm 0.6)\%$ [43].

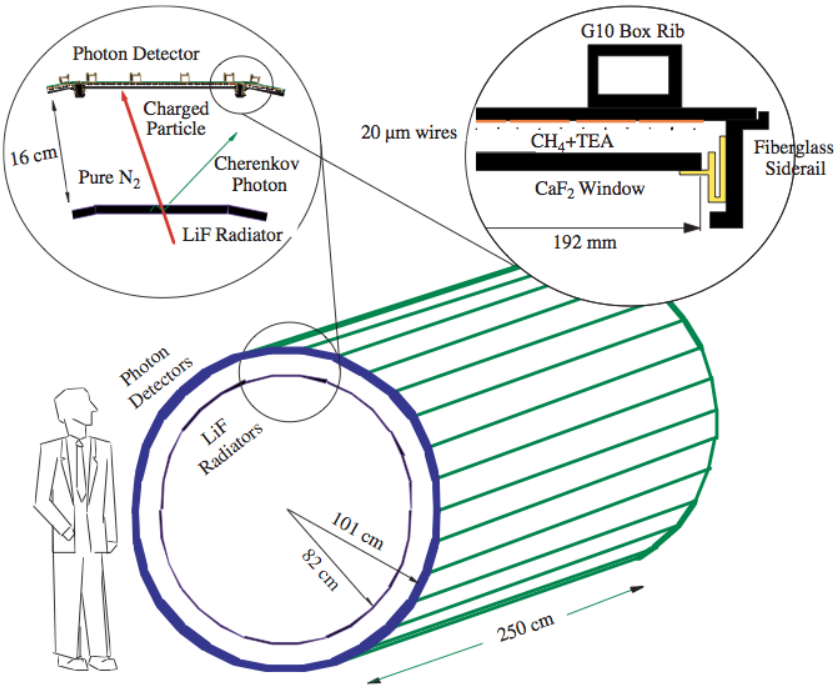

Figure 2.6: Diagram of the CLEO RICH detector, taken from [43].

2.1.6 Calorimetry

The electromagnetic calorimeter comprised 7800 caesium iodide crystals, doped with thallium, each measuring approximately 5 cm square and 30 cm long. These crystals produced a light output, falling with a 900 ns time constant. The barrel, whose coverage extended

from a polar angle of 32°, and endcaps, whose coverage extended up to a polar angle of 36°, provided a 95% solid angle coverage. Nitrogen was pumped through the containers for the CsI crystals in the barrel and endcaps to keep the crystals dry. Four silicon photodiodes were mounted on the rear of each crystal, each connected to a preamplifier which sent the signal outside the detector. Clusters of deposits in crystals were then analysed to estimate the energy of an individual shower.

The energy resolution for photons of energy 5 GeV was 1.5% in the barrel and 2.6% in the endcap, and the angular resolutions were 3 mrad and 9 mrad, respectively. At 100 MeV the energy resolution was 3.8% in the barrel and 5.0% in the endcap and the angular resolutions were 11 mrad and 19 mrad, respectively [38]. Parameterisations of the energy resolution, σ_E, were developed using simulations for the barrel and endcap separately and are given as a function of photon energy, E, in GeV [38]:

$$\frac{\sigma_E}{E}(\%) = \frac{0.35}{E^{0.75}} + 1.9 - 0.1E \text{ (barrel)}, \tag{2.2}$$

$$\frac{\sigma_E}{E}(\%) = \frac{0.26}{E} + 2.5 \text{ (endcap)}. \tag{2.3}$$

2.1.7 Trigger and data acquisition

The first level CLEO III trigger decision was based on the track count or topology in the drift chamber, or the calorimeter shower count and topology. The tracking trigger collated the output from all the wires in the sixteen axial layers and blocks of four-by-four stereo wires. The calorimeter trigger used deposits in the CsI crystals which had been grouped together for adjacent tiles to reduce the trigger processing time. A typical event during CLEO III operation contained around ten showers and ten tracks.

For an instantaneous luminosity of $10^{33}\,\mathrm{cm}^{-2}\,\mathrm{s}^{-1}$ the trigger rate was approximately 80 Hz, broadly divided into the eight trigger channels listed in Table 2.1. In Table 2.1, the different channels are detailed along with their rates relative to the Barrel Bhabha channel which has a rate of approximately 20 Hz.

A very similar trigger configuration operated for CLEO-c with a similar output rate, though the instantaneous luminosity was lower at around $7 \times 10^{32}\,\mathrm{cm}^{-2}\,\mathrm{s}^{-1}$. If a triggered event arrived whilst the detector was still being read out, the new event was discarded, leading to an average dead time of less than 0.3% of the $20\,\mu$s to $30\,\mu$s event readout time.

Table 2.1: CLEO III trigger lines with rate given relative to the Barrel Bhabha channel, extracted from [45].

Name	Prescale	Relative rate
Hadronic	1	0.41
μ-pair	1	1.40
Barrel Bhabha	1	1.0
Endcap Bhabha	8	0.23
Electron + track	1	1.48
τ/radiative	10	0.69
Random	1000	1

Raw events which have been triggered are reconstructed in an offline processing centre, combining tracks and calorimeter showers and forming short-lived particle candidates (e.g. π^0) ready for analysis. The $\frac{dE}{dx}$ and RICH information is added for particles reconstructed from detected tracks.

2.1.8 Simulated samples

In order to produce simulated samples for selection and detector acceptance studies, e^+e^- collisions were simulated using an event generator, QQ [46] for CLEO III and EvtGen [47] for CLEO-c. These generators were used to simulate events produced at collision energies matching those in data. The decays of the resulting short-lived particles could be forced to follow a specific decay chain or allowed to decay according to a generic decay file containing a large number of processes and their respective branching ratios.

The interaction of the generated particles with the detector material was modelled using the GEANT toolkit [48] where the appropriate CLEO III or CLEO-c geometry and detector material were included. The same reconstruction code was applied to the final simulated sample as was applied to data, producing reconstructed events in the same format as the

data but with additional information about the generated particles.

2.2 The LHCb experiment

2.2.1 The Large Hadron Collider (LHC)

The LHC accelerator complex, shown in Figure 2.7, is dominated by a large pp collider which began operation in 2009. The accelerator chain begins with hydrogen gas which, ionised, forms a source of protons which then leave the linear accelerator (LINAC) via the 'PS booster' to enter the Proton Synchrotron (PS). These protons are accelerated in the Super Proton Synchrotron (SPS) to energies of 450 GeV before they enter the 27 km-long LHC tunnel in bunches where, in 2011, each was separated by 50 ns. The data analysed in this thesis were taken in 2011 during which time the collision energy was 7 TeV. The beams were offset at the location of LHCb, 'Point 8' on the LHC ring, to reduce the instantaneous luminosity from the peak in the ATLAS and CMS detectors of $3.7 \times 10^{33}\,\mathrm{cm}^{-2}\,\mathrm{s}^{-1}$ to a maximum of around $3.5 \times 10^{32}\,\mathrm{cm}^{-2}\,\mathrm{s}^{-1}$ for LHCb. This ensured that the average number of visible interactions per bunch crossing was about 1.4 so that pile-up in the detector was kept at a low level [49]. At the ATLAS and CMS collision points, the instantaneous luminosity diminished over time as ongoing collisions depleted the beam's proton content. At LHCb the instantaneous luminosity, and thus the interaction rate, was held constant by compensating for the depleted beams by returning them to closer alignment. This technique of 'luminosity levelling' enabled LHCb to operate at a constant, optimal instantaneous luminosity for the duration of the proton fill, an example of which can be seen in Figure 2.8. In total, LHCb collected data corresponding to an integrated luminosity of $1.0\,\mathrm{fb}^{-1}$ during 2011.

2.2.2 The LHCb detector

LHCb is a single-arm spectrometer with a coverage from 10 mrad to 300 mrad in the bending plane and 250 mrad in the non-bending plane, corresponding to a pseudorapidity range of

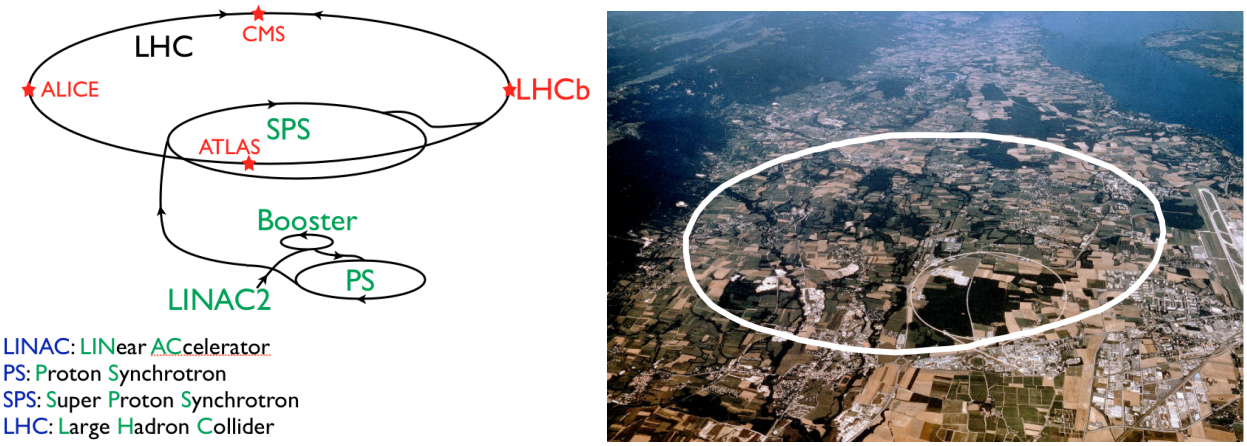

Figure 2.7: Schematic diagram of the LHC accelerator complex, left, and aerial view, courtesy of CERN, right.

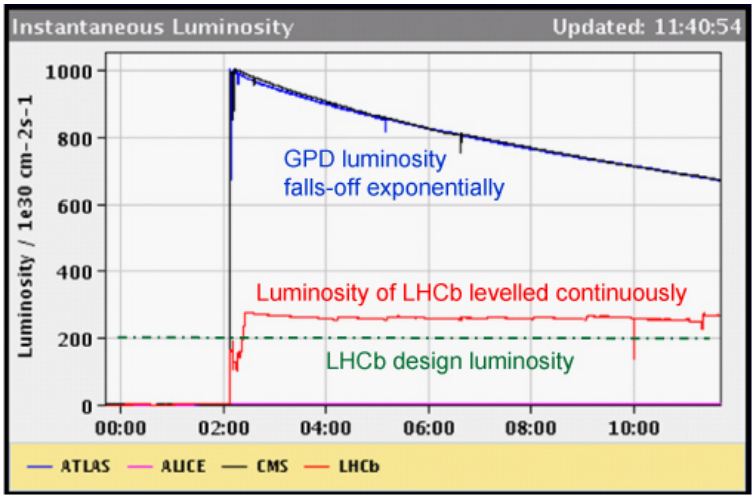

Figure 2.8: Trends in instantaneous luminosity observed in the General Purpose Detectors (GPDs), decreasing due to beam depletion in collisions, and in LHCb where the constant level is achieved by gradually returning the beams to closer alignment during the fill [50].

between 2 and 5. This geometry makes it well suited to the study of events containing particles formed from a $b\bar{b}$ pair where the pair are preferentially produced in the forward direction [51] (see Figure 2.9).

A diagram of the LHCb detector is shown in Figure 2.10, showing the major detector components and defining the coordinate system. The sub-detectors most relevant to this thesis are described in this section, beginning with the vertex locator (VELO) and continuing downstream in the z-direction[1] from the interaction region. The muon chambers, though an essential part of the trigger, are not of central importance for the analysis described in this thesis so are not described here. In the description which follows, transverse quantities (with a 'T' subscript) refer to the quantity defined in the direction transverse to the beam axis.

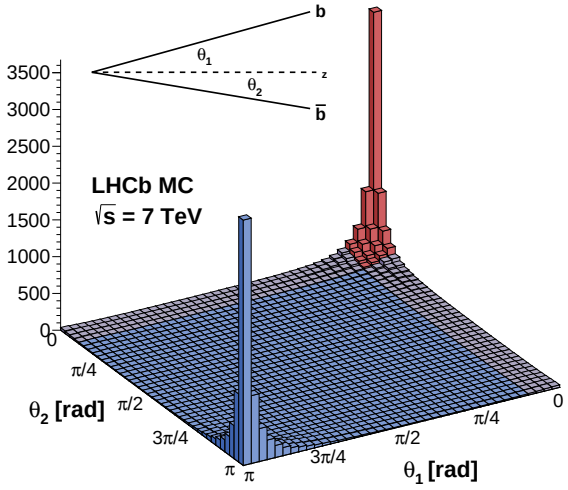

Figure 2.9: Simulated $b\bar{b}$ events showing the propensity for quark pairs to be produced parallel or antiparallel to the z-direction in the centre-of-mass frame [52].

2.2.3 Tracking

The LHCb tracking system consists of several parts, each labelled in Figure 2.10. The Vertex Locator (VELO) and Trigger Tracker (TT) are silicon microstrip detectors, placed before

[1]For LHCb, the 'z-direction' refers to an axis oriented along the beam pipe through the detector with origin in the VELO

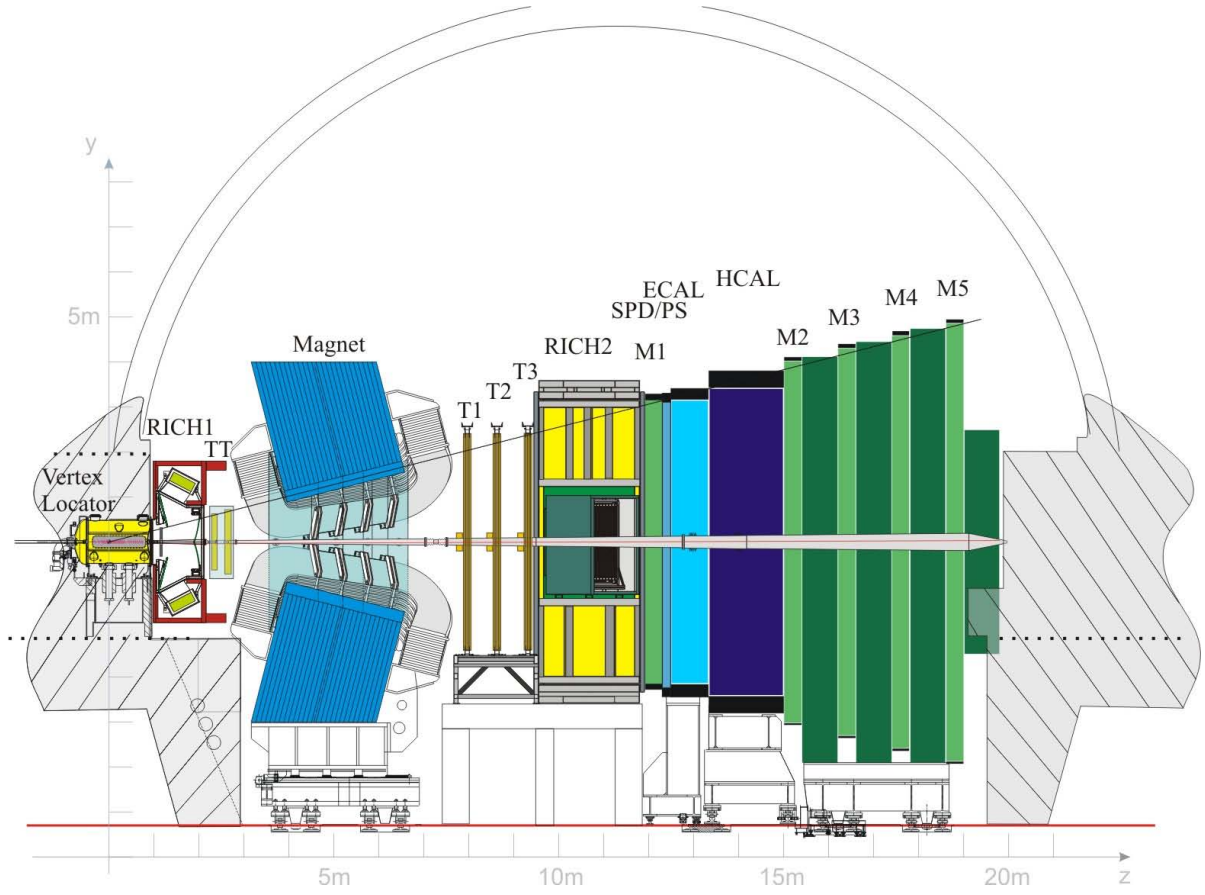

Figure 2.10: Diagram of the LHCb detector located at Point 8 on the LHC accelerator ring.

the bending magnet, and are supplemented by three tracking stations (T1-3) downstream from the interaction point, after the magnet.

The Vertex Locator (VELO)

In order to reconstruct production and decay vertices of short-lived B mesons and D mesons with typical flight distances of 10 mm and 3 mm respectively, a high resolution silicon-strip detector, the VELO, is placed close to the interaction region. The detector is divided into two mobile sections either side of the beam axis and, once the LHC beam has reached a stable circulation, these sections move 29 mm horizontally until the sensor region is only 8.2 mm from the beam. The VELO consists of 84 sensors. Within each half of the VELO, there are 21 modules which are constructed by mounting two sensors back-to-back on a support structure where one sensor is a 'ϕ-type', with radial strips, and one is an 'R-type' with sensors arranged azimuthally, as shown in Figure 2.11(a). The active region extends radially between 8.2 mm and 42 mm from the beam axis.

The VELO modules are enclosed within a vacuum independent of the LHC vacuum. The inner walls of the enclosure which face the beam are corrugated sheets, forming an 'RF-foil' which provides RF shielding from the beam and protects the LHC vacuum from VELO outgassing.

Tracks which lie within the LHCb acceptance cross at least three VELO stations. This allows the VELO to achieve a 4 μm best hit resolution, given an ideal track angle, and a track-finding efficiency greater than 98%. The impact parameter resolution is better than 35 μm for particles with transverse momentum (measured with respect to the beam axis) greater than 1 GeV/c and, for a vertex of 25 tracks, the vertex resolution is 13 μm in the transverse plane [53] and 71 μm along the beam axis [54].

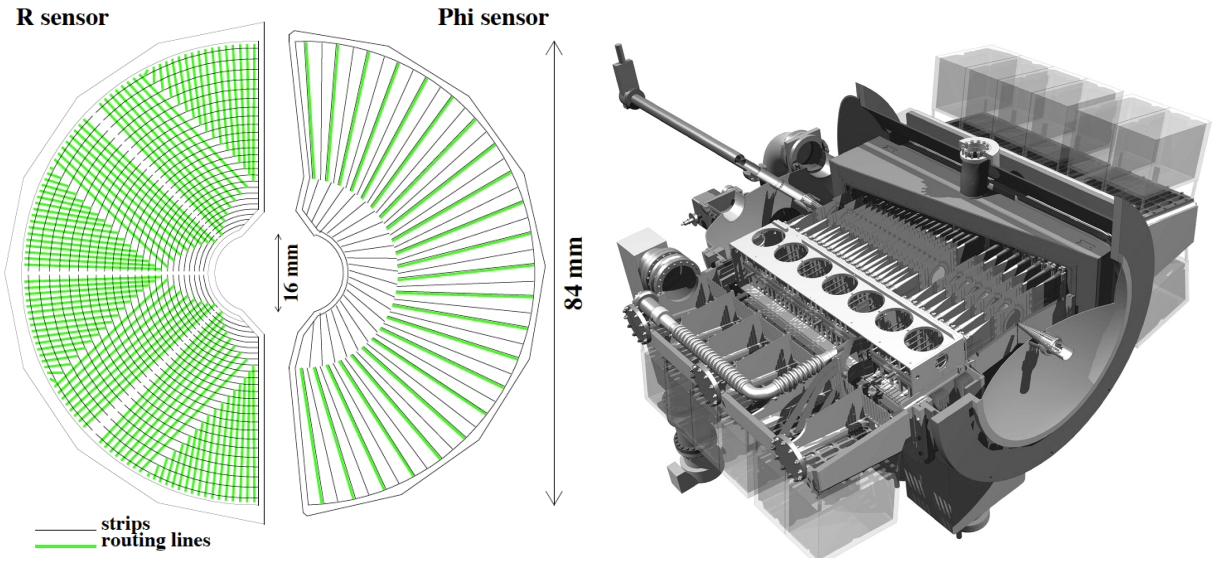

(a) Schematic diagram of the two VELO sensor types, taken from [55].

(b) 3-d CAD image of VELO, taken from [54].

Figure 2.11: The LHCb vertex locator (VELO).

The TT and tracking stations

The next component of the tracking system is the TT, a silicon microstrip detector, immediately upstream of the LHCb magnet. The plane of the detector encloses the whole of the LHCb acceptance, 150 cm wide and 130 cm high.

The final elements of the tracking system are the tracking stations, located downstream from the magnet. The inner tracker (IT) region, 120 cm wide and 40 cm high enclosing the beam-pipe, is covered with silicon microstrips. Like the TT, the IT portion of each tracking station contains four layers where the middle two are rotated about the beam axis by $+5°$ and $-5°$ degrees respectively, relative to the first and fourth layers. The IT modules are enclosed in gas-tight boxes, just as for the TT, through which nitrogen is pumped to prevent condensation occurring and to ensure that the temperature is maintained below 5°C. The outer tracker (OT) region of each tracking station covers the remainder of the tracking station detector plane and is composed of straw chamber modules. These modules contain two layers of 2.4 m-long straw tubes, each with an inner diameter of 4.9 mm. Straw tubes are chosen for the OT region which is defined so that the innermost tubes experience an occupancy below 10% for a luminosity of $2 \times 10^{32}\,\mathrm{cm}^{-2}\,\mathrm{s}^{-1}$. Although the IT covers only 2%

of the tracking station plane, $0.3\,\mathrm{m}^2$, it encounters 20% of the primary particles produced [56].

Track reconstruction algorithms

Tracks in LHCb fall into one of five categories according to which sub-detectors the track registers hits in, as illustrated in Figure 2.12.

- **Long tracks**

  These tracks are formed from hits in the VELO, TT and tracking stations and, as a result, have the highest momentum resolution. Studies with 2011 data indicate a track-finding efficiency of around 97% for those with momentum over $5\,\mathrm{GeV}/c$ [57]. The momentum resolution, $\Delta p/p$, varies between 0.4% and 0.6% over a momentum range from $5\,\mathrm{GeV}/c$ to $100\,\mathrm{GeV}/c$, and the impact parameter resolution is $20\,\mu\mathrm{m}$ for tracks with large transverse momentum [1].

- **Upstream tracks**

  Upstream tracks leave hits in the VELO and TT but are then bent out of the LHCb acceptance as they pass through the magnet and are not used in this analysis.

- **Downstream tracks**

  Downstream tracks leave hits only in the TT and tracking stations. The decay products of long-lived 'V0' particles such as K^0_S mesons are an important source of such tracks. The ratio of K^0_S candidates whose decay vertex is reconstructed beyond the VELO to those whose vertex is reconstructed within it is approximately 2:1.

- **VELO tracks**

  These tracks are found only in the VELO and are used to reconstruct primary vertices and in the trigger, as described in Section 2.2.7.

- **T tracks**

  T tracks are found only in the tracking stations and are used in the reconstruction

process as, for example, seeds for the tracking algorithm in forming long tracks from VELO and T tracks.

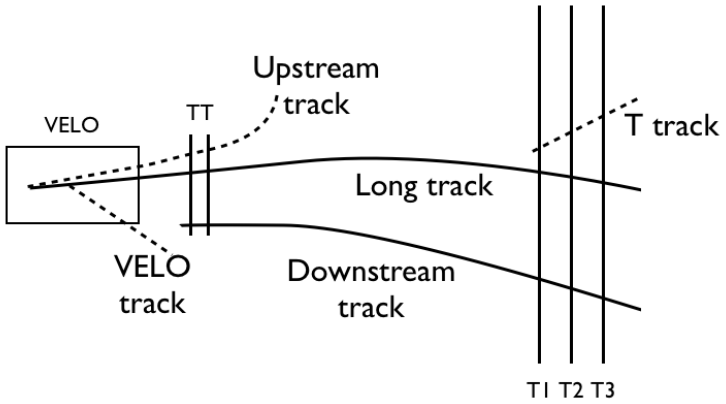

Figure 2.12: Schematic diagram of the five categories of tracks in LHCb [51].

Tracks are initially found in the VELO and tracking stations where the effect of the magnetic field is small, and the full track trajectory through the TT and magnet is then determined by refitting with a Kalman filter [58, 59]. The refit includes treatment of multiple scattering effects and energy loss over the particle trajectory.

After the full reconstruction process, typical invariant mass resolutions are around $8\,\mathrm{MeV}/c^2$ for $B \to J/\psi X$ decays, with a mass constraint applied on the J/ψ, $22\,\mathrm{MeV}/c^2$ for two-body B decays, and $100\,\mathrm{MeV}/c^2$ for $B_s^0 \to \phi\gamma$ [52].

2.2.4 Magnet

The LHCb detector employs a warm dipole magnet to produce an integrated field of 4 Tm for 10 m-long tracks. The magnet surrounds the entire acceptance, has a total resistance of 130 mΩ at a temperature of 20° and weighs 1600 tons [51]. The integrated field upstream of the TT, up to 2.5 m from the interaction point, is 0.12 Tm and that downstream, from 2.5 m to 8.0 m, is 3.6 Tm. The magnet produces a strong magnetic field between the TT and tracking stations but a weak field in the RICH detectors where a significant residual magnetic field would degrade the reconstruction of Cherenkov rings. In order to achieve this and a low field variation inside the detector acceptance, an unusual design was chosen for the

magnet, illustrated in Figure 2.13. The field exhibits non-uniformities of only $\pm 1\%$ across $1\,\mathrm{m}^2$ planes perpendicular to and centred on the beam-pipe from 3 m and 8 m downstream of the interaction point. The RICH detectors are shielded and the field experienced by the photo-detectors in the RICH detectors is less than 2×10^{-3} T.

Given the unusual magnet field, it was mapped using a carefully aligned array of Hall probes, providing measurements within a mesh of $8 \times 8 \times 10\,\mathrm{cm}^3$ units in a region from the interaction point as far as the RICH2 detector. The polarity of the magnetic field is regularly reversed to assist in overcoming systematic uncertainties in measurements of CP asymmetries relating, for example, to detection asymmetries between the left and right portions of the detector. In the study of 2011 data presented in this thesis, approximately half were taken with the field directed downwards and half with it reversed.

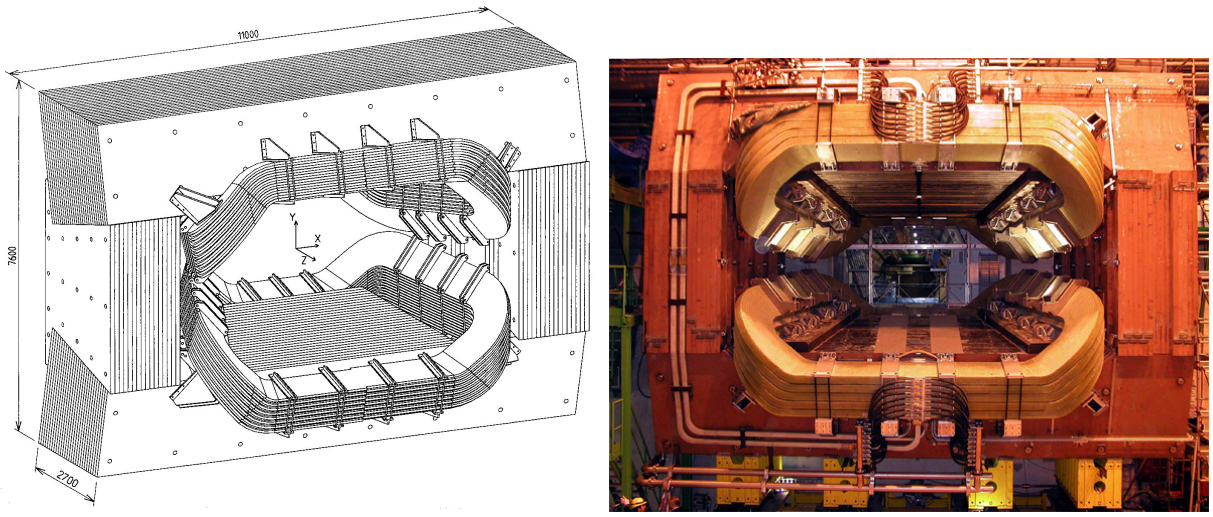

Figure 2.13: The LHCb magnet [60].

2.2.5 Particle identification (PID)

Different types of particles are identified using two RICH detectors, one upstream of the magnet and one downstream. Critical for the analysis described in this thesis is the capacity to separate pions, abundantly present in pp events, from kaons in order to distinguish $B^\pm \to DK^\pm$ and $B^\pm \to D\pi^\pm$ decays, or to help distinguish the $K^0_S\pi^+\pi^-$ final state from $K^0_S K^+ K^-$. Furthermore, particle identification also adds the ability to suppress combinato-

rial backgrounds which are formed by combining random pion tracks in the detector.

The first detector, RICH1 (Figure 2.14), occupies the region between the VELO and TT, from 1.0 m beyond the interaction point to 2.2 m, and covers the full LHCb acceptance. It provides particle identification information for particles with momentum from 1 GeV/c to 60 GeV/c, and is particularly useful for identifying lower-momentum tracks with large polar angles traversing the outer regions of the LHCb acceptance. RICH1 is filled with a fluorobutane (C_4F_{10}) gas radiator. An aerogel radiator is also present but, during early operation, the aerogel radiator was found to absorb the fluorobutane radiator gas which led to a degraded Cherenkov resolution, and the aerogel does not contribute to the PID measurements used in the current analysis.

The second RICH detector, RICH2 (Figure 2.15), does not cover the whole solid angle but instead caters for high-momentum forward tracks, having a polar angle acceptance of ± 120 mrad in the bending plane and ± 100 mrad vertically excluding the beam-pipe region. It lies between 9.5 m and 11.8 m and contains tetrafluoromethane (CF_4) as the radiator, providing PID for particles with momentum between 15 GeV/c and around 100 GeV/c. [51]

Both detectors employ spherical mirrors within the LHCb acceptance to focus the cones of Cherenkov light produced within the radiators, via flat mirrors, onto an array of photo-detectors outside the acceptance.

Photo-detector arrays

The photo-detectors of the RICH system are 'hybrid photo-detectors' (HPDs), as shown in Figure 2.16. Depending on the amount of light incident on the photocathode, a number of photoelectrons are emitted which are accelerated and focused onto a silicon pixel detector over a voltage drop of between 10 kV and 20 kV. The silicon detector layer is divided into 1024 square pixels of side 500 μm. Typically, for an operating voltage of 20 kV, an incident photoelectron causes 5000 electron-hole pairs to be produced at the silicon layer [61]. The photo-detectors are active over 82% of their detector area and are sensitive to light with

wavelength between 200 nm and 600 nm. The quantum efficiency for conversion of photons of wavelength 270 nm incident on the photocathode into electron-hole pairs is 30% [62].

There are 98 photo-detectors in RICH1 and 144 in RICH2, spaced by a distance of around 9 cm, and each surrounded by a Mu-metal layer, supplementing the magnet shielding provided by the iron boxes around the photo-detector arrays. Individual corrections are made to account for any remaining magnetic field distortion effects on the photo-detectors. Electronics modules read out the RICH photo-detectors and transmit an optical signal to the off-detector systems.

Cherenkov rings are reconstructed following a ring-finding pattern recognition procedure by which rings in the photodetector plane are searched for around reconstructed particle tracks. In order to determine the PID information, momentum data from the tracking system is used along with the hits in the photo-detectors to reconstruct Cherenkov rings, determine the Cherenkov angles and thus compute an overall event likelihood. The PID algorithm then maximises the event likelihood by changing the mass hypothesis (e, μ, π, K, p) for each track in a particular order until the overall event likelihood is maximised. In distinguishing electrons and muons, information from the calorimeters and muon systems is employed. Once the overall event likelihood has been maximised, the change in the logarithm of the likelihood, the delta-log likelihood (DLL), is computed for the change in mass hypothesis of each track and the information stored. Each candidate then has associated variables of the form 'DLL($X - \pi$)' for different PID hypotheses, X. Requirements placed on the values of these variables are referred to as 'PID requirements' throughout this thesis and are always accompanied by a requirement that the particle momentum is between 2 GeV/c and 100 GeV/c, according to the momentum range over which the RICH detectors can give useful information. This event-likelihood treatment ensures appropriate treatment of Cherenkov rings which overlap.

The Cherenkov angle resolution achieved using the C_4F_{10} RICH1 radiator is $(0.0927 \pm 0.0001)^\circ$ and for CF_4 in RICH2 is $(0.039 \pm 0.001)^\circ$ [62]. As an example of the separation achieved for different particle types, the calculated Cherenkov angle is shown against track

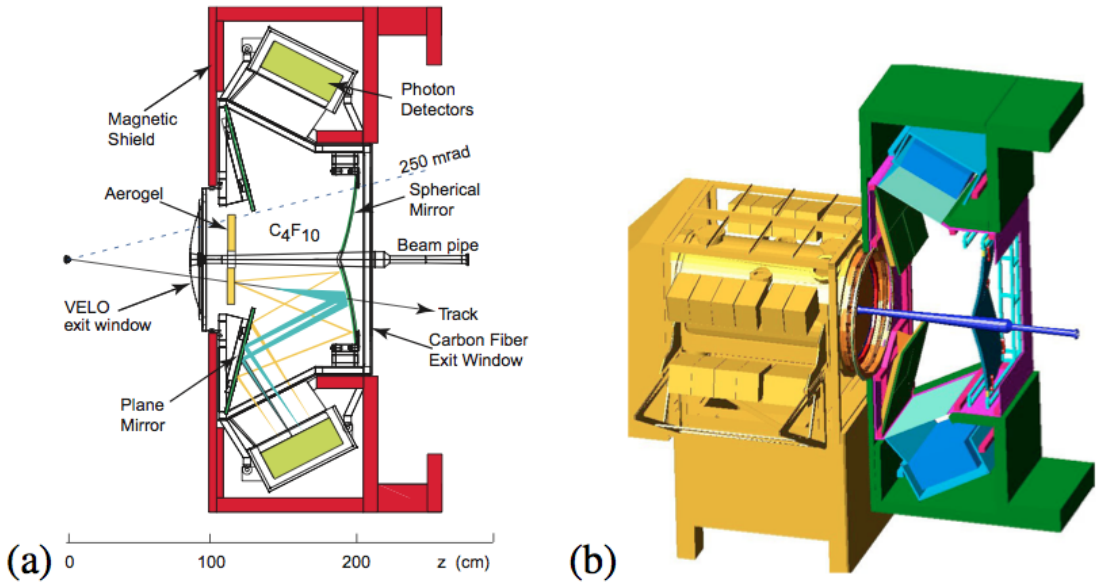

Figure 2.14: The first RICH detector, located upstream of the magnet, shown diagrammatically in cross section from the side in a) and in 3-d in b), in position immediately downstream of the VELO detector. Images taken from [51].

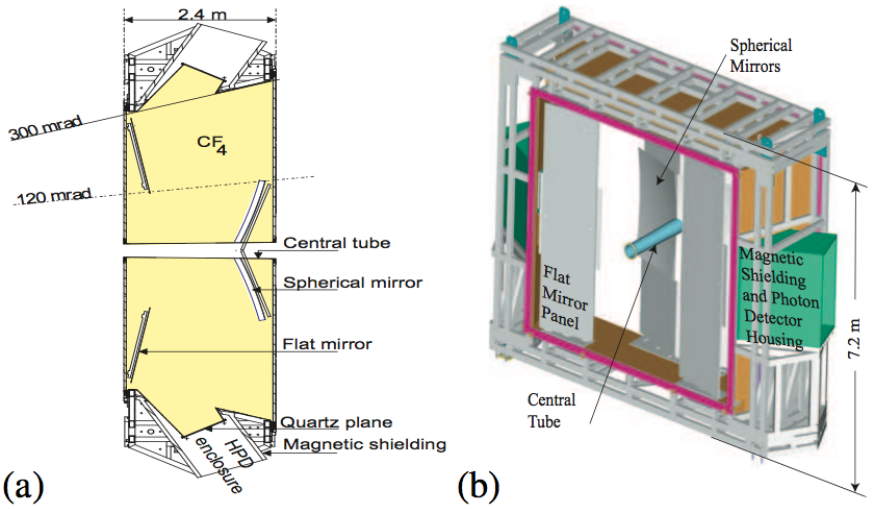

Figure 2.15: The second RICH detector, located downstream of the magnet and beyond the tracking stations T1-3. The detector is shown in cross section from above in a) and in 3-d in b) [51]. The positions of the mirrors and photo-detectors are indicated.

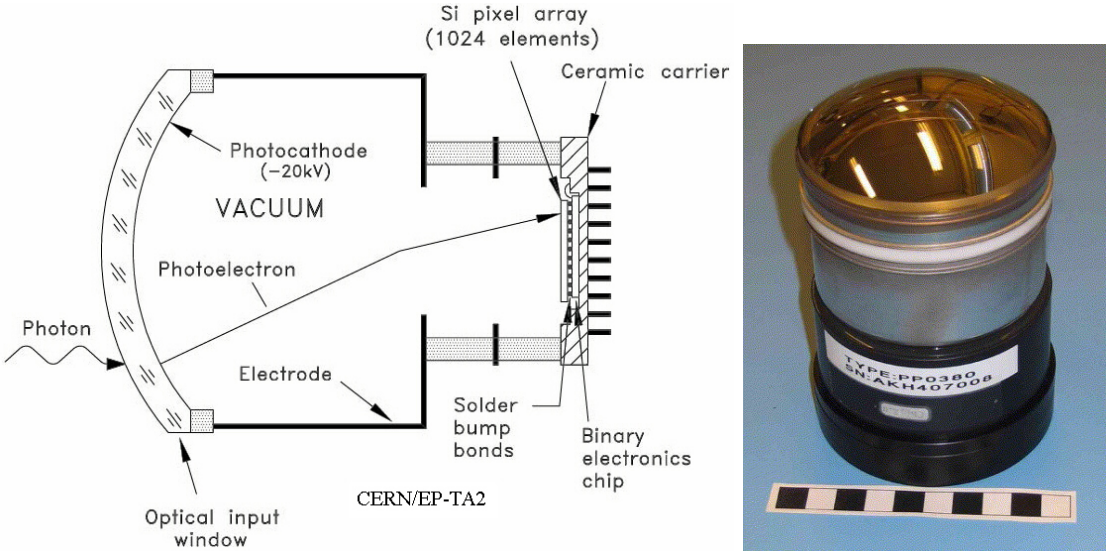

Figure 2.16: Schematic [51] (left) and photograph [63] (right) of a hybrid photo-detector (HPD).

momentum for the RICH1 gas radiator in Figure 2.17. The ability of the RICH detectors to separate pions and kaons is demonstrated using samples of pions and kaons where only kinematic information is employed in the selection and no PID information is used. Figure 2.18 shows the effect of two different PID requirements applied to these samples, giving the efficiency for the preservation of real kaons and the suppression of background from pions mistakenly reconstructed as kaons.

2.2.6 Calorimetry

The primary use of calorimeter information for the analysis presented in this thesis is in the earliest level trigger, as discussed further in Section 2.2.7.

The electromagnetic calorimeter (ECAL) is placed downstream of RICH2, after the first layer of the muon system, and is immediately followed by the hadronic calorimeter (HCAL). The first layer of the ECAL is a scintillator pad detector (SPD) which aids discrimination against showers in the ECAL originating from neutral particles. Subsequently, a thin layer of lead helps to encourage conversion. A pre-shower layer precedes the main ECAL in order to provide feedback on the longitudinal development of the ECAL shower and to aid removal of the large background of showers originating from charged pions. The body of

the ECAL is formed from 66 layers of 2 mm thick lead panels interleaved with 4 mm thick polystyrene-based scintillator panels. The HCAL is formed from alternating panels of iron and scintillating material. The light output from the scintillating tiles in both the ECAL and HCAL is transmitted through wavelength shifting optical fibres to photon multiplier tubes, from which the signal is sent off the detector.

Using measurements made in a test-beam facility, the energy resolution of the ECAL is found to be $\sigma(E)/E \sim 9\%/\sqrt{E} \oplus 1\%$ and that of the HCAL is $\sigma(E)/E \sim (69 \pm 5)\%/\sqrt{E(\,\mathrm{GeV})} \oplus (9 \pm 2)\%$ [51].

2.2.7 Trigger and data acquisition

Beam crossings occured in LHCb at a rate of 20 MHz during 2011, but inelastic pp collisions occurred only at a rate of around 11 MHz. The data-taking efficiency was high, greater than 90%, and the overall trigger efficiency was around 90% for dimuon channels and 30% for multibody hadronic final states. The LHCb trigger is composed of two sequential stages: a fully synchronous Level-0 (L0) trigger and an asynchronous, software-based High Level Trigger (HLT). The output rate of the full trigger is 3 kHz and events passing both stages are stored at this rate. Each stage will be considered in turn, though more details are available elsewhere [49, 51].

The L0 trigger: 40 MHz $\rightarrow$ 900 kHz

The L0 trigger is a hardware trigger, making use of data from the calorimeters and muon chambers to identify the highest E_{T} (energy transverse cluster corresponding to a hadron, electron or photon and to identify the two muons with the highest p_{T} in the muon chambers. These criteria are chosen since decays of heavy hadrons containing a b quark are likely to produce daughter particles with E_{T} or p_{T} of order 1 GeV/c, higher than that expected for light quark events. The number of hits in the SPD (see Section 2.2.6) is used as an indication of the number of tracks to exclude extremely complicated events which would require excessive

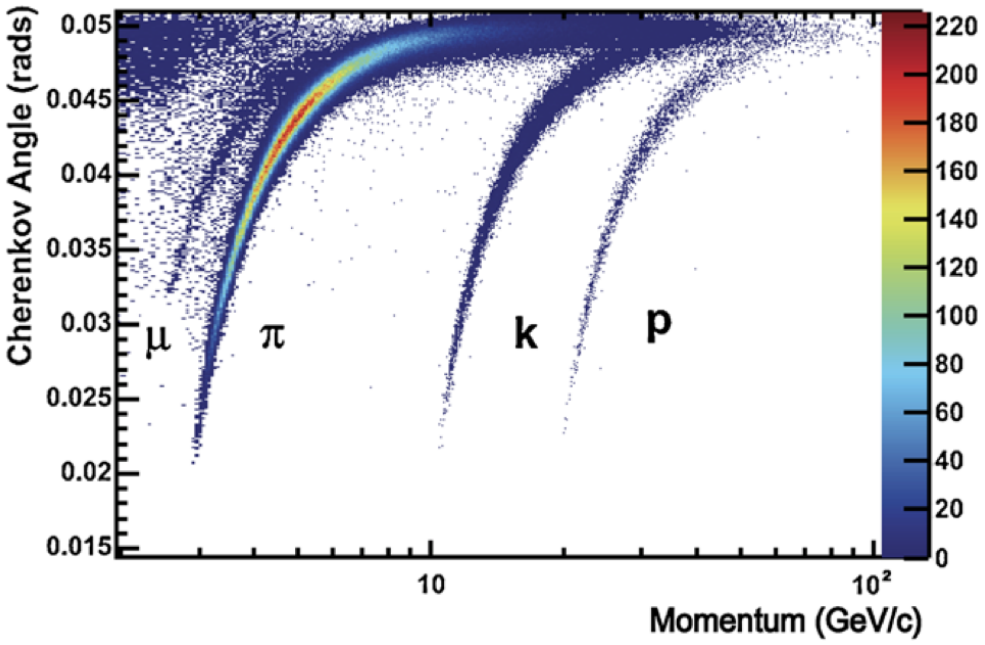

Figure 2.17: Plot of Cherenkov angle determined for particles radiating in the RICH1 gas as a function of track momentum, showing clear separation of particle types at low momenta [62].

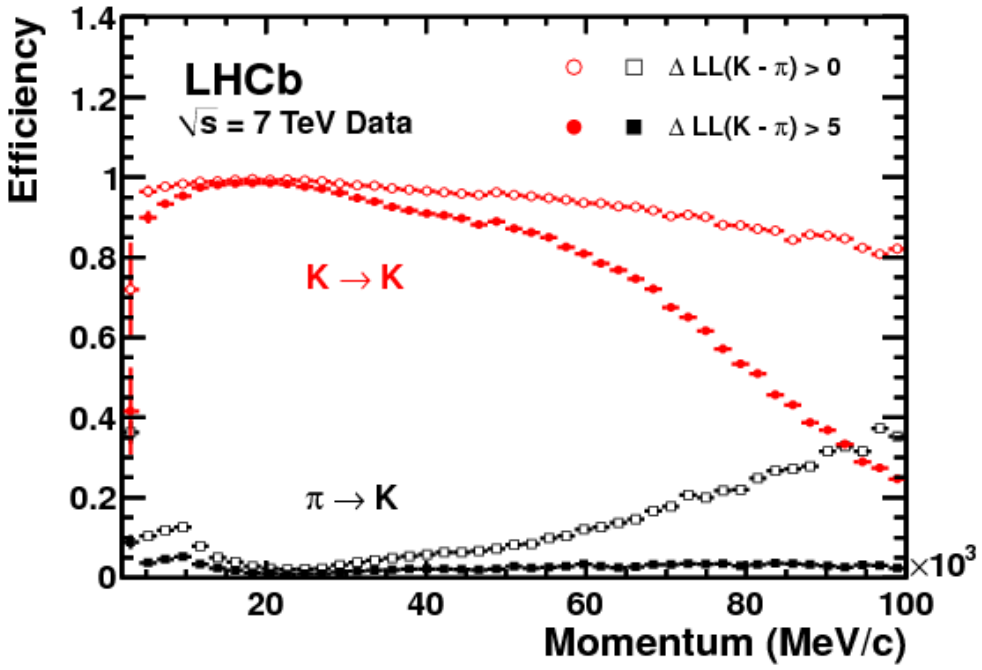

Figure 2.18: Plot of RICH π/K separation ability as a function of track momentum [62]. The circular markers correspond to the efficiency of two PID requirements on kaons and the square markers correspond to the level of background from pions, misidentified as kaons, which survive the PID requirement. The filled markers show the results for a more stringent PID requirement.

computing resources to reconstruct. Setting the maximum number of hits to be 600 causes $(8.8 \pm 0.6)\%$ of hadronic events to be rejected. These requirements reduce the trigger rate to 900 kHz, a rate at which the whole detector can be read out. The efficiency of the L0 trigger with hadron requirements on b- and c-hadron decays is plotted as a function of B or D meson p_T in Figure 2.19.

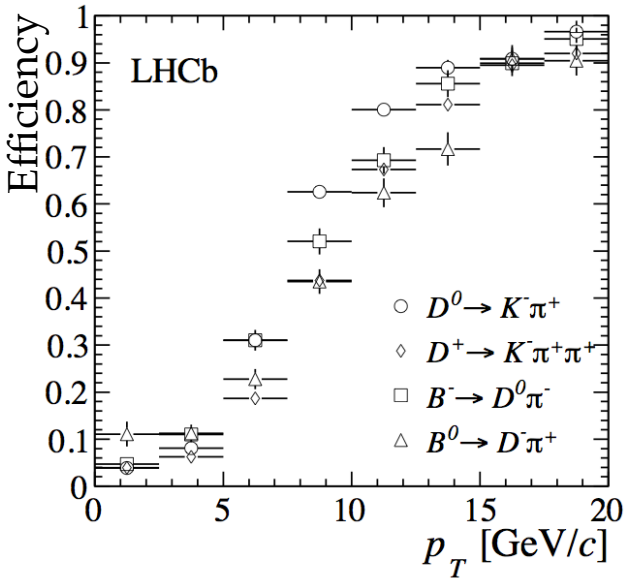

Figure 2.19: L0 hadron trigger efficiency as a function of p_T for various B or D meson decays. For values of p_T above the B meson mass, the efficiency is higher for the final state containing the fewest tracks ($D^0 \to K^-\pi^+$; open circles) than for that with the most ($B^0 \to D^-\pi^+$; open triangles) [49].

The HLT: 900 kHz $\to$ 3 kHz

The High Level Trigger is a software trigger, with 26,110 program instances running on a processing farm [64]. The HLT must make a trigger decision within approximately 30 ms. It does this by dividing the triggering into two HLT stages. In the first, HLT1, a partial reconstruction is performed and requirements are placed upon resulting tracks, reducing the rate at which events are accepted to 43 kHz. In the second, HLT2, a more complete reconstruction is performed.

The mean pp interaction position is determined using all the reconstructed VELO tracks and, where five such tracks originate from a vertex lying within 300 μm in the transverse

plane of the mean interaction position, that new vertex is deemed to be a primary vertex (PV). The HLT1 stage carries out a full pattern recognition in the VELO to reconstruct tracks, requiring them to satisfy a requirement on their minimum impact parameter χ^2, defined as the change in the χ^2 of the associated primary vertex upon removal of the track. The HLT1 requirements include limits on the impact parameter and p_T of non-muon tracks, as in the case of the analysis presented in this thesis, with respect to any PV. Thresholds are set on the momentum and transverse momentum of VELO tracks. The VELO tracks are then matched to hits in the tracking stations in a procedure known as 'forward tracking'. Tracks are then refitted with a Kalman filter [58, 59]. The HLT1 trigger efficiency for several hadronic processes is plotted in Figure 2.20. The greater mass of the B meson explains the higher efficiency for B mesons than D mesons at low parent p_T values, due to the minimum p_T requirement for the track satisfying the trigger criteria and the preference for lower multiplicity events in that region. At higher p_T, higher multiplicity events are more efficiently selected.

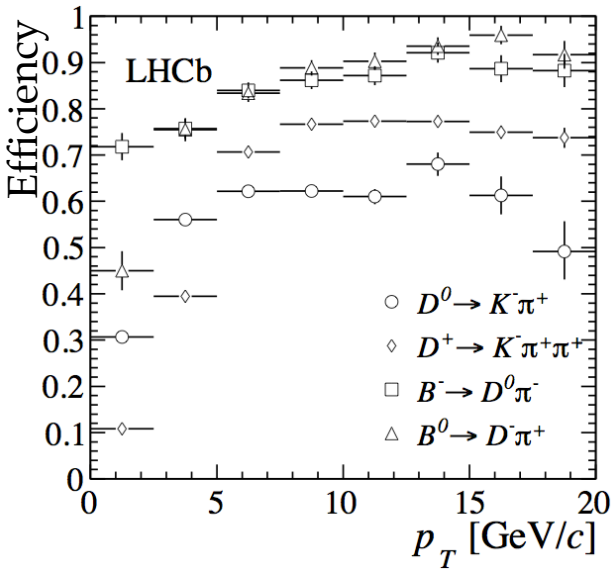

Figure 2.20: Efficiency of the HLT1 trigger on various hadronic modes [49].

After the HLT1 stage the event rate is reduced to such a level that forward tracking can be applied to all VELO tracks and displaced vertices can be reconstructed. The processing time required is limited by requiring the track momenta to be greater than 5 GeV/c and transverse momenta to be greater than 500 MeV/c. The processing time is also limited by

placing requirements on impact parameter, to suppress backgrounds from prompt processes, and track fit quality. In order to maintain good efficiency for decay topologies with many tracks, it is beneficial to trigger on only partially reconstructed $B^{\pm}$ decays, and this is achieved by means of 'topological trigger lines'. These are based on combinations of two to four 'topo-tracks' passing a requirement on their distance of closest approach. The topo-tracks are selected using requirements on their fit quality, impact parameter and muon or electron identification. Tracks are then combined successively to form two-, three- or four-body objects without the need to reconstruct the whole event. A window is placed on the reconstructed mass, adjusted to account for missing tracks,

$$m_{\text{corr}} = \sqrt{m^2 + |p'_{T\text{miss}}|^2} + |p'_{T\text{miss}}|. \tag{2.4}$$

Candidates formed are then selected using a multivariate, boosted decision tree selection based on the following quantities: $\sum |p_T|$, minimum transverse momentum, reconstructed mass, corrected mass, distance of closest approach to primary vertex, impact parameter significance (impact parameter divided by its uncertainty) and flight distance significance. Candidates which pass this stage are stored.

The efficiency of the topological trigger lines are given in Figure 2.21.

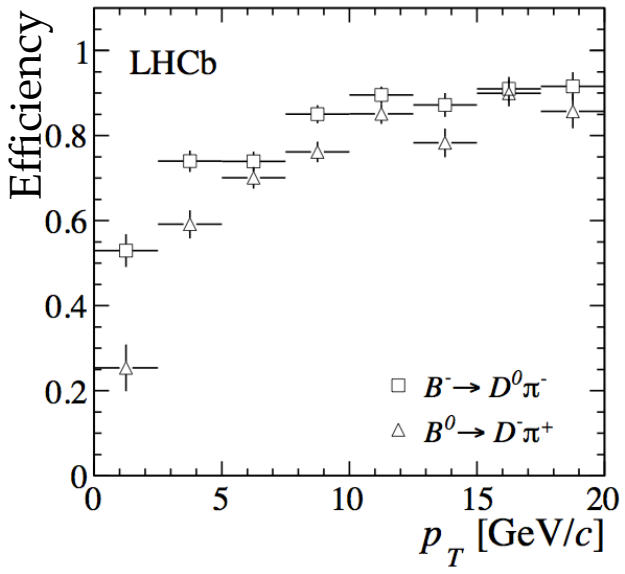

Figure 2.21: Trigger efficiency for the two- and three-body topological trigger lines for $B^- \to D\pi^-$ decays and two-, three- and four-body trigger lines for $B^0 \to D^-\pi^+$ decays [49].

2.2.8 Offline data processing

A centralised offline processing of the stored candidates, known as a 'stripping' of the data, is performed where tracks are fully reconstructed using a complete description of the detector geometry and material and the most accurate detector alignment calibration [65]. Candidates are analysed using basic multivariate selections optimised to select decays of B mesons with a displaced secondary vertex. This process takes around two seconds per event [66]. The requirement that a displaced secondary vertex is found also serves to reduce the random combinatorial background. This data stripping is necessary to produce data sets of manageable proportions for individual user analysis and to avoid unnecessary collaboration-wide repetition of generic selection criteria. The raw data can be stripped again at a later stage if new calibrations or selections are developed.

A further, analysis-specific selection, optimised for the modes under study in this thesis, is later applied. A detailed description of this selection is given in Chapter 4.

2.2.9 Simulated samples

Simulated samples are produced using the LHCb Gauss application [67] where EvtGen [47] simulates the decay of B mesons produced in pp collisions [68], and Pythia 6.4 [69] models the ensuing hadronisation. Photos [70] is used to include radiative processes, and the Geant4 toolkit [71, 48] encodes the particle interactions with the detector material, as described in [72]. For each decay type listed, the simulated sample is required to contain at least one generated signal candidate per event. The simulated data are digitised [73], and tracks are reconstructed using the same software as is used for real data.

3

Studies of the decays $D^0 \to K^0_S K^-\pi^+$ and $D^0 \to K^0_S K^+\pi^-$ at CLEO

This chapter contains the studies of the two decays $D^0 \to K^0_S K^\mp \pi^\pm$ using data from the CLEO III and CLEO-c experiments. For each decay, two amplitude models are constructed. For the first, the $K^*(892)^0 \to K^-\pi^+$ resonance is required to be present, in order to allow comparison with the predictions of SU(3) flavour models. For the second, the aforementioned resonance is not required to be present and the goal is simply the best fit possible to the data. A measurement of the ratio of branching fractions for the two decays is also presented.

3.1 Introduction

As progress is made in making measurements of γ using $B^\pm \to \tilde{D}K^\pm$ decays, exploiting interference in $B^\pm \to [F]_D K^\pm$ decays to a common final state of a neutral D meson, F, many final states are being considered. Each additional D final state brings not only additional statistical power but also different sensitivity in a $B^\pm \to \tilde{D}K^\pm$ measurement of γ, as well as to the hadronic parameters of the B and D decays. Two final states of the neutral D meson which have not yet been exploited in experimental studies are $K^0_S K^-\pi^+$ and $K^0_S K^+\pi^-$. The neutral D meson has a favoured decay route with branching fraction $(3.5 \pm 0.5) \times 10^{-3}$, $D^0 \to K^0_S K^-\pi^+$, and a suppressed one with branching fraction $(2.7 \pm 0.5) \times 10^{-3}$ [74], $D^0 \to K^0_S K^+\pi^-$, examples of which are shown in Figure 3.1, where both are singly Cabibbo-suppressed decays.[1] The γ analysis is therefore 'ADS-like' (see Chapter 1) where the γ

[1] Charge conjugation is implied throughout this chapter.

sensitivity to the CKM phase arises through interference between the amplitudes for $B^- \to [K^0_S K^\pm \pi^\mp]_{D^0} K^-$ and $B^- \to [K^0_S K^\pm \pi^\mp]_{\overline{D^0}} K^-$ or, correspondingly, for B^+.

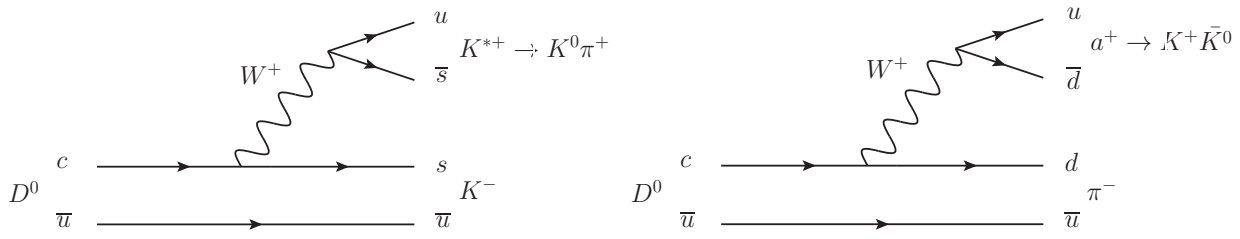

Figure 3.1: Examples of Feynman diagrams for resonances in the favoured and suppressed decay processes under study.

The $D^0 \to K^0_S K^\mp \pi^\pm$ decays can proceed through intermediate resonances which produces a complicated strong-phase variation in the D Dalitz plot and necessitates an understanding of the decay structure before a γ analysis can be carried out. The decays are also of interest since the amplitudes and phases of particular resonances in each mode can be related by means of an approximate SU(3) symmetry. In these modes, particular interest is attached to comparison of the $D^0 \to K^{*0}\bar{K}^0$ and $D^0 \to \bar{K}^{*0}K^0$ resonances where predictions of the relative amplitudes and phases for such singly Cabibbo-suppressed processes have been made [75]. Comparisons of the relative amplitudes and phases of these resonances in the amplitude models determined in the present analysis allow a test of the extent to which flavour SU(3) symmetry is valid in the decays of D mesons.

In this chapter, Dalitz models of the two modes are determined using CLEO III and CLEO-c data. In addition, a new measurement of the ratio of branching fractions for the $D^0 \to K^0_S K^+\pi^-$ and $D^0 \to K^0_S K^-\pi^+$ decays is given.

3.2 Data

The 15.3 fb^{-1} CLEO III data set was collected at a range of e^+e^- collision energies between 7 GeV and 11 GeV, predominantly at the $\Upsilon(4S)$ resonance. Candidate decays are selected from this data set in which the neutral D meson is produced in the decay of a $D^{*+}(D^{*-})$ meson to $D^0\pi^+_s(\overline{D^0}\pi^-_s)$. The charge of the 'soft pion', $\pi^\pm_s$, allows the production flavour of

the neutral D meson to be identified.

The CLEO-c data were collected in $818\,\mathrm{pb}^{-1}$ of e^+e^- collisions at the $\psi(3770)$ resonance where the $\psi(3770)$ subsequently decayed to a pair of D mesons. In the decays of these pairs of D mesons, candidate D^0 decays are selected by searching for the decay of one D meson to the desired final state (e.g. $K^0_S K^-\pi^+$) and for the decay of the other D meson to $K^\mp\pi^\pm$, $K^\mp\pi^\pm\pi^0$ or $K^\mp\pi^\pm\pi^+\pi^-$. The latter are termed 'pseudo-flavour tags', as the final states are dominated by a Cabibbo allowed amplitude. Hence, from the charge of the kaon in the pseudo-flavour tag, the production flavour of the signal D can be inferred.

First the selection of the CLEO III and CLEO-c data is described, followed by the preparation of samples for background studies and simulated samples for acceptance studies.

3.2.1 Candidate selection for CLEO III data

Candidates were reconstructed using CLEO software and criteria were placed on properties of the candidate decays in order to achieve a sample with high purity. The task of preparing a candidate selection is not included in the work presented in this thesis and has been described elsewhere [2], but a summary of the selection procedure is given here. All charged tracks are required to have a small impact parameter with respect to the interaction point, to make an angle with the beam-pipe large enough to lie within the detector acceptance and to lie in a particular momentum range. Tracks are passed to a kinematic, vertex-constrained fit to form K^0_S candidates decaying to two charged pions, distinguished from combinatorial background from prompt pion pairs by the requirement that the K^0_S candidate should fly a significant distance from the interaction point. The K^0_S candidates are combined with a kaon and a pion, distinguished from one another using information from the RICH detector or from dE/dx measurements in the drift chamber, to form a D^0 candidate after a vertex-constrained fit. A final vertex-constrained fit sees the D^0 candidate combined with a pion to form a $D^{*\pm}$ candidate with momentum at least half the maximum possible value, suppressing charm backgrounds originating from B decays. Background is suppressed after each stage of the vertex fitting by placing requirements on the χ^2 of the vertex fit. Events containing

multiple candidates are excluded.

In order to isolate the signal from $D^{*\pm}$ decays, limits are placed on the accepted values of the reconstructed D^0 mass, before the D^0 mass constraint, $15\,\mathrm{MeV}/c^2$ either side of the PDG value for the D^0 mass. A limit is also placed $1\,\mathrm{MeV}/c^2$ either side of the anticipated mass difference, Δm, between the $D^{*\pm}$ and D^0 candidates. These windows, illustrated in Figure 3.2, are approximately three times the width of a Gaussian fitted to the m_D or Δm projection respectively. Fits are performed to the m_D and Δm spectra independently and the fitted signal yields are averaged, where the resulting uncertainty accounts for the statistical uncertainty and the difference between the fitted yields. The level of peaking background from $D^0 \to K^-\pi^+\pi^+\pi^-$ in $D^0 \to K^0_S K^-\pi^+$ is estimated and subtracted from the signal yield [2]. This background is insignificant in the $D^0 \to K^0_S K^+\pi^-$ mode where it is doubly Cabibbo-suppressed. The sample purity is summarised in Table 3.1, where the peaking background yields are determined using simulated samples and the flat background is determined from the fit to data.

The Dalitz plots for the samples and associated projections in the Dalitz variables are given in Figures 3.3 and 3.4. The dominant contribution to the Dalitz structure in both modes appears as a sharp peak in the $K^0_S\pi^\pm$ Dalitz projection at approximately $0.8\,\mathrm{GeV}^2/c^4$, the position expected for the $K^*(892)^\pm \to K^0_S\pi^\pm$ resonance. This vector resonance, as discussed in Section 1.3.1, produces a band in the Dalitz plots where the density of candidates along the band is depleted in the centre, as can be seen most clearly at around $2\,\mathrm{GeV}^2/c^4$ in the $K^0_S K^\pm$ projection in Figures 3.3 and 3.6. The contribution of a broad S-wave component in the $K^0_S\pi^\pm$ channel may account for the significantly larger tails either side of the $K^*(892)^\pm \to K^0_S\pi^\pm$ resonance in the $D^0 \to K^0_S K^+\pi^-$ mode.

3.2.2 Candidate selection in CLEO-c data

The CLEO-c selection approach is very similar to that already described for the CLEO III data. The standard CLEO-c software is used to reconstruct the decay by combining final-state particles for the 'tag-side' D and for the signal D which pass selection criteria

Table 3.1: Summary of signal and background yields for the CLEO III samples.

	$D^0 \to K^0_S K^-\pi^+$	$D^0 \to K^0_S K^+\pi^-$
Number of candidates	697	452
Fitted signal yield (m_D, Δm)	651 ± 27 655 ± 27	400 ± 22 412 ± 23
Average	653 ± 27	406 ± 24
Peaking background	12 ± 2	0
Signal yield − peaking bkg ($\equiv S$)	640 ± 27	406 ± 24
Flat background yield (m_D, Δm)	52 ± 3 53 ± 3	46 ± 3 44 ± 3
Average	52 ± 3	45 ± 4
Total background yield ($\equiv B$)	65 ± 4	45 ± 4
Purity (%) $\equiv \frac{S}{S+B}$	91 ± 1	90 ± 1

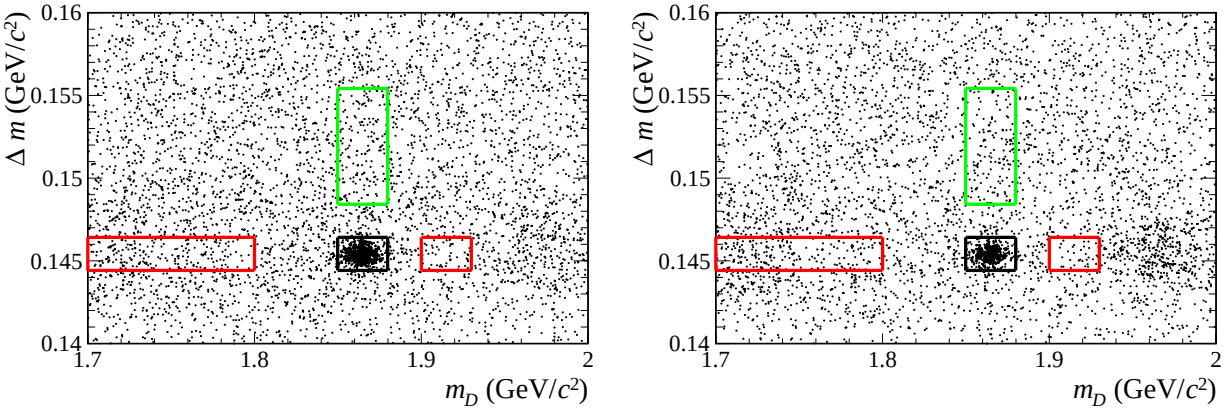

(a) $D^0 \to K^0_S K^-\pi^+$ (b) $D^0 \to K^0_S K^+\pi^-$

Figure 3.2: Distribution of CLEO III candidates in the (m_D, Δm_D) plane after selection. The signal box is shown in black whilst the background boxes (see Section 3.2.3) are shown in red and green.

described in detail elsewhere [2, 76]. These criteria include requirements on the kinematic properties of the tracks and on their geometry, such as their distance of closest approach to the interaction point. They must also register a significant number of hits in the tracker. Selected tracks are assigned a mass hypothesis using information from the RICH detector and dE/dx measurements. More complex objects can then be constructed, such as K^0_S candidates where the flight distance of the K^0_S candidate is required to be greater than twice the uncertainty on that quantity. A narrow window in reconstructed K^0_S mass, $7.5\,\mathrm{MeV}/c^2$ either side of the PDG value, suppresses background from $D^0 \to K^-\pi^+\pi^+\pi^-$ decays. In order to form the $K^\mp\pi^\pm\pi^0$ tag, neutral pion candidates are constructed by combining photon candidates in a vertex with good fit quality. Finally the knowledge of the beam energy is

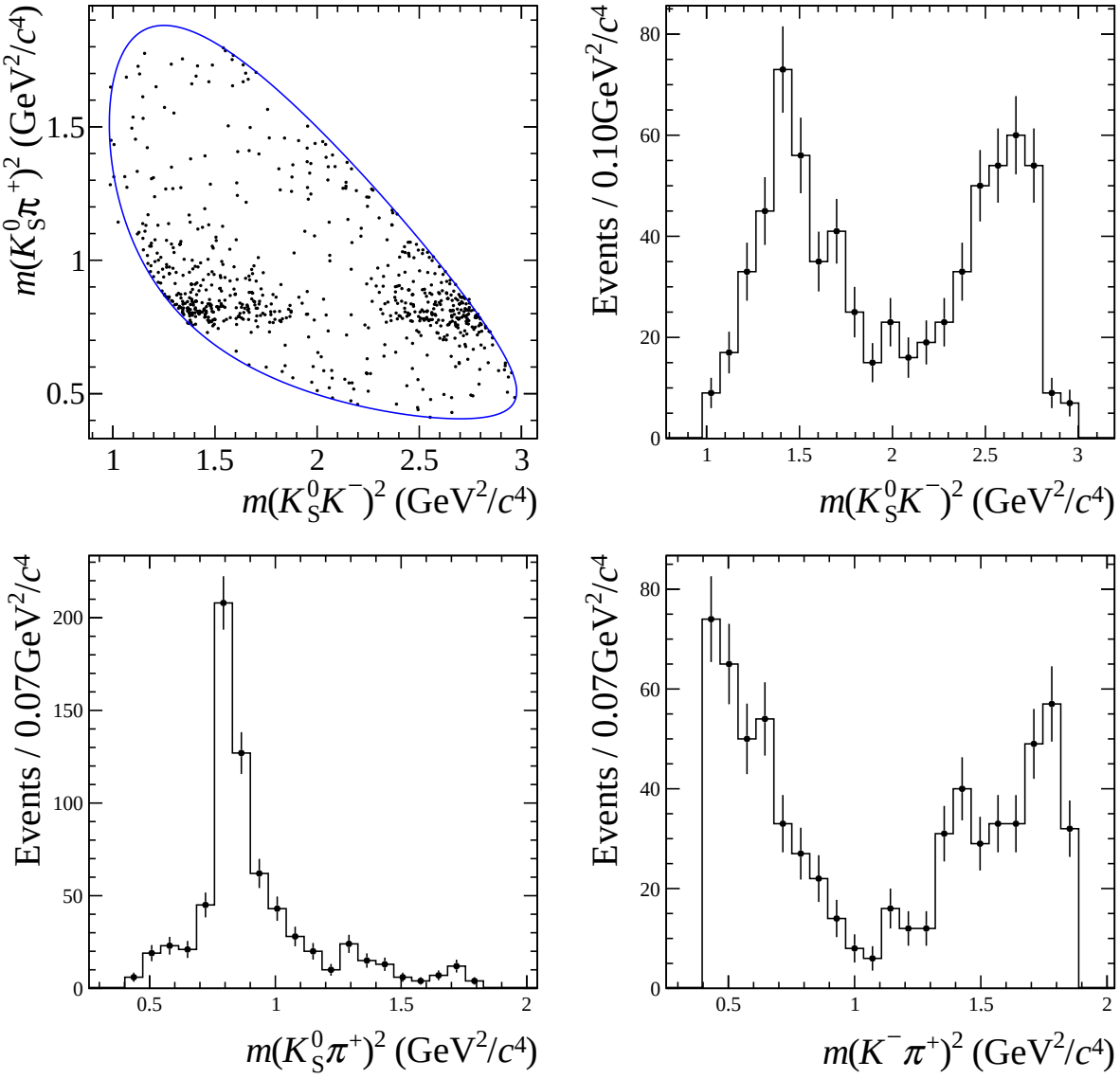

Figure 3.3: Favoured mode $D^0 \to K^0_S K^-\pi^+$ Dalitz plot and projections in CLEO III data.

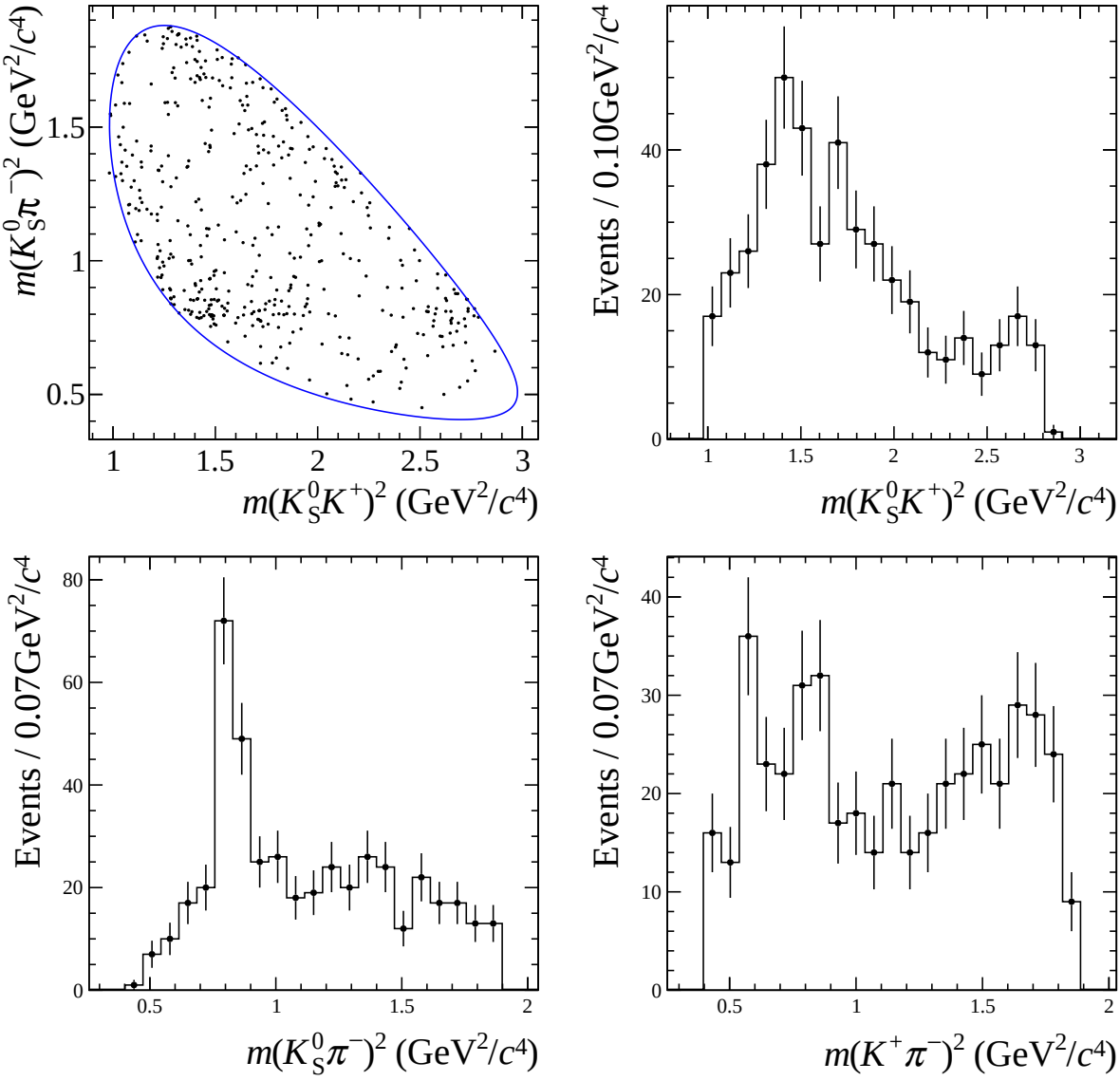

Figure 3.4: Suppressed mode $D^0 \to K^0_S K^+ \pi^-$ Dalitz plot and projections in CLEO III data.

employed to restrict the range of reconstructed D^0 energies. The 'beam-constrained mass', $m_{\rm BC}$, is defined as

$$m_{\rm BC} = \sqrt{s/(4c^4) - p_D^2/c^2}, \tag{3.1}$$

where s is the squared centre-of-mass energy in the collision and p_D is the reconstructed D^0 momentum. Finally two more kinematic fits are applied. The first is to the K^0_S pions with a K^0_S mass constraint and then, if the fit is successful, the second fit is applied to the D^0 candidate daughters with a D^0 meson mass constraint. The candidates passing the selection criteria are considered on the $(m_{\rm (BC,\ tag)}, m_{\rm (BC,\ signal)})$ plane, shown in Figure 3.5. When an event contains multiple candidates, the signal candidate chosen is the one for which its $m_{\rm BC}$ value is closest to the D^0 mass or, in the case of a fully reconstructed tag, the candidate whose average signal and tag $m_{\rm BC}$ lies closest to the D^0 mass.

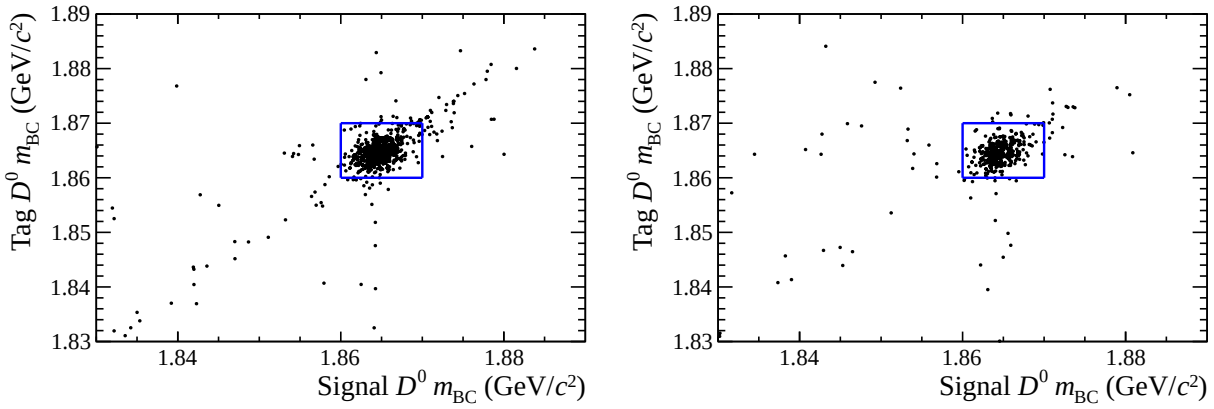

Figure 3.5: Candidates selected from the CLEO-c data set illustrated on the $(m_{\rm (BC,\ tag)}, m_{\rm (BC,\ signal)})$ plane for the favoured mode (left) and suppressed mode (right), where candidates in the three flavour-tag samples have been combined. The blue box indicates the region in which candidates are accepted for the analysis.

The total background contribution is the sum of contributions in the signal box from flat and peaking backgrounds. The only background anticipated to peak in the signal regions is that from the decay $D^0 \to K^-\pi^+\pi^+\pi^-$. The size of this background is assessed using a generic simulated sample containing pairs of $D^0\bar{D}^0$ and pairs of D^+D^-, where each of the D mesons is allowed to decay to a final state according to a measured branching fraction. Other backgrounds are studied by combining sideband regions in the $(m_{\rm (BC,\ tag)}, m_{\rm (BC,\ signal)})$ plane and determining the background yield there. The background

yield in the signal region is calculated by assuming the background to be uniformly distributed in the $(m_{(\text{BC, tag})}, m_{(\text{BC, signal})})$ plane and scaling the yields from the background regions to the signal region by area in this plane. Contributors to the flat background include continuum $e^+e^- \to q\bar{q}$ events, events where only one of the two D mesons is correctly reconstructed and events where the tracks are attached to the wrong D meson. These background yields are combined for all the three tags and are outlined in Table 3.2 [77]. Approximately 44% of the data are selected using the $K^\pm\pi^\mp\pi^0$ tag, 32% from the $K^\pm\pi^\mp\pi^+\pi^-$ tag, and the rest is from the $K^\pm\pi^\mp$ tag.

Dalitz plots and projections are given for both decay modes in Figures 3.6 and 3.7. The same features are apparent in the projections of the Dalitz plot as in the CLEO III data.

Table 3.2: Summary of signal and background yields for the CLEO-c samples.

	$D^0 \to K^0_S K^-\pi^+$	$D^0 \to K^0_S K^+\pi^-$
Number of selected candidates	550	308
Total background yield	49.8 ± 1.5	6.0 ± 0.4
Purity (%)	91.2 ± 0.4	98.0 ± 0.2

3.2.3 Background data samples

After the selection has been applied, the data samples all have a high purity, around 90% or above. The residual background has a non-trivial structure in the Dalitz plot and it is necessary first to model this structure before a fit for the signal models can be attempted. For the CLEO III sample, residual background from $D^0 \to K^-\pi^+\pi^+\pi^-$ decays is at a negligible level. The background present in the signal region can therefore be assumed to be the same as that present in the background boxes in the $(m_D, \Delta m_D)$ plane, shown in Figures 3.2(a) and 3.2(b). The sideband regions marked with a red boundary contain backgrounds which do not contain a correctly reconstructed D^0 or $\bar{D}^0$ meson. The region in green contains decays where the D candidate is likely to be correctly reconstructed but associated with the wrong slow pion.

The number of candidates in the CLEO-c data sidebands is too small for a meaningful

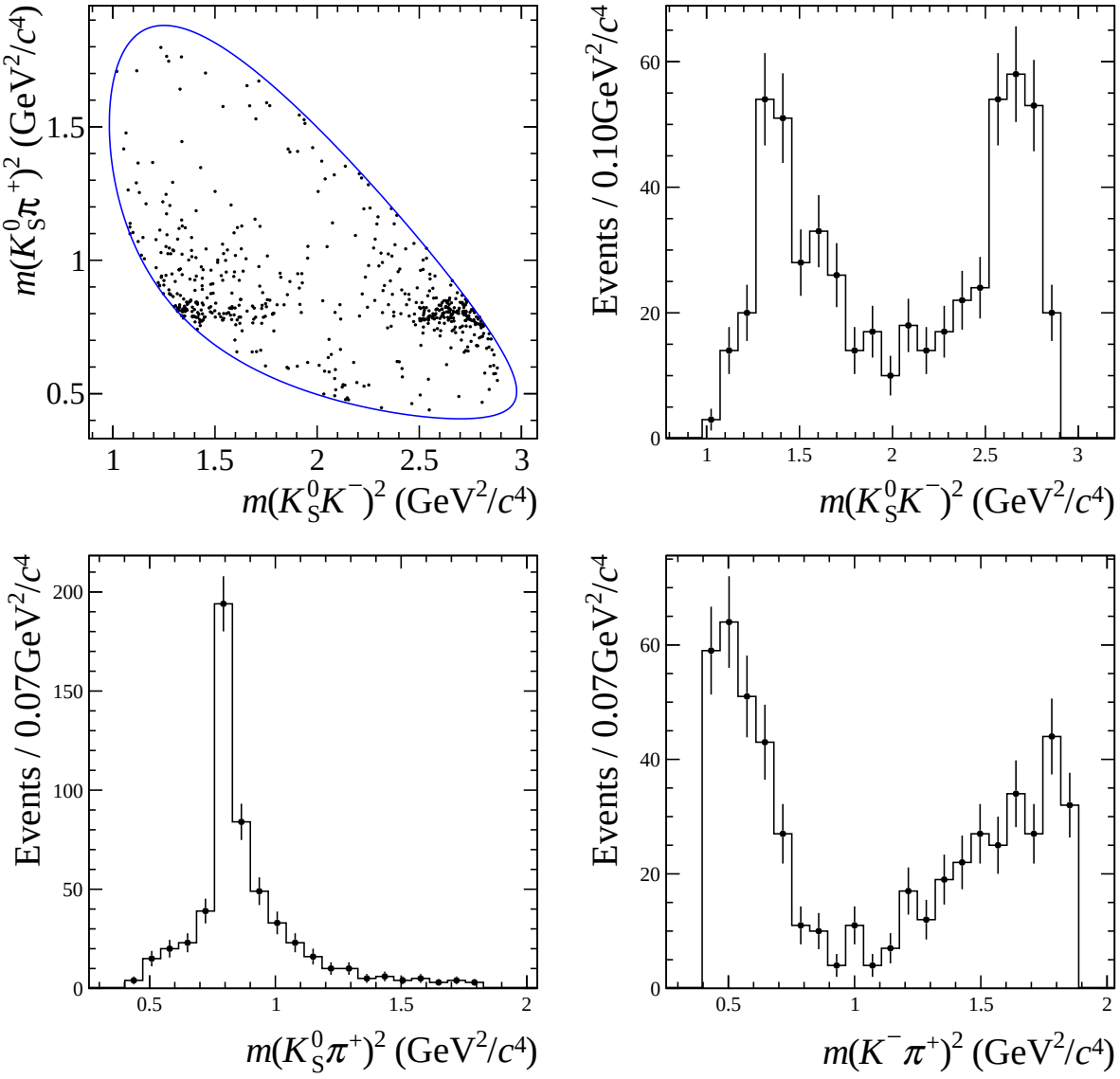

Figure 3.6: Favoured mode $D^0 \to K^0_S K^- \pi^+$ Dalitz plot and projections in CLEO-c data.

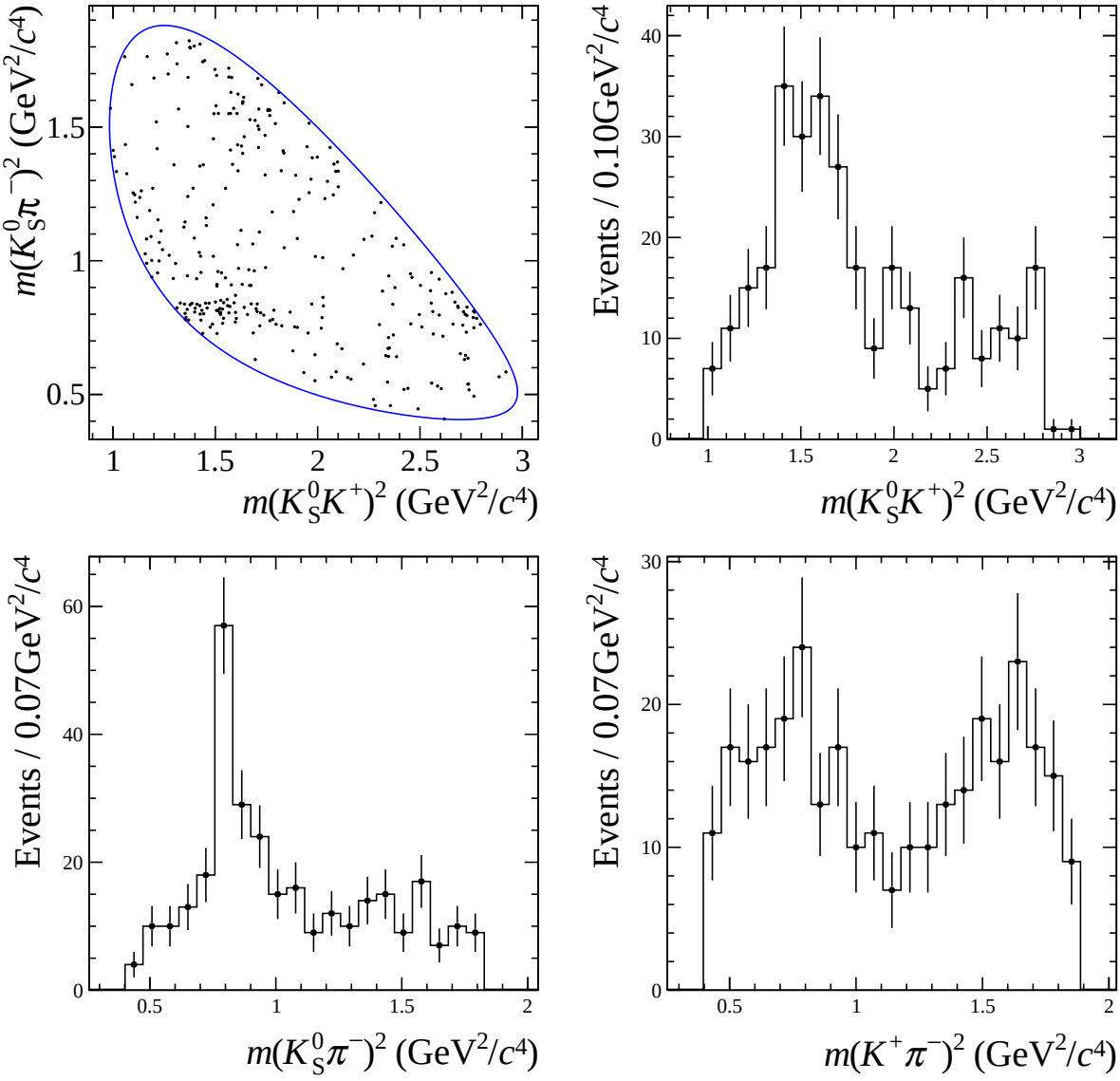

Figure 3.7: Suppressed mode $D^0 \to K^0_S K^+ \pi^-$ Dalitz plot and projections in CLEO-c data.

background study to be performed so a generic sample of simulated $\psi(3770) \to D\bar{D}$ events is used instead, corresponding to an integrated luminosity twenty times larger than that of the CLEO-c sample. The sample was produced with the same detector conditions as for the data-taking.

The candidates selected in the various sub-samples, either from different $(m_D, \Delta m_D)$ regions or from different tags, are combined for the purposes of fitting the background model. Dalitz projections of the background samples for the CLEO III and CLEO-c data are shown in Figures 3.9 to 3.12 where the fits described in Section 3.3.2 are superimposed. Many broad features are common to the background samples for both CLEO III and CLEO-c. There are some notable areas of difference such as in the general shape of the $K^0_S\pi^+$ and $K^-\pi^+$ projections for the favoured mode and the strongly peaking structure in the $K^0_S\pi^-$ projection which is present in the CLEO-c background for the suppressed mode but not as significant in the corresponding CLEO III sample.

3.2.4 Simulated CLEO samples for acceptance studies

In order to determine the variation in CLEO III and CLEO-c reconstruction efficiency across the Dalitz plot, large non-resonant samples are used, which had been generated and passed through the reconstruction software and event selection. Since the samples were generated with no resonant structure, the distribution of generated candidates is flat in the Dalitz plot. The distribution of events in the Dalitz plot after reconstruction and selection is therefore directly proportional to the efficiency distribution.

The CLEO III $D^0 \to K^0_S K^-\pi^+$ sample is selected from $34,961$ generated D^0 decays and a similar number of $\bar{D}^0$. Of these, $2,843$ candidates passed the selection. Similar numbers of events were generated in the $D^0 \to K^0_S K^+\pi^-$ mode, and $2,959$ candidates are selected. In the favoured sample, seven events contain multiple candidates and these are discarded, as are eight events in the suppressed mode, following the treatment applied to the CLEO III data. The simulated sample size is limited and statistical fluctuations are significant so it is necessary to fit a smooth polynomial to parameterise the efficiency variation.

For CLEO-c, a larger Monte Carlo sample of 5.9 million non-resonant signal decay events had been generated and passed through the reconstruction and selection frameworks. Statistical fluctuations are smaller and it is therefore possible to use the sample directly in the fit to account for the CLEO-c efficiency (see Section 3.3.4).

3.3 Modelling

Any pair of final-state particles, $K^0_S K$, $K^0_S\pi$ and $K\pi$, can arise from the decay of a resonance. A list of possible resonances which appear in the PDG [74] and decay to one of these pairs is given in Table 3.3. The masses, widths and J^{PC} of these resonances are given in Table 3.4. The parameters of the $K^*_0(1430)^\pm$ are taken from the *BABAR* analysis in which the S-wave parameters are defined [35]. The ordering of the final-state particles, which is important in order to define unambiguously the sign of the vector spin factor described in Section 1.4.2, is defined in Table 3.5.

Table 3.3: Possible resonances in $D^0 \to K^0_S K^\mp\pi^\pm$.

Decay products		
$K^0_S K$	$K^0_S\pi$	$K\pi$
$a_0(980)$	$K^*(892)$	$K^*(892)^0$
$a_2(1320)$	$K^*(1410)$	$K^*(1410)^0$
$a_0(1450)$	$K^*(1430)$	$K^*(1430)^0$
$\rho(1450)$	$K^*_2(1430)$	$K^*_2(1430)^0$
$\rho(1700)$	$K^*(1680)$	$K^*(1680)^0$

Models are first developed for the background samples and to account for the detector acceptances. These models are then combined with a signal model, whose parameters are allowed to vary, and the simultaneous fit to the CLEO III and CLEO-c data is performed.

3.3.1 Modelling expectations

A $K^*(892)^\pm \to K^0_S\pi^\pm$ resonance is clearly visible in the Dalitz projections in both modes and data sets (Figures 3.3, 3.4, 3.6 and 3.7) and motivates the inclusion of that component in

Table 3.4: Properties of resonances used [74].

Particle	Mass (MeV/c^2)	Width (MeV/c^2)	J^{PC}
$a_0(980)^+$	980 ± 20	$40 - 100$	0^{++}
$K^*(892)^+$	891.66 ± 0.26	50.8 ± 0.9	1^-
$K^*(892)^0$	895.94 ± 0.22	48.7 ± 0.8	1^-
$a_2(1320)^+$	1318.3 ± 0.6	107 ± 5	2^{++}
$K^*(1410)^+$	1414 ± 15	232 ± 21	1^-
$K^*(1410)^0$	1414 ± 15	232 ± 21	1^-
$a_0(1450)^+$	1474 ± 19	265 ± 13	0^{++}
$K^*_0(1430)^+$	1421.5 ± 1.6	247 ± 3	0^+
$K^*_0(1430)^0$	1425 ± 50	270 ± 80	0^+
$\rho(1450)^+$	1465 ± 25	400 ± 60	1^{--}
$K^*_2(1430)^+$	1425.6 ± 1.5	98.5 ± 2.7	2^+
$K^*_2(1430)^0$	1432.4 ± 1.3	109 ± 5	2^+
$\rho(1700)^+$	1720 ± 20	250 ± 100	1^{--}
$K^*(1680)^+$	1717 ± 27	322 ± 110	1^-
$K^*(1680)^0$	1717 ± 27	322 ± 110	1^-

Table 3.5: Particle ordering chosen for spin 1 resonances.

Decay	A	B	C
$D^0 \to \rho^-\pi^+,\ \rho^- \to K^0_S K^-$	K^0_S	K^-	π^+
$D^0 \to K^{*+}K^-,\ K^{*+} \to K^0_S\pi^+$	K^0_S	π^+	K^-
$D^0 \to K^{*0}K^0_S,\ K^{*0} \to K^-\pi^+$	K^-	π^+	K^0_S

every model considered. A broad S-wave component in the $K^0_S\pi^\pm$ channel is expected given its inclusion in models of the $D^0 \to K^-K^+\pi^0$ decay [78], which has the same quark content in the final state as the modes studied here. The need for a contribution from a broad component is particularly clear for the $D^0 \to K^0_S K^+\pi^-$ mode in the $K^0_S\pi$ projection (Figures 3.4 and 3.7). The S-wave component is best modelled as part of the $K^*_0(1430)^\pm \to K^0_S\pi^\pm$ resonance which has been found in previous studies to be well described by a broad resonance coupled to an extended non-resonant contribution (see Section 1.4.1). This component is therefore included in every model. Resonances in the $K^\pm\pi^\mp$ channel are not expected to be major contributors to the models since the processes that produce them are highly suppressed: rescattering between the final-state particles (a low-energy final-state interaction mediated by the strong force) or an exchange diagram as shown in Figure 3.8.

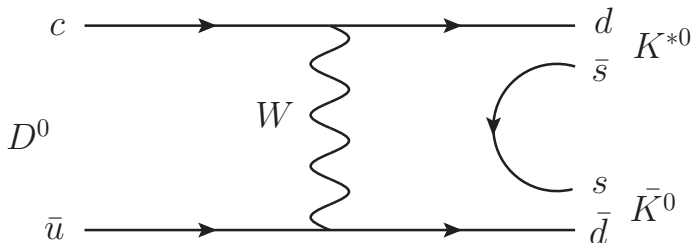

Figure 3.8: Resonances can appear in the $K^\pm\pi^\mp$ channel via a suppressed W exchange mechanism.

3.3.2 Background models for CLEO III and CLEO-c

Models are developed for each background data set and decay mode where each of the four samples are fitted with an incoherent sum of resonant contributions. It is only important to achieve a good, empirical description of the background samples. The MINT software package, described in Section 3.3.4, is employed.

In both the fits to the $D^0 \to K^0_S K^+\pi^-$ data and in the CLEO III $D^0 \to K^0_S K^-\pi^+$ fit, the non-resonant component forms a large fraction of the background model. This component is therefore always included. A further resonance is added incoherently to the background models and the model matching the data most closely is chosen, using the χ^2 test described in Section 3.3.4. This process is repeated until any additional resonance either does not produce a noticeable improvement in the fit or does not contribute significantly. All the background models contain four resonances except the CLEO III $D^0 \to K^0_S K^+\pi^-$ model which contains three, due to further improvement not being found with additional resonances. The resonances used are a mixture of physical resonances, resonances where the lineshape has been modified, such as a Breit-Wigner lineshape used for a $K^*_0(1430)^+ \to K^0_S\pi^+$ resonance or with the spin-dependence removed, or where the resonance pole mass and width have been chosen in order to allow an empirical description of a particular feature.

For the fits to the $D^0 \to K^0_S K^-\pi^+$ data, the largest resonant contributions account for obvious features in the $K^0_S\pi^-$ spectrum, and any other resonances do not occupy more than, in the largest case, 13% of the resulting model. In the $D^0 \to K^0_S K^+\pi^-$ models, there is a large contribution from the $K^*(892)^+ \to K^0_S\pi^+$ resonance, but all remaining resonances

occupy a fraction of the model less than 16% each. The fit results are shown in Figures 3.9 to 3.12.

3.3.3 Modelling the CLEO III and CLEO-c acceptances

The selection is applied to the simulated CLEO III and CLEO-c samples, and the surviving candidates are distributed across the phase space as shown in Figure 3.13. The distributions are approximately flat but show some decrease in efficiency towards the edges nearing the Dalitz boundary, behaviour which is reasonable since this tends to be where one of the three particles has a low momentum and is therefore less likely to be reconstructed. For the CLEO III distribution this is most noticeable at high $K^0_S K$ invariant mass where the pion has very low momentum. In the same way, for the CLEO-c distribution, a drop in efficiency appears where the kaon is nearly at rest at high $K^0_S\pi$ invariant mass.

The CLEO III efficiency shape is fitted using a second order Chebychev polynomial in the transformed Dalitz coordinates $x = M^2_{K^0_S K} - 1.8\,\mathrm{GeV}^2/c^4$ and $y = M^2_{K^0_S \pi} - 1.0\,\mathrm{GeV}^2/c^4$:

$$\epsilon = 1 + p_1 x + p_2 y + p_3 x^2 + p_4 y^2 + p_5 xy. \tag{3.2}$$

The Minuit package [79] is used to vary the parameters $p_1, ..., p_5$ to match the shape of the data in the Dalitz plot. The fit function is nearly flat. The χ^2 per degree of freedom for the fit is 63.8/(70-5) = 0.98 and the χ^2 probability is 52%. The Dalitz projections of the fit to the CLEO III acceptance are shown in Figure 3.14.

3.3.4 Fitting the full amplitude model

Constructing the full fit PDF

The PDF to fit the CLEO III or CLEO-c data, as a function of position point $\vec{x}$ in the Dalitz plot, is

$$P_{\text{CLEO III(-c)}}(\vec{x}) = \beta P_{\text{sig}}(\vec{x}) + (1-\beta) P_{\text{CLEO III(-c) bkg}}(\vec{x}), \tag{3.3}$$

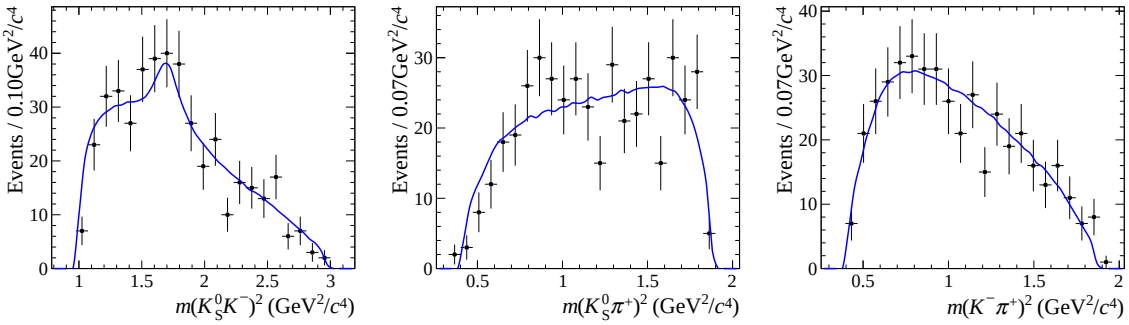

Figure 3.9: Fit to favoured $D^0 \to K^0_S K^-\pi^+$ in CLEO III sideband, $\chi^2/\text{dof} = 1.5$.

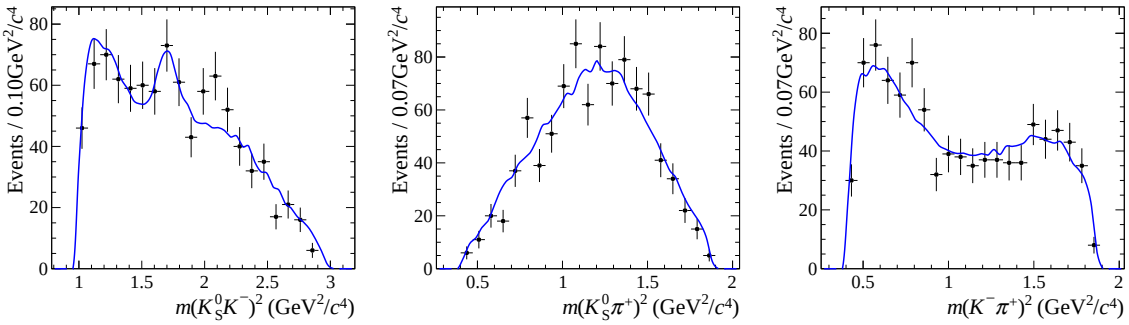

Figure 3.10: Fit to favoured $D^0 \to K^0_S K^-\pi^+$ in CLEO-c MC background, $\chi^2/\text{dof} = 1.1$.

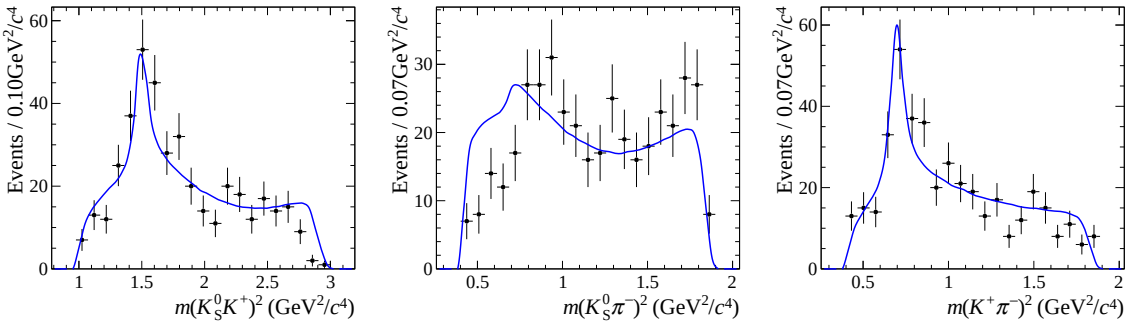

Figure 3.11: Fit to suppressed $D^0 \to K^0_S K^+\pi^-$ in CLEO III sideband, $\chi^2/\text{dof} = 2.4$.

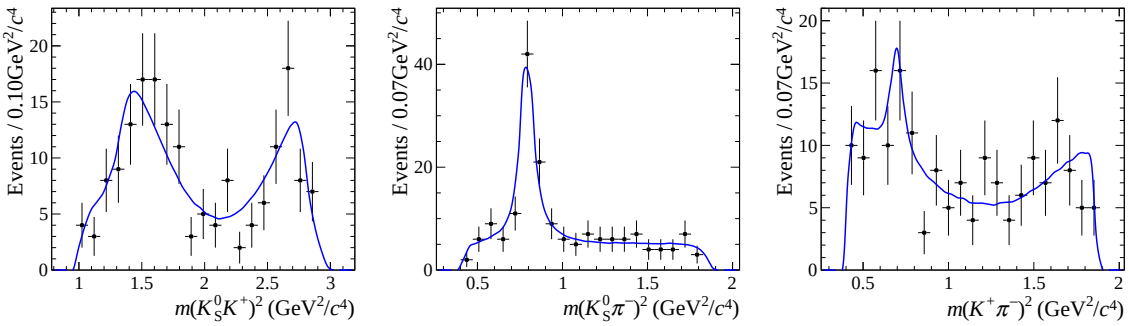

Figure 3.12: Fit to suppressed $D^0 \to K^0_S K^+\pi^-$ in CLEO-c MC background, $\chi^2/\text{dof} = 1.4$.

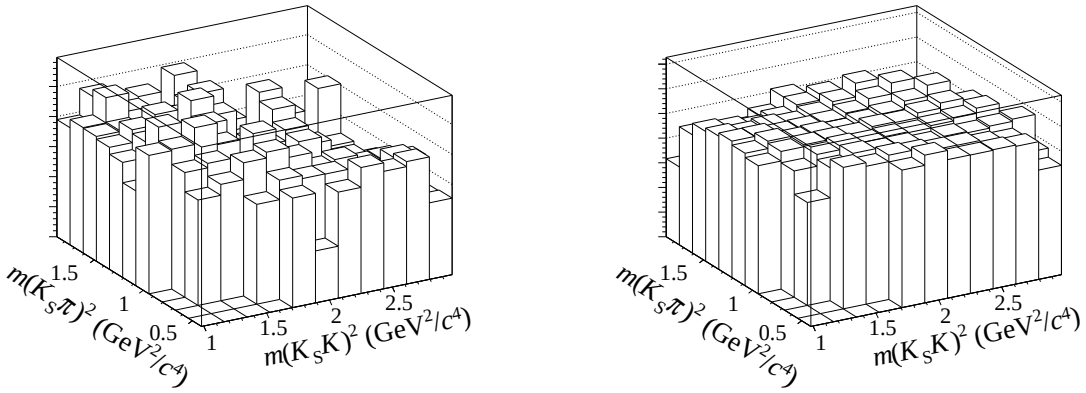

(a) CLEO III (b) CLEO-c

Figure 3.13: CLEO detector acceptances with arbitrary z-axis scale.

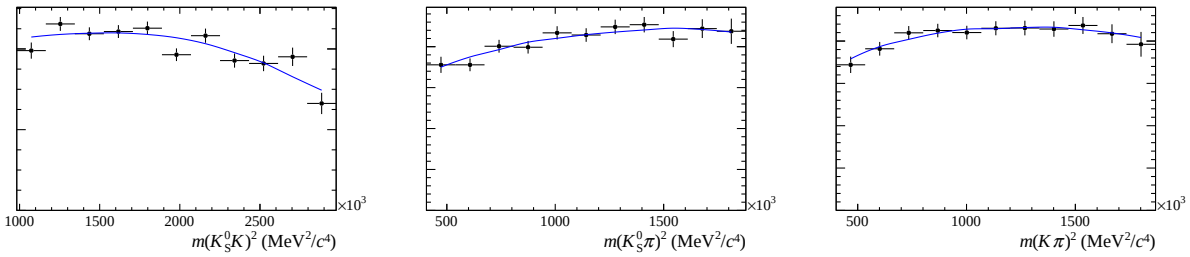

Figure 3.14: CLEO III acceptance parameterisation (blue solid line) superimposed on Monte Carlo simulated data Dalitz projections.

where P_{bkg} is the appropriate CLEO III or CLEO-c background model (Section 3.3.2), P_{sig} is the signal model, and β is the sample purity. Both the signal and background PDFs are normalised.

The background PDF is an incoherent sum of resonant contributions:

$$P_{\text{CLEO III(-c) bkg}}(\vec{x}) = \sum_{i=1}^{N_{\text{cpts}}} f_i^{\text{CLEO III(-c)}} \times P_{\text{bkg, }i}(\vec{x}), \tag{3.4}$$

where N_{cpts} is the number of background components, $P_{\text{bkg, }i}$ is the normalised PDF for each incoherent resonant component in each background model and $f_i^{\text{CLEO III(-c)}}$ is the fraction assigned to each in the two background models.

The Dalitz acceptance is already included with the background shape in the empirical background model so it is not necessary to impose a further efficiency correction. It is,

however, important to include the efficiency effect explicitly in the signal model:

$$P_{\rm sig}(\vec{x}) = \mathcal{N}_{\rm sig} \times |\mathcal{A}_{\text{signal model}}(\vec{x})|^2 \times \epsilon_{\text{CLEO III(-c)}}(\vec{x}). \tag{3.5}$$

In this equation, $\mathcal{A}$ represents the amplitude model common to both the CLEO III and CLEO-c PDFs, constructed using the isobar modelling formalism in Section 1.4; $\mathcal{N}$ is the factor which ensures $P_{\rm sig}$ is normalised; and $\epsilon_{\text{CLEO III(-c)}}$ is the appropriate acceptance function (Section 3.3.3). A functional parameterisation for $\epsilon_{\text{CLEO III}}$ is necessary for the CLEO III sample (see Section 3.3.3) given the limited simulated sample size and large ensuing statistical uncertainties in the fit. For the CLEO-c element of the fit, the detection acceptance is directly implemented using the much larger simulated sample.

The two data sets, one from CLEO III and one from CLEO-c, are fitted simultaneously. To achieve this, a combined likelihood is constructed,

$$f = -2\log(\mathcal{L}_{\text{CLEO III}}) - 2\log(\mathcal{L}_{\text{CLEO-c}}), \tag{3.6}$$

and then minimised. Here,

$$\mathcal{L}_{\text{CLEO III}} = \prod_{i=1}^{N_{\text{cands CLEO III}}} P_{\text{CLEO III}}(\vec{x}), \tag{3.7}$$

where $N_{\text{cands CLEO III}}$ is the number of candidates in the CLEO III sample (an analogous equation exists written for $\mathcal{L}_{\text{CLEO-c}}$). The fact that the overall PDF is normalised means that $N_{\rm cpts} - 1$ coefficients can be varied for a model containing $N_{\rm cpts}$ resonances. In all the models, the $K^*(892)^\pm \to K^0_S\pi^\pm$ resonance is present so it is sensible, for comparison, to make this the fixed resonance in each. In the fit, therefore, the complex coefficients attached to each resonance in the signal model are varied with respect to the fixed $K^*(892)^\pm \to K^0_S\pi^\pm$ resonance.

MINT Dalitz fitting package

The construction of the amplitude model and the subsequent fitting is carried out using the MINT software package [80] which provides an interface to the Minuit minimisation package [81]. The MINT package uses text-based parameter files to indicate which resonances are to be included in the amplitude model and to set the starting values and step sizes for the complex coefficients that are fitted. Resonances are easily combined in a coherent or incoherent manner, with appropriate spin and penetration factors included.

Most significantly, the software automatically carries out the normalisation of the PDF in the Dalitz plot by generating large numbers of events, assigning each a value according to the PDF and then summing these in order to provide a good numerical approximation of the PDF integral. Similarly, the package allows candidates to be generated according to a particular amplitude model in order, for example, to allow visualisation of the PDF. The package enables the complex coefficients between the resonances to vary but is not capable of allowing the parameters of the different lineshapes, including masses and widths, to be fitted.

Developing models

The complex coefficients in each model are separated into their real and imaginary parts, and these are allowed to vary in the fit. For technical reasons, fitting using such Cartesian coordinates is preferable to using polar coordinates (an amplitude and phase), since fitter instabilities easily arise in fitting a phase when an amplitude is small and large fitter biases are often introduced. From the Cartesian coordinates, the amplitude, a_i, and phase, ϕ_i, can be determined trivially. Fits are carried out with different combinations of resonant components, in each case allowing the complex coefficient associated with each resonance to float, until a good fit to the data is achieved.

The $K^*(892)^\pm \to K^0_S\pi^\pm$ and $K^*_0(1430)^\pm \to K^0_S\pi^\pm$ resonances are present in every model. Further components are added to these two, each improving the quality of the fit. The

significance of the contribution from each resonance is assessed by determining its fit fraction, defined as

$$F_i = \frac{\int d\vec{x}|\mathcal{A}_i(\vec{x})|^2}{\int d\vec{x}|\sum_{k=1}^{n}\mathcal{A}_k|^2}, \tag{3.8}$$

where $\mathcal{A}_i$ is the amplitude for the resonance with index i as a function of Dalitz position, $\vec{x}$, and the integration is over the kinematically allowed region. Resonances are added as long as their fit fraction in the final model is statistically significant at the level of 1σ. It is found that models with six significant resonances can be fitted for the $D^0 \to K^0_S K^-\pi^+$ mode and five can be fitted for the $D^0 \to K^0_S K^+\pi^-$ mode where the data sample is smaller.

Interference between resonances occurs and the size of this effect is quantified by calculating an interference fraction between pairs of resonances, defined as

$$F_{ij} = 2 \times \Re\left(\frac{\int d\vec{x}\mathcal{A}_i(\vec{x})\mathcal{A}_j^*(\vec{x})}{\int d\vec{x}|\sum_{k=1}^{n}\mathcal{A}_k|^2}\right), \tag{3.9}$$

where the indices i and j label the pair of resonances. The fit fractions and all interference fractions for a normalised PDF sum to unity. An indication of the overall level of interference between resonances in the model can be determined by summing only the fit fractions. Where the interference fraction is very large it is likely that the effect is not physical but simply due to resonances whose lineshapes are very similar and cancel one another, making very little difference to the overall PDF. Models in which the sum of fit fractions is very large, greater than 150%, are rejected. Since such interference effects are not likely to be physical (but are more likely to be a consequence of the use of two very similar resonance amplitudes in the signal PDF), discarding these models manifesting unphysical interference effects is reasonable.

A figure of merit, now described, is used to rank the models and select the best fit.

Evaluating the results

The models are classified using a χ^2 test in 67 square bins in the Dalitz plot as a figure of merit. These bins are as small as possible in order to produce a stable χ^2 result when

trialled on simulated experiments. The limit in the granularity is imposed such that at least ten events in the CLEO III and CLEO-c samples combined are found in each bin. In particularly sparsely populated Dalitz regions, therefore, neighbouring bins are grouped together until the threshold occupancy is passed. The order in which bins are combined is determined by stepping over the Dalitz plot from side to side, beginning at the bottom left corner and adding square bins together until the required threshold of contained data candidates is passed. The χ^2 is calculated in the conventional way by summing the quantity $\frac{\left(N_{\text{observed}} - N_{\text{expected}}\right)^2}{N_{\text{expected}}}$ over these new bins. The number of degrees of freedom used for the test is $\nu = N_{\text{bins}} - 1 - N_{\text{free fit parameters}}$. The data in the favoured and suppressed samples are shown in Figure 3.15 along with the binning schemes used for the χ^2 test.

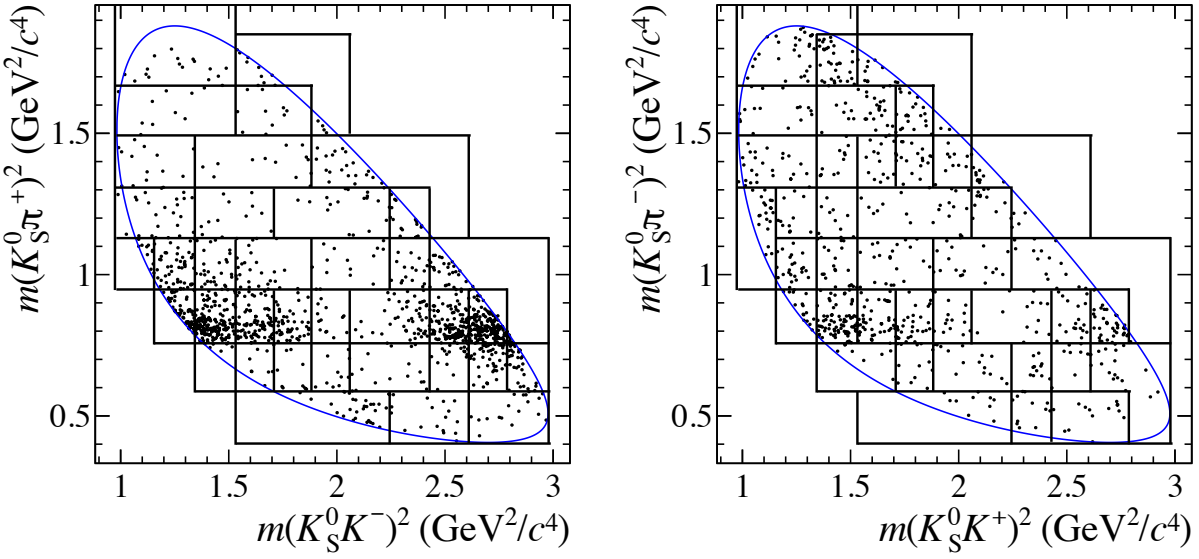

(a) $D^0 \to K^0_S K^-\pi^+$ (b) $D^0 \to K^0_S K^+\pi^-$

Figure 3.15: Binnings used for the χ^2 test for the two data sets where CLEO III and CLEO-c data have been combined.

Final models

Two amplitude models are determined for each of the two decay modes under study. The first is an amplitude model where the $K^*(892)^0 \to K^-\pi^+$ resonance is required to be present, regardless of whether another resonance in its place might yield a better fit χ^2, since models containing $D^0 \to K^{*0}\bar{K}^0$ and $D^0 \to \bar{K}^{*0}K^0$ resonances are of particular interest to theorists (see Section 3.1). This model in the $D^0 \to K^0_S K^-\pi^+$ ($D^0 \to K^0_S K^+\pi^-$) mode is referred

to as 'favoured (suppressed) model 1' through the remainder of this document. The second model is not required to contain the $K^*(892)^0 \to K^-\pi^+$ resonance and is, instead, the combination of resonances which produces the lowest χ^2 in fitting the data. This model for the $D^0 \to K^0_S K^-\pi^+$ ($D^0 \to K^0_S K^+\pi^-$) data is referred to as 'favoured (suppressed) model 2'.

The models are summarised in Table 3.6. The Dalitz projections demonstrate a good match between the model and the data in all cases. The content for models 1 and 2 is very similar, with the only difference being the replacement of the neutral $K^*(892)^0 \to K^-\pi^+$ resonance by another in the best-fit model. The $K^*(892)^\pm \to K^0_S\pi^\pm$ resonance is seen to take a large fit fraction in the models for each mode, as is expected given the clear presence of the resonance in the data Dalitz projections. The S-wave contribution is small in the $D^0 \to K^0_S K^-\pi^+$ mode but much larger for $D^0 \to K^0_S K^+\pi^-$. This behaviour is reasonable given the more prominent broad structure in the Dalitz projections of the data visible in the suppressed mode.

There is a large contribution from the $K^*(1410)^0 \to K^-\pi^+$ resonance in both models 1 and 2 for the $D^0 \to K^0_S K^-\pi^+$ decay. This is initially surprising, given the expected suppression of resonant structure in the $K^-\pi^+$ mode (see Section 3.3). It is, however, misleading to consider the fit fraction of this resonance in isolation and the explanation is found by inspecting the interference fractions between this and other resonances. As can be seen in Tables 3.11 and 3.12, there is significant destructive interference between the $K^*(1680)^+ \to K^0_S\pi^+$ and the $K^*(1410)^0 \to K^-\pi^+$ resonances of -21% for the first model and -27% for the second. The net contribution of the $K^*(1410)^0 \to K^-\pi^+$ resonance to the signal PDF is therefore much smaller than the fit fraction alone suggests and remains compatible with the expectation that the $K^-\pi^+$ spectrum should not contain significant structure.

It is interesting to compare the fitted parameters of the $K^*(892)^0 \to K^-\pi^+$ resonance with predictions from flavour SU(3) symmetry. Reference [82] gives an expectation for the amplitude ratio of the $D^0 \to \overline{K^{*0}}K^0$ and $D^0 \to K^{*+}K^-$ components of 0.138 ± 0.033. This

prediction agrees with the model 1 fit to the data, which for $D^0 \to K^0_S K^-\pi^+$ returns a value of 0.2 ± 0.1. Analysis of a larger data set is necessary before the parameters of this resonance, particularly the phase of the coefficient, can be used for a more revealing comparison.

Table 3.6: Summary of the resonant models with references to the Dalitz projection and detailed model content table, as well as a measure of the fit quality.

Model	Detailed content	Dalitz fit projection	Content	χ^2/dof
$D^0 \to K^0_S K^-\pi^+$ with K^{*0}	Table 3.7, 3.11	Figure 3.16	$K^*(892)^+$, $K^*(892)^0$, $K^*(1410)^0$, $a_0(1450)^-$, $K^*(1680)^+$, $K^*_0(1430)^0$	42.2/26
$D^0 \to K^0_S K^-\pi^+$ without K^{*0}	Table 3.8, 3.12	Figure 3.17	$K^*(892)^+$, $\rho(1700)^-$, $K^*(1410)^0$, $a_0(1450)^-$, $K^*(1680)^+$, $K^*_0(1430)^0$	37.3/26
$D^0 \to K^0_S K^+\pi^-$ with K^{*0}	Table 3.9, 3.13	Figure 3.18	$K^*(892)^-$, $K^*(892)^0$, $a_0(1450)^-$, $K^*_0(1430)^0$, $\rho(1700)^+$	50.9/26
$D^0 \to K^0_S K^+\pi^-$ without K^{*0}	Table 3.10, 3.14	Figure 3.19	$K^*(892)^-$, $K^*_2(1430)^0$, $a_0(1450)^-$, $K^*_0(1430)^0$, $\rho(1700)^+$	46.5/26

Table 3.7: Fit results for favoured $D^0 \to K^0_S K^-\pi^+$ model 1, including statistical and, secondly, systematic uncertainties.

Component	Amplitude	Phase (°)	Fraction (%)
$D^0 \to K^*(892)^+(\to K^0_S\pi^+)K^-$	1.0 (fixed)	0.0 (fixed)	67.6±6.4± 3.8
$D^0 \to K^*(892)^0(\to K^-\pi^+)K^0_S$	0.2±0.1±0.0	96.1±13.2±12.4	1.8±1.7± 0.8
$D^0 \to K^*(1410)^0(\to K^-\pi^+)K^0_S$	8.4±0.7±3.0	-16.7± 7.5 ± 9.2	23.2±3.9± 4.2
$D^0 \to K^*(1680)^+(\to K_S\pi^+)K^-$	15.3±2.3±3.8	148.3±11.1±14.2	22.7±4.4± 5.6
$D^0 \to K^*_0(1430)^+(\to K_S\pi^+)K^-$	1.3±0.3±0.5	-101.0±22.0±12.3	2.5±1.2± 2.0
$D^0 \to a_0(1450)^-(\to K_S K^-)\pi^+$	0.4±0.2±0.1	-26.8±42.3±27.2	1.0±0.9± 0.9
			118.8±9.0±8.3

Table 3.8: Fit results for favoured $D^0 \to K^0_S K^-\pi^+$ model 2, including statistical and, secondly, systematic uncertainties.

Component	Amplitude	Phase (°)	Fraction (%)
$D^0 \to K^*(892)^+(\to K_S\pi^+)K^-$	1.0 (fixed)	0.0 (fixed)	62.2± 4.8 ± 3.9
$D^0 \to K^*(1410)^0(\to K^-\pi^+)K^0_S$	10.3±1.0±2.7	-18.5± 5.6 ± 7.0	32.0± 6.0 ± 19.6
$D^0 \to K^*(1680)^+(\to K_S\pi^+)K^-$	17.1±2.3±2.4	151.6± 8.3 ± 7.3	26.1± 6.0 ± 24.0
$D^0 \to \rho(1700)^-(\to K_S K^-)\pi^+$	5.5±1.8±1.5	23.5±12.5±21.5	4.4± 3.0 ± 3.7
$D^0 \to K^*_0(1430)^+(\to K_S\pi^+)K^-$	1.5±0.3±0.7	-101.5±18.9± 8.7	3.1± 1.2 ± 3.1
$D^0 \to a_0(1450)^-(\to K_S K^-)\pi^+$	0.7±0.2±0.2	-31.7±23.3±16.1	2.3± 1.2 ± 1.5
			130.1±10.3±31.4

Table 3.9: Fit results for suppressed $D^0 \to K^0_S K^+\pi^-$ model 1, including statistical and, secondly, systematic uncertainties.

Component	Amplitude	Phase (°)	Fraction (%)
$D^0 \to K^*(892)^-(\to K_S\pi^-)K^+$	1.0 (fixed)	0.0 (fixed)	20.4±2.1± 0.8
$D^0 \to K^*(892)^0(\to K^+\pi^-)K^0_S$	0.4±0.1±0.0	109.9±10.8±3.7	3.9±1.5± 0.4
$D^0 \to K^*_0(1430)^-(\to K_S\pi^-)K^+$	6.2±0.9±0.5	-114.4± 9.8 ±5.0	18.4±2.8± 1.5
$D^0 \to a_0(1450)^+(\to K_S K^+)\pi^-$	3.1±0.5±0.4	-54.0± 8.6 ±6.4	15.8±4.1± 2.1
$D^0 \to \rho(1700)^+(\to K_S K^+)\pi^-$	11.4±2.2±3.9	90.3± 9.6 ±7.7	6.2±2.1± 2.5
			64.6±6.0±3.7

Table 3.10: Fit results for suppressed $D^0 \to K^0_S K^+\pi^-$ model 2, including statistical and, secondly, systematic uncertainties.

Component	Amplitude	Phase (°)	Fraction (%)
$D^0 \to K^*(892)^-(\to K_S\pi^-)K^+$	1.0 (fixed)	0.0 (fixed)	21.2±2.2± 3.3
$D^0 \to K^*_0(1430)^-(\to K_S\pi^-)K^+$	8.0±0.9±0.7	-71.8±13.4± 9.3	31.5±6.2± 8.0
$D^0 \to \rho(1700)^+(\to K_S K^+)\pi^-$	12.7±2.2±5.4	103.7±16.1±11.2	8.0±2.2± 3.8
$D^0 \to a_0(1450)^+(\to K_S K^+)\pi^-$	1.8±0.4±0.3	-30.1±14.7±10.9	5.8±2.3± 1.6
$D^0 \to K^*_2(1430)^0(\to K^+\pi^-)K^0_S$	4.7±1.5±2.0	-104.1±14.9± 7.5	4.3±2.8± 3.4
			70.7±7.8±10.2

Table 3.11: Interference fit fractions (%) between every pair of resonances in the $D^0 \to K^0_S K^-\pi^+$ model which contains the neutral $K^*(892)^0 \to K^-\pi^+$ resonance. The first uncertainty is statistical and the second is systematic.

	$K^*(892)^0$	$K^*(1410)^0$	$K^*(1680)^-$	$K^*_0(1430)^-$	$a_0(1450)^+$
$K^*(892)^-$	$-0.23\pm0.65\pm0.57$	$-12.29\pm1.23\pm3.42$	$13.62\pm3.32\pm2.17$	$3.38\pm0.88\pm0.63$	$2.56\pm2.09\pm1.71$
$K^*(892)^0$		$-2.81\pm1.55\pm0.79$	$0.23\pm0.27\pm0.75$	$0.57\pm0.30\pm0.24$	$0.26\pm0.30\pm0.12$
$K^*(1410)^0$			$-21.18\pm2.73\pm8.66$	$1.15\pm0.61\pm1.39$	$0.78\pm3.19\pm1.99$
$K^*(1680)^-$				$-6.70\pm1.79\pm2.68$	$0.55\pm4.08\pm2.00$
$K^*_0(1430)^-$					$1.37\pm1.17\pm0.75$

Table 3.12: Interference fit fractions (%) between every pair of resonances in the $D^0 \to K^0_S K^-\pi^+$ model which does not contain the neutral $K^*(892)^0 \to K^-\pi^+$ resonance. The first uncertainty is statistical and the second is systematic.

	$K^*(1410)^0$	$K^*(1680)^-$	$\rho(1700)^+$	$K^*_0(1430)^-$	$a_0(1450)^+$
$K^*(892)^-$	$-14.04\pm1.42\pm2.02$	$13.05\pm2.61\pm4.02$	$3.60\pm1.52\pm3.36$	$3.58\pm0.70\pm0.92$	$4.03\pm1.60\pm1.52$
$K^*(1410)^0$		$-27.47\pm5.29\pm28.07$	$-7.33\pm3.45\pm8.73$	$1.55\pm0.74\pm2.30$	$1.82\pm3.41\pm1.72$
$K^*(1680)^-$			$-4.33\pm2.76\pm7.87$	$-8.06\pm1.93\pm7.16$	$-0.30\pm4.16\pm1.98$
$\rho(1700)^+$				$1.24\pm0.55\pm1.57$	$0.02\pm0.01\pm0.01$
$K^*_0(1430)^-$					$2.49\pm1.34\pm0.86$

Table 3.13: Interference fit fractions (%) between every pair of resonances in the $D^0 \to K^0_S K^+\pi^-$ model which contains the neutral $K^*(892)^0 \to K^-\pi^+$ resonance. The first uncertainty is statistical and the second is systematic.

	$K^*(892)^0$	$K^*_0(1430)^-$	$a_0(1450)^+$	$\rho(1700)^+$
$K^*(892)^-$	$-0.74\pm0.46\pm0.10$	$4.91\pm0.57\pm0.53$	$7.01\pm0.88\pm0.87$	$5.74\pm0.91\pm1.16$
$K^*(892)^0$		$1.34\pm0.54\pm0.33$	$-0.50\pm0.58\pm0.40$	$0.72\pm0.47\pm0.29$
$K^*_0(1430)^-$			$17.39\pm1.52\pm1.69$	$-0.49\pm0.75\pm0.41$
$a_0(1450)^+$				$-0.01\pm0.01\pm0.01$

Table 3.14: Interference fit fractions (%) between every pair of resonances in the $D^0 \to K^0_S K^+\pi^-$ model which does not contain the neutral $K^*(892)^0 \to K^-\pi^+$ resonance. The first uncertainty is statistical and the second is systematic.

	$K^*_0(1430)^-$	$\rho(1700)^+$	$a_0(1450)^+$	$K^*_2(1430)^0$
$K^*(892)^-$	$5.70\pm0.55\pm0.31$	$6.41\pm0.89\pm1.41$	$3.62\pm0.95\pm0.64$	$1.75\pm0.81\pm3.32$
$K^*_0(1430)^-$		$2.07\pm0.85\pm0.80$	$15.25\pm2.21\pm0.91$	$-5.79\pm5.60\pm9.15$
$\rho(1700)^+$			$0.00\pm0.01\pm0.01$	$4.00\pm1.23\pm1.71$
$a_0(1450)^+$				$-3.71\pm1.64\pm2.26$

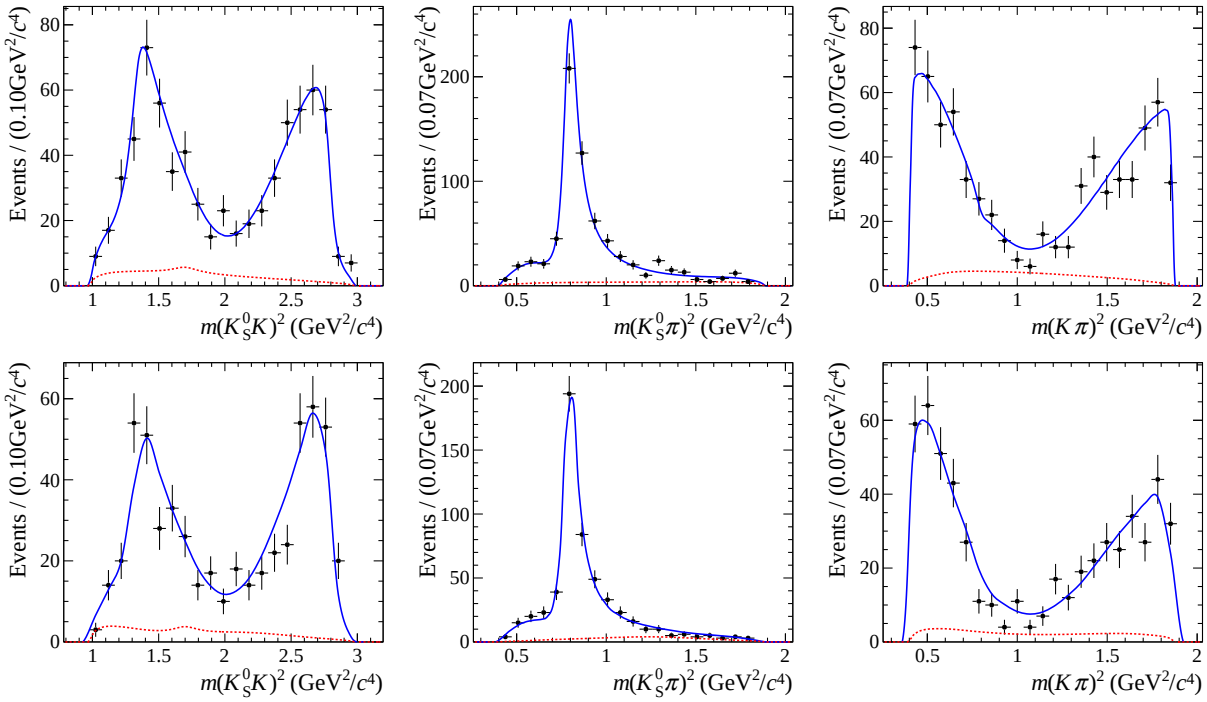

Figure 3.16: CLEO III (upper) and CLEO-c (lower) favoured model 1 Dalitz projections with total (solid blue line) and background (dotted red line) fit PDF superimposed.

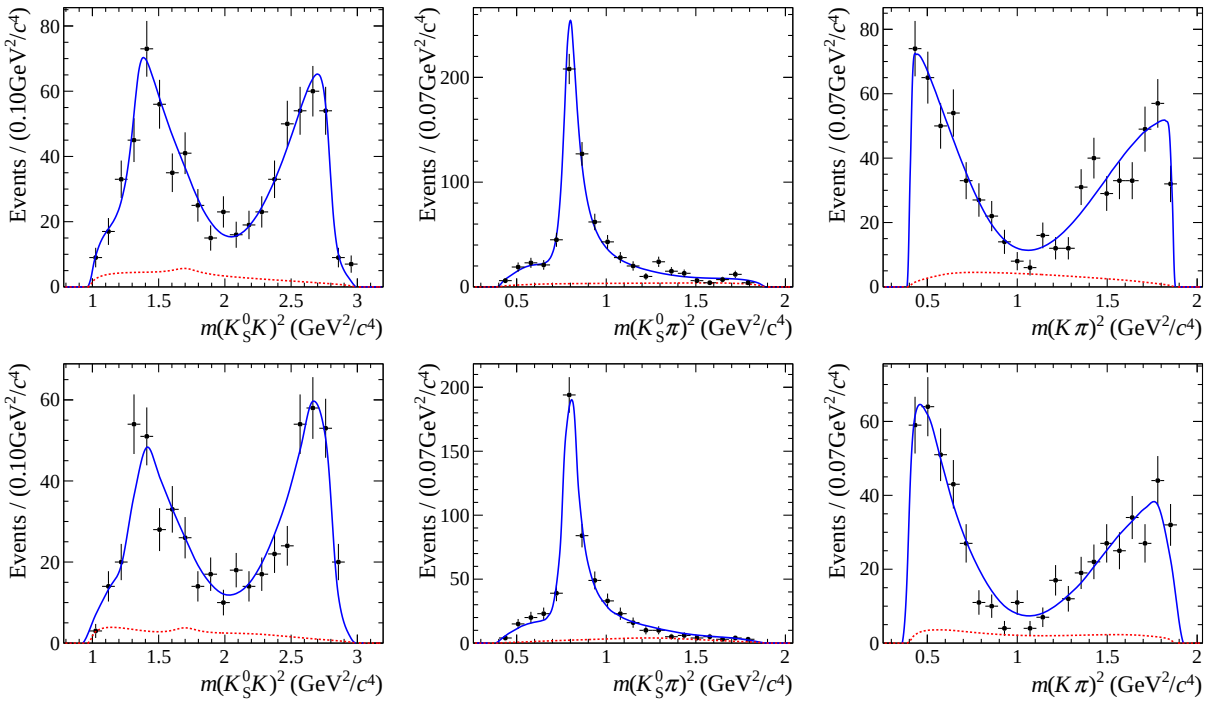

Figure 3.17: CLEO III (upper) and CLEO-c (lower) favoured model 2 Dalitz projections with total (solid blue line) and background (dotted red line) fit PDF superimposed.

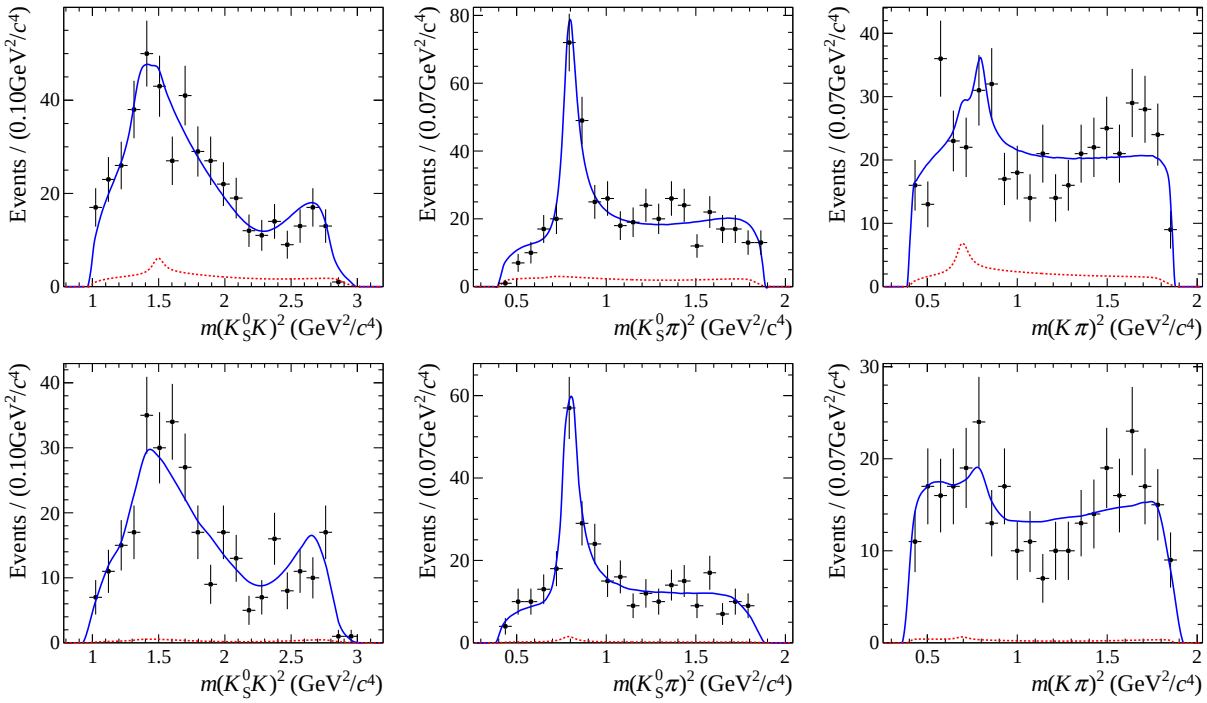

Figure 3.18: CLEO III (upper) and CLEO-c (lower) suppressed model 1 Dalitz projections with total (solid blue line) and background (dotted red line) fit PDF superimposed.

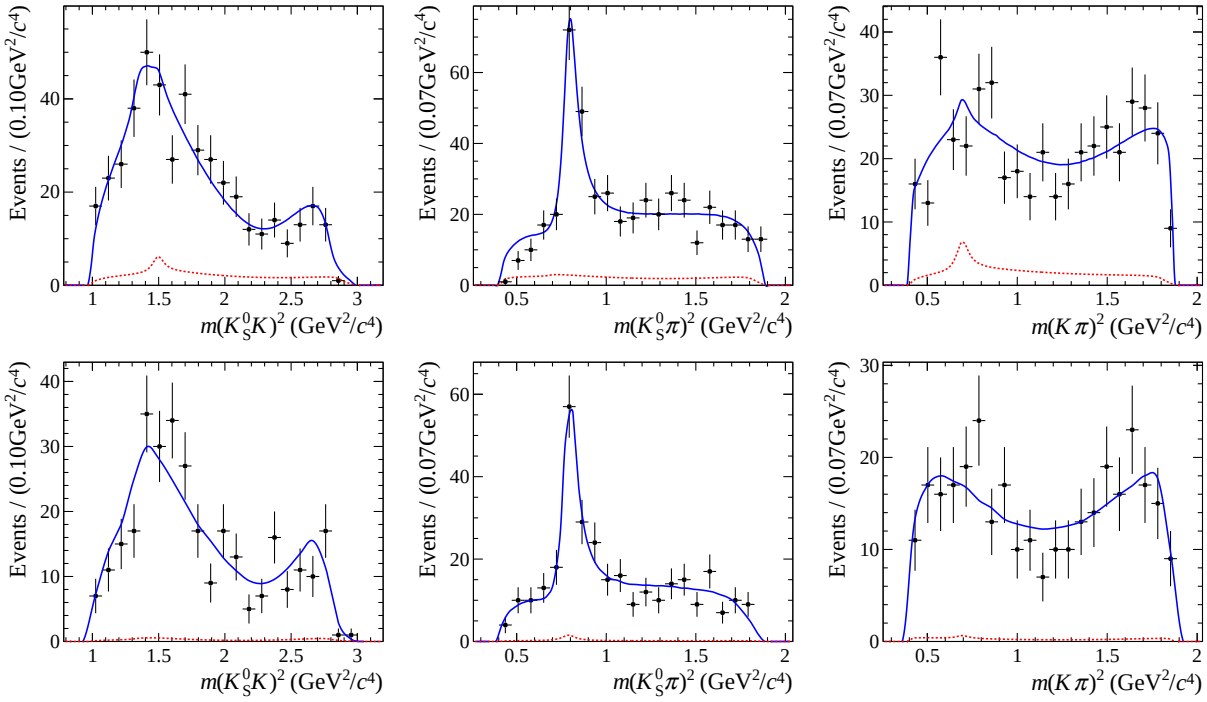

Figure 3.19: CLEO III (upper) and CLEO-c (lower) suppressed model 2 Dalitz projections with total (solid blue line) and background (dotted red line) fit PDF superimposed.

3.4 Systematic uncertainties on the amplitude models

A number of different sources of systematic uncertainty are considered, the most significant of which are the uncertainties on the parameters used to describe the lineshapes of the different resonances. The systematic studies undertaken are summarised in the following sections. The systematic uncertainties on each model parameter are given as a fraction of the statistical uncertainties in Tables 3.15 and 3.16 for model 1 in each mode.

3.4.1 Resonance lineshape parameters

The uncertainties on the masses and widths used to describe each of the resonances are given in Table 3.4. To evaluate the errors on the model parameters arising from these uncertainties, the fit to data is repeated using a model in which the mass or width of one of the signal resonances has been moved up or down by one multiple of its uncertainty. This is repeated for the masses and widths of the different resonances and the average absolute changes in the parameters are determined for the shifts up and down. The changes for the masses and widths of all the resonances are then combined in quadrature.

For the LASS lineshape of the $K^*_0(1430)^\pm \to K^0_S\pi^\pm$ resonance, which defines the S-wave contribution, the uncertainties from the *BABAR* description of the lineshape are used and varied in the same way as the mass and width parameters. The resulting changes of the model parameters are then combined with the changes found above.

3.4.2 Blatt-Weisskopf penetration factors

The matrix element for each resonance in the decay contains a penetration factor (see Section 1.4) which depends upon the meson radius. For the D meson this is conventionally chosen to be 5 $(\mathrm{GeV}/c)^{-1}$, and for the resonance the conventional value is 1.5 $(\mathrm{GeV}/c)^{-1}$ [83]. In order to determine the uncertainty on the model parameters arising from the uncertainty on these radii, the data fit is repeated where the D^0 and resonance radii are replaced

by the values 1.5 $(\mathrm{GeV}/c)^{-1}$ and 0.5 $(\mathrm{GeV}/c)^{-1}$, respectively, and the displacements in the fit parameters from their original fitted values are taken as the systematic uncertainty.

The magnitude of the displacements introduced in the meson radii is motivated with reference to the measurements of these radii ($(5.0 \pm 0.5)\,(\mathrm{GeV}/c)^{-1}$ and $(1.6 \pm 1.3)\,(\mathrm{GeV}/c)^{-1}$, respectively) made by the E791 collaboration [84] and to the precedent set by other amplitude analyses in evaluating this systematic uncertainty [83]. It should be noted that in [83], the resonance meson radius was changed only from $1.5\,(\mathrm{GeV}/c)^{-1}$ to $1.0\,(\mathrm{GeV}/c)^{-1}$ to evaluate the systematic uncertainty, and that the treatment of that input parameter presented in this thesis is therefore more conservative. The radii are decreased rather than increased so that, as the radii approach zero, the form factors tended towards unity (the most radical replacement possible).

The effect is most pronounced when the model contains large contributions from resonances whose pole mass lies significantly outside the Dalitz plot and whose contribution is therefore primarily through the tail of the resonance. A change in the form factor for a resonance results in perturbations to the PDF which increase with distance from the resonance pole mass. This explains the larger changes in the model parameters for the $D^0 \to K^0_S K^-\pi^+$ models which contain larger contributions from resonances lying outside the phase space than for the $D^0 \to K^0_S K^+\pi^-$ models. This large effect for particular resonances is discussed further in Section 3.4.10.

3.4.3 Quantum coherence in CLEO-c data

The CLEO-c data sample contains some contamination at a low level from events where the tag-side D meson decays via a doubly Cabibbo-suppressed (DCS) process instead of the dominant, Cabibbo-favoured (CF) decay assumed. In such cases, the inferred flavour of the signal D is mistaken and a decay which is $D^0 \to K^0_S K^+\pi^-$ could be wrongly considered as $\bar{D}^0 \to K^0_S K^+\pi^-$. Since the initial flavour is not known, the amplitudes for these two cases combine coherently and a more correct equation for the amplitude which matches the

$D^0 \to K^0_S K^-\pi^+$ CLEO-c sample is

$$\mathcal{A}_{\text{total}} = \mathcal{A}_{\text{CF tag}}\mathcal{A}_{D^0\to K^0_S K^-\pi^+} + \mathcal{A}_{\text{DCS tag}}\mathcal{A}_{D^0\to K^0_S K^+\pi^-}. \tag{3.10}$$

Since the magnitude of the pure DCS contribution is negligible, the contamination in each sample resulting from quantum coherence arises chiefly through the interference term between the two terms in Equation 3.10. This can be quantified by

$$\mathcal{A}_{\text{tot}} = \mathcal{A}_{D^0\to K^0_S K^-\pi^+} + 0.05 \times 0.7 e^{i\delta_{\text{Q. coh.}}} \times \mathcal{A}_{D^0\to K^0_S K^+\pi^-}, \tag{3.11}$$

where the factor 0.05 is the approximate ratio of DCS to CF amplitudes, determined as the ratio of the CKM elements appropriate to the two amplitudes [74]. The interference is reduced still further by the factor 0.7, which is necessary to include since interference effects in the 3- and 4-body decays are diluted by the presence of intermediate resonances. This dilution is quantified by means of a 'coherence factor' [85] which, for the $K^\pm\pi^\mp\pi^0$ mode has been measured to be ~ 0.3 and for the $K^\pm\pi^\mp\pi^+\pi^-$ to be ~ 0.8 [86]. The factor of 0.7 is the average of the coherence factors for the three tag types, $K^\pm\pi^\mp$, $K^\pm\pi^\mp\pi^+\pi^-$ and $K^\pm\pi^\mp\pi^0$, weighted by the sizes of the three samples.

The uncertainty is determined by taking the difference in the fit parameters when the usual PDF is fitted to data and when the PDF used to fit the data is altered by the addition of an amplitude contribution from the opposite mode.

The phase difference, $\delta_{\text{Q. coh.}}$, between the $D^0 \to K^0_S K^+\pi^-$ and $D^0 \to K^0_S K^-\pi^+$ decays is unknown so tests are made at $0, \pi/2, \pi$ and $3\pi/2$. The largest changes in the fit parameters are seen generally with a phase difference of 0 so these shifts are conservatively taken to represent the systematic effect.

3.4.4 CLEO III mis-tag

The CLEO III data samples of $D^{*\pm}$ decays are contaminated by a contribution from decays where the pion associated with the reconstructed neutral D meson is incorrectly chosen and the flavour of the D meson wrongly inferred. This mis-tag rate is measured in a similar analysis to be $(0.64 \pm 0.05)\%$ [87] and, at such a low level, is neglected in the fit. The effect of neglecting the mis-tag is quantified by adding, incoherently, a contribution to the CLEO III fit PDF from the PDF developed for the other D^0 decay mode. For example, to evaluate this systematic uncertainty for the $D^0 \to K^0_S K^-\pi^+$ model parameters, the fit to data is repeated with a modified fit PDF where a small contribution is added to the PDF using the model developed for the $D^0 \to K^0_S K^+\pi^-$ mode (suppressed mode model 1, given in Table 3.9). A similar procedure is performed to determine the systematic uncertainty for the $D^0 \to K^0_S K^+\pi^-$ model, where a small contribution from the $D^0 \to K^0_S K^-\pi^+$ model PDF is added to the $D^0 \to K^0_S K^+\pi^-$ fit PDF incoherently.

For the fit to the $D^0 \to K^0_S K^-\pi^+$ CLEO III data sample, the PDF is then

$$P_{\text{CLEO III}} = P_{D^0 \to K^0_S K^-\pi^+} + 0.0064 \times P_{D^0 \to K^0_S K^+\pi^-}, \tag{3.12}$$

where P is the appropriate PDF. A similar relation can be written for the new PDF used to fit the $D^0 \to K^0_S K^+\pi^-$ CLEO III data. The data are refitted using the new PDF and the shift on each model parameter is taken to be the systematic uncertainty.

3.4.5 Background models

Imperfections in the CLEO III and CLEO-c background models impact upon the signal model fit results, as the signal model is forced to accommodate residual background features. The degree to which the signal model parameters are affected by changes in the background model is assessed by producing an alternative model for the CLEO III or CLEO-c backgrounds. In each case, the alternative background fit is chosen from the set of those tested during the background modelling stage and is related to the original background model

through removal, addition or replacement of one or two of the background resonance components. The alternative model has a higher χ^2 per degree of freedom in the background fit. Alternative background models are developed where some of the resonances are removed to change the background shapes.

The full fit to the data is repeated with either the CLEO III or CLEO-c background models replaced. The shifts in the fit parameters are then combined in quadrature to determine the systematic uncertainties.

3.4.6 Sample purities

There is an uncertainty on the levels of background contamination in the data samples. Since the modelled background shapes are not flat, a change in the background fraction changes the signal parameters as the model accounts for the changed distribution of events in the Dalitz plot.

The effect on the model parameters is calculated for shifts of the CLEO III or CLEO-c background fractions up or down by an amount equal to the uncertainties. The largest shift on each fit parameter is chosen between the two produced by an upwards or downwards background fraction shift. The changes found when changing the CLEO III and CLEO-c background fractions are then combined in quadrature.

3.4.7 Detector acceptance

The sensitivity of the model parameters to the detector acceptance is studied by developing new parameterisations for both the CLEO III and CLEO-c acceptances and repeating the fit to data using these new acceptance models.

- **CLEO III acceptance**

  The CLEO III acceptance is refitted with a third order polynomial, instead of the previous second order. The fitted Dalitz projections are shown in Figure 3.20.

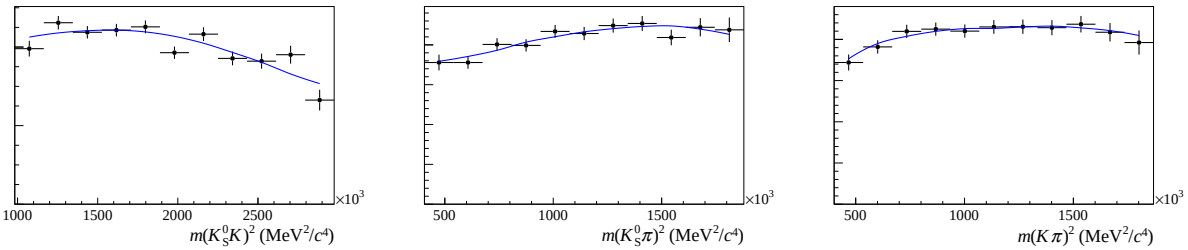

Figure 3.20: Simulated CLEO III data (black data points with errors) showing the combined reconstruction and selection efficiency effect on the Dalitz projections. The new fit is superimposed (solid blue line).

- **CLEO-c acceptance**

  The CLEO-c acceptance is parameterised using a third order Chebychev polynomial, instead of using the events directly in the fit. The fit projections are shown in Figure 3.21.

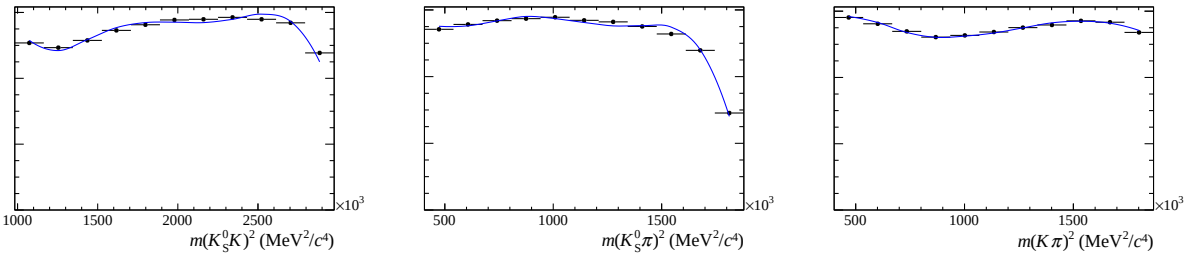

Figure 3.21: Simulated CLEO-c data (black data points with errors) showing the combined reconstruction and selection efficiency effect on the Dalitz projections. The fit is superimposed (solid blue line).

The new parameterisations for the CLEO III and CLEO-c acceptances are inserted separately in the fit to data in order to determine the effect on the central values of the signal model parameters. The shifts are calculated and combined in quadrature for the two new acceptances.

3.4.8 Momentum resolution

The finite CLEO III and CLEO-c detector resolutions result in a smearing of the Dalitz coordinates of reconstructed candidates, an effect which is not accounted for in the fit. Limitations in the availability of 'truth' information in the CLEO III simulated data samples

mean that the effect can only be studied using the CLEO-c simulated data. The study of the systematic uncertainty is determined using only CLEO-c simulated data, and is assumed to be the same at CLEO III. The procedure involves a number of steps. Firstly, the momentum resolution for each daughter particle is determined using simulated CLEO-c data. Secondly, the amplitude models, with the same resonant content as described in Section 3.3.4, are fitted to the CLEO-c data alone. Finally, the CLEO-c data are smeared according to the determined momentum resolutions, and the CLEO-c data are refitted. The displacements in the model parameters are taken to be the systematic uncertainty arising from the finite momentum resolution, and assumed to apply to the CLEO III data as well.

First of all, the smearing factors are determined from the distributions of the difference between the reconstructed and true momenta of the K^0_S, $K^\mp$ and $\pi^\pm$ particles in simulated signal samples, shown in Figure 3.22. The distributions are fitted with a double Gaussian PDF, the form of which is

$$f_1 \times \text{Gaussian}(m_1, \sigma_1) + (1 - f_1) \times \text{Gaussian}(m_1, \sigma_2). \tag{3.13}$$

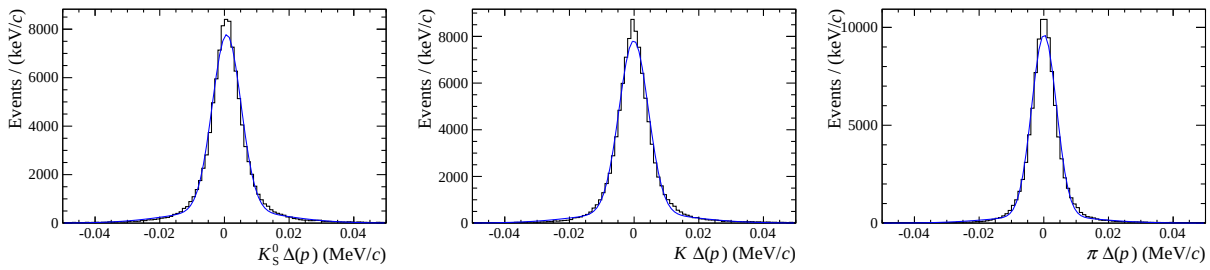

Figure 3.22: Difference between reconstructed and generated particle momenta for simulated CLEO-c data,$\Delta(p) =$ (reconstructed momentum $-$ generated momentum (MeV/c)), for each daughter particle.

The CLEO-c data alone are fitted. The momenta of the daughters are then smeared randomly according to the factors determined using the simulated samples, and the data are then refitted and the displacement of each model parameter with respect to the first fit is calculated. The CLEO-c data are then reverted to their original state and another random smearing is performed before the next refit. This is repeated and the average displacement of the model parameters for the different random smearings is taken to represent the effect

of ignoring detector resolution. Points which migrate outside the Dalitz boundary are still included in the fit.

3.4.9 Fitter bias

In order to determine whether the fit procedure returns unbiased results and correctly estimated uncertainties, a study using simulated experiments is performed. Data samples are generated according to the fitted model to which appropriate background contributions are added and acceptance effects applied. The generated data are then fitted and the difference in the generated and fit parameter values are studied over the sample of simulated experiments, particularly to check the pull distributions for each of the fitted real and imaginary parts for each resonance and for the fit fractions for each parameter. The distributions are adequately described by a Gaussian function of unit width. The average change in each fit parameter is taken as the bias on that parameter, as shown in column IX of Tables 3.15 and 3.16.

3.4.10 Summary of systematic uncertainties

For each model, the different systematic uncertainties on each parameter are combined in quadrature. The shifts in each parameter arising from each source are given as a fraction of the statistical uncertainty in Tables 3.15 and 3.16 for model 1 in each mode.

The majority of the fit parameters listed in the two tables are statistically limited but systematic uncertainties are significant relative to the statistical uncertainties, particularly for the parameters of the $D^0 \to K^0_S K^-\pi^+$ model. The largest contribution arises from the uncertainty on the parameters defining the Blatt-Weisskopf penetration factors (column I). This is particularly marked for the $K^*(1410)^0 \to K^-\pi^+$ and $K^*(1680)^+ \to K^0_S\pi^+$ resonances in the $D^0 \to K^0_S K^-\pi^+$ model. That this systematic uncertainty should produce such a large uncertainty for these parameters is not surprising since the variation of penetration factor parameters has a larger effect on the resonance amplitude further from the resonance pole

mass. In the case of these two resonances, the pole mass lies some considerable distance beyond the kinematic limits of the Dalitz plot, so that the contribution of these resonances to the model is entirely through the shape of the tails in the resonance, which are sensitive to the choice of penetration factors.

Aside from the uncertainties attached to the penetration factor, the other most significant source of uncertainty is that on the resonance masses and widths (column II). In this case, the size of the contribution of this uncertainty is much more consistent across the different components in the models. The combined absolute systematic uncertainty for each model is shown in the model descriptions in Tables 3.7 to 3.10. The total systematic uncertainty is also propagated to the interference fractions shown in Tables 3.11 to 3.14.

Discussion of the relevance of the amplitude model measurements for tests of SU(3) flavour symmetry, in addition to those already presented in Section 3.3.4, are given in the conclusion in Section 6.1.1.

Table 3.15: Systematic uncertainties on the fit fractions, F_i, amplitudes, $|a_i|$, and phases, ϕ_i, in units of statistical standard deviations (σ) for the decay $D^0 \to K^0_S K^-\pi^+$ model 1. The different contributions are: (I) Blatt–Weisskopf penetration factors, (II) mass and width of resonances, (III) quantum correlations, (IV) CLEO III mis-tag, (V) background models, (VI) sample purities, (VII) acceptance, (VIII) Dalitz resolution, and (IX) fitter bias.

	Source (σ)									Total (σ)
	I	II	III	IV	V	VI	VII	VIII	IX	
$K^*(892)^+K^-$ F_i	0.36	0.33	0.13	0.08	0.08	0.15	0.16	0.05	0.18	0.59
$K^*(892)^0K^0_S$ $\|a_i\|$	0.19	0.24	0.06	0.09	0.12	0.16	0.14	0.06	0.06	0.42
$K^*(892)^0K^0_S$ ϕ_i	0.87	0.28	0.11	0.02	0.10	0.08	0.11	0.07	0.05	0.94
$K^*(892)^0K^0_S$ F_i	0.21	0.21	0.05	0.10	0.13	0.19	0.16	0.05	0.21	0.47
$K^*(1410)^0K^0_S$ $\|a_i\|$	4.35	0.85	0.23	0.04	0.09	0.07	0.09	0.01	0.12	4.44
$K^*(1410)^0K^0_S$ ϕ_i	1.13	0.39	0.05	0.07	0.17	0.13	0.12	0.01	0.13	1.23
$K^*(1410)^0K^0_S$ F_i	0.96	0.35	0.32	0.04	0.07	0.07	0.06	0.02	0.05	1.08
$K^*(1680)^+K^-$ $\|a_i\|$	1.53	0.41	0.07	0.08	0.10	0.15	0.14	0.03	0.21	1.62
$K^*(1680)^+K^-$ ϕ_i	1.15	0.41	0.03	0.09	0.11	0.17	0.16	0.02	0.26	1.28
$K^*(1680)^+K^-$ F_i	1.20	0.32	0.17	0.00	0.03	0.02	0.12	0.02	0.09	1.26
$K^*_0(1430)^+K^-$ $\|a_i\|$	1.44	0.32	0.20	0.08	0.14	0.15	0.21	0.02	0.39	1.57
$K^*_0(1430)^+K^-$ ϕ_i	0.49	0.19	0.08	0.02	0.08	0.04	0.13	0.00	0.05	0.56
$K^*_0(1430)^+K^-$ F_i	1.51	0.35	0.15	0.07	0.12	0.13	0.18	0.03	0.16	1.59
$a_0(1450)^-\pi^+$ $\|a_i\|$	0.41	0.35	0.20	0.04	0.08	0.08	0.15	0.02	0.08	0.61
$a_0(1450)^-\pi^+$ ϕ_i	0.42	0.44	0.18	0.03	0.04	0.06	0.08	0.04	0.06	0.64
$a_0(1450)^-\pi^+$ F_i	0.54	0.24	0.29	0.02	0.10	0.04	0.22	0.01	0.73	1.01

Table 3.16: Systematic uncertainties on the fit fractions, F_i, amplitudes, $|a_i|$, and phases, ϕ_i, in units of statistical standard deviations (σ) for the decay $D^0 \to K^0_S K^+\pi^-$ model 1. The different contributions are: (I) Blatt–Weisskopf penetration factors, (II) mass and width of resonances, (III) quantum correlations, (IV) CLEO III mis-tag, (V) background models, (VI) sample purities, (VII) acceptance, (VIII) Dalitz resolution, and (IX) fitter bias.

	Source (σ)									Total (σ)
	I	II	III	IV	V	VI	VII	VIII	IX	
$K^*(892)^-K^+$ F_i	0.23	0.21	0.20	0.05	0.03	0.04	0.11	0.00	0.02	0.39
$K^*(892)^0K^0_S$ $\lvert a_i\rvert$	0.13	0.37	0.04	0.03	0.03	0.02	0.05	0.00	0.08	0.41
$K^*(892)^0K^0_S$ ϕ_i	0.20	0.24	0.03	0.01	0.04	0.02	0.12	0.00	0.04	0.34
$K^*(892)^0K^0_S$ F_i	0.10	0.23	0.01	0.02	0.02	0.04	0.07	0.01	0.07	0.27
$K^*_0(1430)^-K^+$ $\lvert a_i\rvert$	0.33	0.33	0.10	0.03	0.02	0.03	0.08	0.00	0.19	0.52
$K^*_0(1430)^-K^+$ ϕ_i	0.23	0.43	0.07	0.02	0.01	0.02	0.03	0.00	0.13	0.51
$K^*_0(1430)^-K^+$ F_i	0.31	0.37	0.09	0.03	0.02	0.01	0.08	0.00	0.15	0.52
$a_0(1450)^+\pi^-$ $\lvert a_i\rvert$	0.58	0.56	0.08	0.02	0.01	0.02	0.04	0.01	0.06	0.81
$a_0(1450)^+\pi^-$ ϕ_i	0.46	0.58	0.06	0.01	0.02	0.01	0.04	0.00	0.04	0.75
$a_0(1450)^+\pi^-$ F_i	0.43	0.24	0.03	0.00	0.01	0.01	0.03	0.01	0.17	0.52
$\rho(1700)^+\pi^-$ $\lvert a_i\rvert$	1.25	1.22	0.05	0.00	0.02	0.01	0.07	0.01	0.09	1.75
$\rho(1700)^+\pi^-$ ϕ_i	0.36	0.71	0.09	0.00	0.01	0.01	0.06	0.00	0.02	0.80
$\rho(1700)^+\pi^-$ F_i	1.01	0.68	0.01	0.01	0.01	0.01	0.09	0.01	0.02	1.22

3.5 Measurement of the branching fraction ratio of $D^0 \to K^0_S K^+\pi^-$ and $D^0 \to K^0_S K^-\pi^+$ decays

Determination of the ratio of branching fractions in the two modes is necessary to prepare for a measurement of γ using $B^\pm \to [K^0_S K\pi]_D K^\pm$ decays. Firstly, the quantity

$$R_D = \frac{\Gamma(D^0 \to K^0_S K^+\pi^-)}{\Gamma(D^0 \to K^0_S K^-\pi^+)}, \tag{3.14}$$

where Γ indicates the partial width, is, if mixing effects are neglected, equal to the square of the amplitude ratio r_D for these two modes which enters Equations 1.10 and 1.11. Secondly, the value of R_D is a necessary input to the analysis to measure the coherence factor. Finally, knowledge of this parameter will also be required in the future, should a mixing analysis be performed in the decay of neutral D mesons to the $K^0_S K^\mp\pi^\pm$ final state [88].

The ratio is measured using CLEO III data only in order to avoid any bias from the effect of quantum correlations present in the CLEO-c data. The background-corrected signal

yields, S, in Table 3.1 must be corrected for different acceptance effects for the two modes and different contaminations in each sample as a result of mis-tagged $D^{*\pm}$ decays. The ratio is measured in two regions: firstly over the whole Dalitz plot and secondly in a window $\pm 100\,\mathrm{MeV}/c^2$ around the $K^*(892)^\pm \to K^0_S\pi^\pm$ resonance. The restricted Dalitz region is chosen because the dominance of a single $K^*(892)^\pm \to K^0_S\pi^\pm$ resonance within the region in both modes leads to an expectation that the coherence between the two modes should be high within this region. High coherence may lead to improved sensitivity to γ, despite the reduction in statistics from the total Dalitz plot. The region is highlighted in Figure 3.23 and contains approximately 70% of the $D^0 \to K^0_S K^-\pi^+$ data and approximately 40% of the $D^0 \to K^0_S K^+\pi^-$ data. The background-corrected yields are given in Table 3.17 where the yields inside the restricted region are shown for the first time, and the yields in the whole Dalitz plot repeat those given earlier in Table 3.1.

Table 3.17: Background corrected signal yields in the two Dalitz plot regions *before* correction for mis-tag and acceptance effects.

Mode	Whole Dalitz plot	$K^*(892)^\pm \to K^0_S\pi^\pm$ window
$D^0 \to K^0_S K^-\pi^+$	640 ± 27	445 ± 22
$D^0 \to K^0_S K^+\pi^-$	406 ± 24	166 ± 14

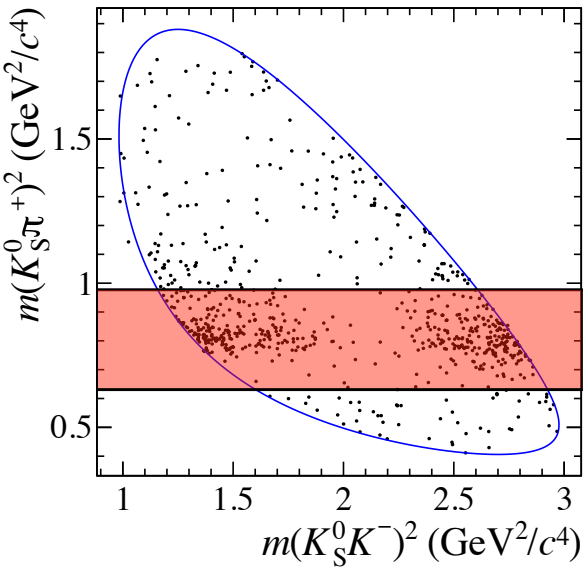

Figure 3.23: Illustration of the restricted Dalitz region referred to in the main text regarding the determination of R_D.

3.5.1 Mis-tag correction

In CLEO III data, the rate at which neutral D mesons are mis-tagged is 0.64%, as first stated in Section 3.4.4. Across the whole Dalitz plot, the rate at which $D^0 \to K^0_S K^+\pi^-$ decays contaminate the $D^0 \to K^0_S K^-\pi^+$ sample through the mis-tag effect is $0.64\% \times R_D$, and the rate at which $D^0 \to K^0_S K^-\pi^+$ decays contaminate the $D^0 \to K^0_S K^+\pi^-$ sample is $\frac{0.64\%}{R_D}$.

In the restricted region around the $K^*(892)^\pm$ resonance the former of these two mis-tag rates becomes $0.64\% \times R_D \times \frac{f_{K^0_S K^+\pi^-}}{f_{K^0_S K^-\pi^+}}$ and the latter becomes $\frac{0.64\%}{R_D} \times \frac{f_{K^0_S K^-\pi^+}}{f_{K^0_S K^+\pi^-}}$, where $f_{K^0_S K^-\pi^+}$ ($f_{K^0_S K^+\pi^-}$) is the fraction of $K^0_S K^-\pi^+$ ($K^0_S K^+\pi^-$) decays which, according to the amplitude models, falls inside this region of the Dalitz plot.

3.5.2 Acceptance correction

The efficiency correction for each mode is determined by integrating the model of the CLEO III detector acceptance weighted by the density according to amplitude model 1 across the Dalitz plot. The efficiency corrections enter as a ratio multiplying the raw ratio of signal candidates in the two modes in Equation 3.14. Since the same efficiency function is used for each mode, the absolute normalisation of the efficiency function cancels and is therefore not necessary to compute.

The efficiency correction factor, used to multiply the ratio of $D^0 \to K^0_S K^+\pi^-$ to $D^0 \to K^0_S K^-\pi^+$ decays, is given by

$$\eta = \frac{\int_{region} d\vec{x} P_{fav}(\vec{x})\epsilon(\vec{x})}{\int_{region} d\vec{x} P_{sup}(\vec{x})\epsilon(\vec{x})}, \tag{3.15}$$

where $P_{fav/sup}$ are the PDFs determined from the fit to data. In this equation, ϵ represents the CLEO III acceptance function. The efficiency correction factors are determined to be

$$\begin{aligned} \eta_{\text{whole Dalitz plot}} &= 0.9405, \text{ and} \\ \eta_{K^*(892)^\pm \text{ window}} &= 0.9702. \end{aligned}$$

3.5.3 Corrected ratios

The ratios of the yields in the two modes after the corrections specified are applied are

$$R_{D,\text{ whole Dalitz plot}} = 0.592 \pm 0.044, \text{ and}$$
$$R_{D,K^*(892)^\pm\text{ window}} = 0.356 \pm 0.034.$$

3.5.4 Systematic uncertainties

Systematic uncertainties on this calculation arising as a result of uncertainty on the detector acceptance function, on the model PDFs and on the signal or background yields are summarised in Table 3.18. No systematic uncertainty is attached due to the correction for the very small ($0.64 \pm 0.05\%$) mis-tag rate [87]. This is because the implemented mis-tag correction modifies the result by an amount approximately ten times smaller than the statistical uncertainty. The uncertainty on the mis-tag rate is ten times smaller than the mis-tag rate itself, rendering any systematic uncertainty negligible in magnitude.

Table 3.18: Summary of systematic uncertainties relating to the calculation of R_D.

Source	Region	
	Whole Dalitz plot	Restricted region
Peaking background	ΔR_D=0.0023	ΔR_D=0.0014
Acceptance function	$\Delta\eta$=0.0085	$\Delta\eta$=0.0039
Models	$\Delta\eta$=0.0275	$\Delta\eta$=0.0172

Peaking background

The peaking background fraction in the signal yield extracted from fits to the CLEO III m_D and Δm distributions is estimated using simulated background samples. Assuming the background yield (28) and total (1,468) to be Poisson-distributed, the systematic error on R_D is calculated. There is no peaking background observed in the suppressed mode, but for

the favoured mode, the absolute uncertainty on the background fraction, $\frac{28}{1468}$, is

$$\frac{28}{1468} \times \sqrt{\frac{1}{28} + \frac{1}{1468}} = 0.0036. \tag{3.16}$$

This is propagated through to an absolute uncertainty, ΔR_D, by multiplying it by the raw ratio of the yields in Table 3.17.

Detector acceptance

The systematic uncertainty on the efficiency correction factor as a result of the uncertainty in the model used to parameterise the detector acceptance is determined by changing the CLEO III efficiency parameterisation. The alternative parameterisation described in Section 3.4.7 is used to calculate the efficiency correction, and the changes observed are taken as the systematic uncertainty on the correction factor.

Models

There is an uncertainty on the efficiency correction factor arising from the different possible models which can be used in the integration to describe the distribution of signal events in the Dalitz plot. To estimate this uncertainty, the correction factor is evaluated using various different models. Three alternative models are used for each mode in combination with each of the models used in the calculation of the correction factor so far. The first alternative is the second fit model presented in the main text for each mode. The second and third are the next best models taken from the six-resonance fits for the favoured mode, and from the five-resonance fits for the suppressed mode.

The largest change in the correction factor for the various combinations is taken as the systematic uncertainty.

3.5.5 Final result

The final results, including systematic uncertainties, are

$$\begin{aligned} R_{D,\text{ whole Dalitz plot}} &= 0.592 \pm 0.044(\text{stat.}) \pm 0.018(\text{syst.}), \text{ and} \\ R_{D,K^*(892)^\pm\text{ window}} &= 0.356 \pm 0.034(\text{stat.}) \pm 0.007(\text{syst.}). \end{aligned}$$

It is not surprising that the value in the restricted region should be lower than that across the whole Dalitz plot. Not only is the $D^0 \to K^0_S K^+\pi^-$ mode suppressed with respect to $D^0 \to K^0_S K^-\pi^+$ but the $K^*(892)^\pm \to K^0_S\pi^\pm$ resonance is also less important in the former than in the latter, meaning the candidates are not so strongly concentrated in the restricted region in the $D^0 \to K^0_S K^+\pi^-$ mode.

4

Preparing an LHCb γ measurement using $B^{\pm} \to [K^0_S h^+ h^-]_D K^{\pm}$

In this chapter the tools are presented for a model-independent analysis of CP violation using $B^{\pm} \to [K^0_S h^+ h^-]_D K^{\pm}, h = \pi/K$ decays in LHCb data, building on the material presented in Section 1.2. The fit for the CP parameters (dependent upon γ) involves division of the data into regions of the Dalitz plot, as described separately in Chapter 5.

4.1 Introduction

The chapter begins with a discussion of the division of the Dalitz plot into regions for the analysis in Section 4.2. The hadronic input parameters c_i, s_i and K_i are described and the values used are presented in Section 4.3. A summary of the method employed for the analysis at LHCb is given in Section 4.4 and the data preparation is described in Section 4.5. In order to characterise the final data sample, the fit performed to the $B^{\pm}$ invariant mass spectrum is detailed in Section 4.6.

4.2 Choice of Dalitz plot division

Performing an analysis in regions, or bins, of the Dalitz plot in order to avoid taking strong phase difference measurements from a $D^0 \to K^0_S \pi^+ \pi^-$ amplitude model, but instead using CLEO measurements of the average strong phase, invariably leads to some loss of statistical

sensitivity with respect to an unbinned, model-dependent analysis. As seen in Equation 1.47, the variation of the strong phase difference $\Delta\delta_D$ over an extended Dalitz region i produces the somewhat diluted average strong phase measurements c_i and s_i. It is intuitively clear that these diluted quantities, which pre-multiply the parameters of interest $x_\pm$ and $y_\pm$ in Equation 1.47, reduce the sensitivity of the measurement to γ. Very large bins containing large variations in the strong phase difference across a bin are likely to result in a much reduced statistical sensitivity for the analysis.

In the first proposal [29] of such a model-independent analysis, the regions considered had a simple rectangular structure in the Dalitz plot (Figure 1.10). In fact, it has been found that a careful choice of binning scheme significantly improves the sensitivity to measurement of CP violating effects [89].

A simple approach for optimising the statistical sensitivity of a binned analysis is to choose Dalitz regions over which the strong phase variation is as small as possible and, indeed, this has been proposed [90]. An amplitude model can be used to give information about the expected behaviour of the strong phase difference across the Dalitz plot in order to guide the choice of Dalitz regions. This method has been pursued [91], using an amplitude model developed by the *BABAR* collaboration in 2008 [92]. The division produces eight bins either side of the Dalitz symmetry axis $m^2_+ = m^2_-$, each spanning an equal range of values of the strong phase difference, and the average strong phase information can be measured at CLEO. This 'equal strong-phase binning' can be seen in Figure 4.1(a) where each coloured region corresponds to a different bin in the strong phase difference. The structure of the chosen regions is seen to embody the main features of the $D^0 \to K^0_S \pi^+ \pi^-$ resonant content, particularly the vertical and horizontal structure arising from the $D^0 \to K^*(892)^{\pm}\pi^{\mp}$ resonance. Practically, the strong-phase regions are defined in a two-dimensional histogram where each cell is of dimension $0.0054\,\mathrm{GeV}^2/c^4 \times 0.0054\,\mathrm{GeV}^2/c^4$, adequate given the CLEO Dalitz resolution found in simulated data to be $0.006\,\mathrm{GeV}^2/c^4$ and the LHCb Dalitz resolution of between $0.004\,\mathrm{GeV}^2/c^4$ and $0.006\,\mathrm{GeV}^2/c^4$.

Although the division of the Dalitz plot into bins containing equal variation of strong

phase difference is a natural choice of binning, it is not guaranteed that it is the optimal one for measurement of γ. The effect of varying strong phase in diluting the c_i and s_i is reduced, but it is still possible for the magnitude of the D^0 decay amplitude to vary dramatically across the bin and diminish the overall contribution of the bin to the evaluation of the binning Q-value. A means to assess the statistical sensitivity of different Dalitz divisions was proposed in [89]. The figure of merit, Q, is a ratio of two quantities:

$$Q^2 = \frac{\Sigma_i \left(\frac{1}{\sqrt{K_i}} \frac{\mathrm{d}K_i}{\mathrm{d}x}\right)^2 + \left(\frac{1}{\sqrt{K_i}} \frac{\mathrm{d}K_i}{\mathrm{d}y}\right)^2}{\int_{\mathcal{D}} \left[\left(\frac{1}{\sqrt{|\mathcal{A}_{B^-}|^2}} \frac{\mathrm{d}|\mathcal{A}_{B^-}|^2}{\mathrm{d}x}\right)^2 + \left(\frac{1}{\sqrt{|\mathcal{A}_{B^-}|^2}} \frac{\mathrm{d}|\mathcal{A}_{B^-}|^2}{\mathrm{d}y}\right)^2\right] \mathrm{d}\mathcal{D}}, \tag{4.1}$$

where Q takes values between 0 and 1, $\mathcal{A}_{B^-}$ is shorthand for $\mathcal{A}_{B^- \to [K^0_S \pi^+ \pi^-] K^-}(m^2_+, m^2_-)$ as defined in Equation 1.26, and the other symbols have been defined earlier. The numerator is the change in the yields in all the various Dalitz plot regions, as a number of standard deviations, caused by a variation of the CP parameters $x_{\pm}$ and $y_{\pm}$. The denominator is the same variation as expected for the unbinned case, given by the infinite-bin limit. For the equal strong-phase binning scheme, and assuming the model from [92], the value of Q is found to be 0.786, implying a 21% loss in statistical sensitivity compared to the model-dependent, unbinned approach [91].

To find the optimal binning scheme, an algorithm was developed, as described in [89], to adjust the equal strong-phase binning scheme in order to maximise the value of Q. This algorithm was employed in [91] for the 2008 *BABAR* amplitude model and is summarised here. The algorithm proceeds by randomly selecting a cell from the definition histogram of the equal strong-phase binning. 90% of the time, if the cell is found to lie on a Dalitz bin boundary, it is transferred to the adjacent bin and the Q-value is recomputed. If it increases then the new binning definition is retained. This dominant process allows the bin boundaries to move. In the remaining 10% of the time the cell is randomly assigned to any of the Dalitz bins and, again, the new configuration is retained if the Q-value increased. This second, subdominant process allows bins to grow inside other Dalitz bins. The iterative procedure concludes when no significant increase in Q-value can be found. The algorithm can give rise

to very fine structures which are of a size comparable to the experimental resolution. This feature could introduce a vulnerability to systematic uncertainty where finite resolution and a densely populated Dalitz region could produce an imbalanced migration of points from one Dalitz bin to another. To avoid this, and given the fact that the amplitude model is not guaranteed to be a perfect description of reality, such small features are smoothed by considering a square collection of 11×11 cells around each test cell. If less than 30% of these surrounding cells match the test cell assignment, it is reassigned to the most common cell assignment in the square collection. The Q-value of the resulting Dalitz binning, shown in Figure 4.1(b), is found to be 0.887, a considerable improvement on the equal strong-phase binning, yielding an expected statistical sensitivity very close to that of the limiting, unbinned case. Given the significantly increased anticipated γ sensitivity of this binning, the original equal strong-phase binning is not considered further here and results are only presented for the latter case.

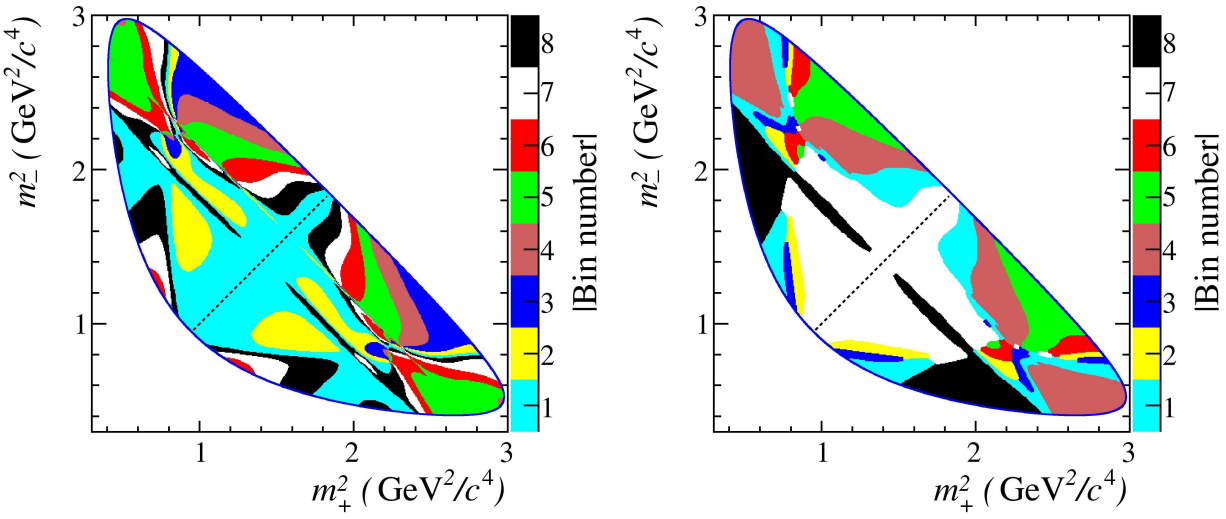

(a) Equal strong-phase binning

(b) Optimised binning

Figure 4.1: Dalitz binning scheme for $D^0 \to K^0_S \pi^+ \pi^-$ resulting from equal strong-phase difference variation, referred to in the text as the 'equal strong-phase binning', and the optimised Dalitz binning which achieves the highest Q-value, henceforth referred to as the 'optimised binning'. Only the optimised binning is used in the analysis described here.

A similar procedure was followed for $D^0 \to K^0_S K^+ K^-$. This time the equal strong-phase binning, shown in Figure 4.2, only contained two Dalitz bins either side of the symmetry axis $m^2_+ = m^2_-$. The cells in the Dalitz binning bitmap are $0.0018\,\text{GeV}^2/c^4 \times 0.0018\,\text{GeV}^2/c^4$,

small compared to the CLEO experimental resolution of $0.005\,\text{GeV}^2/c^4$ and the LHCb experimental resolution of $0.002\,\text{GeV}^2/c^4$ ($0.003\,\text{GeV}^2/c^4$) for $K^0_S K^+ K^-$ candidates formed using K^0_S candidates with long (downstream) pion tracks. The Q-value of the equal strong-phase binning was found to be 0.771 and, given that this value was not found to improve significantly after the same optimisation procedure was applied as for $K^0_S \pi^+ \pi^-$, and given the relatively low statistics available in the $B^{\pm} \to [K^0_S K^+ K^-]_D K^{\pm}$ mode in 2011 LHCb data, this is the only $D^0 \to K^0_S K^+ K^-$ binning scheme considered further here.

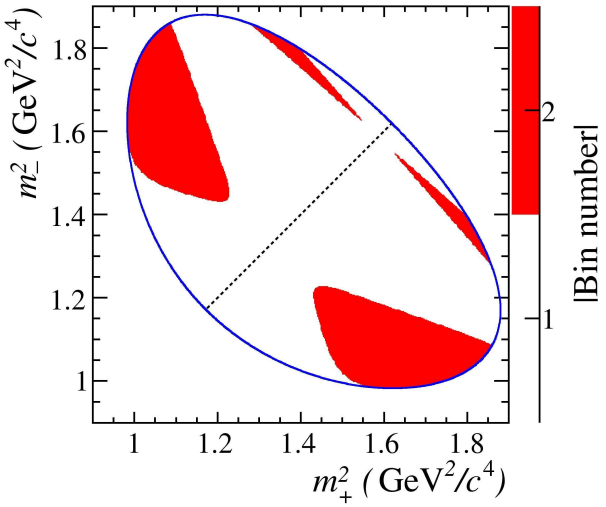

Figure 4.2: Equal strong-phase binning scheme for $D^0 \to K^0_S K^+ K^-$.

4.3 External inputs: K_i, c_i and s_i

Measurements of the K_i parameters, by *BABAR* , and the c_i and s_i parameters, by the CLEO collaboration [91], have been made for both $D^0 \to K^0_S \pi^+ \pi^-$ and $D^0 \to K^0_S K^+ K^-$.

4.3.1 Determination of K_i

The values of K_i, defined in Equations 1.43 and 1.44, are proportional to the fraction of $D^0 \to K^0_S h^+ h^-$ decays found in bin i.

The values were determined by integrating amplitude models for the decays over each Dalitz bin. The 2008 *BABAR* model [92] was used for $D^0 \to K^0_S \pi^+ \pi^-$ and the 2010 *BABAR* model

[93] for $D^0 \to K^0_S K^+ K^-$. This does not introduce a significant model dependence to the measurement since the model reproduces the data distribution of $K^0_S h^+ h^-$ candidates around the Dalitz plot very closely. Significant modelling uncertainties would only be introduced if phase information in the Dalitz plot was required, since the phase variation depends very strongly on the resonant content of the model and the parameterisation of the resonances. To determine the absolute value of K_i requires knowledge of the $D^0 \to K^0_S h^+ h^-$ branching fraction, but as the analysis only requires knowledge of the relative values, these are the values presented in Table 4.1.

Table 4.1: Values of K_i in each $K^0_S h^+ h^-$ Dalitz bin for the binning schemes as determined from the models from [92] for $K^0_S \pi^+ \pi^-$ and [93] for $K^0_S K^+ K^-$.

Bin i	K_i (%)	
	$K^0_S \pi^+ \pi^-$ binning	$K^0_S K^+ K^-$ binning
-8	2.2	–
-7	11.4	–
-6	7.5	–
-5	5.4	–
-4	10.9	–
-3	14.4	–
-2	14.4	21.1
-1	9.2	22.5
1	2.2	28.6
2	0.5	27.8
3	0.4	–
4	6.6	–
5	3.1	–
6	0.4	–
7	5.3	–
8	6.3	–

4.3.2 Measurements of c_i and s_i

The values of c_i and s_i in bins of the Dalitz plot have been determined by the CLEO collaboration by exploiting the quantum coherence of $D\bar{D}$ pairs produced in $\psi(3770)$ resonance decays [91]. The $D\bar{D}$ pair is produced in a $C = -1$ quantum state, the same as that of the $\psi(3770)$. The decay of one of the D mesons is reconstructed in a 'CP tag' final state, allowing

an inference as to the CP state of the 'signal' D decaying to the final state of interest, be it $K^0_S\pi^+\pi^-$ or $K^0_S K^+ K^-$. In this case, the distribution of signal candidates between the bins in the Dalitz plot, $\Gamma_i^{\mathrm{CP}\pm}$, where CP± corresponds to the tag CP state, is given [91] by the relation

$$\Gamma_i^{\mathrm{CP}\pm} = h_{CP\pm}(K_i \pm 2c_i\sqrt{K_i K_{-i}} + K_{-i}), \tag{4.2}$$

where $h_{CP\pm}$ are normalisation factors. As is apparent from the equation, these only give sensitivity to values of c_i. Added sensitivity can be found by using $D^0 \to K^0_S h^+ h^-$ as a D tag as well as the signal mode. This requires analysis of two Dalitz plots, where the yield of candidates for which the tag D decay falls in Dalitz bin i and the signal D decay falls in bin j of its Dalitz plot, is given by

$$\Gamma_{ij} = h_{\mathrm{corr}}\left(K_i K_{-j} + K_{-i}K_j - 2\sqrt{K_i K_{-j} K_{-i} K_j}(c_i c_j + s_i s_j)\right), \tag{4.3}$$

where h_{corr} is again a normalisation factor. This brings crucial sensitivity to the values of s_i. The decays $\psi(3770) \to [K^0_S h^+ h^-][K^0_L h^+ h^-]$ are approximately twice as abundant as $\psi(3770) \to [K^0_S h^+ h^-][K^0_S h^+ h^-]$ so that still further sensitivity can be gained through the use of $K^0_L h^+ h^-$ as a tag. In that case, given that K^0_S and K^0_L have opposite CP, the equation for the yield of candidates where the $K^0_L h^+ h^-$ decay falls in bin j and the $K^0_S h^+ h^-$ in bin i is

$$\Gamma'_{ij} = h_{\mathrm{corr}}\left(K_i K'_{-j} + K_{-i}K'_j + 2\sqrt{K_i K'_{-j} K_{-i} K'_j}(c_i c'_j + s_i s'_j)\right), \tag{4.4}$$

where primed quantities refer to the K^0_L decay. The CP-tagged $K^0_L h^+ h^-$ decay yield, in analogy to Equation 4.2, is

$$\Gamma_i'^{\pm} = h'_{CP\pm}(K'_i \mp 2c'_i\sqrt{K'_i K'_{-i}} + K'_{-i}). \tag{4.5}$$

This improves the precision of the measurement of c_i and s_i because the differences $\Delta c_i = c'_i - c_i$ and $\Delta s_i = s'_i - s_i$ can be constrained with very weak model assumptions [91]. The

different tags used are summarised in Table 4.2.

Table 4.2: Summary of tags used in the CLEO-c determination of c_i and s_i [91].

Signal	CP-even tags	CP-odd tags	Mixed-CP tags
$K^0_S\pi^+\pi^-$	K^+K^-, $\pi^+\pi^-$, $K^0_S\pi^0\pi^0$, $K^0_L\pi^0$	$K^0_S\pi^0$, $K^0_S\eta(\gamma\gamma)$, $K^0_S\omega$	$K^0_S\pi^+\pi^-$
$K^0_L\pi^+\pi^-$	K^+K^-, $\pi^+\pi^-$	$K^0_S\pi^0$, $K^0_S\eta(\gamma\gamma)$	$K^0_S\pi^+\pi^-$
$K^0_S K^+K^-$	K^+K^-, $\pi^+\pi^-$, $K^0_S\pi^0\pi^0$, $K^0_L\pi^0$, $K^0_L\eta(\gamma\gamma)$, $K^0_L\eta(\pi^+\pi^-\pi^0)$, $K^0_L\omega$, $K^0_L\eta'$	$K^0_S\pi^0$, $K^0_S\eta(\gamma\gamma)$, $K^0_S\eta(\pi^+\pi^-\pi^0)$, $K^0_S\omega$, $K^0_S\eta'$, $K^0_L\pi^0\pi^0$	$K^0_S\pi^+\pi^-$, $K^0_L\pi^+\pi^-$, $K^0_S K^+K^-$
$K^0_L K^+K^-$	$K^0_S\pi^0$, $K^0_S\eta(\gamma\gamma)$, $K^0_S\eta(\pi^+\pi^-\pi^0)$	$K^0_S\pi^0$, $K^0_S\eta(\gamma\gamma)$, $K^0_S\eta(\pi^+\pi^-\pi^0)$, $K^0_S\omega$, $K^0_S\eta'$	$K^0_S\pi^+\pi^-$, $K^0_S K^+K^-$

Fitting these samples, the values of c_i and s_i obtained for the $K^0_S h^+ h^-$ final states in the various binning schemes are given in Table 4.3. The values of c'_i and s'_i determined are not relevant for the studies presented in this thesis but can be found in [91]. The results are shown in pictorial form in Figure 4.3. The results lie close to a circle of unit radius in c_i, s_i space, which defines the limit for infinitely small bins.

Table 4.3: Fit results for c_i and s_i in the binning schemes considered for the two $K^0_S h^+ h^-$ modes [91]. As explained in Section 1.5, the values in positive and negative bins are related by $c_i = c_{-i}$ and $s_i = -s_{-i}$. The first uncertainty is statistical and the second is systematic.

i	$K^0_S\pi^+\pi^-$ binning		$K^0_S K^+K^-$ binning	
	c_i	s_i	c_i	s_i
1	$-0.009\pm0.088\pm0.094$	$0.438\pm0.184\pm0.045$	$0.818\pm0.107\pm0.037$	$-0.445\pm0.215\pm0.143$
2	$0.900\pm0.106\pm0.082$	$0.490\pm0.295\pm0.261$	$-0.746\pm0.083\pm0.035$	$-0.229\pm0.220\pm0.079$
3	$0.292\pm0.168\pm0.139$	$1.243\pm0.341\pm0.123$	–	–
4	$-0.890\pm0.041\pm0.044$	$0.119\pm0.141\pm0.038$	–	–
5	$-0.208\pm0.085\pm0.080$	$-0.853\pm0.123\pm0.035$	–	–
6	$0.258\pm0.155\pm0.108$	$-0.984\pm0.357\pm0.165$	–	–
7	$0.869\pm0.034\pm0.033$	$0.041\pm0.132\pm0.034$	–	–
8	$0.798\pm0.070\pm0.047$	$0.107\pm0.240\pm0.080$	–	–

4.4 Overview of measurement procedure

The measurement of CP violation at LHCb divides naturally into three stages that are summarised here. The first is the selection of candidate decays, which is described in detail

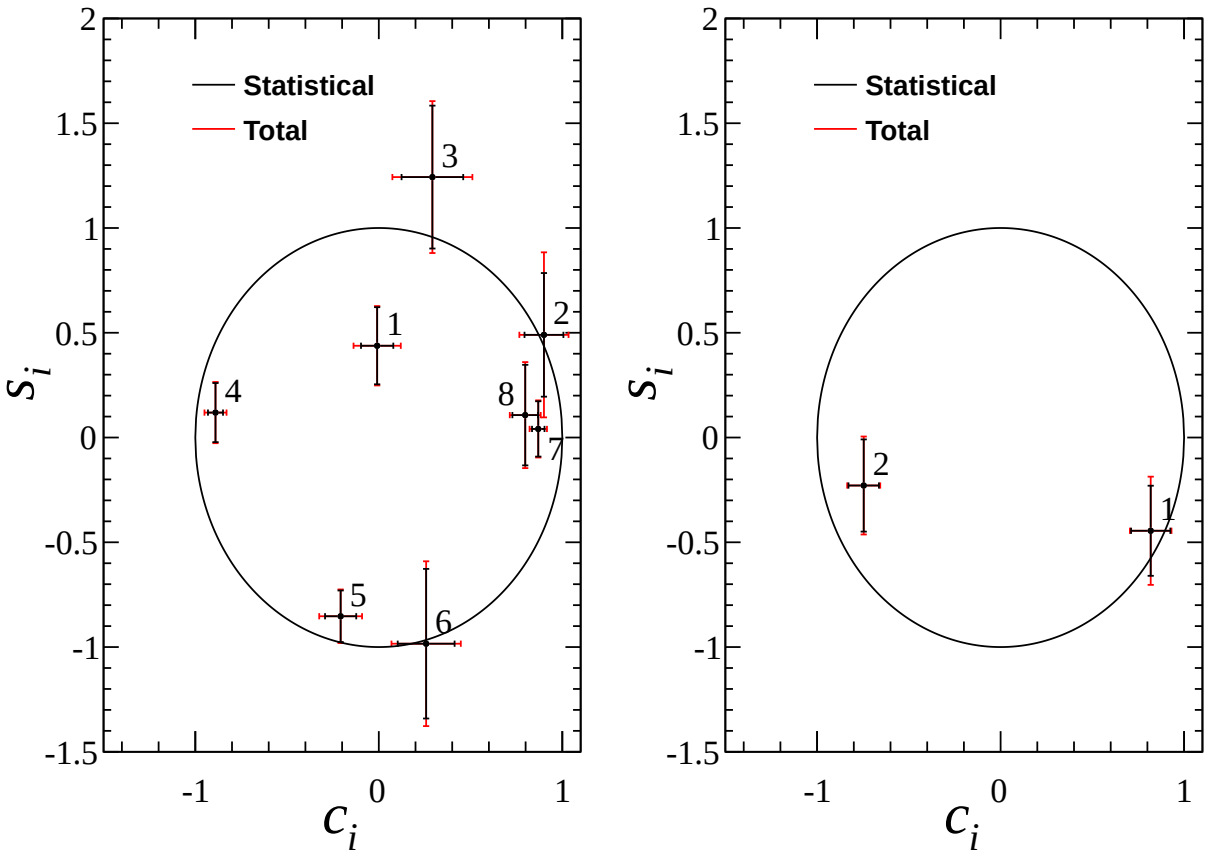

(a) 8 bins in $D^0 \to K^0_S \pi^+ \pi^-$

(b) 2 bins in $D^0 \to K^0_S K^+ K^-$

Figure 4.3: CLEO measurements of c_i and s_i in the various binning schemes for the two $K^0_S h^+ h^-$ modes [91]. The fit results are shown in black with statistical errors and with red error bars indicating the total uncertainty. The circle of radius 1 forms the limit for an infinite number of bins. The variation of strong phase difference across each bin causes the amplitude-weighted averages c_i and s_i to tend to move further inside this limit.

in Section 4.5, and the characterisation of the $B^{\pm}$ invariant mass spectrum, described in Section 4.6. The second comprises the fit which is performed on the data, leading to a determination of the $x_{\pm}$ and $y_{\pm}$ parameters described previously. This fit is detailed in Chapter 5. Finally, some work is necessary to extract γ, r_B and δ_B from the measured values of $x_{\pm}$ and $y_{\pm}$, and this procedure is presented in Section 5.6. An overview of each of these stages is provided here.

4.4.1 Candidate selection

The LHCb software framework is used to reconstruct candidate $B^{\pm} \to [K^0_S h^+ h^-]_D K^{\pm}$ decays in the 2011 LHCb data set and a set of selection criteria is applied to provide a sample of candidates with high signal purity, suppressing dominant backgrounds. The most significant contamination in the $B^{\pm} \to \tilde{D}K^{\pm}$ sample from $B^{\pm} \to \tilde{D}\pi^{\pm}$ decays is suppressed using particle identification criteria available from the LHCb Ring Imaging Cherenkov Detector. As well as reconstructing $B^{\pm} \to [K^0_S h^+ h^-]_D K^{\pm}$ decays, the $B^{\pm} \to [K^0_S h^+ h^-]_D \pi^{\pm}$ mode is also reconstructed in its own right.

When K^0_S candidates are formed using two long (downstream) pion tracks, they are referred to as LL (DD) candidates (no candidates exist which are constructed from one long and one downstream track). Similarly, a $B^{\pm}$ candidate formed using a LL (DD) K^0_S, is described in the same way. The $B^{\pm}$ invariant mass resolution is expected to be better for LL candidates. These are therefore selected separately from DD candidates.

4.4.2 Use of $B^{\pm} \to \tilde{D}\pi^{\pm}$ as a control mode

Two properties of this mode make it particularly useful in this study. Firstly, it is topologically and kinematically similar to the signal and is abundant, with a visible branching fraction approximately ten times larger than that of the $B^{\pm} \to \tilde{D}K^{\pm}$ signal mode. Secondly, the amplitude ratio $r_B^{\pi} = \frac{|\mathcal{A}_{B^- \to \bar{D}^0 \pi^-}|}{|\mathcal{A}_{B^- \to D^0 \pi^-}|}$ is expected to have a value an order of magnitude smaller than that for the $B^{\pm} \to \tilde{D}K^{\pm}$ mode, as can be seen by consideration of the CKM

elements which relate the two factors:

$$r_B^{\pi} \sim r_B \times \left| \frac{V_{cd}/V_{cs}}{V_{ud}/V_{us}} \right| \sim \frac{r_B}{20}. \tag{4.6}$$

The first of these properties makes this abundant mode useful to control aspects of the fit to the $B^{\pm} \to \tilde{D}K^{\pm}$ invariant mass spectrum, as described later in Section 4.6. The second means that interference effects between $B^- \to \bar{D}^0\pi^-$ and $B^- \to D^0\pi^-$ can be assumed to be negligible. By comparing the yield in bins of the Dalitz plot to that expected from a flavour-tagged sample of $D^0 \to K^0_S h^+ h^-$ decays, variation of the LHCb acceptance over the Dalitz plot can be accounted for. This is described in more detail in Chapter 5 where the fit in Dalitz bins is described.

4.4.3 Fits performed

For the measurement of CP violation it is necessary to have access to the yield of signal $B^{\pm} \to [K^0_S h^+ h^-]_D K^{\pm}$ decays in the data sample, in each of the Dalitz regions defined in Section 4.2. This is achieved by means of two fits: a 'global' fit to the $B^{\pm}$ invariant mass spectrum for the candidates in the Dalitz plot, and a 'binned' fit, to the spectra within each Dalitz region.

Global fit

This fit is performed in order to determine parameters of a PDF for each component in the invariant mass spectrum. The invariant mass spectrum for candidate $B^{\pm} \to [K^0_S h^+ h^-]_D K^{\pm}$ decays is fitted with PDFs for the following components:

- a signal component,
- a PDF describing background decays which are partially reconstructed and mistaken for signal candidates,

- candidates formed by combining random tracks arising in the detector from different sources (so-called combinatorial background) and

- a component to describe the background from misidentified $B^{\pm} \to \tilde{D}\pi^{\pm}$ decays in the $B^{\pm} \to \tilde{D}K^{\pm}$ selection.

This fit is performed to each sample of LL and DD $B^{\pm} \to [K^0_S h^+ h^-]_D K^{\pm}$ candidates, regardless of the candidate's location in the $\tilde{D}$ Dalitz plot. The $B^{\pm} \to [K^0_S h^+ h^-]_D \pi^{\pm}$ sample is fitted simultaneously and used to fix the yield of misidentified decays in the $B^{\pm} \to [K^0_S h^+ h^-]_D K^{\pm}$ spectrum.

Binned fit

Following the first fit, the $B^{\pm} \to \tilde{D}K^{\pm}$ and $B^{\pm} \to \tilde{D}\pi^{\pm}$ candidates are divided according to the position of each candidate in the $\tilde{D}$ Dalitz plot. The parameters of the invariant-mass PDFs are assumed to be the same in each bin and are fixed to the values determined in the first fit. It is necessary to correct for the effect of a varying acceptance across the Dalitz plot on the $B^{\pm} \to [K^0_S h^+ h^-]_D K^{\pm}$ yields. The correction factors are determined by assuming the absence of interference in $B^{\pm} \to \tilde{D}\pi^{\pm}$ decays and then comparing to predicted yields of $D^0 \to K^0_S h^+ h^-$ decays in each bin, i.e. the values of K_i.

Simultaneous fits are therefore performed to the invariant mass spectra for the candidate $B^{\pm} \to \tilde{D}K^{\pm}$ and $B^{\pm} \to \tilde{D}\pi^{\pm}$ decays in each Dalitz bin for each K^0_S type (LL/DD). The yield of $B^{\pm} \to [K^0_S h^+ h^-]_D K^{\pm}$ signal candidates in each Dalitz region is not independently floated but is instead related through Equation 1.47 to the CP parameters $x_{\pm}$ and $y_{\pm}$, allowing determination of these parameters. The $x_{\pm}$ and $y_{\pm}$ parameters have a simple geometrical relationship to γ, r_B and δ_B, shown in Figure 4.4. In the figure, the value of half the opening angle between the two (x, y) vectors is equal to the parameter γ and the length of each vector is equal to the measurement of r_B in the B^+ or B^- data, respectively. Fitting in such Cartesian quantities rather than polar coordinates (γ, r_B and δ_B) is preferable because the bias introduced by the fitter is expected to be smaller. It also avoids problems encountered

in fitting the phases when the amplitude r_B is small and problems where the value of r_B approaches its lower bound in the fit at 0.

It is made explicit in Equation 1.47 that the overall yield normalisations are separate for B^+ and B^- which means that consideration of $B^{\pm}$ production asymmetries or $K^{\pm}$ and $\pi^{\pm}$ detection asymmetries is not necessary. In this analysis, the sensitivity to γ arises not through the overall $B^{\pm}$ asymmetry but rather through the γ dependence of the Dalitz distribution of the $B^{\pm} \to \tilde{D}K^{\pm}$ candidates.

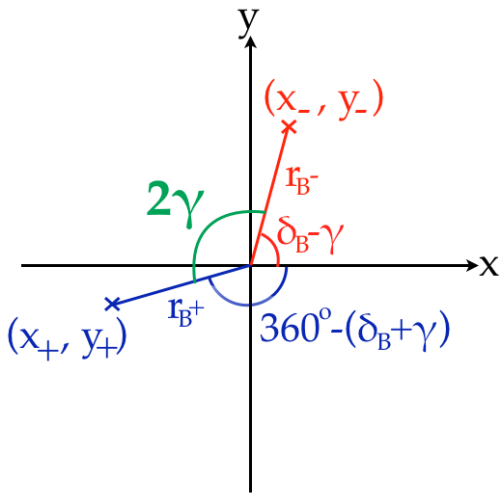

Figure 4.4: Illustration of the geometrical relationship between the analysis observables ($x_{\pm}$ and $y_{\pm}$) and γ, r_B and δ_B.

4.4.4 Determination of γ

Although the values of γ, r_B and δ_B can be estimated using their basic geometrical relationships to the $x_{\pm}$, $y_{\pm}$ observables, the most reliable extraction requires a Feldman-Cousins statistical treatment as is described in Chapter 5.

4.5 Preparation of $B^{\pm} \to [K^0_S h^+ h^-] h'^{\pm}$ sample

Candidates are selected from pp collision data at a centre-of-mass energy of 7 TeV collected by LHCb during the 2011 data-taking period, corresponding to a total integrated luminosity of $1\,\text{fb}^{-1}$. In Section 4.5.1, the triggering and reconstruction of candidates in data are briefly reviewed, though more details of the generic processing are provided earlier in Chapter 2, and in Section 4.5.2 the specific selection criteria applied to select a high purity signal sample are discussed. A description of the suppression of specific backgrounds is also given in Section 4.5.2 and a summary of simulated data, used chiefly in Chapter 5, is given in Section 4.5.3.

4.5.1 Candidate triggering, reconstruction and stripping

The hadronic trigger required that at least one shower in the HCAL was assigned a transverse energy greater than 3.5 GeV and that there were fewer than 600 hits in the SPD. Of the events triggered by the L0, 60% contain a signal candidate, where at least one track passed general requirements for a hadronic decay, and 40% contain another decay in the event, which triggered one of the other trigger requirements independently of the signal candidate. At the HLT1 stage, candidates were required to satisfy a requirement on their minimum impact parameter χ^2 (defined as the change in the vertex χ^2 when the track considered is removed from the vertex) as well as p_T with respect to the beam direction and track χ^2, and then a multivariate selection was employed at the HLT2 stage to suppress efficiently the combinatorial background.

Candidate $B^{\pm} \to [K^0_S h^+ h^-]_D h'^{\pm}$ decays are reconstructed using LHCb software during a central data processing stage. $B^{\pm}$ candidates are formed by reconstructing their decay products in reverse order to the decay: $K^0_S (\to \pi^+\pi^-)$, $\tilde{D} \to K^0_S h^+ h^-$ and finally $B^{\pm} \to \tilde{D} h'^{\pm}$. Loose data stripping is applied in which requirements are placed on tracks and composite particles to control the number of candidates formed and to limit the size of the resulting, centrally produced data set. The loose criteria include requirements on the χ^2 of tracks

as well as their p_T or minimum impact parameter χ^2. For composite particles, the quality of the vertex fit is also considered. In order to suppress backgrounds involving random tracks, a generic, multivariate selection is applied to select candidate decays including a $b \to c$ transition, typified by their displaced secondary D vertex and exploiting the $B^{\pm}$ decay kinematics. Mass windows are placed on the composite particle candidates: $467 \to 527\,\text{MeV}/c^2$ for the K^0_S, $\pm 100\,\text{MeV}/c^2$ for the D^0, and $4750 \to 7000\,\text{MeV}/c^2$ for the $B^{\pm}$. The distributions of the invariant mass in the $B^{\pm} \to [K^0_S \pi^+ \pi^-]_D K^{\pm}$ mode after this general stripping selection are shown for the $B^{\pm}$, $\tilde{D}$ and K^0_S candidates in Figure 4.5 to illustrate the significant level of background which remains. The number of events surviving this general selection in the $B^{\pm} \to [K^0_S \pi^+ \pi^-]_D \pi^{\pm}$ mode is 671,841.

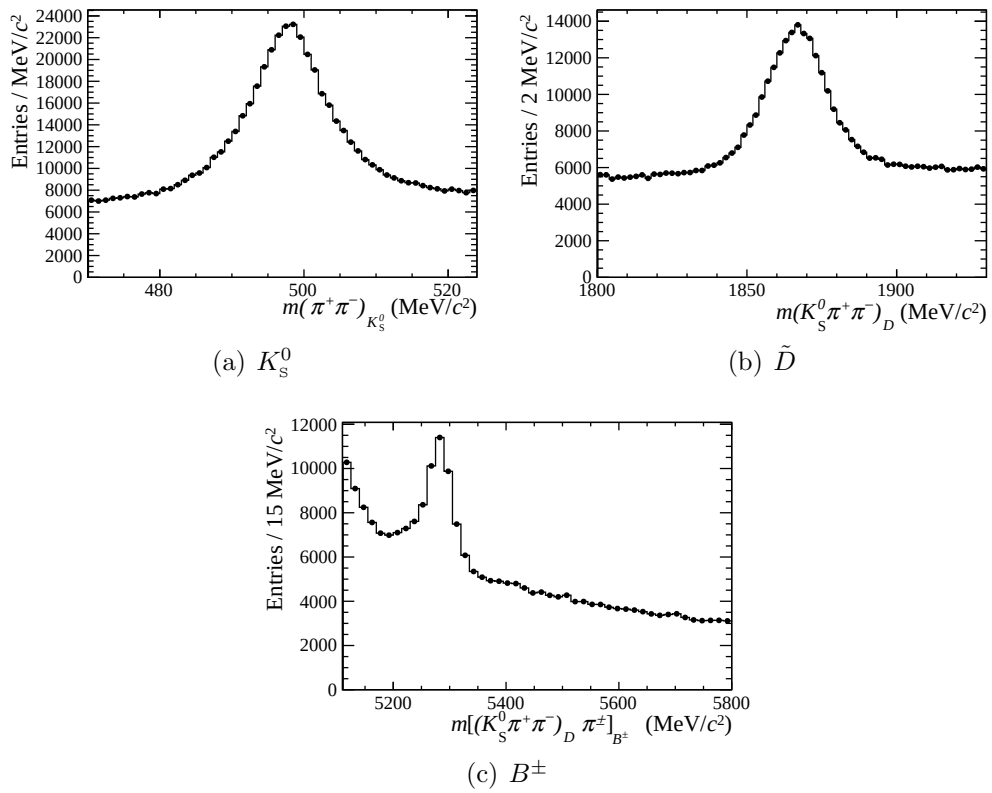

(a) K^0_S (b) $\tilde{D}$

(c) $B^{\pm}$

Figure 4.5: Invariant mass spectra for $B^{\pm}$, $\tilde{D}$ and K^0_S candidates after generic selection stage.

4.5.2 Selection criteria

A summary of the offline selection criteria applied is given in Table 4.4. After the initial reconstruction of the $\tilde{D}$ meson the spread in reconstructed $\tilde{D}$ mass causes a blurring of the $\tilde{D}$ Dalitz boundary for reconstructed candidates, and significant movement of candidates around the Dalitz plot. To remedy this, the $B^{\pm}$ and daughter decay vertices are refitted where the $\tilde{D}$ and K^0_S masses are constrained to their PDG values and the daughter particle four-momenta are adjusted within their reconstruction uncertainties. The $B^{\pm}$ momentum is required to point back to the associated primary vertex. The Dalitz coordinate resolution is improved significantly by this refit, as can be seen in Figures 4.6(a) for LL candidates and 4.6(b) for DD candidates. The result of this operation is that all but 0.4% of the candidates assume kinematically allowed Dalitz positions, and the 0.4% which do not are excluded only because the constrained D^0 mass differs very slightly between that defined in the software package which performs the refit and that used by *BABAR* to define the Dalitz bins and phase space boundary.

A final set of selection criteria is applied consecutively to the sample with the aim of maximising the purity of the final sample and suppressing specific backgrounds. The selection comprises primarily requirements on the topological and kinematic properties of the decay, which effectively suppress the level of background candidates formed from random track combinations. The most effective requirement at reducing this combinatorial background is that placed on the χ^2 of the refit to the $B^{\pm}$ decay, followed by the maximum impact parameter requirement for the $B^{\pm}$ and demanding that the $B^{\pm}$ should fly a significant distance before decaying. The minimum impact parameter of the bachelor pion or kaon from the $B^{\pm}$ decay is particularly important to reduce such backgrounds. Such impact parameter requirements are placed on all the pion or kaon tracks used to form the $B^{\pm}$ decay. The effects of these criteria on signal and sideband DD candidates after the generic selection stage are illustrated in Figure 4.7 with no other requirements made, where the simulated and sideband samples have been normalised in area in the plots to ease comparison of the distribution shapes. The sideband is defined as the region in $B^{\pm}$ invariant mass between

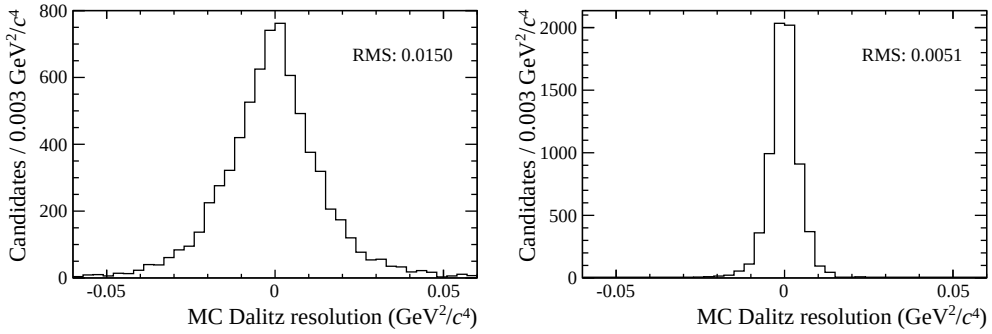

(a) LL candidates

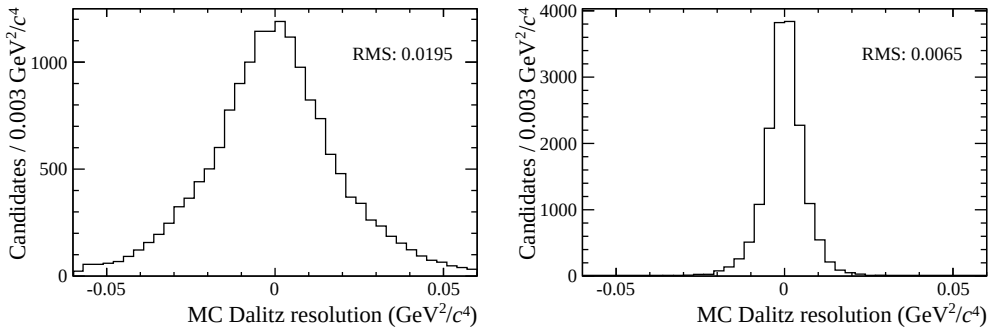

(b) DD candidates

Figure 4.6: Dalitz resolution studied in Monte Carlo simulated $B^{\pm} \to [K^0_S \pi^+ \pi^-]_D K^{\pm}$ samples before (left) and after (right) refit with D and K^0_S mass constraints. The resolution is determined by calculating the reconstructed invariant masses squared and subtracting from the generated value of the invariant mass squared in each case. The resolutions for the $K^0_S \pi^+$ and $K^0_S \pi^-$ Dalitz coordinates are both entered in the same plot.

5400 MeV/c^2 and 5900 MeV/c^2.

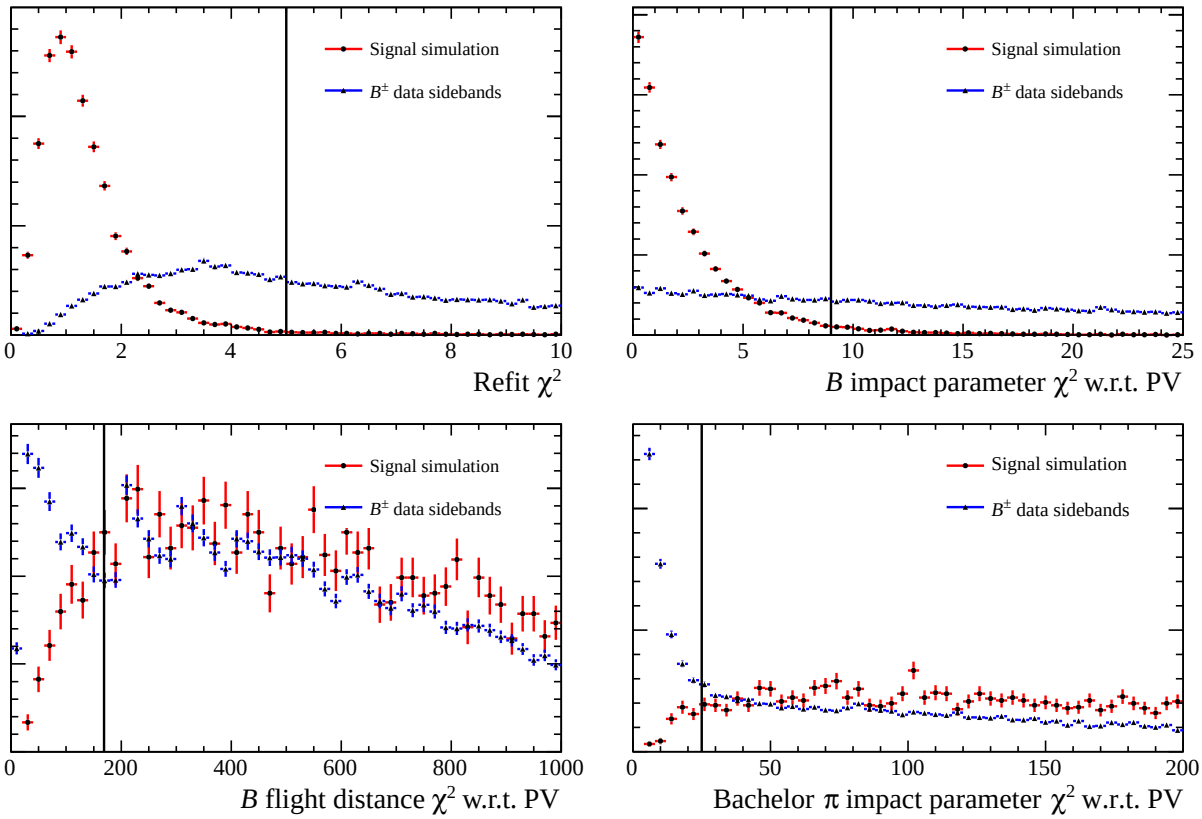

Figure 4.7: Comparison of variable distributions in a simulated signal sample (red points) and $B^{\pm}$ sideband DD candidate sample (blue points) where the two histograms are normalised to equal area. In each case, a vertical line indicates the value of a requirement placed on this variable (see Table 4.4).

Another requirement which is important for reducing combinatorial backgrounds is that that the momenta of composite particles should align well with their displacement vector from their production vertex, which is again unlikely to be satisfied by candidates containing wrongly associated tracks. For each of these criteria, the efficiency of the requirement alone on simulated signal decay candidates is at least 95%, but the fraction of candidates in the $B^{\pm}$ sideband mass range 5700 MeV/c^2 to 5900 MeV/c^2 that survive each requirement varies from around 20%, for the refit χ^2 on LL candidates (35% on DD candidates), to 80% for requirements on the displacement vector alignment with the momentum vector. The criteria are often set differently for decays containing a LL or DD K^0_S candidate given the significant differences in track positions in the detector and invariant mass resolution; the invariant mass resolution for K^0_S candidates is 2.9 MeV/c^2 for LL candidates and 4.8 MeV/c^2 for DD. For the

reconstructed D^0 meson, the resolution is $8.7\,\mathrm{MeV}/c^2$ for decays to a LL K^0_S candidate and $11.9\,\mathrm{MeV}/c^2$ for decays to a DD K^0_S.

Mass windows are placed in the K^0_S and D^0 invariant mass spectrum, enhancing the signal purity, at values of $15\,\mathrm{MeV}/c^2$ and $25\,\mathrm{MeV}/c^2$ either side of the PDG value of the K^0_S and D^0 masses, respectively.

In order to enable separation of $B^{\pm} \to \tilde{D}\pi^{\pm}$ decays from $B^{\pm} \to \tilde{D}K^{\pm}$ decays, PID information from the RICH detectors is demanded for the candidates. The RICH detectors are effective for particles with momentum below a limit at $100\,\mathrm{GeV}/c$, so this upper limit is explicitly enforced and a requirement is then made on the likelihood for the particle to be a pion or kaon, dividing the reconstructed sample once more.

The same selection criteria are used for $K^0_S K^+ K^-$ candidates, but in this case, owing to the fact that the branching fraction of $B^{\pm} \to [K^0_S \pi^+ \pi^-]_D h'^{\pm}$ is around six times larger than that of $B^{\pm} \to [K^0_S K^+ K^-]_D h'^{\pm}$, it is necessary to treat the background where the two pions from the $\tilde{D}$ meson are misidentified as kaons. In order to achieve this, an extra requirement is made using the RICH particle identification information that the kaon daughters of the D^0 meson should be identified as kaons.

Specific background studies

Four distinct categories of non-combinatorial background require special treatment:

- **Background from $D^0 \to \pi^+\pi^-\pi^+\pi^-$ decays**

  There is potential for $D^0 \to \pi^+\pi^-\pi^+\pi^-$ decays to mimic $D^0 \to K^0_S \pi^+\pi^-$ decays in the case where two of the final pions are randomly chosen to construct a K^0_S candidate. This background only exists in the sample containing K^0_S candidates made with long pions; it does not pose a risk to the downstream K^0_S sample since the very requirement that the candidate K^0_S daughter tracks should have originated outside the VELO is sufficient to suppress pions from heavy meson decays. The background is studied in the sample containing K^0_S particles made from long pions, by considering the $B^{\pm}$ invariant mass

Table 4.4: Final selection requirements for long and downstream $B^{\pm} \to [K^0_S \pi^+ \pi^-]_D K^{\pm}$ candidates. Identical requirements apply for $B^{\pm} \to [K^0_S \pi^+ \pi^-]_D \pi^{\pm}$ but with reversal of the bachelor candidate $K - \pi$ likelihood requirement to $\mathrm{DLL}(K - \pi) < 4$. The selections for the $K^0_S K^+ K^-$ final state are the same but with the addition of a $(K - \pi)$ identification likelihood requirement at -5 for each of the D-daughter kaons. In cases where the requirement is made relative to a primary vertex (PV), the PV is that associated to the decay candidate. 'IP' indicates 'impact parameter' and 'FD' indicates 'flight distance'.

Quantity	Long K^0_S	Downstream K^0_S
Both K^0_S pion candidates		
IP χ^2 with respect to PV	> 16	> 4
K^0_S candidate		
FD χ^2 from D^0 decay vertex	> 100	–
Refit mass (with constraint only on D^0)	$\pm 15\,\mathrm{MeV}/c^2$ PDG	$\pm 15\,\mathrm{MeV}/c^2$ PDG
Cosine of angle between K^0_S momentum and displacement from D^0 decay vertex	> 0.99	> 0.99
Both D^0 pion candidates		
IP χ^2 with respect to PV	> 9	> 16
D^0 candidate		
Mass before refit	$\pm\ 25\,\mathrm{MeV}/c^2$ PDG	$\pm\ 25\,\mathrm{MeV}/c^2$ PDG
Cosine of angle between D^0 momentum and displacement from $B^{\pm}$ decay vertex	> 0.99	> 0.99
$D^0 - B^{\pm}$ vertex separation in z-direction	> 0	> 0
D^0 IPχ^2 with respect to PV	> 9	> 9
Bachelor candidate		
Bachelor RICH information available	true	true
Momentum	$< 100\,\mathrm{GeV}/c$	$< 100\,\mathrm{GeV}/c$
Logarithm of ratio of kaon and pion particle ID likelihoods	> 4	> 4
IP χ^2 with respect to PV	> 25	> 25
$B^{\pm}$ candidate		
Cosine of angle between $B^{\pm}$ momentum and displacement from PV	> 0.9999	> 0.99995
FD χ^2 with respect to PV	> 169	> 169
IP χ^2 with respect to PV	< 9	< 9
Decay variables		
Refit χ^2	< 5	< 5

for particles whose K^0_S candidate is found in the sidebands of the K^0_S invariant mass spectrum after the offline selection is applied. The $B^{\pm} \to [\pi^+\pi^-\pi^+\pi^-]_D\pi^{\pm}$ background would produce a nearly flat distribution in K^0_S invariant mass but would peak in $B^{\pm}$ invariant mass. The K^0_S sidebands used for the study are shown in Figure 4.8, where the final selection has been relaxed to remove requirements relating to the refit of the decay tree. This is necessary because the refit is found to distort the K^0_S sideband such that it is no longer clear where the K^0_S peak ends and the sculpted sideband begins. The reimposition of the refit will, in fact, further suppress the $D^0 \to \pi^+\pi^-\pi^+\pi^-$ background whose topology does not lend itself to the refit, so the estimate made using the relaxed selection is considered to be conservative.

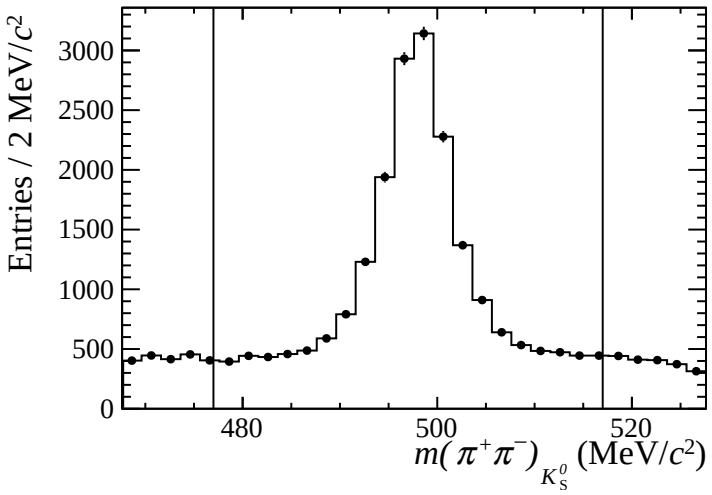

Figure 4.8: Invariant mass spectrum for K^0_S candidates in data made with long pions, including the sidebands used for study of $D^0 \to \pi^+\pi^-\pi^+\pi^-$ background, after removal of cuts pertaining to the refit of the decay tree and replacement of these requirements by cuts on the raw quantities before any refit.

In these K^0_S sidebands, a peak in the $B^{\pm}$ invariant mass spectrum is visible in Figure 4.9(a), but this is found to be suppressed by placing a minimum requirement on the flight distance χ^2, computed by taking the square of the quotient of K^0_S flight distance and its associated uncertainty and requiring the result to be greater than 100. The same invariant mass spectrum after application of this criterion is in Figure 4.9(b) where the absence of any significant structure at the $B^{\pm}$ mass indicates that the flight requirement removes the $D^0 \to \pi^+\pi^-\pi^+\pi^-$ background.

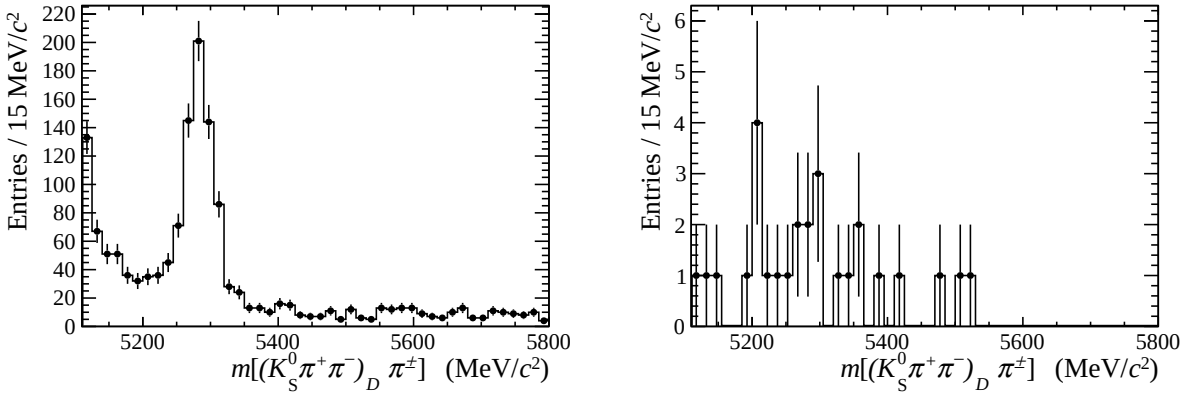

(a) Before K^0_S flight distance χ^2 cut

(b) After K^0_S flight distance χ^2 cut

Figure 4.9: Invariant mass of the $B^{\pm}$ candidates in the K^0_S sidebands in data before and after application of the K^0_S flight distance χ^2 cut. Requirements on refitted quantities are replaced with cuts on raw quantities before the refit.

- **Misidentification of $K^0_S K^+ K^-$ or $K^0_S K^{\pm}\pi^{\mp}$ decays as $K^0_S \pi^+\pi^-$**

  The possibility for $B^{\pm} \to [K^0_S K^{\pm} K^{\mp}]_D K^{\pm}$ or $B^{\pm} \to [K^0_S K^{\pm}\pi^{\mp}]_D K^{\pm}$ to be mistaken for $B^{\pm} \to [K^0_S \pi^{\pm}\pi^{\mp}]_D K^{\pm}$ is studied in simulated samples where at least one candidate decay is present in each event. Firstly a sample of 1,050,000 simulated $B^{\pm} \to [K^0_S K^{\pm} K^{\mp}]_D K^{\pm}$ candidate decays is reconstructed as $B^{\pm} \to [K^0_S \pi^{\pm}\pi^{\mp}]_D K^{\pm}$ by assigning the D daughters a pion mass, using the LHCb software framework. The candidates are passed through the final selection detailed earlier. This allows an upper limit to be placed on the reconstruction and selection efficiency of $B^{\pm} \to [K^0_S K^{\pm} K^{\mp}]_D K^{\pm}$ decays generated in the LHCb detector acceptance, reconstructed as $B^{\pm} \to [K^0_S \pi^{\pm}\pi^{\mp}]_D K^{\pm}$ and passing the selection to be 2.86×10^{-6} at the 95% confidence level. The reconstruction efficiency for $B^{\pm} \to [K^0_S \pi^{\pm}\pi^{\mp}]_D K^{\pm}$ is $(2.07 \pm 0.03) \times 10^{-3}$. Given these two efficiencies and the relative branching fractions for $D^0 \to K^0_S \pi^+\pi^-$ and $D^0 \to K^0_S K^+ K^-$, the limit on the number of cross-feed candidates from $B^{\pm} \to [K^0_S K^{\pm} K^{\mp}]_D K^{\pm}$ is 0.15 in the final data sample, at the 95% confidence level. A similar cross-feed limit is placed on background from $B^{\pm} \to [K^0_S K^{\pm}\pi^{\mp}]_D K^{\pm}$ decays using a sample of 2,020,000 simulated $B^{\pm} \to [K^0_S K^{\pm}\pi^{\mp}]_D K^{\pm}$ decays, and the contamination after the offline selection is, similarly, found to be negligible after the offline selection has been applied.

  Similar studies of the background in the $B^{\pm} \to [K^0_S K^+ K^-]_D h^{\pm}$ sample are made using simulated samples and, after addition of particle identification requirements on the D

daughter kaons, the contamination from $D^0 \to K^0_S \pi^+ \pi^-$ and $D^0 \to K^0_S K^{\mp} \pi^{\pm}$ is found to be negligible.

- **Background from charmless $B^{\pm}$ decays**

  Backgrounds from processes with no intermediate D^0, such as $B^{\pm} \to K^{*\pm} K^{\pm} \pi^{\mp}$, typically have a branching fraction an order of magnitude lower than the $B^{\pm} \to \tilde{D} K^{\pm}$ mode under consideration. Such charmless processes are suppressed by addition of the requirement that the D^0 vertex position must lie downstream of the $B^{\pm}$ vertex in the z-direction. The effectiveness of this requirement is tested by considering the D^0 high mass sidebands where, as before, the refit quantities have been replaced with their raw values and other refit cuts have been removed. The sideband $60\,\text{MeV}/c^2$ above the nominal D^0 mass is shown in Figure 4.10, confirming in data the expectation from simulation studies that no signal should be present. After application of the D^0 vertex position requirement, no significant charmless signal is seen in the sideband.

  Had any structure of marginal significance been seen in the plots in Figure 4.10, this would likely be suppressed once requirements on refitted quantities had been reintroduced since the requirement of a good-quality refit, necessitating a good quality D vertex, suppresses charmless backgrounds still further.

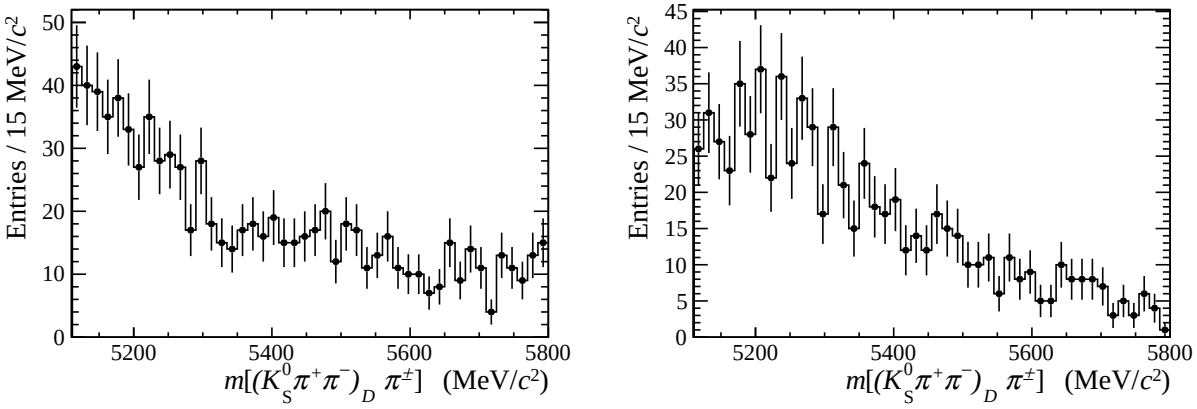

(a) LL K^0_S (b) DD K^0_S

Figure 4.10: Invariant mass spectrum for $B^{\pm}$ candidates in LL and DD data samples in the high D mass sideband. The full selection has been applied but requirements on refitted quantities have been replaced by quantities before the refit and the requirement on the refit χ^2 has been removed.

- **Partially reconstructed backgrounds**

  A significant background structure from partially reconstructed physics processes remains after the final selection has been applied. Naturally, this is most visible in the low invariant mass region of the $B^{\pm}$ spectrum, but can also result in background candidates which lie underneath the signal peak at around $5280\,\mathrm{MeV}/c^2$. The background results mainly from $B^{\pm} \to D\rho^{\pm}$ and $B^{\pm} \to D^*X$ where a pion from the ρ or X decay is misidentified as the usual bachelor pion from the $B^{\pm} \to \tilde{D}h^{\pm}$ decay. This background is studied in simulated data and is modelled empirically in the fit to the $B^{\pm}$ invariant mass spectrum. The model for this background is described in Section 4.6.4.

Selection efficiency

The efficiency with which simulated $B^{\pm} \to [K^0_S \pi^+ \pi^-]_D \pi^{\pm}$ signal candidates are centrally triggered and reconstructed with loose selection requirements is approximately 0.8% with respect to a sample generated such that all tracks lie within the LHCb acceptance. The final selection criteria are optimised in order to maximise signal yield whilst obtaining a high sample purity. The efficiency of the final selection on signal candidates in the resulting sample, including all the requirements in Table 4.4, is 60%, and these final selection criteria reject 99% of the combinatorial background.

The efficiency for $B^{\pm} \to [K^0_S \pi^+ \pi^-]_D K^{\pm}$ candidates is 10% lower because of the requirement placed on the particle identification information for the bachelor particle. The addition of loose PID criteria on the kaons from the $\tilde{D}$ decay in selecting $B^{\pm} \to [K^0_S K^+ K^-]_D \pi^{\pm}$ to reject background from $D^0 \to K^0_S \pi^+ \pi^-$ produces only a marginal loss in efficiency.

Candidates selected from the same pp event

After the selection has been applied, less than 0.4% of the candidates are found to belong to the same event. Since these candidates are likely to share one or more tracks, only the candidate with the lowest χ^2 per degree of freedom from the refit is retained. Because of a

small difference between the nominal D^0 mass used in the LHCb refit and that used in the bin definitions, approximately 0.4% of the candidates are found to have been reconstructed such that their D^0 Dalitz coordinates lie outside the kinematic boundary, and these are also discarded.

To illustrate the effect of the selection, the invariant mass spectrum of triggered $B^{\pm} \to [K^0_S \pi^+ \pi^-]_D \pi^{\pm}$ candidates immediately after the loose, central data stripping is shown in Figure 4.11(a), reproducing the $B^{\pm}$ spectrum in Figure 4.5, where the samples containing K^0_S candidates from long and downstream pion tracks have been combined. The selection outlined in Table 4.4 is then applied, including the refit, and the spectrum produced is shown in Figure 4.11(b).

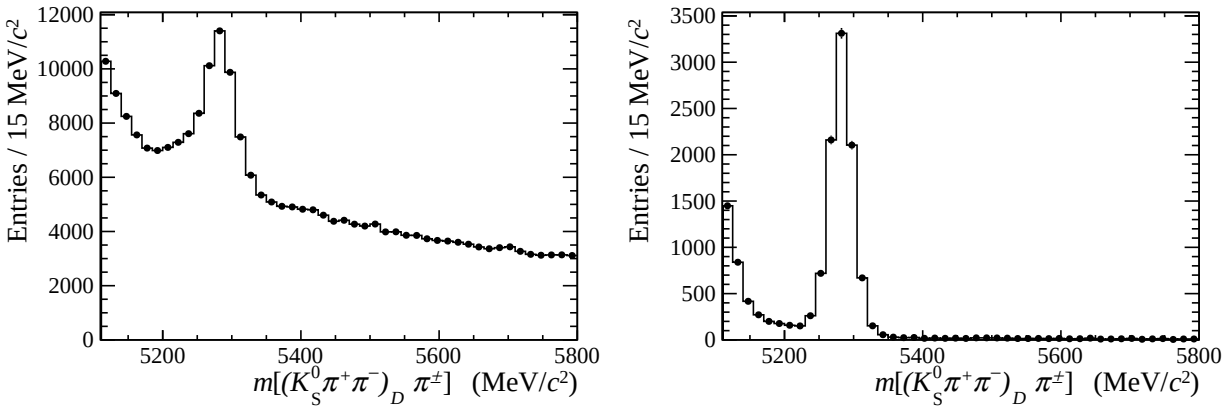

(a) Central reconstruction with loose selection requirements

(b) After final selection requirements are applied

Figure 4.11: Invariant mass spectrum of long and downstream $B^{\pm} \to [K^0_S \pi^+ \pi^-]_D \pi^{\pm}$ candidates before (left) and after (right) the final set of selection criteria, detailed in Table 4.4, are applied.

4.5.3 Simulated samples

A number of different simulated samples are used to study specific backgrounds which could contaminate the samples of candidates in the modes under study, as well as a generic sample composed of $B^{\pm}$, B^0, B^0_s and Λ_b decays. Trigger requirements are applied in order to achieve consistency with the data. The samples are summarised in Table 4.5 where each event must contain at least one simulated candidate decay and candidates are generated within the

LHCb acceptance.

Table 4.5: Summary of background samples considered.

Sample	Number of events
$B \to DX$ generic sample total	96,026,000
$B^{\pm} \to DX$	37,425,000
$B^0 \to DX$	39,136,000
$B^0_s \to DX$	9,751,000
$\Lambda_b \to DX$	9,715,000
$B^0 \to D^0(K^0_S\pi^+\pi^-)\rho(770)^0$	767,000
$B^0 \to D^{*\pm}(2010)(D^0(K^0_S\pi^+\pi^-)\pi^{\pm})K^{\mp}$	520,000
$B^0 \to D^{*\pm}(2010)(D^0(K^0_S\pi^+\pi^-)\pi^{\pm})\pi^{\mp}$	510,000
$B^0 \to D^{*\pm}(2010)(D^0(K^0_S\pi^+\pi^-)\pi^{\pm})\rho(770)^{\mp}$	1,171,000
$B^{\pm} \to D^0(K^0_S\pi\pi)\rho(770)^{\pm}$	1,526,000
$B^{\pm} \to D^{*0}(2010)(D^0(K^0_S\pi^+\pi^-)\{\pi^0,\gamma\})K^{\pm}$	520,000
$B^{\pm} \to D^{*0}(2010)(D^0(K^0_S\pi^+\pi^-)\{\pi^0,\gamma\})\pi^{\pm}$	1,050,000
$B^{\pm} \to D^{*0}(2010)(D^0(K^0_S\pi^+\pi^-)\{\pi^0,\gamma\})\rho(770)^{\pm}$	1,824,182
$B^0 \to D(K^0_S\pi\pi)K^{*0}$	255,000
$\Lambda^0_b \to D(K^0_S\pi^+\pi^-)pK^-$	1,510,000

4.6 Characterisation of candidate sample

This section describes first the characterisation of the $B^{\pm}$ invariant mass spectrum for the signal ($B^{\pm} \to [K^0_S h^+ h^-]_D K^{\pm}$) and control ($B^{\pm} \to [K^0_S h^+ h^-]_D \pi^{\pm}$) modes before any division according to regions of the Dalitz plot. This 'global fit' (see Section 4.4.3) is used to fix the parameters of the functions used later to fit the spectrum in each Dalitz bin. Two global fits are produced: one for the case where the $K^0_S\pi^+\pi^-$ and $K^0_S K^+ K^-$ final states are fitted simultaneously, and one for a fit to the $K^0_S\pi^+\pi^-$ final state alone. This global fit is accomplished by a simultaneous fit to the full data sample, divided into signal and control samples using the PID of the bachelor particle, and further divided into long and downstream K^0_S samples. In the following descriptions of the components which are modelled in the $B^{\pm}$ mass spectrum, the parameters which are shared between the fits in the various sub-samples are identified. The sharing of any parameters is justified by comparison to simulated samples.

The range of $B^{\pm}$ invariant mass used in the fit is between 5110 MeV/c^2 and 5800 MeV/c^2.

The lower limit is chosen as far below the signal peak as possible but still within the range where a good description of the structure at low mass is available. The higher limit is chosen to give a long tail of background from random track combinations, since this aids the fit of a linear PDF to this very small structure.

4.6.1 The signal component

The signal components in $B^{\pm} \to \tilde{D}K^{\pm}$ and $B^{\pm} \to \tilde{D}\pi^{\pm}$ for both $K^0_S\pi^+\pi^-$ and $K^0_S K^+K^-$ are described by a Gaussian function with asymmetric tails, the functional form of which is

$$f(m; m_0, \alpha_L, \alpha_R, \sigma) = \frac{1}{N} \begin{cases} \exp[-(m-m_0)^2/(2\sigma^2 + \alpha_L(m-m_0)^2)], m < m_0; \\ \exp[-(m-m_0)^2/(2\sigma^2 + \alpha_R(m-m_0)^2)], m > m_0. \end{cases} \quad (4.7)$$

This shape is seen to fit well to simulated signal decays, divided into each of the categories used to separate the data in the final fit. The fit parameters resulting from the fit to simulated data in the different categories are given in Table 4.6. The $B^{\pm}$ mass parameter, m_0, is seen to be consistent across the eight categories and justifies the use of a common mass parameter in the simultaneous fit to data. The consistency of the tail parameters, α_L and α_R, between fits to $B^{\pm} \to \tilde{D}K^{\pm}$ and $B^{\pm} \to \tilde{D}\pi^{\pm}$, for both $K^0_S\pi^+\pi^-$ and $K^0_S K^+K^-$, justifies the use of common α_L and α_R parameters between the $B^{\pm} \to \tilde{D}K^{\pm}$ and $B^{\pm} \to \tilde{D}\pi^{\pm}$ fits, regardless of the $\tilde{D}$ final state.

The width of the $B^{\pm}$ peak fitted is expected to be narrower for $B^{\pm} \to \tilde{D}K^{\pm}$ than for $B^{\pm} \to \tilde{D}\pi^{\pm}$ as a result of the reduced energy release value for that decay. The ratio between the two can be studied in simulated decays. A simultaneous fit is applied to $B^{\pm} \to [K^0_S\pi^+\pi^-, K^0_S K^+K^-]_D K^{\pm}$ and $B^{\pm} \to [K^0_S\pi^+\pi^-, K^0_S K^+K^-]_D \pi^{\pm}$ where the tail parameters are shared but the widths are free to float independently. The fit results for the floating parameters are given in Table 4.7. The consistency of the ratios in these fit results justifies sharing the ratio between the LL and DD K^0_S samples in the fit to data, along with floating the $B^{\pm} \to \tilde{D}K^{\pm}$ signal width separately for LL and DD. This reduces the number of width

parameters by one compared to fitting the $B^{\pm} \to \tilde{D}K^{\pm}$ and $B^{\pm} \to \tilde{D}\pi^{\pm}$ widths separately.

Table 4.6: Fit parameters for Gaussian with asymmetric tails, used to fit signal Monte Carlo decay samples where PID criteria are the same as those in data.

Mode	K^0_S type	Parameter		Fit result for $B^{\pm} \to \tilde{D}\pi^{\pm}$	Fit result for $B^{\pm} \to \tilde{D}K^{\pm}$
$K^0_S\pi^+\pi^-$	LL	α_L		0.123 ± 0.008	0.121 ± 0.008
		α_R		0.083 ± 0.008	0.087 ± 0.009
		m_0	(MeV/c^2)	5279.1 ± 0.3	5279.5 ± 0.3
		σ	(MeV/c^2)	11.9 ± 0.2	11.3 ± 0.2
	DD	α_L		0.138 ± 0.005	0.131 ± 0.005
		α_R		0.079 ± 0.006	0.084 ± 0.006
		m_0	(MeV/c^2)	5279.3 ± 0.2	5279.8 ± 0.2
		σ	(MeV/c^2)	11.9 ± 0.2	10.9 ± 0.2
$K^0_S K^+ K^-$	LL	α_L		0.10 ± 0.01	0.09 ± 0.02
		α_R		0.06 ± 0.02	0.07 ± 0.02
		m_0	(MeV/c^2)	5279.7 ± 0.4	5279.2 ± 0.4
		σ	(MeV/c^2)	12.1 ± 0.4	11.2 ± 0.4
	DD	α_L		0.12 ± 0.01	0.12 ± 0.01
		α_R		0.08 ± 0.01	0.09 ± 0.01
		m_0	(MeV/c^2)	5279.5 ± 0.3	5279.0 ± 0.3
		σ	(MeV/c^2)	11.5 ± 0.2	10.9 ± 0.2

Table 4.7: Fit results for simultaneous fit to $B^{\pm} \to \tilde{D}K^{\pm}$ and $B^{\pm} \to \tilde{D}\pi^{\pm}$ signal Monte Carlo where the tail parameters for the asymmetric Gaussian PDF are shared but the widths are free to float independently.

Mode	K^0_S type	Parameter		Value
$K^0_S\pi^+\pi^-$	LL	$\sigma(DK)$	(MeV/c^2)	11.2±0.2
		α_L		0.131±0.003
		α_R		0.084±0.004
		$\frac{\sigma(D\pi)}{\sigma(DK)}$		1.05±0.02
	DD	$\sigma(DK)$	(MeV/c^2)	10.9±0.1
		α_L		0.138±0.002
		α_R		0.083±0.003
		$\frac{\sigma(D\pi)}{\sigma(DK)}$		1.09±0.02
$K^0_S K^+ K^-$	LL	$\sigma(DK)$	(MeV/c^2)	10.7±0.3
		$\frac{\sigma(D\pi)}{\sigma(DK)}$		1.08±0.04
	DD	$\sigma(DK)$	(MeV/c^2)	10.8±0.2
		$\frac{\sigma(D\pi)}{\sigma(DK)}$		1.06±0.02

4.6.2 Modelling $B^{\pm} \to \tilde{D}\pi^{\pm}$ decays misidentified as $B^{\pm} \to \tilde{D}K^{\pm}$

The decay $B^{\pm} \to \tilde{D}\pi^{\pm}$ is used as a control mode in this analysis because of its abundance and the low level of interference expected between the $B^{\pm} \to D^0\pi^{\pm}$ and $B^{\pm} \to \bar{D}^0\pi^{\pm}$ decay amplitudes. Moreover, when selecting $B^{\pm} \to \tilde{D}K^{\pm}$ decays, imperfections in the PID mean that there is a significant residual background from $B^{\pm} \to \tilde{D}\pi^{\pm}$ decays. The shape is modelled by a Crystal Ball function [94], which combines a Gaussian function, with associated mean, μ, and width, σ, and a power law tail. The order of the power-law tail is determined by the parameter n, and the relative size of the tail contribution with respect to the Gaussian core is determined by the parameter α (a negative value of α gives a tail situated to the right of the Gaussian peak). The yield assigned to this function is fixed with reference to the fitted yield of the $B^{\pm} \to \tilde{D}\pi^{\pm}$ control mode and the measured performance of the bachelor PID criteria to follow. In contrast, the relative branching fractions of the two modes mean that the $B^{\pm} \to \tilde{D}K^{\pm}$ pollution in the $B^{\pm} \to \tilde{D}\pi^{\pm}$ sample is negligible.

The function used to model this misidentified component in the $B^{\pm} \to \tilde{D}K^{\pm}$ spectrum is validated using simulated samples of $B^{\pm} \to [K^0_S h^+ h^-]_D \pi^{\pm}$ decays where, during reconstruction, the bachelor particle hypothesis is swapped from $\pi^{\pm}$ to $K^{\pm}$ and the offline selection applied to the reconstructed candidates. All selection criteria are applied and, as usual when using simulated samples, the candidate decays studied are truth-matched to have originated in signal decays.

The parameters of the Crystal Ball function are common between samples containing the two K^0_S types and for the two $\tilde{D}$ final states. Since the shape of the misidentified background is affected by the momentum-dependent PID requirements, this assumption is justified by the similarity between the momentum distributions of bachelor particles in simulated data for each sample. The $K^0_S\pi^+\pi^-$ samples are compared in Figure 4.12(a) and the $K^0_S K^+ K^-$ samples in Figure 4.12(b), where the LL $K^0_S\pi^+\pi^-$ remains in grey shading. The distributions are seen to be consistent.

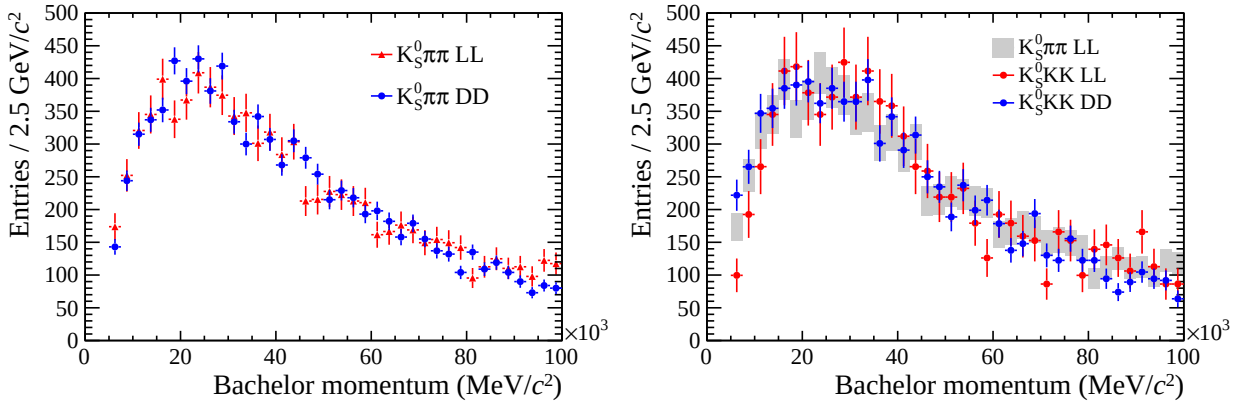

(a) $K^0_S\pi^+\pi^-$ (b) $K^0_S K^+ K^-$

Figure 4.12: Bachelor momentum distributions for LL and DD K^0_S simulated samples in both $\tilde{D}$ final states, where $B^{\pm} \to \tilde{D}\pi^{\pm}$ decays are reconstructed as $B^{\pm} \to \tilde{D}K^{\pm}$. The $K^0_S\pi^+\pi^-$ samples are compared on the left. The $K^0_S K^+ K^-$ samples are compared on the right, where the LL $K^0_S\pi^+\pi^-$ points are left in filled grey markers to allow comparison.

Efficiency determination of bachelor particle identification

To determine the PID efficiency, a large sample of pions and kaons is used, selected with low background from the 2011 LHCb data set using only kinematic criteria and without the use of any RICH information. The pions and kaons are produced in the decay of a D^0 meson whose flavour is tagged in a $D^{*+} \to D^0\pi^+$ ($D^{*-} \to \bar{D}^0\pi^-$) decay. These calibration samples are reweighted such that their transverse momentum and pseudorapidity distributions match those of bachelor particles in data. The sample to match with the reweighting contains $B^{\pm} \to \tilde{D}\pi^{\pm}$ decays selected in the standard way but without the use of PID information and with the additional requirement that the $B^{\pm}$ mass should lie within 50 MeV/c^2 of the $B^{\pm}$ PDG mass. The efficiency of the PID criteria can then be simply determined through application of the criteria to this 'PID-free' sample. The method assumes identical momentum and pseudorapidity distributions for the pion and kaon from the $B^{\pm}$ decay. The calibration is performed once for the $B^{\pm} \to [K^0_S\pi^+\pi^-]_D\pi^{\pm}$ sample and assumed to be the same for the $B^{\pm} \to [K^0_S K^+ K^-]_D\pi^{\pm}$ sample, given the agreement in their simulated momentum distributions.

The PID efficiencies determined for the criteria used in the data selection are given in

Table 4.8, separated by magnet polarity and averaged according to the integrated luminosity of the data collected with each polarity. The very large sample sizes mean that the statistical uncertainties of these values are $\sim 0.01\%$, and are negligible in the analysis. The rate at which reconstructed $B^{\pm} \to \tilde{D}\pi^{\pm}$ candidates are misidentified as $B^{\pm} \to \tilde{D}K^{\pm}$ decays is $\frac{1-\epsilon_\pi}{\epsilon_\pi}$ and leads to a misidentification rate of 4.2%.

Table 4.8: Efficiency, for kinematically selected pions or kaons, of the respective PID requirement: DLL$(K-\pi) > 4$ for kaons and DLL$(K-\pi) < 4$ for pions. The uncertainties on these efficiencies are of order 0.02% for kaons and 0.01% for pions.

Particle	Magnet polarity	K^0_S sample	Efficiency of PID likelihood cut (%)
ϵ_K	up	LL	85.5
	down	LL	84.8
	average	LL	**85.1**
	up	DD	85.3
	down	DD	86.3
	average	DD	**85.9**
ϵ_π	up	LL	96.1
	down	LL	96.0
	average	LL	**96.0**
	up	DD	96.0
	down	DD	96.0
	average	DD	**96.0**

4.6.3 Combinatorial backgrounds

Within the limited mass window considered, the background from random combinations of tracks used to form a $B^{\pm}$ candidate is expected to have an approximately linear distribution in $B^{\pm}$ invariant mass. This background is therefore modelled using a linear function in every sample. The slope of this function is allowed to vary independently in the fit to each except the $B^{\pm} \to [K^0_S K^+ K^-]_D K^{\pm}$ sample in which, due to its low statistics in general and low combinatorial background in particular, the function is flat. The combinatorial background is lower here than in $K^0_S \pi^+ \pi^-$ due to the added PID requirement on the D^0 daughter kaons. The linear function is seen to fit the data well in Figures 4.15.

4.6.4 Partially reconstructed backgrounds

Given the large number of possible contributions from various modes, the structure is modelled empirically by deriving a reconstructed shape in $B^{\pm}$ invariant mass from a large simulated data set containing a 'cocktail' of decays which are considered likely to contribute. The simulated data set is composed of decays of $B^{\pm}$, B^0, B^0_s and Λ^0_b particles, weighted by their approximate hadronisation fractions: 0.4, 0.4, 0.1 and 0.1 respectively [95].

The yields after selection of $B^{\pm} \to [K^0_S h^+ h^-]_D K^{\pm}$ in the simulated cocktail sample are too small to be used to derive a shape for this background but do reveal that the main partially reconstructed backgrounds arise from decays involving a real D meson. This is expected given both that the refit applied requires a good D vertex to be formed and also since no significant structure is seen in the $B^{\pm}$ invariant mass spectrum in the D^0 sidebands. In describing backgrounds stemming from the partial reconstruction of a $B^{\pm}$ decay involving a D^0 meson, the final state of the $\tilde{D}$ meson is not important and the much more abundant $K^{\pm}\pi^{\mp}$ final state can be used. The same partially reconstructed background shape can be used as was employed in the $B^{\pm} \to [h^+ h^-]_D K^{\pm}$ analysis [24], where the reconstructed yield from the simulated data set is much higher. The same shape is used for modelling the background in both categories of K^0_S decay and in both the $K^0_S \pi^+ \pi^-$ and $K^0_S K^+ K^-$ final states. It does, however, differ for $B^{\pm} \to \tilde{D} K^{\pm}$ and $B^{\pm} \to \tilde{D} \pi^{\pm}$ decays.

The shape is determined for the $B^{\pm} \to [h^+ h^-]_D K^{\pm}$ analysis, ensuring that differences between simulated and real data are corrected for. Candidates are reconstructed using standard LHCb software and selection criteria appropriate to the $B^{\pm} \to [h^+ h^-]_D K^{\pm}$ analysis are applied. $B^{\pm} \to \tilde{D} h^{\pm}$ decays are identified using the generator information present for each candidate and are then excluded. A smearing of the invariant mass distribution is applied given the slightly better mass resolution observed in simulated data, and the momenta of the candidate decay tracks are rescaled to match the position of the $B^{\pm}$ mass peak in data. The sample is then divided using the known PID of the bachelor candidate (K or π) and the two samples are combined, each weighted according to the determined PID cut efficiency. Finally, the shape is extracted by a Kernel Estimation [96] smoothing of

the invariant mass distribution. The invariant mass shape determined for this background is shown in Figure 4.13 where the shape has been superimposed upon the low-statistics yield of simulated candidates reconstructed and selected in the $B^{\pm} \to [K^0_S \pi^+ \pi^-]_D h^{\pm}$ mode. The description is seen to be acceptable, though the yield of candidates remaining is too low for a rigorous comparison.

A limitation of assuming the same shape as in the $B^{\pm} \to [h^+ h^-]_D K^{\pm}$ analysis is that the PDF does not include a contribution from for $B^0_s \to \tilde{D} K^{*0}$ backgrounds. This is because the PDF is determined through the study of the $B^{\pm} \to [K^{\pm}\pi^{\mp}]_D K^{\pm}$ mode, where the bachelor and D-daughter kaon have the same charge, in which the possible background from $B^0_s \to [K^{\pm}\pi^{\mp}]_{D^0} [K^{\pm}\pi^{\mp}]_{K^*(892)^0}$ decay is heavily suppressed. The B^0_s background is more significant in the $B^{\pm} \to [K^{\mp}\pi^{\pm}]_D K^{\pm}$ or $B^{\pm} \to [K^0_S h^+ h^-]_D K^{\pm}$ samples which are not dominated by a Cabibbo favoured $D^0 \to K^-\pi^+$ decay.

The B^0_s background is modelled independently using the same Crystal Ball function as was used to account for it in the $B^{\pm} \to [h^+ h^-]_D K^{\pm}$ analysis ($m_0 = 5205\,\text{MeV}/c^2, \sigma_L = 94.9\,\text{MeV}/c^2, \sigma_R = 16.5\,\text{MeV}/c^2, \alpha_L = 0.47$ and $\alpha_R = 0.1$) and, after verifying in the cocktail sample, the same fixed yield of this extra B^0_s component is used as in that analysis such that it contributes 6% of the partially reconstructed background yield.

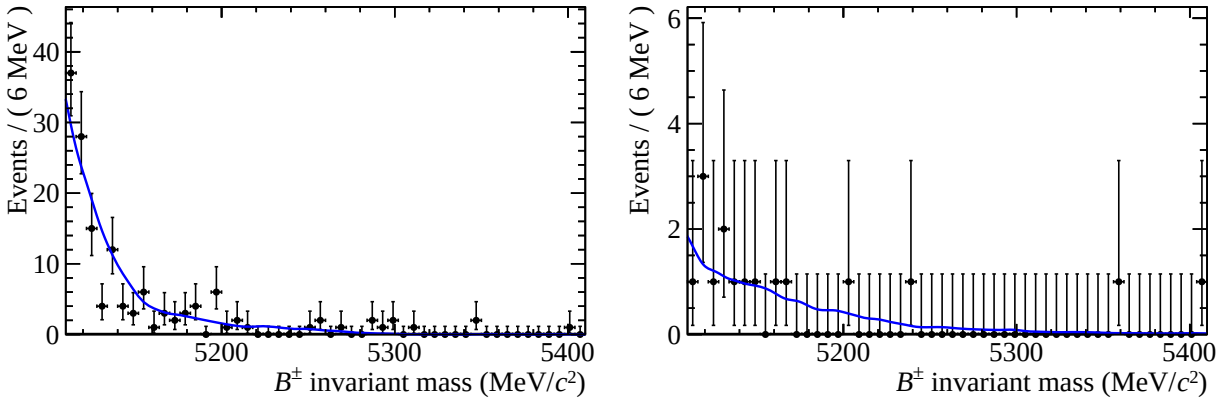

(a) Shape for $B^{\pm} \to \tilde{D}\pi^{\pm}$

(b) Shape for $B^{\pm} \to \tilde{D}K^{\pm}$

Figure 4.13: Comparison of the partially reconstructed background PDF shape (blue line), determined in the analysis of $B^{\pm} \to [K\pi]_D h^{\pm}$ [24], with the invariant mass distribution (black data points) of simulated candidates remaining after selection in the $B^{\pm} \to [K^0_S \pi^+ \pi^-]_D \pi^{\pm}$ (left) and $B^{\pm} \to [K^0_S \pi^+ \pi^-]_D K^{\pm}$ (right) modes.

4.6.5 Summary of fit to the data

The analysis is performed for the $B^{\pm} \to [K^0_S \pi^+ \pi^-]_D h^{\pm}$ and $B^{\pm} \to [K^0_S K^+ K^-]_D h^{\pm}$ samples fitted simultaneously and the $B^{\pm} \to [K^0_S \pi^+ \pi^-]_D h^{\pm}$ data set on its own, allowing for an assessment of the effect on the observables of adding the $\tilde{D} \to K^0_S K^+ K^-$ final state. The global fit to the invariant mass spectrum is therefore performed for these two cases.

The components of the final PDF are summarised in Table 4.9 where attention is drawn to the common parameters in the various simultaneous fits.

4.6.6 Results for simultaneous fit to the $B^{\pm} \to [K^0_S \pi^+ \pi^-]_D h^{\pm}$ and $B^{\pm} \to [K^0_S K^+ K^-]_D h^{\pm}$ samples

The simultaneous fit to the data in all the categories is performed and the fit projections are presented in Figure 4.14. The same projections are shown in Figure 4.15 with a logarithmic y-axis, to make the fit in the high $B^{\pm}$ invariant-mass region more easily visible. The combinatorial background PDF is not specifically labelled in these figures given its very low yield. Nevertheless, the presence of this fit component is clear, given that it is the only component which contributes in the high invariant mass region. The yields corresponding to each component, integrated over the whole mass range in the fit are given in Table 4.10 and the yields of the PDF components integrated inside a signal window around the $B^{\pm}$ peak (5247 MeV/c^2 to 5317 MeV/c^2) are given in Table 4.11. The fitted values for parameters of the component PDFs are given in Table 4.12. Quantities of interest, derived from the fit output, are given in Table 4.13. It should be noted that these quantities include the number of $B^{\pm} \to \tilde{D} K^{\pm}$ candidates, since this yield is calculated from the yield of $B^{\pm} \to \tilde{D} \pi^{\pm}$ and the ratio $\frac{n_{DK}}{n_{D\pi}}$ which, instead, are floated in the fit.

Table 4.9: Summary of relations between PDF components.

Component	Common parameters
$B^{\pm}$ signal: Gaussian with asymmetric tails	• All aspects of signal shape are common to $K^0_S\pi^+\pi^-$ and $K^0_S K^+ K^-$. • Mean of Gaussian shared between $B^{\pm} \to D\pi^{\pm}$ and $B^{\pm} \to DK^{\pm}$ and between LL and DD K^0_S samples. • Tail parameter α_L common to signal and control modes but separate for LL and DD K^0_S samples. • Tail parameter α_R common to signal and control modes but separate for LL and DD K^0_S samples. • Ratio of Gaussian widths, $\frac{\sigma_{B^{\pm}\to\tilde{D}K^{\pm}}}{\sigma_{B^{\pm}\to\tilde{D}\pi^{\pm}}}$, common to the K^0_S samples. • Ratio of yields in both signal and control modes, $\frac{n_{B^{\pm}\to\tilde{D}K^{\pm}}}{n_{B^{\pm}\to\tilde{D}\pi^{\pm}}}$, common to the K^0_S samples.
$B^{\pm} \to \tilde{D}\pi^{\pm}$ mis-ID as $B^{\pm} \to \tilde{D}K^{\pm}$: Crystal Ball	• All aspects of the shape (mean, width, n and α) are common in the fits to both K^0_S samples and for $K^0_S\pi^+\pi^-$ and $K^0_S K^+ K^-$. • Yield fixed according to the yield of $B^{\pm} \to \tilde{D}\pi^{\pm}$ signal and pre-determined misidentification rate.
Part. reco. background: PDF taken from simulated $B^{\pm} \to [K^+\pi^-]_D h^{\pm}$	• Shape common to fits for both K^0_S samples and between $K^0_S\pi^+\pi^-$ and $K^0_S K^+ K^-$.
$B^{\pm} \to [K^0_S K^+ K^-]_D K^{\pm}$ combinatorial: Linear function	• For the combinatorial background in this decay channel alone, the slope of the linear function is fixed to 0 for both LL and DD K^0_S. In other decay channels the slope is allowed to vary.

Table 4.10: Fitted yields, integrated across the whole mass range (5110 MeV/c^2 to 5800 MeV/c^2). The ratio $\frac{n_{DK}}{n_{D\pi}}$ has been corrected for different pion and kaon PID efficiency effects.

Mode	Fit component	LL K^0_S	DD K^0_S
	Ratio $\frac{n_{DK}}{n_{D\pi}}$	0.0849 ± 0.0047	
$B^\pm \to [K^0_S\pi^+\pi^-]_D\pi^\pm$	Signal	3049±61	6169±88
	Combinatorial background	187±28	674±52
	Partially reconstructed background	1068±38	2323±56
$B^\pm \to [K^0_S\pi^+\pi^-]_D K^\pm$	Combinatorial background	73±28	224±47
	Partially reconstructed background	181±20	395±31
$B^\pm \to [K^0_S K^+K^-]_D\pi^\pm$	Signal	452±22	979±32
	Combinatorial background	36±11	122±17
	Partially reconstructed background	157±14	328±20
$B^\pm \to [K^0_S K^+K^-]_D K^\pm$	Combinatorial background	6±5	25±9
	Partially reconstructed background	36±7	47±8

Discussion of fit to invariant mass spectrum

The total number of signal $B^\pm \to \tilde{D}K^\pm$ candidates, combining LL and DD K^0_S samples, is determined for each D^0 final state and found to be 697 ± 30 for $K^0_S\pi^+\pi^-$, where the sample purity is 86% within the standard $B^\pm$ signal window, and 108 ± 5 for $K^0_S K^+K^-$ where the sample purity is 88% within the standard window. A significant source of background arises from the more abundant $B^\pm \to \tilde{D}\pi^\pm$ decay where the bachelor is misidentified. The misidentification rate is around 4%, giving 382 ± 19 misidentified candidates in the $B^\pm \to [K^0_S\pi^+\pi^-]_D K^\pm$ sample and 60 ± 7 in the $B^\pm \to [K^0_S K^+K^-]_D K^\pm$ sample.

It is of interest to determine the ratio of $B^\pm \to \tilde{D}K^\pm$ to $B^\pm \to \tilde{D}\pi^\pm$ yields seen in these two modes, and to compare this ratio to that measured with different D^0 final states, such as the related two-body analysis [24]. The ratio is found to be $(8.49 \pm 0.47)\%$, consistent with the measurement for the $K^\mp\pi^\pm$ final state, $(7.74 \pm 0.12(\text{stat.}) \pm 0.18(\text{syst.}))\%$.

The shape parameters of the fitted PDF which are free to vary in the fit converge upon reasonable values. The Gaussian widths of the $B^\pm \to \tilde{D}K^\pm$ signal components are somewhat larger in data ((13.8 ± 0.9) MeV/c^2) than seen in simulated decays ((11.2 ± 0.2) MeV/c^2). As expected, the width of the $B^\pm \to \tilde{D}\pi^\pm$ peak is found to be larger than that of $B^\pm \to \tilde{D}K^\pm$

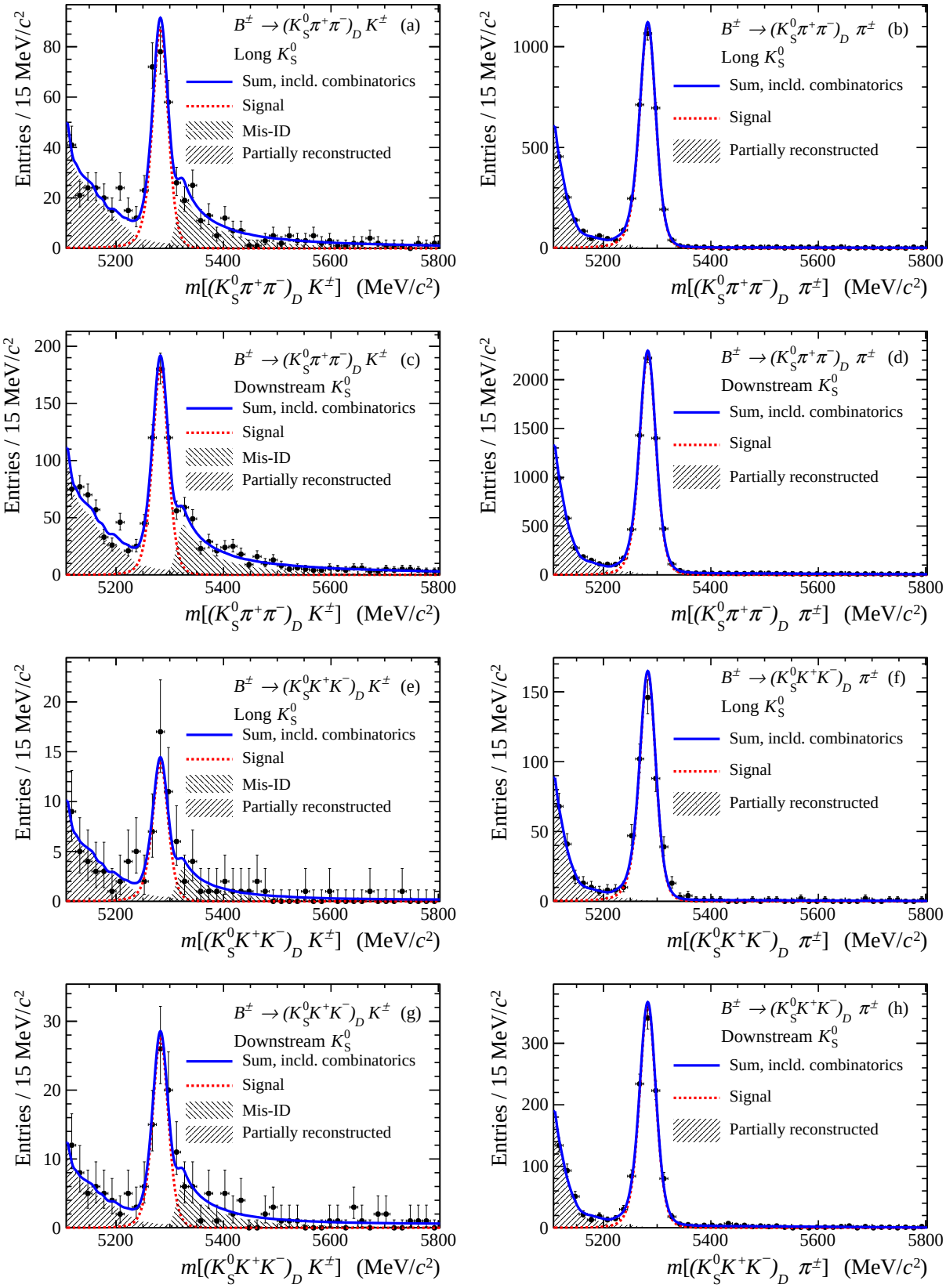

Figure 4.14: Projections of the simultaneous fit to the invariant mass distributions of $B^\pm \to [K^0_S h^+ h^-]_D h^\pm$ candidates. The $K^0_S\pi^+\pi^-$ samples are shown in (a, c, e, g) and the $K^0_S K^+K^-$ samples in (b, d, f, h) whilst long (a, b, e, f) and downstream (c, d, g, h) K^0_S samples are separated. The overall fit PDF is marked with a solid blue line and other components are also indicated: $B^\pm \to \tilde{D}h^\pm$ signal (red), misidentified $B^\pm \to \tilde{D}\pi^\pm$ (shading with negative slope), and partially reconstructed background (shading with positive slope).

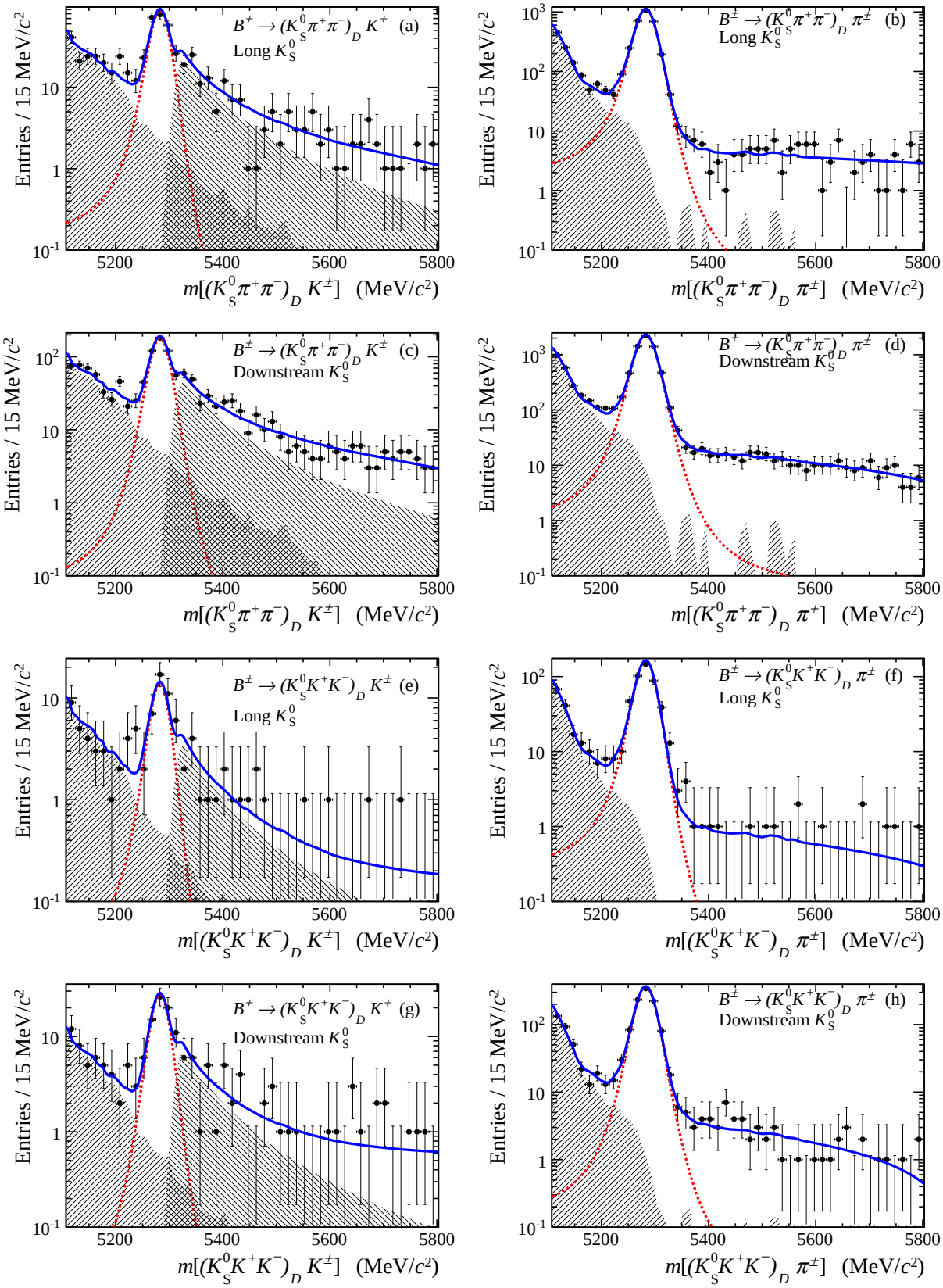

Figure 4.15: Invariant mass spectra for $B^{\pm} \to [K^0_S h^+ h^-]_D K^{\pm}$ and $B^{\pm} \to [K^0_S h^+ h^-]_D \pi^{\pm}$ decays for long and downstream K^0_S events with fit superimposed where the vertical scale is logarithmic, aiding visibility of the fit to the combinatorial background component. The figures are laid out and the components are identified in the same way as the data fits in Figure 4.14.

Table 4.11: Fitted yields, integrated inside a signal window around the $B^\pm$ peak (5247 MeV/c^2 to 5317 MeV/c^2).

Mode	Fit component	LL K^0_S	DD K^0_S
$B^\pm \to [K^0_S\pi^+\pi^-]_D\pi^\pm$	Signal	2809±56	5755±82
	Combinatorial background	22±3	90±7
	Partially reconstructed background	25±1	55±1
$B^\pm \to [K^0_S\pi^+\pi^-]_D K^\pm$	Signal	213±13	441±25
	Misidentified $B^\pm \to \tilde{D}\pi^\pm$	11±3	22±5
	Combinatorial background	9±4	29±6
	Partially reconstructed background	11±1	25±2
$B^\pm \to [K^0_S K^+K^-]_D\pi^\pm$	Signal	417±20	913±29
	Combinatorial background	5±1	18±2
	Partially reconstructed background	3.7±0.3	7.7±0.5
$B^\pm \to [K^0_S K^+K^-]_D K^\pm$	Signal	32±2	70±4
	Misidentified $B^\pm \to \tilde{D}\pi^\pm$	1.6±1.2	3±2
	Combinatorial background	0.6±0.5	2.5±0.9
	Partially reconstructed background	2.2±0.4	2.9±0.5

Table 4.12: Fitted values for the PDF parameters for the simultaneous fit to the $K^0_S\pi^+\pi^-$ and $K^0_S K^+K^-$ samples.

Mode	Component	Parameter	Fit result
Common	Signal	μ (MeV/c^2)	5282.6±0.2
		α_L (LL)	0.154±0.015
		α_L (DD)	0.126±0.013
		α_R (LL)	0.089±0.015
		α_R (DD)	0.094±0.011
	Misidentified $B^\pm \to \tilde{D}\pi^\pm$	μ (MeV/c^2)	5325.3±4.4
		α	-0.24±0.13
		n	3.0±2.0
		σ (MeV/c^2)	12±5
$B^\pm \to \tilde{D}\pi^\pm$	Signal	$\frac{\sigma(D\pi)}{\sigma(DK)}$	1.051±0.065
	Combinatorial	Slope $K^0_S\pi^+\pi^-$ (LL)	-0.30±0.22
		Slope $K^0_S\pi^+\pi^-$ (DD)	-0.64±0.08
		Slope $K^0_S K^+K^-$ (LL)	-0.62±0.30
		Slope $K^0_S K^+K^-$ (DD)	-0.83±0.12
$B^\pm \to \tilde{D}K^\pm$	Signal	σ (LL) (MeV/c^2)	13.76±0.90
		σ (DD) (MeV/c^2)	13.93±0.89
	Combinatorial	Slope $K^0_S\pi^+\pi^-$ (LL)	-0.49±0.43
		Slope $K^0_S\pi^+\pi^-$ (DD)	-0.52±0.26

Table 4.13: Quantities derived from the results for the simultaneous fit to the $K^0_S\pi^+\pi^-$ and $K^0_S K^+ K^-$ data samples.

Mode	Component	LL K^0_S	DD K^0_S
$B^{\pm} \to [K^0_S\pi^+\pi^-]_D K^{\pm}$	Signal	229±13	468±27
	Misidentified $B^{\pm} \to \tilde{D}\pi^{\pm}$	126±11	256±16
$B^{\pm} \to [K^0_S K^+ K^-]_D K^{\pm}$	Signal	34±2	74±5
	Misidentified $B^{\pm} \to \tilde{D}\pi^{\pm}$	19±4	41±6
$B^{\pm} \to \tilde{D}\pi^{\pm}$	σ_{signal}	14.5±1.3	14.6±1.3

but not significantly so, with a ratio of 1.05±0.06. This result can be compared to 1.07±0.01 in simulated data. The parameters fitted for the Crystal Ball shape for the misidentified component are reasonable, with a small, negative value for α, a value of n consistent with unity and an overall shape similar to that seen in simulated samples.

4.6.7 Results for the fit to the $B^{\pm} \to [K^0_S\pi^+\pi^-]_D h^{\pm}$ data set alone

Using only the $B^{\pm} \to [K^0_S\pi^+\pi^-]_D h^{\pm}$ data, the simultaneous fit to the data in all the categories is performed and results are given for the component yields in Table 4.14, the PDF fit parameters in Table 4.15 and derived quantities in Table 4.16. The fit projections are not shown because, to the eye, they are identical to those in Figure 4.14. As expected, all the fitted values for the yields and PDF parameters, as well as the derived quantities, lie within one multiple of their statistical uncertainties from the value determined by the simultaneous fit using both final states and, in most cases, within 25% of that statistical uncertainty.

Table 4.14: Fitted yields, integrated across the whole mass range (5110 MeV/c^2 to 5800 MeV/c^2). The ratio $\frac{n_{DK}}{n_{D\pi}}$ has been corrected for PID efficiency effects.

Mode	Fit component	LL K^0_S	DD K^0_S
	Ratio $\frac{n_{DK}}{n_{D\pi}}$	0.0856 ± 0.0049	
$B^{\pm} \to [K^0_S\pi^+\pi^-]_D\pi^{\pm}$	Signal	3039±61	6182±91
	Combinatorial background	199±27	664±54
	Partially reconstructed background	1065±38	2319±56
$B^{\pm} \to [K^0_S\pi^+\pi^-]_D K^{\pm}$	Combinatorial background	73±28	218±48
	Partially reconstructed background	180±20	395±31

Table 4.15: Fitted values for the PDF parameters for the fit to the $K^0_S\pi^+\pi^-$ data sample alone.

Mode	Component	Parameter	Fit result
Common	Signal	μ (MeV/c^2)	5282.6±0.2
		α_L (LL)	0.153±0.015
		α_L (DD)	0.131±0.014
		α_R (LL)	0.079±0.017
		α_R (DD)	0.098±0.012
	Misidentified $B^{\pm} \to \tilde{D}\pi^{\pm}$	μ (MeV/c^2)	5327.9±4.0
		α	-0.27±0.14
		n	2.5±1.8
		σ (MeV/c^2)	12±4
$B^{\pm} \to \tilde{D}\pi^{\pm}$	Signal	$\frac{\sigma(D\pi)}{\sigma(DK)}$	1.029±0.064
	Combinatorial	Slope $K^0_S\pi^+\pi^-$ (LL)	-0.37±0.20
		Slope $K^0_S\pi^+\pi^-$ (DD)	-0.63±0.08
$B^{\pm} \to \tilde{D}K^{\pm}$	Signal	σ (LL) (MeV/c^2)	13.93±0.95
		σ (DD) (MeV/c^2)	14.05±0.94
	Combinatorial	Slope $K^0_S\pi^+\pi^-$ (LL)	-0.51±0.45
		Slope $K^0_S\pi^+\pi^-$ (DD)	-0.52±0.29

Table 4.16: Quantities derived from the results for the fit to the $K^0_S\pi^+\pi^-$ data sample alone.

Mode	Component	LL K^0_S	DD K^0_S
$B^{\pm} \to [K^0_S\pi^+\pi^-]_D K^{\pm}$	Signal	230±14	473±28
	Misidentified $B^{\pm} \to \tilde{D}\pi^{\pm}$	126±11	257±16
$B^{\pm} \to \tilde{D}\pi^{\pm}$	Signal width	14.3±1.3	14.5±1.3

5

Measurement of CP violation using $B^{\pm} \to [K^0_S h^+ h^-]_D K^{\pm}$ at LHCb

The analysis of the $B^{\pm} \to [K^0_S h^+ h^-]_D K^{\pm}$ data in regions of the Dalitz plot is now presented, resulting in a measurement of the fit parameters $x_{\pm}$ and $y_{\pm}$. From this measurement the CKM phase γ can be determined.

5.1 Introduction

Following the selection procedure described in Section 4.5, the D^0 Dalitz plots are plotted in Figures 5.1 and 5.2 where only candidates with a refitted $B^{\pm}$ invariant mass between $5247\,\text{MeV}/c^2$ and $5317\,\text{MeV}/c^2$ are shown. The data, for candidates with $B^{\pm}$ invariant mass between $5100\,\text{MeV}/c^2$ and $5800\,\text{MeV}/c^2$, are first divided into the Dalitz regions pictured in Figure 4.1(b) for $D^0 \to K^0_S \pi^+ \pi^-$ and Figure 4.2 for $D^0 \to K^0_S K^+ K^-$. The PDFs determined in Section 4.6 are used to fit the candidates in each region. The fits are performed simultaneously with the yields of all the background components and the yield of $B^{\pm} \to \tilde{D}\pi^{\pm}$ candidates free to float independently. The yield of $B^{\pm} \to \tilde{D}K^{\pm}$ candidates is not free to vary in each region, but is determined as in Equation 1.47 from the total number of B^+ (B^-) candidates and the values of x_+, y_+ (x_-, y_-), which are also parameters of the fit. Measurements of $x_{\pm}$ and $y_{\pm}$ are made for the $K^0_S \pi^+ \pi^-$ final state on its own and after addition of $K^0_S K^+ K^-$, in order to demonstrate the gain in statistical power from the inclusion of this latter sample. The systematic uncertainties affecting the measurements of the $x_{\pm}$, $y_{\pm}$ observables are then assigned, followed by the extraction of constraints on γ, r_B and δ_B.

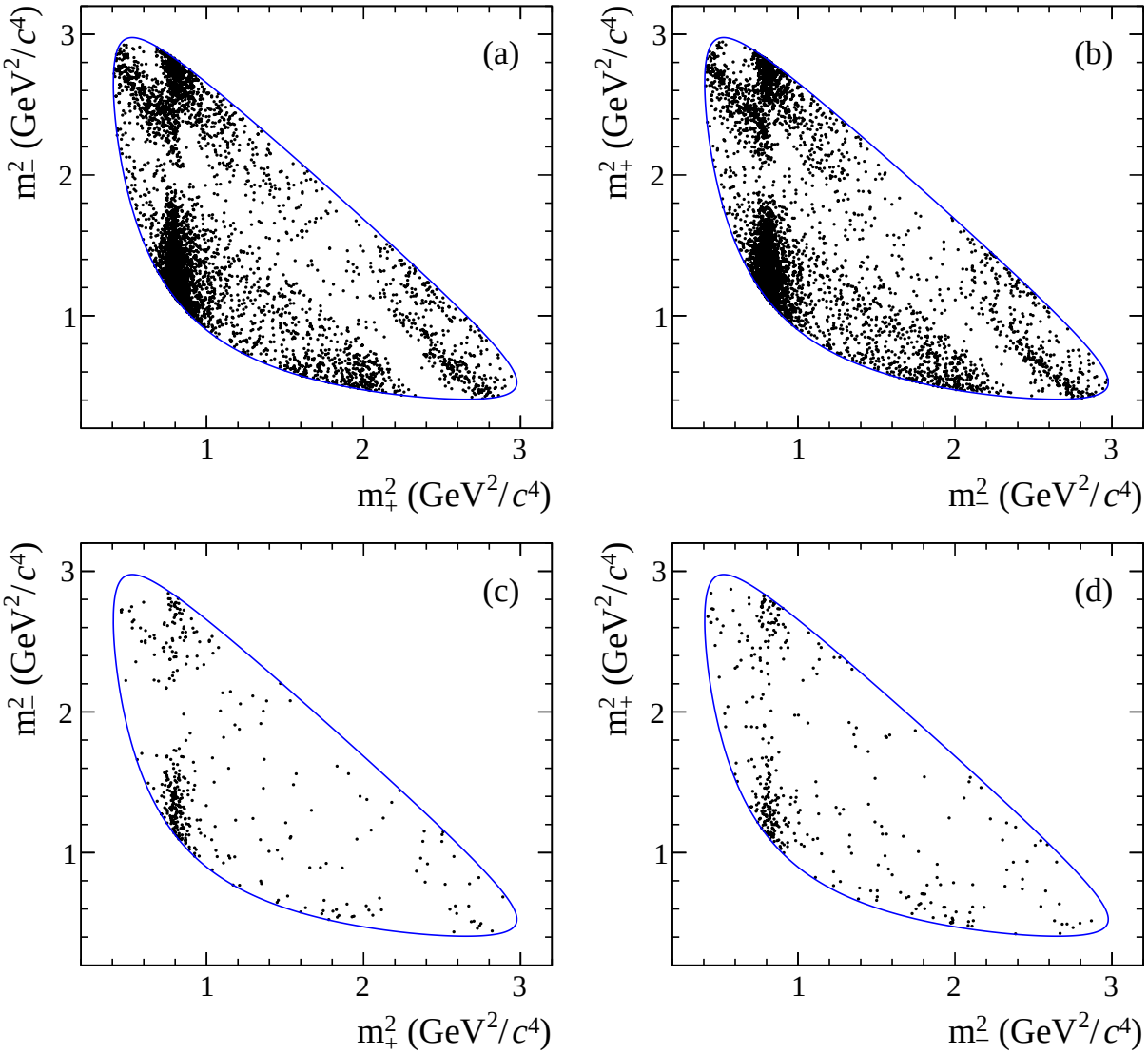

Figure 5.1: D^0 Dalitz plots for $B^{\pm} \to [K^0_S \pi^+ \pi^-]_D h^{\pm}$ data where the $B^{\pm}$ invariant mass lies in the range $5247\,\text{MeV}/c^2 \to 5317\,\text{MeV}/c^2$. Figures (a, b) show $B^{\pm} \to \tilde{D}\pi^{\pm}$ candidates and (c, d) show $B^{\pm} \to \tilde{D}K^{\pm}$ candidates. The samples are split into (a, c) B^+ and (b, d) B^-. Multiple candidates are excluded, as are candidates lying outside the Dalitz kinematic boundary.

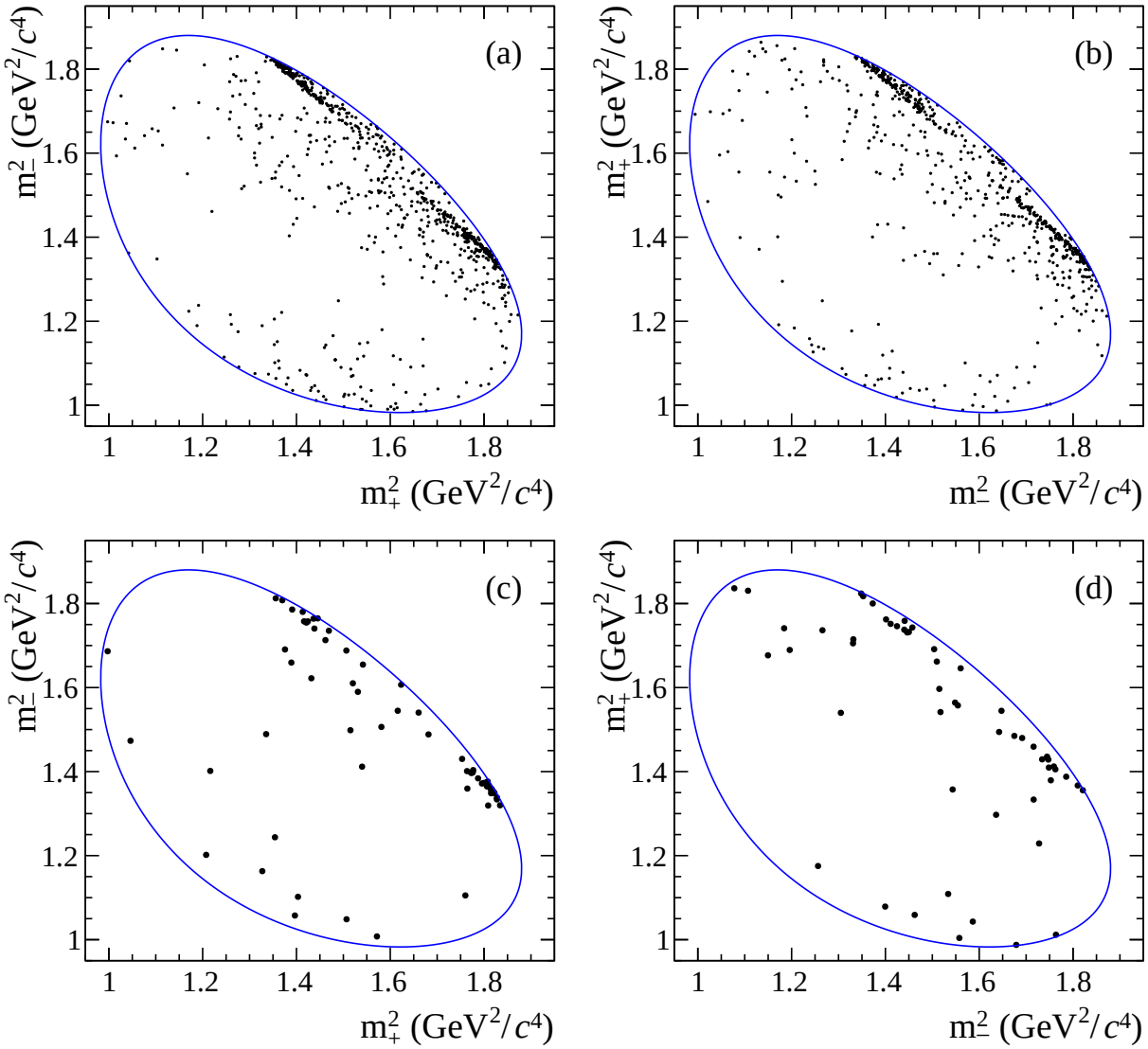

Figure 5.2: D^0 Dalitz plots for $B^{\pm} \to [K^0_S K^+ K^-]_D h^{\pm}$ data where the $B^{\pm}$ invariant mass lies in the range $5247\,\text{MeV}/c^2 \to 5317\,\text{MeV}/c^2$. Figures (a, b) show $B^{\pm} \to \tilde{D}\pi^{\pm}$ candidates and (c, d) show $B^{\pm} \to \tilde{D}K^{\pm}$ candidates. The samples are split into (a,c) B^+ and (b,d) B^-. Multiple candidates are excluded, as are candidates lying outside the Dalitz kinematic boundary.

5.2 Fit likelihood for the observables $x_{\pm}$ and $y_{\pm}$

The Minuit [79] package is used to maximise a likelihood function applied to the selected candidates in the data samples. The candidates are separated by the charge of the B meson and by whether the K^0_S is composed of long or downstream daughter pion tracks. The quantity $-2\log\mathcal{L}_{\rm tot}$ is minimised where the total log-likelihood, $\log\mathcal{L}_{\rm tot}$ in Equation 5.1, is the sum of a log-likelihood for the $B^{\pm} \to \tilde{D}\pi^{\pm}$ data and of a log-likelihood for the $B^{\pm} \to \tilde{D}K^{\pm}$ data in each of the charge and K^0_S-type categories for each D final state, $f = K^0_S\pi^+\pi^-, K^0_S K^+ K^-$:

$$\log\mathcal{L}_{\rm tot} = \sum_f \left(\log\mathcal{L}^f_{D\pi^+} + \log\mathcal{L}^f_{D\pi^-} + \log\mathcal{L}^f_{DK^+} + \log\mathcal{L}^f_{DK^-} \right). \tag{5.1}$$

For the sake of clarity, the superscript f, labelling the D final state, is omitted from the discussion which follows since the likelihoods for $K^0_S\pi^+\pi^-$ and $K^0_S K^+ K^-$ have the same form.

The $B^{\pm} \to \tilde{D}\pi^{\pm}$ log-likelihood is formed from a signal component, denoted $\mathcal{S}(m)$, as a function of $B^{\pm}$ invariant mass after the refit; a combinatorial background component, $\mathcal{B}(m)_1$; and a partially reconstructed background component, denoted $\mathcal{B}(m)_2$. The shapes of the components are fixed to the values determined in Section 4.6 but the yields, $N(Dh^{\pm})^{\rm sig,\ bkg}_{i,t}$, of the three components are free to vary independently in each region, labelled i. The shapes are assumed to be the same for different Dalitz regions and charges but are different for different K^0_S candidate types, labelled by the index $t =$ LL, DD, as described in Section 4.6. The log-likelihood is

$$\log\mathcal{L}_{D\pi^{\pm}} = \sum_{t=\{LL,DD\}} \sum_{i=-N_{\rm bins}}^{N_{\rm bins}} \sum_{k=1}^{\mathcal{N}_{D\pi^{\pm}\ {\rm cands,\ bin}\ i}} \log\left(N(D\pi^{\pm})^{\rm sig}_{i,t}\mathcal{S}(m)^{D\pi}_t + \sum_{j=1}^{2} N(D\pi^{\pm})^{\rm bkg}_{i,t,j}\mathcal{B}(m)^{D\pi}_{t,j} \right), \tag{5.2}$$

where $N_{\rm bins}$ is eight for $K^0_S\pi^+\pi^-$ and two for $K^0_S K^+ K^-$. The value of invariant mass, m, is different for each candidate, labelled by k, in the sample. It should be noted that the total number of candidates, $\mathcal{N}_{D\pi^{\pm}\ {\rm cands,\ bin}\ i}$, is distinct from the component yields, $N(D\pi^{\pm})^{\rm sig}_{i,t}$ and $N(D\pi^{\pm})^{\rm bkg}_{i,t,j}$.

The log-likelihood for the $B^{\pm} \to \tilde{D}K^{\pm}$ sample is very similar in form, differing mainly by the addition of a third background component corresponding to $B^{\pm} \to \tilde{D}\pi^{\pm}$ candidates misidentified as $B^{\pm} \to \tilde{D}K^{\pm}$:

$$\log \mathcal{L}_{DK^{\pm}} = \sum_{t=\{LL,DD\}} \sum_{i=-N_{\text{bins}}}^{N_{\text{bins}}} \sum_{k=1}^{\mathcal{N}_{DK^{\pm}\text{ cands, bin } i}} \log \left(N(DK^{\pm})^{\text{sig}}_{i,t} \mathcal{S}(m)^{DK}_{t} + \sum_{j=1}^{3} N(DK^{\pm})^{\text{bkg}}_{i,t,j} \mathcal{B}(m)^{DK}_{t,j} \right). \tag{5.3}$$

In the $B^{\pm} \to \tilde{D}K^{\pm}$ case, however, the signal yields are not allowed to vary independently but are instead related to a total $B \to \tilde{D}K$ signal yield for each charge by

$$\begin{aligned} N(DK)^{B^- \text{ sig}}_{\pm i,t} &= N(DK^-)^{\text{sig, tot}} \\ &\quad \times \left(\epsilon^{B^-}_{i,t} h^-_t [K_{\pm i} + (x_-^2 + y_-^2) K_{\mp i} + 2\sqrt{K_i K_{-i}} (x_- c_{\pm i} \pm y_- s_{\pm i})] \right), \text{ and} \\ N(DK)^{B^+ \text{ sig}}_{\pm i,t} &= N(DK^+)^{\text{sig, tot}} \\ &\quad \times \left(\epsilon^{B^+}_{i,t} h^+_t [(x_+^2 + y_+^2) K_{\pm i} + K_{\mp i} + 2\sqrt{K_i K_{-i}} (x_+ c_{\pm i} \mp y_+ s_{\pm i})] \right), \end{aligned} \tag{5.4}$$

where the symbols $K_i, c_i, s_i, x_{\pm}$ and $y_{\pm}$ have been defined previously and the two new symbols for efficiency, $\epsilon^{B^{\pm}}$, and normalisation, h, are now detailed. The variation of the efficiency with which candidates are detected, reconstructed and selected depending upon position in the Dalitz plot is determined for the $\tilde{D}K$ sample by comparing the observed distribution of $\tilde{D}\pi$ candidates in the Dalitz plot with that expected for a flavour-tagged D^0 distribution. This assumes that the $\tilde{D}\pi$ system exhibits no interference between the D^0 and $\bar{D}^0$ amplitudes so that $B^- \to [K^0_S h^+ h^-]_D \pi^-$ candidates are distributed in the same way as a $D^0 \to K^0_S h^+ h^-$ decay and $B^+ \to [K^0_S h^+ h^-]_D \pi^+$ candidates are distributed in the same way as the corresponding $\bar{D}^0$ decay. The efficiency in bin $+i$ is assumed to be the same as that in the opposing bin $-i$:

$$\epsilon^{B^{\pm}}_{i,t} = \frac{\left(N(D\pi^{\pm})^{\text{sig}}_{i,t} + N(D\pi^{\pm})^{\text{sig}}_{-i,t} \right)}{(K_i + K_{-i})}. \tag{5.5}$$

It is only important to have information about the variation of the efficiency between regions

in the Dalitz plot, as is determined in this equation. The absolute efficiency is not required since it cancels in the normalisation, $h^{\pm}$. Defining the efficiency in this way, separately for B^+ and B^-, avoids the need to correct the efficiencies for pion detection asymmetries in the $\tilde{D}\pi^{\pm}$ sample.

The normalisation factors are defined as

$$h_t^{\pm} = \frac{1}{\sum_{i=-N_{\rm bins}}^{N_{\rm bins}} f_{i,t}^{\pm}}, \tag{5.6}$$

where

$$\begin{aligned} f_{\pm i,t}^{-} &= \epsilon_{i,t}^{B^-}[K_{\pm i} + (x_-^2 + y_-^2)K_{\mp i} + 2\sqrt{K_i K_{-i}}(x_- c_{\pm i} \pm y_- s_{\pm i})], \text{ and} \\ f_{\pm i,t}^{+} &= \epsilon_{i,t}^{B^+}[(x_+^2 + y_+^2)K_{\pm i} + K_{\mp i} + 2\sqrt{K_i K_{-i}}(x_+ c_{\pm i} \mp y_+ s_{\pm i,t})]. \end{aligned} \tag{5.7}$$

Normalising to the total number of $B^{\pm} \to \tilde{D}K^{\pm}$ candidates separately for DK^+ and DK^- makes the analysis insensitive to any global asymmetry between the two, and thus avoids the need to correct for production or detection charge asymmetries.

5.2.1 Discarding the overall charge asymmetry

The procedure by which the normalisation is separated for DK^+ and DK^- results in removing any sensitivity to the global charge asymmetry, but this asymmetry carries very little information given the small size of the current data set. By summing the $B^{\pm} \to \tilde{D}K^{\pm}$ yields in Equation 1.47 over all Dalitz regions, the totals of B^+ and B^- signal candidates are found to be

$$\begin{aligned} N^{\rm tot}_{B^- \to [K^0_S \pi^+ \pi^-]K^-} &\propto 1 + r_B^2 + 4\sum_{i=1}^{N_{\rm bins}} \sqrt{K_i K_{-i}} c_i x_-, \text{ and} \\ N^{\rm tot}_{B^+ \to [K^0_S \pi^+ \pi^-]K^+} &\propto 1 + r_B^2 + 4\sum_{i=1}^{N_{\rm bins}} \sqrt{K_i K_{-i}} c_i x_+, \end{aligned} \tag{5.8}$$

and the global charge asymmetry is then

$$\mathcal{A}_{\text{global}} = \frac{(x_+ - x_-) \times 2 \sum_{i=1}^{N_{\text{bins}}} \sqrt{K_i K_{-i}} c_i}{1 + r_B^2 + (x_+ + x_-) \times 2 \sum_{i=1}^{N_{\text{bins}}} \sqrt{K_i K_{-i}} c_i}. \tag{5.9}$$

For the usual values of K_i and c_i (Tables 4.1 and 4.3), and values for r_B, δ_B and γ of 0.1, 130° and 70° respectively [16], the global asymmetry is estimated in the absence of any production asymmetry to be ≈ 0.01 for $K^0_S \pi^+ \pi^-$ and ≈ 0.02 for $K^0_S K^+ K^-$. This corresponds to a difference of seven $K^0_S \pi^+ \pi^-$ candidates and two for $K^0_S K^+ K^-$, which are very small numbers compared to the sizes of the statistical uncertainties on the yields found in the current data sample. The effect can be neglected without significant loss in sensitivity.

5.3 Bias on fit results for the $x_{\pm}$ and $y_{\pm}$ observables

Biases in the fit results for $x_{\pm}$ and $y_{\pm}$ can occur when fitting such a small data set with a complicated likelihood function in many variables. A combination of limits in the allowed ranges of fit parameters and the sometimes subtle variations in the likelihood function can result in systematic offsets in the fit parameters. Such biases usually diminish as statistics increase. In order to test for a bias in the measurements of $x_{\pm}$ and $y_{\pm}$, large numbers of simulated experiments are undertaken where candidates are generated in each Dalitz region. The invariant mass spectra are then fitted using the same procedure as used in the fit to data.

5.3.1 Generator configuration

The signal yields generated in each region are determined according to Equation 5.4, taking the values of γ, δ_B and r_B to be 70°, 130° and 0.1 respectively (i.e. $x_+ = -0.094$, $x_- = 0.050$, $y_+ = -0.034$ and $y_- = 0.087$). The partially reconstructed background is given the same Dalitz distribution as the $B^{\pm} \to \tilde{D}\pi^{\pm}$ candidates and the $(B^{\pm} \to \tilde{D}\pi^{\pm}) \to (B^{\pm} \to \tilde{D}K^{\pm})$ misidentified background yield in each region is determined from the $B^{\pm} \to \tilde{D}\pi^{\pm}$ yields and

the known PID efficiencies. The distribution of the combinatorial background is assigned after studying the characteristics of this background component in data using the unphysical reconstruction of like-sign pions in the D decay (i.e. reconstructing '$[K^0_S\pi^{\pm}\pi^{\pm}]h^{\pm}$'). Around half the combinatorial background is composed of events containing a real $D^0 \to K^0_S\pi^+\pi^-$ or $\bar{D}^0 \to K^0_S\pi^+\pi^-$ decay and, therefore, 25% of this combinatorial background is distributed around the Dalitz plot according to the distribution of a D^0 and 25% according to that of a $\bar{D}^0$. The remaining combinatorial background, which does not contain a real D^0, is distributed uniformly across the Dalitz plot in the generated samples.

The efficiency applied to the candidates is determined in each region by considering simulated $B^{\pm} \to \tilde{D}K^{\pm}$ decays, passed through the standard reconstruction and selection. These are generated without any intermediate resonances, so the variation across the Dalitz plot is proportional to the acceptance.

5.3.2 Fitting

The generated samples are fitted using the same procedure as applied in the fit to data. The fit has no access to the efficiencies inserted in the generation or to the means by which the backgrounds are distributed.

The bias is determined by repeating the generation and fitting process many times and determining the displacement of the mean values of the fitted parameters from their generated values. Sufficiently large numbers of simulated experiments are carried out so that the bias uncertainty is only around 0.001 in the $x_{\pm}$,$y_{\pm}$ parameters. The biases are reported in Table 5.1.

Table 5.1: Fitter biases on the $x_{\pm}$ and $y_{\pm}$ observables.

	$\Delta(x_+)$	$\Delta(x_-)$	$\Delta(y_+)$	$\Delta(y_-)$
$K^0_S\pi^+\pi^-$ only	-0.003	-0.003	-0.013	-0.005
Adding $K^0_S K^+ K^-$	-0.003	-0.002	-0.010	-0.002

The variation of the biases for different values of γ, r_B and δ_B used in the signal candidate

generation is taken as a systematic uncertainty arising from this correction procedure. This uncertainty is largest for the y_+ observable whose central value is very small. This reduces considerably when the relevant $x_{\pm}, y_{\pm}$ central value is large. In the case that the central value is large, the spread of determined bias corrections, depending on the input values of γ, r_B and δ_B, is reduced. The pull distributions for each of the parameters have a width consistent with unity, indicating that the uncertainties determined on each are an accurate measure of the observed distribution of the fitted values from all the simulated experiments.

5.4 Results of fit to data

5.4.1 Fit procedure

The fit to data contains two steps. In the first step, the fit is performed and the fitted yields of combinatorial and partially reconstructed backgrounds which are less than 0.1 are noted. In the second step, the fit is repeated with these yields fixed to zero. The fit is applied first to the $K^0_S \pi^+ \pi^-$ sample alone and then with the $K^0_S K^+ K^-$ data added and in each case the bias determined previously is used to correct the measurements of $x_{\pm}$ and $y_{\pm}$.

5.4.2 Fit results

The results are given in Table 5.2 where only the statistical uncertainties on each parameter are given. The only non-zero correlations in each case are between the x_+,y_+ or x_-,y_- pairs of parameters. The uncertainties most reduced by the addition of the $K^0_S K^+ K^-$ data are those for x_+ and x_-, as expected given the low values of s_i in the $K^0_S K^+ K^-$ final state which reduce the sensitivity to the $y_{\pm}$ parameters.

The results for the data sample before and after the $K^0_S K^+ K^-$ data are added are compatible. Since the low $K^0_S K^+ K^-$ sample size means that it is impossible to apply the fit to that data alone, the compatibility is verified by first calculating the difference in the central values for the $x_{\pm}$ and $y_{\pm}$ parameters before and after the addition of the $K^0_S K^+ K^-$ data.

This difference is then compared to the uncorrelated uncertainty determined by subtracting in quadrature the statistical uncertainty after addition of the $K^0_S K^+ K^-$ data from that found before addition of the $K^0_S K^+ K^-$ sample. For all but the y_+ parameter, this uncertainty is larger than the difference in each central value and thus accounts for it.

To account for the difference in the y_+ central values, it is necessary to consider the systematic uncertainties on the parameter. Considering the uncertainty arising from the errors on the CLEO inputs (see Section 5.5.1) is more than sufficient to explain the difference. Subtracting the systematic uncertainty arising from this source in quadrature for the $K^0_S \pi^+ \pi^-$-only fit and that including the $K^0_S K^+ K^-$ data results in an uncertainty which is larger than the difference in the y_+ central values, as required to explain it. The results with and without the addition of the $K^0_S K^+ K^-$ data are therefore compatible.

Table 5.2: Fit results for $K^0_S \pi^+ \pi^-$ data alone and when combined with $K^0_S K^+ K^-$ data.

	$K^0_S \pi^+ \pi^-$ alone	$K^0_S \pi^+ \pi^-$ and $K^0_S K^+ K^-$
x_+	-0.086 ± 0.054	-0.103 ± 0.045
x_-	0.016 ± 0.048	0.001 ± 0.043
y_+	-0.003 ± 0.037	-0.009 ± 0.037
y_-	0.014 ± 0.054	0.027 ± 0.052
$\rho(x_+, y_+)$	0.169	0.173
$\rho(x_-, y_-)$	-0.118	-0.106

A summary of the fitted signal yields is given in Table 5.3. The projections of the fit onto the $B^{\pm}$ invariant mass spectra in each of the Dalitz regions for the $K^0_S \pi^+ \pi^-$ and $K^0_S K^+ K^-$ data are given in Appendix A, in Figures A.1 to A.4 for $K^0_S \pi^+ \pi^-$ and Figures A.5 and A.6 for $K^0_S K^+ K^-$. The projections illustrate the low statistics in some regions of the D^0 Dalitz plot but this is not problematic for the fit because the shapes of the PDFs are fixed in every region; only the yields of the components are allowed to vary in each Dalitz region.

Likelihood contours for the results of the fit to $K^0_S \pi^+ \pi^-$ and $K^0_S K^+ K^-$ data together are given in Figure 5.3, produced for (x_+,y_+) by fixing the values of x_+ and y_+ then refitting for x_-, y_- and the other parameters and recording the likelihood. For that in (x_-,y_-), the refit is performed varying x_+, y_+ and the other parameters. With reference to Figure 4.4, the value of r_B can be estimated from this likelihood plot and it is immediately clear that, for

the B^- results, the central value of r_B is low compared to the expectation of 0.1, although the measurement uncertainties are significant. The value of γ estimated from Figure 5.3 is approximately 45°. The uncertainty on this value is large, and is considered in more detail at the end of this chapter in Section 5.6.

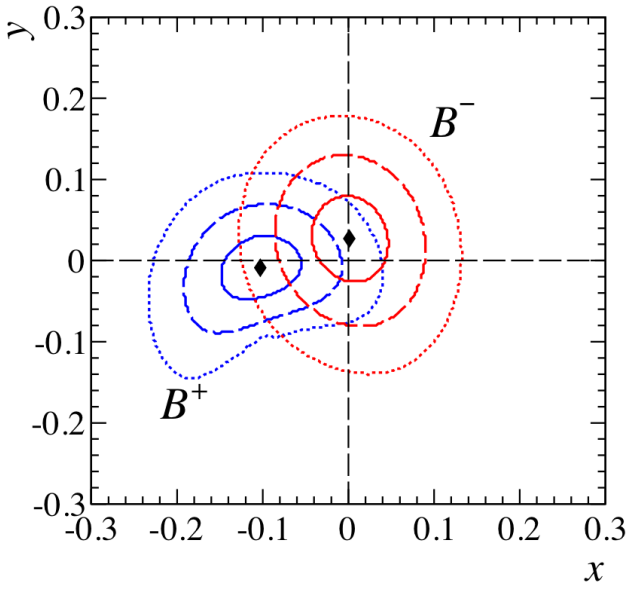

Figure 5.3: Likelihood scans with the one, two and three standard deviation contours shown for (x_+,y_+) and (x_-,y_-), superimposed on the same plane.

Table 5.3: Fit yields of signal candidates for combined $K^0_S\pi^+\pi^-$ and $K^0_S K^+ K^-$ data

Variable	Value
$K^0_S\pi^+\pi^-$ sample	
$n(DK^+)_{LL}$	123.8±12.1
$n(DK^-)_{LL}$	114.1±11.8
$n(DK^+)_{DD}$	235.5±16.9
$n(DK^-)_{DD}$	225.9±16.6
$K^0_S K^+ K^-$ sample	
$n(DK^+)_{LL}$	22.0±5.1
$n(DK^-)_{LL}$	20.1±4.9
$n(DK^+)_{DD}$	37.3±6.6
$n(DK^-)_{DD}$	32.3±6.2

Having carried out the fit to the data in the different Dalitz regions to extract $x_\pm$ and $y_\pm$, it is of interest to assess how well that fit in fact describes the $B^{\pm} \to \tilde{D}K^{\pm}$ yields in the Dalitz regions. This is achieved by repeating the Dalitz fit but allowing the yields of $B^+ \to \tilde{D}K^+$ and $B^- \to \tilde{D}K^-$ to float in each Dalitz region and for each K^0_S type, rather than

dictating that the signal yields in the different regions must be related back to the $x_{\pm}$ and $y_{\pm}$ observables. The yields given the measurements of $x_{\pm}$ and $y_{\pm}$ and the independently-floated yields are compared for the sum and difference of the B^+ and B^- yields in Figure 5.4. To enable the B^+ and B^- results to be conveniently shown on the same plot, an effective bin number is defined which is the same as the usual bin number for B^+ candidates but is -1 times the bin number for B^- candidates. One way in which CP violation is manifested is by producing differences between the B^+ and B^- yields in each effective bin. For this plot of $N_{B^+ - B^-}$, the prediction for the zero CP violation case is added as a dashed line. This band is not centred on values of zero in every bin because of the different efficiency corrections for B^+ and B^- yields in each Dalitz region. The uncertainty on the zero CP violation prediction corresponds to the statistical uncertainty on the different B^+ and B^- efficiency corrections, determined from $B^{\pm} \to \tilde{D}\pi^{\pm}$ data as usual, in each bin.

The yields determined from the fit to the $x_{\pm}$ and $y_{\pm}$ observables are seen to match the independently-fitted yields. For the plot of $N_{B^+ + B^-}$ the agreement is such that the χ^2 probability is 10%. For the plot of $N_{B^+ - B^-}$, the χ^2 probability is 34%. The comparison is worse when the independently-fitted values for $N_{B^+ - B^-}$ are compared to those expected for no CP violation, yielding a χ^2 probability of 16%. This demonstrates that the results are more consistent with the CP violating case, though the significance of the comparison is clearly statistically limited.

5.5 Systematic uncertainties

The method for obtaining each systematic uncertainty on the $x_{\pm}$ and $y_{\pm}$ observables is now described and, to allow for comparison, the individual systematic uncertainties determined on each observable are given together at the end of this section in Table 5.19.

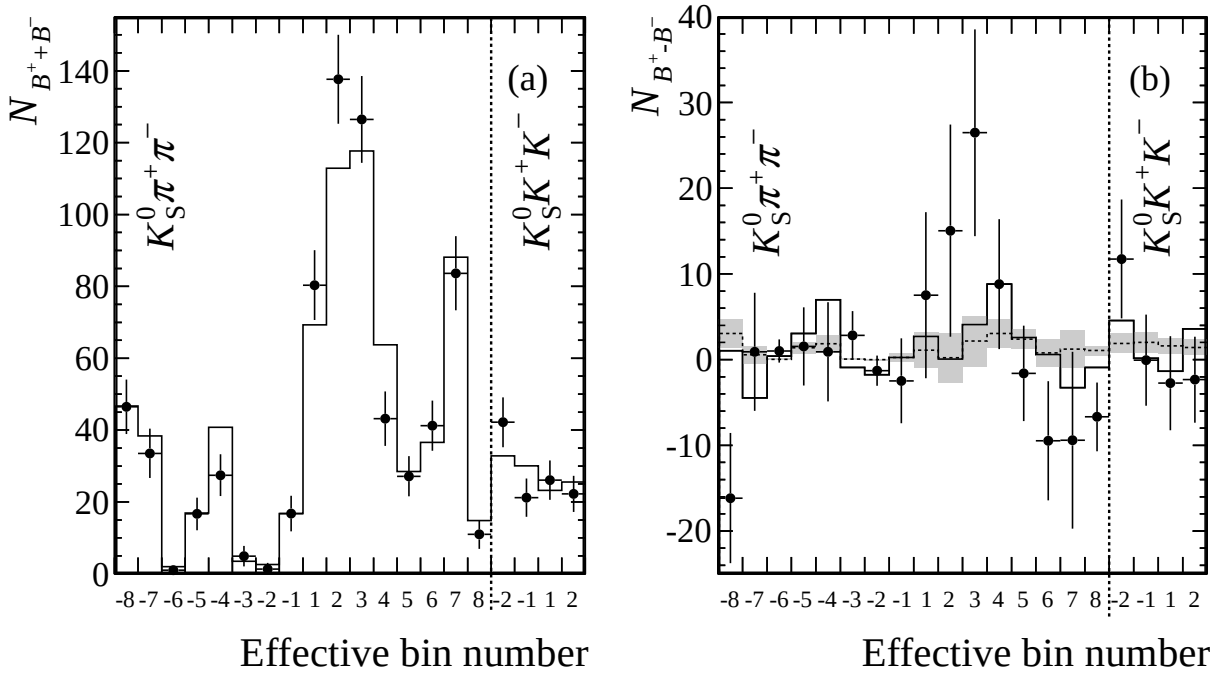

Figure 5.4: Comparison between the yields in each Dalitz region resulting from the fit for the $x_{\pm}$ and $y_{\pm}$ parameters (solid line) or from a fit for the $B^{\pm} \to \tilde{D}K^{\pm}$ yields independently in each Dalitz region (black points with errors). In (a), the sum of the B^+ yields in region i and the B^- yields in region $-i$ are given. In (b), the difference is shown and the predicted difference in the case of zero CP violation is added as a dashed line for comparison. The uncertainty on this predicted value is given by the grey band, and arises because of the statistical uncertainties on the applied efficiency correction (different for B^+ and B^-).

5.5.1 CLEO-c input parameters

The values of c_i and s_i measured by the CLEO collaboration multiply the $x_{\pm}$ and $y_{\pm}$ parameters in the equations determining the Dalitz distribution of $B^{\pm} \to \tilde{D}K^{\pm}$ candidates. The uncertainties on the c_i and s_i parameters propagate through to uncertainties on $x_{\pm}$ and $y_{\pm}$. The magnitudes of the c_i, s_i uncertainties are given in Table 4.3 and the correlations between the c_i, s_i measurements can be found in the additional material in [91].

In order to account for the correlations between the measurements of c_i and s_i, a Cholesky decomposition is used, effectively a square root [97] of the correlation matrix of the c_i, s_i parameters. Next, a vector is randomly generated according to the matrix extracted from the Cholesky decomposition. Finally, each element of this vector is then multiplied by the uncertainty on the appropriate parameter and used to displace the value of the c_i and s_i parameters in a new fit to the binned data. This process of displacing the c_i and s_i parameters and then refitting is repeated approximately five hundred times and the root mean square of the distribution for the fitted values of each observable is taken as the systematic uncertainty given in Table 5.4.

Table 5.4: Systematic uncertainties arising from the CLEO inputs.

	$\sigma(x_+)$	$\sigma(x_-)$	$\sigma(y_+)$	$\sigma(y_-)$
$K^0_S\pi^+\pi^-$ only	0.016	0.008	0.027	0.024
Adding $K^0_S K^+ K^-$	0.014	0.006	0.030	0.023

The systematic uncertainties are significant; between 20% and 75% of the statistical uncertainties on the observables. The uncertainty incurred on the $y_{\pm}$ observables is larger than that for $x_{\pm}$ because the uncertainties on the measurements of the s_i parameters, which multiply $y_{\pm}$, are larger than those on the c_i parameters, which multiply $x_{\pm}$.

The dependence of this systematic uncertainty upon the size of the sample is significant and this is understood by considering the statistical dependence of an expression for the variation of the observables, generically labelled x or y, with the c_i and s_i parameters. For illustration, consider the quantity $\frac{dx}{dc}$, which can be determined from the overall log-

likelihood, $\mathcal{L}$, using the fact that

$$\frac{dx}{dc} \propto \frac{\partial^2 \mathcal{L}}{\partial x \partial c} \left[\frac{\partial^2 \mathcal{L}}{\partial x^2} \right]^{-1}. \tag{5.10}$$

The likelihood, $\mathcal{L}$, can be written as

$$\mathcal{L} = \sum_i \frac{(N_i - \bar{N}_i)^2}{2N_i}. \tag{5.11}$$

In the equation above, N_i are the observed yields in each bin and $\bar{N}_i$ are the expected yields, written using quantities which have been defined before:

$$\bar{N}_i = h[K_i + (x^2 + y^2)K_{-i} + 2\sqrt{K_i K_{-i}}(xc_i - ys_i)]. \tag{5.12}$$

This gives

$$\frac{dx}{dc} \propto h\sigma(x)^2 \left[\frac{N_i - \bar{N}_i}{N_i} \right] + \mathcal{O}(x, y...), \tag{5.13}$$

where $\sigma(x)$ is the measured uncertainty on x. The product of h and $\sigma(x)$ is independent of N_i so the sample-size dependence arises from the second factor where statistical fluctuations will affect the size of the systematic. For a very large sample, the statistical effect will be minimised and the uncertainty arising from this source will instead be dominated by the systematic difference between the measured and true values of c_i and s_i, leading to a constant value for the ratio $\frac{N_i - \bar{N}_i}{N_i}$. The size of the systematic uncertainty determined in this analysis arising from uncertainties on the c_i and s_i parameters can, therefore, be expected to fall in a future analysis of a larger data set.

5.5.2 Uncertainties on the parameters of the invariant-mass spectrum PDFs

The parameters of the PDF components used to fit the $B^{\pm}$ invariant mass spectrum in each Dalitz plot region are fixed to the values determined in the global fit. The propagation of

the uncertainties on the parameters through to the uncertainties on the $x_{\pm}$,$y_{\pm}$ observables requires that correlations between the different parameters of the various PDF components are accounted for. Using a similar method to that described for the propagation of the CLEO input uncertainties, a Cholesky decomposition is used to produce a set of random displacements, accounting for correlations between the parameters, for each of the parameters of the invariant-mass PDF. These are used to displace the fixed PDF parameters in a new fit to the binned data. This process is repeated approximately five hundred times and the root mean square of the distribution for each of the $x_{\pm}$,$y_{\pm}$ observables is taken as the systematic uncertainty given in Table 5.5. The resulting systematic uncertainties are approximately 10% of the size of the statistical uncertainties on the observables.

Table 5.5: Uncertainties arising from the propagation of the uncertainties on the mass fit PDF parameters.

	$\sigma(x_+)$	$\sigma(x_-)$	$\sigma(y_+)$	$\sigma(y_-)$
$K^0_S\pi^+\pi^-$ only	0.006	0.004	0.004	0.004
Adding $K^0_S K^+ K^-$	0.006	0.004	0.004	0.004

5.5.3 Interference effects in the decay $B^{\pm} \to \tilde{D}\pi^{\pm}$

The analysis method assumes no interference in the $B^{\pm} \to \tilde{D}\pi^{\pm}$ decay and that, therefore, the $B^{\pm} \to \tilde{D}\pi^{\pm}$ signal candidates are distributed between the Dalitz regions in the same way as a flavour-tagged sample. Under this assumption, the yield of $B^{\pm} \to \tilde{D}\pi^{\pm}$ candidates in each Dalitz region can be divided by the expected fraction of flavour tagged $K^0_S h^+ h^-$ decays in that region to determine a quantity proportional to the efficiency and then used to correct the $B^{\pm} \to \tilde{D}K^{\pm}$ yields for efficiency effects.

This assumption is disrupted, however, by the fact that interference between the $B^- \to D^0\pi^-$ and the suppressed $B^- \to \bar{D}^0\pi^-$ (or $B^+ \to D^0\pi^+$ and $B^+ \to \bar{D}^0\pi^+$) decay amplitudes is expected, albeit at a low level. The consequent systematic uncertainty on the efficiency evaluation is studied in simulated experiments. The parameters of the interference are analogous to those used in the $B^{\pm} \to \tilde{D}K^{\pm}$ case and are denoted r^{π}_B, δ^{π}_B and γ. Although

the value of δ_B^π is unknown, the value of r_B^π can be estimated with reference to the CKM matrix elements, comparing Figure 5.5 to Figure 1.3. From this, the ratio of the amplitude factors $\frac{r_B^\pi}{r_B}$ is given by

$$\frac{r_B^\pi}{r_B} \sim \frac{|V_{cd}V_{ud}|}{|V_{cs}V_{us}|} \sim \lambda^2 \sim 0.05, \tag{5.14}$$

which, assuming a value of $r_B \sim 0.1$, implies a value of $r_B^\pi \sim 0.005$. In order to be conservative, and in the light of recent measurements which indicate that the value of r_B^π may be higher [98], a value of $r_B^\pi = 0.02$ is used for this systematic study.

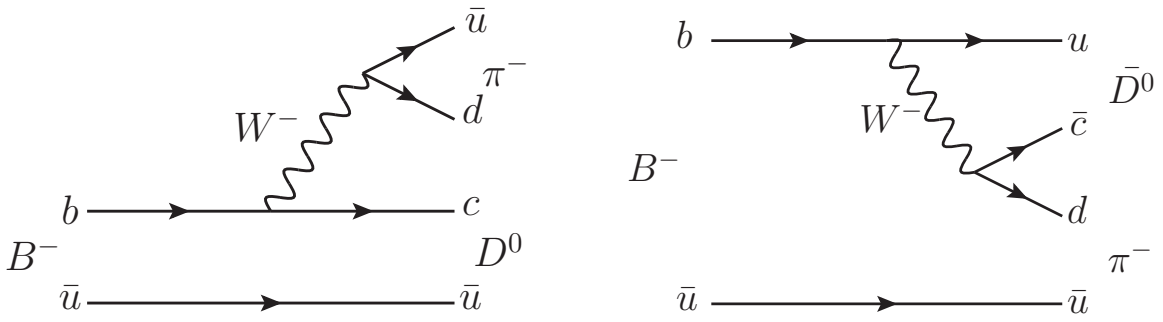

(a) Decay via D^0 (b) Decay via $\bar{D}^0$

Figure 5.5: Feynman diagrams for tree-level $B^- \to \tilde{D}\pi^-$ decays.

The yields of $B^{\pm} \to \tilde{D}\pi^{\pm}$ candidates in each Dalitz region, given values of $r_B^\pi = 0.02$ and $\gamma = 70°$, are generated for various values of δ_B^π, and the usual fit is applied where the absence of interference is assumed in the $B^{\pm} \to \tilde{D}\pi^{\pm}$ system. The largest changes in the values of $x_\pm$ and $y_\pm$ are found for a value $\delta_B^\pi = 100°$, so the process is repeated a large number of times with this value of δ_B^π and the average displacements in the values of $x_\pm$ and $y_\pm$, after correcting for intrinsic fitting bias, are taken as the systematic uncertainties. These are given in Table 5.6. The uncertainty acquired here is dependent upon the value of δ_B^π chosen and, for the choice of $\delta_B^\pi = 100°$, leads to an uncertainty on $x_\pm$ around 30% compared to that on $y_\pm$ of around 10%.

Table 5.6: Systematic uncertainties arising from the assumption of no interference in the $B^{\pm} \to \tilde{D}\pi^{\pm}$ system.

	$\sigma(x_+)$	$\sigma(x_-)$	$\sigma(y_+)$	$\sigma(y_-)$
$K^0_S\pi^+\pi^-$ only	0.015	0.012	0.002	0.005
Adding $K^0_S K^+ K^-$	0.015	0.013	0.002	0.004

5.5.4 Differences in efficiency variation across the Dalitz plot for the decays $B^{\pm} \to \tilde{D}K^{\pm}$ and $B^{\pm} \to \tilde{D}\pi^{\pm}$

The efficiency-correction method assumes that the variation of efficiency across the Dalitz plot is the same for $B^{\pm} \to \tilde{D}K^{\pm}$ candidates as for $B^{\pm} \to \tilde{D}\pi^{\pm}$ candidates. The efficiency variation for $B^{\pm} \to \tilde{D}\pi^{\pm}$ is determined by comparing the distribution of $B^{\pm} \to \tilde{D}\pi^{\pm}$ candidates between the Dalitz regions in data to that distribution expected for a flavour-tagged D^0 decay. Although the analysis is insensitive to a difference in the overall efficiency for $B^{\pm} \to \tilde{D}K^{\pm}$ and $B^{\pm} \to \tilde{D}\pi^{\pm}$ decays, and although the uncertainty attached to interference in the $B^{\pm} \to \tilde{D}\pi^{\pm}$ system has been computed, an uncertainty still remains due to the fact that the $B^{\pm} \to \tilde{D}K^{\pm}$ efficiency variation between Dalitz regions could be different to the $B^{\pm} \to \tilde{D}\pi^{\pm}$ variation, given the different bachelor hadron kinematics and consequential differences in the D, and therefore D-daughter, momenta. The effect is considered in simulated $B^{\pm} \to \tilde{D}K^{\pm}$ and $B^{\pm} \to \tilde{D}\pi^{\pm}$ samples which have been generated with a non-resonant Dalitz distribution, where the number of candidates in each Dalitz region after reconstruction and selection is divided by the number which would be expected. The distributions are shown in Figure 5.6 for $B^{\pm} \to [K^0_S\pi^+\pi^-]_D K^{\pm}$ and Figure 5.7 for $B^{\pm} \to [K^0_S\pi^+\pi^-]_D\pi^{\pm}$, where the different K^0_S types are kept separate and where the vertical axis has an arbitrary scale and minimum at zero in each case. The efficiency distributions for the long and downstream K^0_S samples exhibit the same trends, with relatively lower efficiencies in Dalitz regions 3, 4 and 5 compared to the others. These trends are similar between the $B^{\pm} \to \tilde{D}K^{\pm}$ and $B^{\pm} \to \tilde{D}\pi^{\pm}$ data; the systematic uncertainty arises from any differences between these two. The equivalent distributions for $K^0_S K^+ K^-$ are given in Figure 5.8 for $B^{\pm} \to [K^0_S K^+ K^-]_D K^{\pm}$ and Figure 5.9 for $B^{\pm} \to [K^0_S K^+ K^-]_D\pi^{\pm}$ where the sample sizes are much smaller.

To determine the systematic uncertainty on the observables arising from the differences in efficiency variation, simulated experiments are performed where the generated $B^{\pm} \to \tilde{D}K^{\pm}$ and $B^{\pm} \to \tilde{D}\pi^{\pm}$ candidates have an efficiency applied according to the results of these simulated-data studies. The generated data are then fitted in the usual fashion, with the $B^{\pm} \to \tilde{D}\pi^{\pm}$ data used to efficiency-correct the $B^{\pm} \to \tilde{D}K^{\pm}$ yields. Repeating the generation and fitting procedure many times, the mean displacement of each $x_{\pm}$ and $y_{\pm}$ observable from its generated value, after correction for the intrinsic fitting bias, is taken as the systematic uncertainty. These are given in Table 5.7 and the largest is 10% of the statistical uncertainty.

Table 5.7: Systematic uncertainties arising from different $B^{\pm} \to \tilde{D}K^{\pm}$ and $B^{\pm} \to \tilde{D}\pi^{\pm}$ efficiency variations.

	$\sigma(x_+)$	$\sigma(x_-)$	$\sigma(y_+)$	$\sigma(y_-)$
$K^0_S\pi^+\pi^-$ only	0.002	0.002	0.003	0.002
Adding $K^0_S K^+ K^-$	0.002	0.002	0.003	0.002

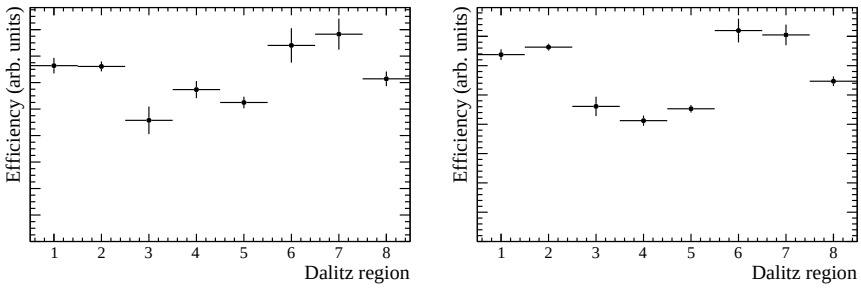

Figure 5.6: Efficiency variation for simulated $B^{\pm} \to [K^0_S\pi^+\pi^-]_D K^{\pm}$ sample for LL K^0_S tracks (left) and DD K^0_S tracks (right). The minimum of the y-axis is 0.

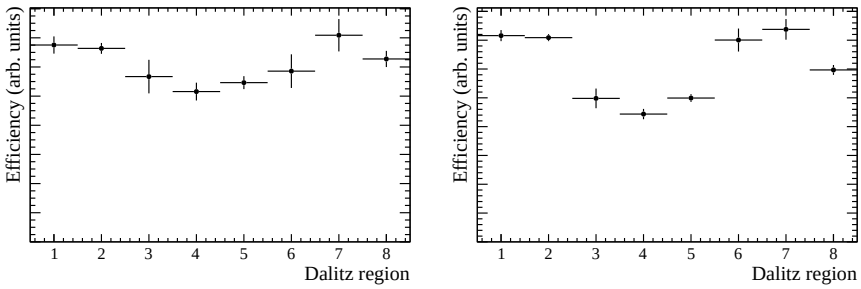

Figure 5.7: Efficiency variation for simulated $B^{\pm} \to [K^0_S\pi^+\pi^-]_D \pi^{\pm}$ sample for LL K^0_S tracks (left) and DD K^0_S tracks (right). The minimum of the y-axis is 0.

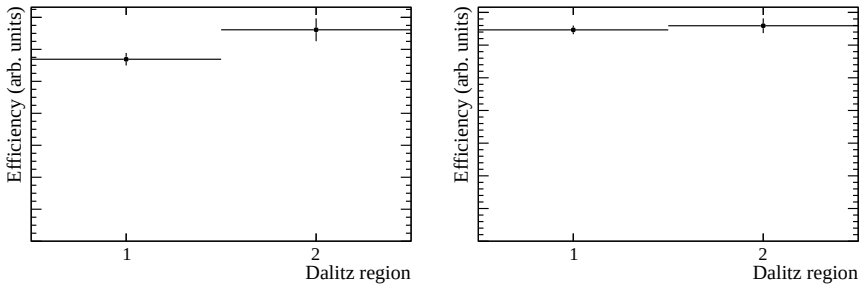

Figure 5.8: Efficiency variation for simulated $B^{\pm} \to [K^0_S K^+ K^-]_D K^{\pm}$ sample for LL K^0_S tracks (left) and DD K^0_S tracks (right). The minimum of the y-axis is 0.

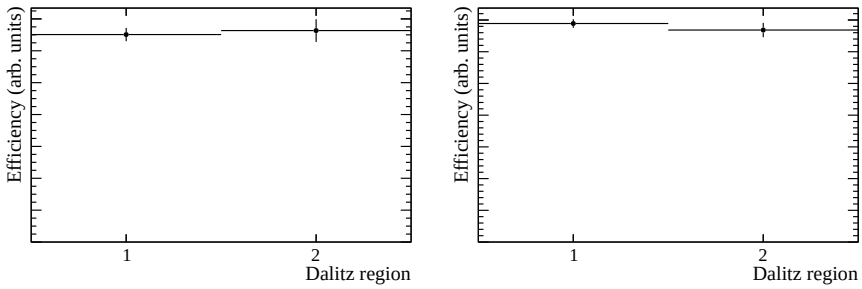

Figure 5.9: Efficiency variation for simulated $B^{\pm} \to [K^0_S K^+ K^-]_D \pi^{\pm}$ sample for LL K^0_S tracks (left) and DD K^0_S tracks (right). The minimum of the y-axis is 0.

5.5.5 Effect of efficiency variation inside Dalitz regions on the c_i and s_i parameters

A variation of the $B^{\pm} \to \tilde{D} K^{\pm}$ Dalitz acceptance within a Dalitz bin, combined with variation of the D strong phase difference in that region, changes the values of c_i and s_i which should apply in that Dalitz bin. The efficiency treatment presented here involves multiplication of the whole yield equation by an efficiency correction factor which is integrated across the whole bin, as presented in Equation 5.7. This is an appropriate way to correct the K_i and K_{-i} terms but does not correct the values of c_i and s_i. These should rather be calculated by

$$\begin{aligned} c_i &= \frac{\int_i dp \epsilon_{-,+} A_{+,-} A_{-,+} \cos(\Delta\delta_D)}{\int_i dp \epsilon_{-,+} A_{+,-} A_{-,+}}, \text{ and} \\ s_i &= \frac{\int_i dp \epsilon_{-,+} A_{+,-} A_{-,+} \sin(\Delta\delta_D)}{\int_i dp \epsilon_{-,+} A_{+,-} A_{-,+}}, \end{aligned} \tag{5.15}$$

where the variables have all been defined earlier in Chapter 1. Using the amplitude models for the $D^0 \to K^0_S h^+ h^-$ candidate distribution, referred to in Section 4.2, and an appropriate Dalitz acceptance function, the values of c_i and s_i can be calculated.

To assign a systematic uncertainty arising from the absent efficiency-correction of the c_i and s_i parameters, an efficiency variation is determined using simulated data in square Dalitz cells whose size is set to be as small as possible given the simulated statistics available. The variation in the relative efficiencies between the small Dalitz cells, shown in Figure 5.10(b) (5.11(b)) for LL (DD), can be compared by eye to the average efficiencies determined in the standard Dalitz regions in Figure 5.10(a) (Figure 5.11(a)) for LL (DD). It can be seen that in parts of the Dalitz plot, particularly near the lower-left boundary, the variation is significant on a scale comparable to the size of the standard Dalitz regions and, accordingly, the systematic effect should be evaluated. The scales on the z-axis are arbitrary and are not common to the plots in either of the figures, although the z-axis minimum (dark blue) is zero throughout. The purpose of the figures is to demonstrate the scale over which significant efficiency variation occurs and to show that significant efficiency variation is present within Dalitz regions and hence needs to be considered as a possible source of systematic bias.

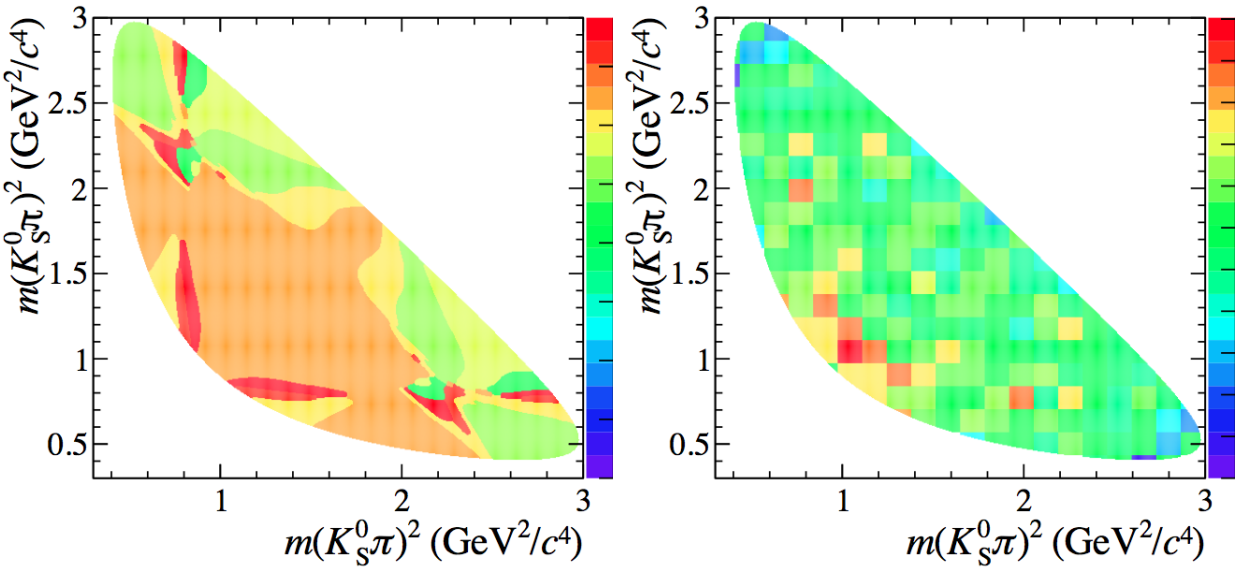

(a) Average Monte Carlo efficiency in Dalitz regions used in the analysis.

(b) Finely binned Dalitz efficiency.

Figure 5.10: Dalitz efficiencies for simulated $B^{\pm} \to \tilde{D} K^{\pm}$ candidates with LL K^0_S decays assuming symmetry under $\pi^+ \leftrightarrow \pi^-$ exchange. Arbitrary and unrelated vertical scales.

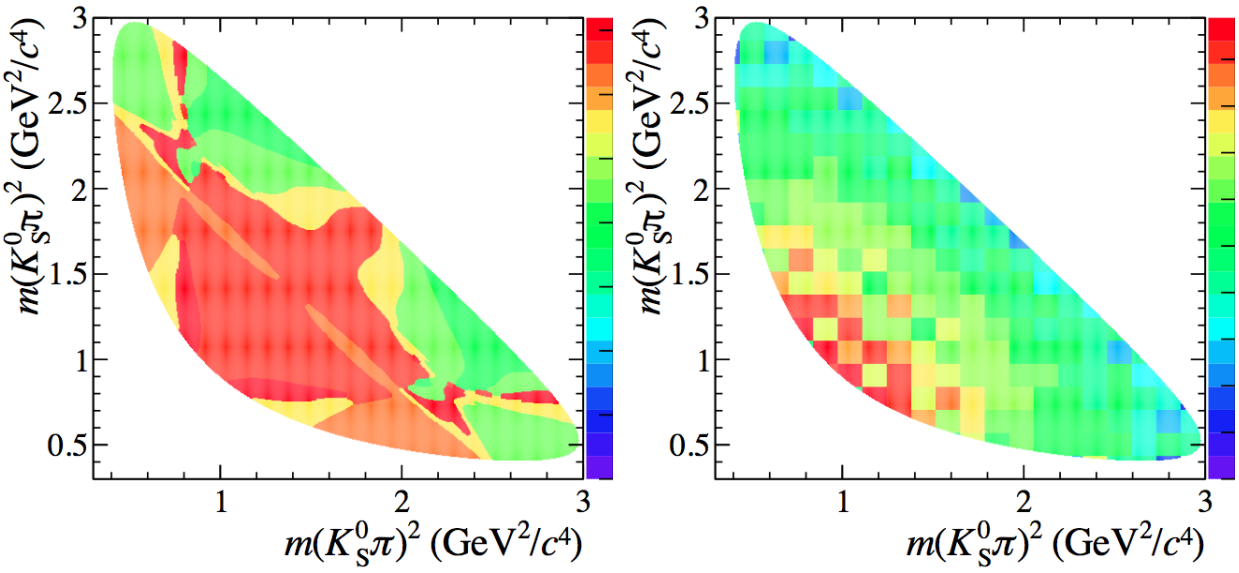

(a) Average efficiency in standard Dalitz regions.

(b) Finely binned Dalitz efficiency.

Figure 5.11: Dalitz efficiencies for simulated $B^{\pm} \to \tilde{D}K^{\pm}$ candidates with DD K^0_S decays assuming symmetry under $\pi^+ \leftrightarrow \pi^-$ exchange. Arbitrary and unrelated vertical scales.

Using the two efficiency histograms and the calculations given in Equation 5.15, the difference can be estimated between the c_i or s_i value found by assuming the efficiency to be flat in each Dalitz region and that found allowing for variation inside the bin. By repeating the fit to data many times where the values of c_i and s_i are varied according to Gaussian functions whose widths are equal to these differences, the spreads in fitted values of the $x_{\pm}$ and $y_{\pm}$ observables are determined and are taken as the systematic uncertainties, given in Table 5.8. The difference in the values of c_i and s_i found using the two efficiency determinations given in Figures 5.10 and 5.11 are less than 20% of the statistical uncertainties on the c_i and s_i inputs (see Section 4.3.2), so it is reasonable that the resulting systematic uncertainties should be smaller than those associated with the use of the CLEO inputs, considered earlier in Section 5.5.1. The uncertainties are less than 10% of the statistical uncertainties.

Table 5.8: Systematic uncertainties arising from the effect of efficiency variations within Dalitz regions on the c_i and s_i parameters.

	$\sigma(x_+)$	$\sigma(x_-)$	$\sigma(y_+)$	$\sigma(y_-)$
$K^0_S\pi^+\pi^-$ only	0.002	0.001	0.002	0.001
Adding $K^0_S K^+ K^-$	0.002	0.002	0.003	0.002

5.5.6 Effect of a tracking charge asymmetry on the efficiency determination

The data-driven efficiency determination using $B^{\pm} \to \tilde{D}\pi^{\pm}$ candidates assumes the efficiency is equal in symmetrically opposing Dalitz regions such that $\epsilon_i = \epsilon_{-i}$. This symmetry would be broken if a tracking charge asymmetry is present for pions, though such an asymmetry is expected to be small, or kaons, where the effect could be larger. Any potential effect is ameliorated by virtue of the fact that the LHCb magnet polarity is regularly switched and that roughly half the data set was collected with each polarity.

The possible systematic effect is studied by removing the assumption that $\epsilon_i = \epsilon_{-i}$ and determining the efficiency in regions on either side of the Dalitz symmetry axis separately in a new fit to the data. For the $K^0_S \pi^+ \pi^-$ data, where the data distribution is very asymmetrical in the Dalitz plot, this leads to some Dalitz regions with very low candidate populations which introduce large statistical uncertainties on the efficiencies determined compared to the standard method. These large statistical uncertainties mask the effect of removing the symmetry assumption. For the $K^0_S K^+ K^-$ data, the distribution is more symmetrical and the introduced statistical uncertainties in the low-population bins are smaller. This means that the efficiency can be determined with less vulnerability to statistical fluctuations and, consequently, any difference is more likely to be due to a tracking asymmetry effect.

The fit results are given in Table 5.9 under the standard configuration and where the assumption of Dalitz symmetry is removed in the efficiency determination for both data sets or just for the $K^0_S K^+ K^-$ data set. Since the pion tracking asymmetry is expected to be small and no statistically significant deviation is seen, the displacements in the $x_{\pm}$ and $y_{\pm}$ observables are taken from the case where the symmetrical efficiency assumption is only removed for the $K^0_S K^+ K^-$ data. It is probable that even these displacements are merely statistical, arising from the increased uncertainties on the efficiency corrections after removing the Dalitz symmetry requirement. In case they are not, the displacements, which are less than 5% of the statistical uncertainties, are taken as a conservative systematic uncertainty, given in Table 5.10.

Table 5.9: Results of fit to data where the standard assumption of symmetrical Dalitz plot efficiency is removed for the $K^0_S\pi^+\pi^-$ and $K^0_S K^+ K^-$ data combined, and for the $K^0_S K^+ K^-$ data alone.

Observable	Standard fit	Remove assumption for $K^0_S K^+ K^-$ only	Remove assumption for both (not used)
x_+	-0.105 ± 0.045	-0.105 ± 0.045	-0.110 ± 0.046
x_-	-0.001 ± 0.043	-0.001 ± 0.043	0.002 ± 0.044
y_+	-0.019 ± 0.037	-0.018 ± 0.038	-0.018 ± 0.039
y_-	0.025 ± 0.052	0.028 ± 0.052	0.022 ± 0.057

Table 5.10: Systematic uncertainties arising from the assumption of zero tracking charge asymmetry.

	$\sigma(x_+)$	$\sigma(x_-)$	$\sigma(y_+)$	$\sigma(y_-)$
$K^0_S\pi^+\pi^-$ only	–	–	–	–
Adding $K^0_S K^+ K^-$	< 0.001	< 0.001	0.001	0.003

5.5.7 Migration of candidates in the Dalitz plot

The uncertainties on the reconstructed particles' four-momenta propagate through to an uncertainty on the candidate's coordinate in the Dalitz plot. If the candidate is produced at a point suitably close to the boundary of a Dalitz region, this reconstruction error could lead to a migration between Dalitz regions. For a uniformly populated Dalitz plot, however, this effect would cancel since such migrations would occur in both directions at the same rate along each bin boundary, but if the Dalitz plot has a non-uniform structure with a densely populated region on one side of the boundary and a sparsely populated region on the other, the migration would be uneven. This would produce an effective loss or gain in efficiency for the Dalitz regions. Since the efficiency correction of the $B^{\pm} \to \tilde{D}K^{\pm}$ yields is determined from the $B^{\pm} \to \tilde{D}\pi^{\pm}$ data where this migration would also be present, the effect is accounted for, assuming the $B^{\pm} \to \tilde{D}\pi^{\pm}$ and $B^{\pm} \to \tilde{D}K^{\pm}$ Dalitz plots have the same structure. This, however, is not quite true since the interference in the $B^{\pm} \to \tilde{D}K^{\pm}$ Dalitz plot perturbs its Dalitz structure with respect to the $B^{\pm} \to \tilde{D}\pi^{\pm}$ case where less interference is expected, so the migration would not be completely identical in $B^{\pm} \to \tilde{D}K^{\pm}$ and $B^{\pm} \to \tilde{D}\pi^{\pm}$ decays. This must be accounted for.

The size of the reconstruction uncertainty is determined using simulated data. Comparing the generated and reconstructed Dalitz coordinates, a resolution of 0.004 GeV^2/c^4 is seen for LL candidates and 0.006 GeV^2/c^4 for DD candidates. The different Dalitz regions are defined according to a finely-binned two-dimensional histogram whose cell dimension is $0.0054\,\text{GeV}^2/c^4$ (see Section 4.2). Given that the reconstruction error is of a similar scale to the cell dimensions, only a fraction of the candidates in a cell adjacent to the boundary of a Dalitz region are likely to change their region assignment as a result of this migration effect. As a result, the overall systematic effect is expected to be small.

To assess the difference in $B^{\pm} \to \tilde{D}K^{\pm}$ and $B^{\pm} \to \tilde{D}\pi^{\pm}$ efficiencies, large samples of simulated candidates are generated with a Dalitz structure according to $D^0 \to K^0_S h^+ h^-$ amplitude models, assuming no interference in $B^{\pm} \to \tilde{D}\pi^{\pm}$ decays and values of r_B, γ and δ_B of 0.2, 70° and 130° respectively for $B^{\pm} \to \tilde{D}K^{\pm}$. The value of r_B used is larger than the 0.1 expected in order to ensure that the difference between the Dalitz structure for $B^{\pm} \to \tilde{D}\pi^{\pm}$ and $B^{\pm} \to \tilde{D}K^{\pm}$ is not underestimated in this systematic study. The Dalitz coordinates of the generated candidates are smeared according to the determined reconstruction uncertainty, and the efficiencies for the $B^{\pm} \to \tilde{D}K^{\pm}$ and $B^{\pm} \to \tilde{D}\pi^{\pm}$ candidates are determined in the different Dalitz bins. In no bin is the resulting efficiency difference between $B^{\pm} \to \tilde{D}K^{\pm}$ and $B^{\pm} \to \tilde{D}\pi^{\pm}$ more than 2%.

To assess the size of the systematic uncertainty on the $x_{\pm}$, $y_{\pm}$ observables, the different $\tilde{D}\pi^{\pm}$ and $\tilde{D}K^{\pm}$ efficiencies after smearing are used to generate simulated experiments, just as in Section 5.5.4. The simulated data are fitted using the standard fitting configuration, where the efficiencies for $\tilde{D}K^{\pm}$ are assumed to be the same as those determined in $\tilde{D}\pi^{\pm}$, and the mean displacement in these simulated experiments for the $x_{\pm}$, $y_{\pm}$ observables, after correction for the intrinsic fitting bias, is taken as the systematic uncertainty. The uncertainties are given in Table 5.11. As anticipated, the effect is not a large one, being less than 10% of the statistical uncertainty for each of the observables.

Table 5.11: Systematic uncertainties arising from migration effects.

	$\sigma(x_+)$	$\sigma(x_-)$	$\sigma(y_+)$	$\sigma(y_-)$
$K^0_S\pi^+\pi^-$ only	0.004	0.004	0.002	0.002
Adding $K^0_S K^+ K^-$	0.004	0.004	0.002	0.002

5.5.8 Variation of the partially reconstructed background shape with position in the Dalitz plot

The same PDF, described in Section 4.6.4, is used to describe the partially reconstructed background in the invariant mass fit in every Dalitz region. In reality, although this is not accounted for in the fit to data, the various partially reconstructed background components are distributed between the Dalitz regions differently depending on the flavour of the intermediate D meson. Given that the differing invariant mass shapes for the different components contribute to the overall shape at a different level in the various Dalitz regions, the partially reconstructed background should form a different shape in the invariant mass spectrum in each region. The various contributing backgrounds are studied using simulated samples, but these are not large enough to allow determination of a separate partially reconstructed background PDF for each Dalitz region to use in the standard fit.

The uncertainty on the $x_\pm$ and $y_\pm$ parameters incurred by fitting the changing background shape with a single partially reconstructed background shape is expected to be limited given the considerable separation between this background and the signal peak. To evaluate a systematic uncertainty, the dominant contributions to the background structure are determined, the shape of each type of background in the invariant mass spectrum is modelled and the distribution of the background in the Dalitz plot is found. This allows a study to be performed using simulated experiments where candidates are generated in each Dalitz region with a different partially reconstructed background shape according to the results of the background investigation, and then fitted in the usual configuration with a common shape to determine the effect on the $x_\pm$, $y_\pm$ parameters.

Determining significant backgrounds

A set of significant contributions to the $B^{\pm} \to \tilde{D}\pi^{\pm}$ and $B^{\pm} \to \tilde{D}K^{\pm}$ partially reconstructed backgrounds is found by applying the standard reconstruction and selection procedure to the generic cocktail sample described in Section 4.6.4, and inspecting the decay categories that survive the selection, and by considering those backgrounds which were found to be important for the related $B^{\pm} \to [h^+ h'^-]_D K^{\pm}$ analysis [24]. All the significant contributions are found to arise from decays involving a real D meson in the decay. A weighting factor is determined for each background with respect to the signal decay under consideration ($B^{\pm} \to \tilde{D}\pi^{\pm}$ or $B^{\pm} \to \tilde{D}K^{\pm}$) as follows:

$$W = \frac{\epsilon_{\rm bg}}{\epsilon_{\rm sig}} \times \frac{\mathcal{B}_{\rm bg}}{\mathcal{B}_{\rm sig}}, \tag{5.16}$$

where $\epsilon_{\rm bg}$ and $\epsilon_{\rm sig}$ are the efficiencies of the reconstruction and selection process for background and signal and $\mathcal{B}_{\rm sig}$ or $\mathcal{B}_{\rm bg}$ are the relative branching fractions in each case.

Determining the distributions in the Dalitz plot

There are four significant components in the $B^{\pm} \to \tilde{D}\pi^{\pm}$ spectrum, detailed in Table 5.12, and the invariant mass distribution of each is given in Figure 5.12(a). Other contributions are found to be at least an order of magnitude smaller than the smallest of these four, and are thus ignored. Assuming low interference between the D^0 and $\bar{D}^0$ decay routes for the $B^- \to \tilde{D}\rho^-$ and $B^- \to \tilde{D}^*\pi^-$ modes, the first three backgrounds listed in Table 5.12 should be dominated by an intermediate $\bar{D}^0$ (D^0) when reconstructing a B^- (B^+) and will therefore be distributed in the Dalitz plot in the same way as a $\bar{D}^0$ (D^0) decay. The $B^0 \to D^0\rho^0$ background will form a B^- or B^+ candidate depending upon which ρ^0 daughter is chosen by chance as the bachelor pion candidate and is therefore equally likely to be distributed as D^0 or $\bar{D}^0$. However, the $B^0 \to D^0\rho^0$ background is only around 1% of the $B^{\pm} \to \tilde{D}\pi^{\pm}$ partially reconstructed background and this D^0-like distribution in an otherwise $\bar{D}^0$-distributed background is negligible. Since all the dominant background constituents

are distributed in the same way, the assumption that the same PDF can be used in each Dalitz region is justified. No variation in the partially reconstructed background shape for $B^{\pm} \to \tilde{D}\pi^{\pm}$ decays is anticipated and in the discussion which follows, therefore, no such variation is generated.

Table 5.12: Table of the most significant partially reconstructed background sources in the $B^{\pm} \to \tilde{D}\pi^{\pm}$ spectrum with weight and distribution category given, as defined in the main text.

Mode	Weight
$B^- \to \tilde{D}^*\pi^-$	0.2493±0.0147
$B^- \to \tilde{D}\rho^-$	0.1029±0.0154
$B^0 \to D^{*+}\pi^-$	0.0437±0.0030
$B^0 \to D^0\rho^0$	0.0045±0.0008

The situation is not so straightforward for the partially reconstructed background in the $B^{\pm} \to \tilde{D}K^{\pm}$ spectrum. In this case, there are more sources of background which contribute, as detailed in Table 5.13 and as shown in Figure 5.12(b). The $B^- \to D^{*0}K^-$ component, which constitutes 41% of the total partially reconstructed background, is distributed in the Dalitz plot in the same way as $B^- \to \tilde{D}K^-$ signal (see Equations 5.4) but with $r_B^{D^*} \sim 0.14$ and $\delta_B^{D^*} \sim 300°$ [74]. The backgrounds in category 2 form 53% of the partially reconstructed background and are, for a reconstructed B^- (B^+), distributed in the same way as a flavour-tagged D^0 ($\bar{D}^0$) sample, assuming negligible interference between D^0 and $\bar{D}^0$ as appropriate. The remaining 6% of the background which appears in category 3 is, for a reconstructed B^- (B^+), distributed in the same way as $\bar{D}^0$ (D^0).

Determining PDFs in invariant mass

In order to evaluate the systematic effect, the background samples are grouped and a PDF in invariant mass is determined for each category, as shown in Figure 5.13. For categories 1 and 2, this involves a simple exponential fit to the grouped candidates whereas for category 3 the functional form is taken from the study of the $B^0_s \to \bar{D}^0 K^{*-}$ background in the related $B^{\pm} \to [h^+ h'^-]_D K^{\pm}$ analysis [24]. To evaluate the systematic uncertainty, candidates are generated in each Dalitz region using a different partially reconstructed background shape

Table 5.13: Table of most significant partially reconstructed background sources in $B^{\pm} \to \tilde{D}K^{\pm}$ spectrum with weight and distribution category given, as defined in the main text.

Mode	Weight	Distribution category
$B^- \to D^{*0}K^-$	0.2430±0.0233	1
$B^- \to D^0\rho^-$	0.1159±0.0308	2
$B^- \to D^{*0}\pi^-$	0.1133±0.0205	2
$B^0 \to D^{*+}K^-$	0.0486±0.0049	2
$B^0 \to D^{*+}\pi^-$	0.0408±0.0104	2
$B^0_s \to \bar{D}^0 K^{*-}$	0.0393±0.0124	3
$B^0 \to D^0 K^{*-}$	0.0053±0.0010	2
$B^0 \to D^0\rho^0$	0.0044±0.0013	Half 2, half 3

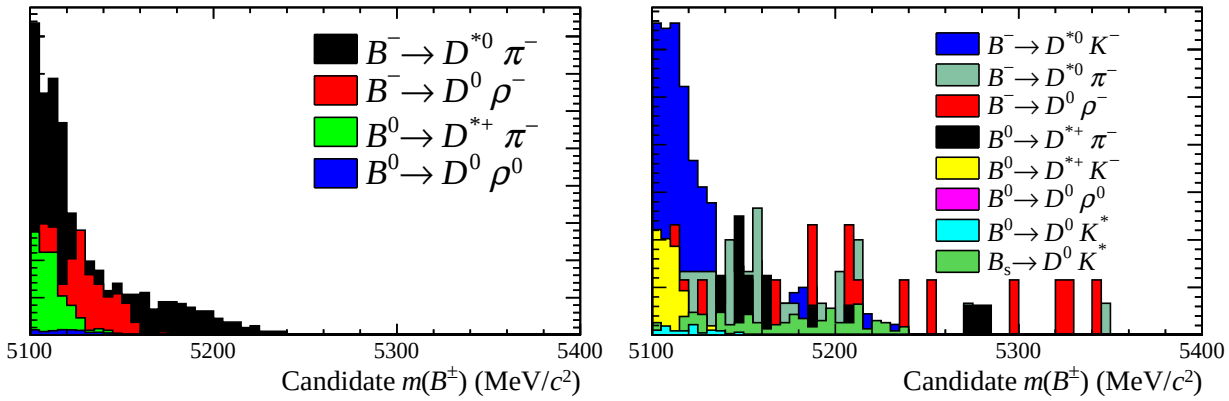

(a) $B^{\pm} \to \tilde{D}\pi^{\pm}$ (b) $B^{\pm} \to \tilde{D}K^{\pm}$

Figure 5.12: Invariant mass distributions of dominant background sources selected from simulated samples and each assigned a weight described in the main text.

in the $B^{\pm} \to \tilde{D}K^{\pm}$ spectrum. To determine the shape in each region, the candidates in each of the three background categories are divided between the Dalitz regions according to their expected weightings and the PDF shape is determined by combining the three PDFs in Figure 5.13 appropriately. The generated data are then fitted in the usual way with a single PDF for the partially reconstructed background in all the Dalitz regions. Repeating with a large number of simulated experiments, the mean displacement in the $x_{\pm}$, $y_{\pm}$ observables is taken as the systematic uncertainty given in Table 5.14, after correction for the inherent fitting bias. The small size of the uncertainty, typically around 5% of the statistical uncertainty, is reasonable given the small fraction of partially reconstructed background candidates which enter the region around the signal peak.

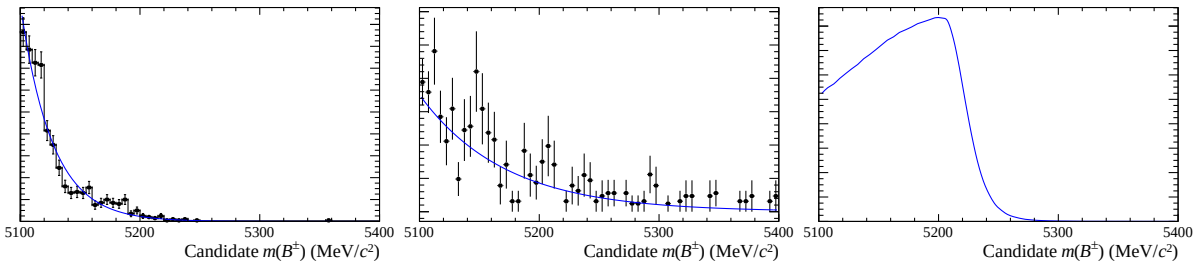

(a) Category 1 (b) Category 2 (c) Category 3

Figure 5.13: PDFs (blue line) assigned to the different partially reconstructed background categories appearing in the $B^{\pm} \to \tilde{D}K^{\pm}$ invariant mass spectrum.

Table 5.14: Systematic uncertainties arising from the uncertainty on the description of the partially reconstructed background.

	$\sigma(x_+)$	$\sigma(x_-)$	$\sigma(y_+)$	$\sigma(y_-)$
$K^0_S\pi^+\pi^-$ only	0.003	0.001	0.002	0.001
Adding $K^0_S K^+ K^-$	0.002	0.002	0.002	0.003

5.5.9 Rate of $B^{\pm} \to \tilde{D}\pi^{\pm}$ decays misidentified as $B^{\pm} \to \tilde{D}K^{\pm}$

The yield of $B^{\pm} \to \tilde{D}\pi^{\pm}$ candidates misidentified as $B^{\pm} \to \tilde{D}K^{\pm}$ is determined from the yield of $B^{\pm} \to \tilde{D}\pi^{\pm}$ signal candidates and the PID efficiencies presented in Table 4.8, which

relate simply to the misidentification rate, $\eta_{\pi \to K}$, as follows:

$$\eta_{\pi \to K} = \frac{1 - \epsilon_{\pi}}{\epsilon_{\pi}}. \tag{5.17}$$

This misidentification background forms a peaking structure in the $B^{\pm} \to \tilde{D} K^{\pm}$ invariant mass spectrum to the right of the signal peak, as seen in Figure 4.14. The shape of the misidentified background is fitted (see Section 4.6.2) and the yield is fixed as described above.

The uncertainty on the PID efficiency for pions which determines the misidentification rate is taken to be 0.2%. This is the same uncertainty as was used to evaluate the corresponding systematic uncertainty in the related $B^{\pm} \to [hh']_D K^{\pm}, (h, h' = \{\pi, K\})$ analysis [24] where the difference between the pion efficiency evaluated using the same calibration procedure as described in Section 4.6.2 and that determined by allowing the misidentification rate to vary in the fit was 0.2%. Since the smaller sample size in the present analysis prevents the same procedure being used in this case to determine the systematic uncertainty, the error on the misidentification rate determined in the $B^{\pm} \to [hh']_D K^{\pm}$ analysis is assumed.

To determine the uncertainty on the $x_{\pm}$, $y_{\pm}$ observables, studies are performed using simulated experiments where the number of candidates for the misidentification background is generated using a misidentification rate which varies in each study according to a Gaussian function. The mean of the function is the usual misidentification rate and the width is the 0.2% systematic uncertainty. The generated data are then fitted in the standard way with the misidentification rate fixed to the value determined from Table 4.8. The mean displacement of the $x_{\pm}$,$y_{\pm}$ values from their generated values, after correction for intrinsic fitting bias, is taken as the systematic uncertainty, as presented in Table 5.15. The effect of such a small variation in the misidentification rate on the signal yields measured is expected to be small, given that the fraction of such events entering the signal region is low. This is indeed found to be the case and the uncertainties on the observables are less than 5% of the statistical errors.

Table 5.15: Systematic uncertainties arising from the uncertainty on the misidentification rate.

	$\sigma(x_+)$	$\sigma(x_-)$	$\sigma(y_+)$	$\sigma(y_-)$
$K^0_S\pi^+\pi^-$ only	< 0.001	< 0.001	< 0.001	0.002
Adding $K^0_S K^+ K^-$	0.002	0.001	< 0.001	0.002

5.5.10 Variation across the Dalitz plot of the invariant-mass shape for the misidentified background from $B^{\pm} \to \tilde{D}\pi^{\pm}$ decays

The shape of the function in the $B^{\pm} \to \tilde{D}K^{\pm}$ invariant mass spectrum which models the background from misidentified $B^{\pm} \to \tilde{D}\pi^{\pm}$ decays is assumed to be the same in every Dalitz region. The shape of the misidentified background depends upon the kinematics of the bachelor particle which are correlated to those of the D^0 meson. The D^0 meson kinematics are correlated to the kinematic arrangement of its daughters and the corresponding position in the Dalitz plot. It is necessary, therefore, to estimate the effect of the position in the Dalitz plot upon the bachelor kinematics and, through this, on the shape of the misidentified background. Estimation of the effect is achieved by determining PDFs to describe the misidentified background in simulated samples over two ranges of bachelor particle momentum: 0 to 60 GeV/c and 60 to 100 GeV/c. The fractions of candidates falling into these two bins of bachelor momentum are determined for each Dalitz region, combining regions on opposite sides of the Dalitz symmetry axis. Using these fractions and the PDFs in the two momentum bins, a new misidentified background PDF is determined for each Dalitz region. Candidates are generated according to the usual fit configuration, except that these new misidentified background PDFs are used. The generated samples are fitted in the conventional way, assuming a single misidentified background PDF which is determined from the simulated data without division into bins of bachelor momentum. After running many simulated experiments, the mean displacements of the $x_{\pm}$, $y_{\pm}$ observables from their generated values, after correction for the fitting bias, are taken as the systematic uncertainties, given in Table 5.16. The fact that these uncertainties are typically less than 5% of the statistical uncertainties is reasonable, given that only a small fraction of misidentified candidates enter

the region under the signal peak.

Table 5.16: Systematic uncertainties arising from the uncertainty on the description of the misidentified $B^{\pm} \to \tilde{D}\pi^{\pm}$ background.

	$\sigma(x_+)$	$\sigma(x_-)$	$\sigma(y_+)$	$\sigma(y_-)$
$K^0_S\pi^+\pi^-$ only	0.001	0.001	< 0.001	< 0.001
Adding $K^0_S K^+ K^-$	0.003	0.001	< 0.001	0.001

5.5.11 Fixed $B^{\pm} \to [K^0_S K^+ K^-]_D K^{\pm}$ combinatorial background PDF slope

The limited statistics in the $B^{\pm}$ invariant mass spectrum for $B^{\pm} \to [K^0_S K^+ K^-]_D K^{\pm}$ decays mean that it is impossible, when performing the fit described in Section 4.6, to allow the slope of the linear combinatorial background to vary and return a meaningful shape. A flat function is therefore used. To determine the systematic uncertainty on the $x_{\pm}$, $y_{\pm}$ observables as a result of this assumption, candidates are generated in the $B^{\pm} \to [K^0_S K^+ K^-]_D K^{\pm}$ spectrum where the combinatorial background slope used for the generator PDF is fixed to a negative value found by averaging the slopes of the LL and DD fits for $B^{\pm} \to [K^0_S \pi^+ \pi^-]_D K^{\pm}$. The generated candidates are then fitted using the standard configuration where the $B^{\pm} \to [K^0_S K^+ K^-]_D K^{\pm}$ combinatorial background function is flat. After repeating this procedure many times, the mean displacement of the fitted observables from their generated values, after correction for the intrinsic fitting bias (Table 5.1), is taken as the systematic uncertainty, given in Table 5.17. The size of the systematic uncertainty is small, around 5% of the statistical uncertainty for each observable.

Table 5.17: Systematic uncertainties arising from fixing the $B^{\pm} \to [K^0_S K^+ K^-]_D K^{\pm}$ combinatorial background PDF slope.

	$\sigma(x_+)$	$\sigma(x_-)$	$\sigma(y_+)$	$\sigma(y_-)$
$K^0_S\pi^+\pi^-$ only	–	–	–	–
Adding $K^0_S K^+ K^-$	0.002	0.001	0.001	0.002

5.5.12 Summary of systematic uncertainties

The systematic uncertainties detailed in the previous sections are given in Table 5.19, both for the case where only the $K^0_S\pi^+\pi^-$ data are considered and for the case where both $K^0_S\pi^+\pi^-$ and $K^0_S K^+ K^-$ data are fitted simultaneously. The 'efficiency effects' uncertainty combines in quadrature the effects due to differing $B^{\pm} \to \tilde{D}K^{\pm}$ and $B^{\pm} \to \tilde{D}\pi^{\pm}$ efficiencies (Section 5.5.4), efficiency variations across Dalitz regions (Section 5.5.5) and the tracking charge asymmetry effect (Section 5.5.6). The bias correction uncertainty has been discussed previously in Section 5.3.

The largest errors on the measurements of the $x_{\pm}$ and $y_{\pm}$ observables are their statistical uncertainties, though the low statistical uncertainty on the measurement of y_+ does mean that the CLEO-c input errors yield an uncertainty on y_+ only a little smaller. The other CLEO-c uncertainties are all between 15% and 45% of the statistical uncertainty and are larger for the $y_{\pm}$ parameters than for the $x_{\pm}$ parameters as a consequence of there being larger uncertainties on the measurements of s_i, which multiply $y_{\pm}$, than on c_i, which multiply $x_{\pm}$.

The LHCb sources of systematic uncertainty are combined in quadrature to give a total for each observable which lies between 15% and 40% of the statistical uncertainty. The dominant LHCb source of systematic uncertainty is the assumption that interference in the $B^{\pm} \to \tilde{D}\pi^{\pm}$ system is negligible and that, for efficiency correction, the distribution of those candidates in the Dalitz plot is the same as that for the appropriate flavour-tagged D^0 or $\bar{D}^0$ sample. This uncertainty is dependent upon the choice of values for the parameters describing interference in the $B^{\pm} \to \tilde{D}\pi^{\pm}$ system, particularly in the light of recent results which suggest that r_B^{π} could be as high as 0.02, compared to the previously anticipated value of around 0.01.

Apart from the effect of interference in the $B^{\pm} \to \tilde{D}\pi^{\pm}$ system, where the uncertainty on the different observables depends greatly on the choice of input parameters, the different sources of systematic uncertainty generally produce an uncertainty on the four $x_{\pm}$, $y_{\pm}$

observables at a similar level.

The final results for the values of the $x_{\pm}$ and $y_{\pm}$ observables are given in Table 5.18.

Table 5.18: Fit results for $K^0_S\pi^+\pi^-$ data alone and when combined with $K^0_S K^+ K^-$ data. For each observable, the first uncertainty is statistical. The second and third are systematic and arise from the LHCb sources of systematic uncertainty and from the propagation of uncertainties on the CLEO-c inputs, respectively.

	$K^0_S\pi^+\pi^-$ alone	$K^0_S\pi^+\pi^-$ and $K^0_S K^+ K^-$
x_+	$-0.086 \pm 0.054 \pm 0.017 \pm 0.016$	$-0.103 \pm 0.045 \pm 0.018 \pm 0.014$
x_-	$0.016 \pm 0.048 \pm 0.014 \pm 0.008$	$0.001 \pm 0.043 \pm 0.015 \pm 0.006$
y_+	$-0.003 \pm 0.037 \pm 0.009 \pm 0.027$	$-0.009 \pm 0.037 \pm 0.008 \pm 0.030$
y_-	$0.014 \pm 0.054 \pm 0.008 \pm 0.024$	$0.027 \pm 0.052 \pm 0.009 \pm 0.023$

Table 5.19: Summary of systematic uncertainties on $x_{\pm}$, $y_{\pm}$ observables for the fit to the $K^0_S\pi^+\pi^-$ data alone and for the fit when the $K^0_S K^+ K^-$ data are added.

Source	$K^0_S\pi^+\pi^-$ data alone				$K^0_S\pi^+\pi^-$ and $K^0_S K^+ K^-$ data combined			
	x_+	x_-	y_+	y_-	x_+	x_-	y_+	y_-
Statistical	0.054	0.048	0.037	0.054	0.045	0.043	0.037	0.052
1) Parameters of the global fit	0.006	0.004	0.004	0.004	0.006	0.004	0.004	0.004
2) Ignoring interference in $B^{\pm} \to \tilde{D}\pi^{\pm}$	0.015	0.012	0.002	0.005	0.015	0.013	0.002	0.004
3) Efficiency effects	0.003	0.002	0.004	0.002	0.003	0.003	0.004	0.004
4) Bias correction	0.002	0.002	0.006	0.003	0.002	0.002	0.005	0.003
5) Migration in the Dalitz plot	0.004	0.004	0.002	0.002	0.004	0.004	0.002	0.002
6) Part. reco. bg. shape	0.003	0.001	0.002	0.001	0.002	0.002	0.002	0.003
7) $B^{\pm} \to \tilde{D}\pi^{\pm}$ mis-ID bg. shape	0.001	0.001	< 0.001	< 0.001	0.003	0.001	< 0.001	0.001
8) $B^{\pm} \to \tilde{D}\pi^{\pm}$ mis-ID rate	< 0.001	< 0.001	< 0.001	0.002	0.002	0.001	< 0.001	0.002
9) $K^0_S K^+ K^-$ combinatorial background slope	$-$	$-$	$-$	$-$	0.002	0.001	0.001	0.002
Total $(1-9)$	0.017	0.014	0.009	0.008	0.018	0.015	0.008	0.009
CLEO inputs	0.016	0.008	0.027	0.024	0.014	0.006	0.030	0.023

5.6 Extraction of γ

Values of γ, r_B and δ_B are determined using the $x_{\pm}$, $y_{\pm}$ fit results for the fit to the combined $K^0_S\pi^+\pi^-$ and $K^0_S K^+ K^-$ samples. The extraction requires that the values of $r_B^+(=\sqrt{x_+^2+y_+^2}) = r_B^-(=\sqrt{x_-^2+y_-^2}) = r_B$ and performs a fit to extract the best values of r_B, δ_B and γ in the light of this requirement. The method used to determine central values for γ, r_B and δ_B and their confidence intervals from the measurements of $x_{\pm}$ and $y_{\pm}$ is the same as that used in the $B^{\pm} \to [K^0_S\pi^+\pi^-]_D K^{\pm}$ analysis performed by the Belle collaboration [99] and the same Fortran code is used. The effects of CP violation or mixing in the charm system are ignored.

There are two stages to the extraction of values for γ, r_B and δ_B: firstly the central values must be derived from the measured values of $x_{\pm}$ and $y_{\pm}$, and secondly the confidence intervals must be determined for each parameter.

5.6.1 Derive central values for r_B, δ_B and γ

A Gaussian function is used to find the probability for *observing* a particular set of $\vec{z} \equiv (x_+, x_-, y_+, y_-)$ values given *true* values $\vec{z'} \equiv (x'_+, x'_-, y'_+, y'_-)$:

$$\mathcal{P}(\vec{z}|\vec{z'}) = \mathcal{N} \exp\left(-\frac{1}{2}\Delta\vec{z}^{\top}\mathbf{M}^{-1}\Delta\vec{z}\right). \tag{5.18}$$

where $\Delta\vec{z} = \vec{z} - \vec{z'}$ and $\mathcal{N}$ is the function normalisation. The error matrix, $\mathbf{M}$, is taken from the fit to data.

The values of r_B, δ_B and γ which best agree with the data can now be determined. For successive values of r_B, δ_B and γ, a set of $x'_{\pm}$, $y'_{\pm}$ values are computed using the usual relations. The values of r_B, δ_B and γ are then varied in order to maximise the Gaussian function in Equation 5.18. The best-fit values are found to be $\gamma = 45°$, $r_B = 0.07$ and $\delta_B = 138°$.

5.6.2 Determine confidence interval for the r_B, δ_B and γ parameters

Since the strength of the constraints which can be determined for γ and δ_B depends upon r_B, the fact that r_B is measured to be lower than the anticipated value of 0.1 leads to large uncertainties on the phases. A frequentist treatment is used to determine the confidence interval in the set of parameters $\vec{\mu}$ (r_B, δ_B, γ) corresponding to the observed values, $\vec{z}$. The confidence level, α, for a set of $x_{\pm}$, $y_{\pm}$ values in some domain $\mathcal{D}$ of the ($x_{\pm}$, $y_{\pm}$) space is defined, for a given $\vec{\mu}$, to be

$$\alpha(\mu) = \frac{\int_{\mathcal{D}(\mu)} p(\vec{z}|\vec{\mu}) dz}{\int_{\text{inf}} p(\vec{z}|\vec{\mu}) dz}. \tag{5.19}$$

The conditional probability $p(\vec{z}|\vec{\mu})$ is $\mathcal{P}(\vec{z}|\vec{z'})$ in Equation 5.18, where $\vec{z'}$ is now the set of $x_{\pm}$, $y_{\pm}$ values which corresponds to the $\vec{\mu}$ parameters. The integration domain $\mathcal{D}$ in ($x_{\pm}$, $y_{\pm}$) space is chosen according to a Feldman-Cousins ordering [100]. To determine the ordering, the quantity $\mathcal{R}$ is constructed such that

$$\mathcal{R}(z|\mu) = \frac{p(\vec{z}|\vec{\mu})}{p(\vec{z}|\vec{\mu}_{\text{best}}(z))}. \tag{5.20}$$

For a given $\vec{\mu}$, points are added to the region in ($x_{\pm}$, $y_{\pm}$) space, beginning with the highest values of $\mathcal{R}$ until the required probability coverage is reached. Having obtained the confidence interval at a given confidence level in ($x_{\pm}$, $y_{\pm}$) space for different values of $\vec{\mu}$, a set of $\vec{\mu}$ values can be determined which enclose the observed $x_{\pm}$, $y_{\pm}$ value in the determined $x_{\pm}$, $y_{\pm}$ confidence interval. Confidence intervals are determined for one standard deviation in $\vec{\mu}$ at the 20% confidence level. The confidence levels for the two and three standard deviation intervals are 74% and 97% respectively as required for a three dimensional Gaussian distribution. The method is the same as that used [101] by the Belle collaboration in their Dalitz analysis of $B^{\pm} \to [K^0_S \pi^+ \pi^-]_D K^{\pm}$ decays [99].

The central values and confidence intervals are given here, where the statistical and systematic uncertainties are combined for $x_{\pm}$ and $y_{\pm}$. Correlations between the $x_{\pm}$, $y_{\pm}$ values are accounted for in the statistical and CLEO-related systematic uncertainties, but

those in the LHCb case are taken to be uncorrelated. All correlations are found to be negligible other than those between the x_+ and y_+ parameters (0.222) and between the x_- and y_- parameters (-0.103). Figure 5.14 shows the confidence level projections onto the (γ, r_B) and (γ, δ_B) planes.

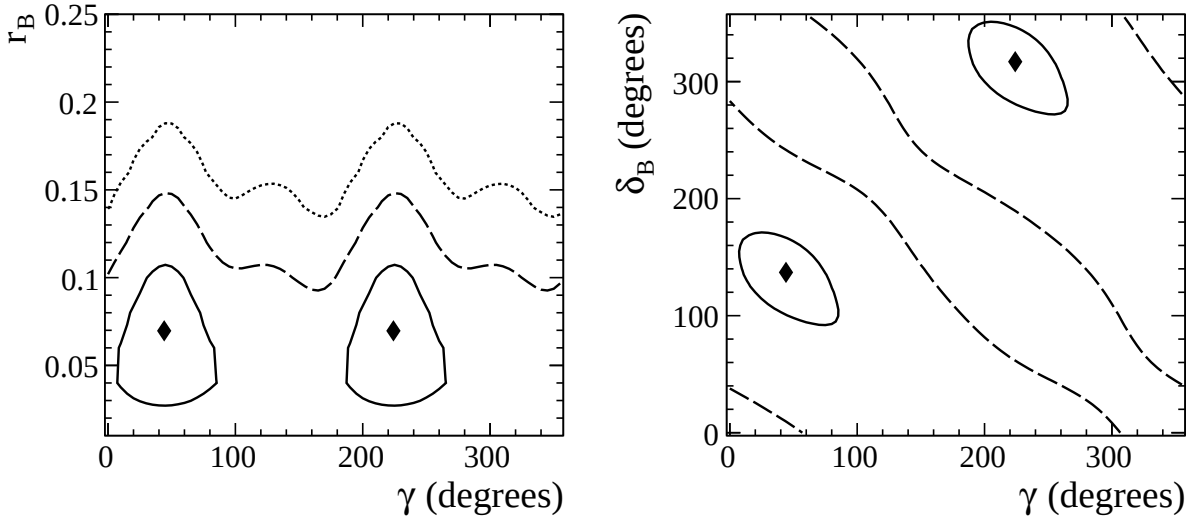

(a) (γ,r_B) (b) (γ,δ_B)

Figure 5.14: Confidence level scans at one (solid line), two (dashed line) and three (dotted line) standard deviations for the γ, r_B and δ_B parameters, where the statistical and systematic uncertainties have been combined as described in the main text. The best-fit values for γ, r_B and δ_B are marked.

The one standard deviation confidence intervals for each parameter are determined by projecting the confidence level into one dimension for each parameter and determining the value of the parameter where the projected confidence-level value is 0.2. The results found are

$$\gamma = \left(45^{+43}_{-38}\right)^{\circ},$$

$$r_B = 0.07 \pm 0.04, \text{ and}$$

$$\delta_B = \left(138^{+35}_{-46}\right)^{\circ}.$$

The relatively low precision of the measurement of γ and δ_B is, as stated, a consequence of the low value of r_B, despite the good precision with which the $x_\pm$ and $y_\pm$ observables are measured.

6 Conclusions

In conclusion, the main results of the studies presented in this thesis are summarised, their significance assessed and prospects for future developments are considered.

6.1 CLEO analysis of $D^0 \to K^0_S K^-\pi^+$ and $D^0 \to K^0_S K^+\pi^-$

Chapter 3 documents amplitude analyses carried out of $D^0 \to K^0_S K^-\pi^+$ and $D^0 \to K^0_S K^+\pi^-$ decays, using the combined CLEO III and CLEO-c data sets. After selection there were 1247 $D^0 \to K^0_S K^-\pi^+$ candidates and 760 $D^0 \to K^0_S K^+\pi^-$ candidates available for analysis, where the purity of the data sets was 90% or above. Models were developed to account for background Dalitz structure and detector acceptance effects and amplitude models were fitted to the data in the two modes, containing six resonances in the favoured mode and five in the suppressed. For each mode, two models were produced. In the first, the $K^*(892)^0 \to K^-\pi^+$ resonance was required to be included in the model given the interest from theorists in this component. In the second the resonance was not forced to be present and this yielded an improved fit quality. The models in Tables 3.7 to 3.10 are summarised in Table 6.1 for the $D^0 \to K^0_S K^-\pi^+$ mode and Table 6.2 for $D^0 \to K^0_S K^+\pi^-$. No other amplitude models have been published in these modes; only a preliminary result based on an early *BABAR* data set is in existence [102].

A measurement of the ratio of the branching fractions, $\frac{\Gamma(D^0\to K^0_S K^+\pi^-)}{\Gamma(D^0\to K^0_S K^-\pi^+)}$, for the two decays has also been made using CLEO III data. The ratio has been measured for candidates in the whole Dalitz plot and for candidates in a kinematically restricted region around the

Table 6.1: Model descriptions for fits to $D^0 \to K^0_S K^-\pi^+$ with (model 1) and without (model 2) the $K^*(892)^0 \to K^-\pi^+$ resonance.

Favoured model 1, $\chi^2/d.o.f. = 42.2/26$		Favoured model 2, $\chi^2/d.o.f. = 37.3/26$	
Component	Fraction (%)	Component	Fraction (%)
$D^0 \to K^*(892)^+(\to K^0_S,\pi^+),K^-$	67.6±6.4±3.8	$D^0 \to K^*(892)^+(\to K_S,\pi^+),K^-$	62.2± 4.8 ± 3.9
$D^0 \to K^*(892)^0(\to K^-,\pi^+),K^0_S$	1.8±1.7±0.8	$D^0 \to K^*(1410)^0(\to K^-,\pi^+),K^0_S$	32.0± 6.0 ± 19.6
$D^0 \to K^*(1410)^0(\to K^-,\pi^+),K^0_S$	23.2±3.9±4.2	$D^0 \to K^*(1680)^+(\to K_S,\pi^+),K^-$	26.1± 6.0 ± 24.0
$D^0 \to K^*(1680)^+(\to K_S,\pi^+),K^-$	22.7±4.4±5.6	$D^0 \to \rho(1700)^-(\to K_S,K^-),\pi^+$	4.4± 3.0 ± 3.7
$D^0 \to K^*_0(1430)^+(\to K_S,\pi^+),K^-$	2.5±1.2±2.0	$D^0 \to K^*_0(1430)^+(\to K_S,\pi^+),K^-$	3.1± 1.2 ± 3.1
$D^0 \to a_0(1450)^-(\to K_S,K^-),\pi^+$	1.0±0.9±0.9	$D^0 \to a_0(1450)^-(\to K_S,K^-),\pi^+$	2.3± 1.2 ± 1.5
	118.8±9.0±8.3		**130.1±10.3±31.4**

Table 6.2: Model descriptions for fits to $D^0 \to K^0_S K^+\pi^-$ with (model 1) and without (model 2) the $K^*(892)^0 \to K^-\pi^+$ resonance.

Suppressed model 1, $\chi^2/d.o.f. = 50.9/26$		Suppressed model 2, $\chi^2/d.o.f. = 46.5/26$	
Component	Fraction (%)	Component	Fraction (%)
$D^0 \to K^*(892)^-(\to K_S,\pi^-),K^+$	20.4±2.1±0.8	$D^0 \to K^*(892)^-(\to K_S,\pi^-),K^+$	21.2±2.2± 3.3
$D^0 \to K^*(892)^0(\to K^+,\pi^-),K^0_S$	3.9±1.5±0.4	$D^0 \to K^*_0(1430)^-(\to K_S,\pi^-),K^+$	31.5±6.2± 8.0
$D^0 \to K^*_0(1430)^-(\to K_S,\pi^-),K^+$	18.4±2.8±1.5	$D^0 \to \rho(1700)^+(\to K_S,K^+),\pi^-$	8.0±2.2± 3.8
$D^0 \to a_0(1450)^+(\to K_S,K^+),\pi^-$	15.8±4.1±2.1	$D^0 \to a_0(1450)^+(\to K_S,K^+),\pi^-$	5.8±2.3± 1.6
$D^0 \to \rho(1700)^+(\to K_S,K^+),\pi^-$	6.2±2.1±2.5	$D^0 \to K^*_2(1430)^0(\to K^+,\pi^-),K^0_S$	4.3±2.8± 3.4
	64.6±6.0±3.7		**70.7±7.8±10.2**

$K^*(892)^\pm \to K^0_S\pi^\pm$ resonance. The final results are

$$\frac{\Gamma(D^0 \to K^0_S K^+\pi^-)}{\Gamma(D^0 \to K^0_S K^-\pi^+)} = \begin{cases} 0.592 \pm 0.044(\text{stat.}) \pm 0.018(\text{syst.}), & \text{whole Dalitz plot; and} \\ 0.356 \pm 0.034(\text{stat.}) \pm 0.007(\text{syst.}), & K^*(892)^\pm \to K^0_S\pi^\pm \text{ window,} \end{cases}$$

where the precision is a factor of four better than that of the value obtained by taking the ratio of the branching fractions as reported in the PDG [74].

6.1.1 Consequences for tests of flavour SU(3) symmetry

The D Dalitz analysis itself is of interest in studying the extent to which D decays preserve flavour SU(3) symmetry. Assuming flavour SU(3) symmetry allows the $D \to 3P$ (where P is a pseudoscalar meson) decays $D^0 \to K^0K^-\pi^+$ and $D^0 \to \bar{K^0}K^+\pi^-$ to be related and allows prediction of the relative amplitudes and phases of $D \to PV$ (where V is a vector meson) resonances in the Dalitz plot. Predictions exist [82, 75] relating the amplitudes of vector resonances in the modes studied in this thesis and are most usefully tested against the most

significant vector resonance, the $K^*(892) \to K\pi$, present in both the $D^0 \to K^0_S K^-\pi^+$ and $D^0 \to K^0_S K^+\pi^-$ decays. Concerning the charged resonance channel, the amplitude for the $D^0 \to K^*(892)^- K^+$ process is suppressed relative to the $D^0 \to K^*(892)^+ K^-$ decay because the $W^\pm$ boson must couple to the pseudoscalar particle in the former and the vector particle in the latter. Flavour SU(3) symmetry leads one to expect that the amplitude ratio for the two processes would be equal to $\frac{|\mathcal{A}(D^0\to K^{*-}\pi^+)|}{|\mathcal{A}(D^0\to \rho^{*+}K^-)|}$ which has been measured to be 0.685 ± 0.032 [82, 75].

For the neutral resonances, the ratio of amplitudes for $D^0 \to \bar{K}^*(892)^0 K^0$ or $D^0 \to K^*(892)^0 \bar{K}^0$ to $D^0 \to K^{*+}K^-$ is predicted to be 0.138 ± 0.033 (0.307 ± 0.035) where the two results correspond to different values of the $\eta - \eta'$ mixing angle, $\theta_\eta = 19.5^\circ$ (11.7°), chosen in [82]. It is necessary to consider different values of the $\eta - \eta'$ mixing angle since, to make the predictions, results for measurements in many different processes are added to a global fit, where a number involve η resonances. The results differ, in many cases significantly, depending on the value of this poorly-known parameter of the $\eta - \eta'$ system. The measured ratios determined using the fit fractions for the resonances in Tables 3.7 and 3.9 and the ratio of branching fractions in Section 3.5, after correction for phase space effects due to the difference in masses of the K^0 and $K^\mp$ mesons, are given in Table 6.3. Theoretical predictions are also given for two values of the $\eta - \eta'$ mixing angle.

Table 6.3: Amplitude ratios for resonances in the Dalitz plots as measured in this thesis, with a comparison to the theoretical predictions achieved assuming flavour SU(3) symmetry as given in [82].

Amplitude ratio	Thesis	Theory	
	measurement	$\theta_\eta = 19.5^\circ$	$\theta_\eta = 11.7^\circ$
$\frac{D^0\to K^*(892)^- K^+}{D^0\to K^*(892)^+ K^-}$	0.423 ± 0.037	0.685 ± 0.032	0.685 ± 0.032
$\frac{D^0\to \bar{K}^*(892)^0 K^0}{D^0\to K^*(892)^+ K^-}$	$0.231^{+0.121}_{-0.231}$	0.138 ± 0.033	0.307 ± 0.035
$\frac{D^0\to K^*(892)^0 \bar{K}^0}{D^0\to K^*(892)^+ K^-}$	$0.261^{+0.051}_{-0.061}$	0.138 ± 0.033	0.307 ± 0.035

The ratio of amplitudes for the charged vector resonances measured in this thesis does not show good agreement with the predicted value, where flavour SU(3) symmetry is assumed. In the neutral $K^*(892)$ system, comparison is complicated by the low significance of the neutral

vector resonances in the amplitude models (see Tables 3.7 and 3.9) where, in fact, the models with the best fit quality (Tables 3.8 and 3.10) did not contain this neutral resonance at all. It is known that flavour SU(3) is an imperfect symmetry given the significantly larger strange quark mass compared to that of the up or down quarks and this goes some way to explain the disagreement between the observed and predicted values here.

6.1.2 Future prospects for amplitude modelling systematics

Systematic uncertainties on the fit parameters associated with the amplitude modelling procedure are of a magnitude approaching that of the statistical uncertainty. The largest sources relate to the definition of the resonance descriptions. The effect is most significant on the $D^0 \to K^0_S K^- \pi^+$ model due to the uncertainty in defining the penetration factors for the $K^*(1410)$ and $K^*(1680)$ resonances. In this case the effect is particularly large due to the pole mass of these resonances lying beyond the phase space boundary, even though their final contribution in the model is rather small. A route to avoid such significant systematic limitation in future might include restricting such cancelling combinations with very little overall significance, a procedure which may be aided by improved ability to distinguish such resonances in a larger data sample.

It may be possible to reduce the sub-leading systematic uncertainty in the analysis arising from the knowledge of the masses and widths of the different resonances. Correlations between the resonances were neglected when the uncertainty was calculated, and each resonance mass or width was varied independently. The resulting displacements were combined in quadrature. Accounting for correlations may lead to a reduced uncertainty from this source.

6.1.3 Future prospects for more sensitive tests of flavour SU(3) symmetry

Further analysis of the resonant structure in $D^0 \to K^0_S K^-\pi^+$ and $D^0 \to K^0_S K^+\pi^-$ decays could be performed by exploiting the full BaBar or Belle data sets. Alternatively, LHCb data taken in 2011 and 2012 could be used, in which around 100,000 $D^0 \to K^0_S K^-\pi^+$ candidates and 70,000 $D^0 \to K^0_S K^+\pi^-$ candidates are expected. Such studies would be less vulnerable to statistical fluctuations and thus more sensitive to resonant structure in the decays, making resolution of the $K^*(892)^0 \to K^-\pi^+$ resonance easier. These would allow for more precise tests of relative phase predictions for this resonance, by comparison to predictions made using flavour SU(3) symmetry.

Studies of these data sets would also allow for further improvement in the measurement of the ratio of the branching fractions for the two D decays, R_D, which is important to allow extraction of γ from a CP violation study in the mode $B^\pm \to \tilde{D}K^\pm$ using the $D^0 \to K^0_S K^-\pi^+$ and $D^0 \to K^0_S K^+\pi^-$ final states.

6.1.4 Future prospects for use of the $D^0 \to K^0_S K^\mp\pi^\pm$ final state for a measurement of γ in $B^\pm \to \tilde{D}K^\pm$ decays

The amplitude models will be of use in modelling the variation of the strong phase difference between D^0 and $\bar{D}^0$ decays across the Dalitz plot as an input to a $B^\pm \to \tilde{D}K^\pm$ Dalitz analysis. Such a study could already be performed using the available 2011 and 2012 LHCb data samples, but would be statistically limited given that only around 200 $B^\pm \to \tilde{D}K^\pm$ signal candidates are likely to be available in this data set.

Alternatively, a model-independent measurement could be made using a measurement of the coherence factor and average strong phase difference which have been measured in [2].

6.1.5 Future prospects for the use of $D^0 \to K^0_S K^\mp \pi^\pm$ in charm mixing and CP violation studies

LHCb recently became the first experiment to make an independent observation of charm mixing in the decay of neutral D mesons to $K^\mp\pi^\pm$ [103]. As proposed in [88], the decay of a neutral D meson to $K^0_S K^\mp \pi^\pm$ could also be used as an additional channel to study $D^0 - \bar{D}^0$ mixing and, through such a time dependent analysis, to search for indirect CP violation in the charm system.

CP violation has yet to be observed in the charm system and the singly Cabibbo suppressed $D^0 \to K^0_S K^\mp \pi^\pm$ decays provide a potential new search channel for a time-integrated, direct CP violation study. It is particularly attractive to search for CP violation in the resonant structure of the decays, either using a binned technique where CP violation is considered in regions of the Dalitz plot or by using an amplitude analysis which could distinguish differences resulting from CP violation in the resonant content of models of $D^0 \to K^0_S K^-\pi^+$ and $D^0 \to K^0_S K^+\pi^-$ decays. Further into the future, with a much larger data set, such a model-dependent analysis could be extended to a time-dependent study with sensitivity to measurement of indirect CP violation.

6.2 LHCb CP violation analysis of $B^\pm \to [K^0_S h^+ h^-]_D K^\pm$ decays

Chapters 4 and 5 document an analysis of CP violation in $B^\pm \to [K^0_S h^+ h^-]_D K^\pm$ decays using the $1\,\text{fb}^{-1}$ LHCb data set collected during 2011. Decays of the neutral D meson to $K^0_S\pi^+\pi^-$ and, less frequently, to $K^0_S K^+ K^-$ are used. The final sample for study has a purity greater than 90% and contains 756 ± 29 $B^\pm \to [K^0_S h^+ h^-]_D K^\pm$ candidates. The measurement of CP violation is made in terms of the observables $x_\pm = r_B \cos(\delta_B \pm \gamma)$ and $y_\pm = r_B \sin(\delta_B \pm \gamma)$ and the $K^0_S\pi^+\pi^-$ sample is first fitted alone, then with the $K^0_S K^+ K^-$ data added. The results are reproduced in Table 6.4. The likelihood contours extracted are shown in Figure 6.1, from

which it is clear that the value of r_B measured is lower than the expected value of 0.1 for the B^- sample, leading to a corresponding low sensitivity to γ.

A Feldman-Cousins statistical treatment allows the results from the fit to the combined sample to be used to determine constraints on the underlying parameters, yielding $r_B = 0.07 \pm 0.04$, $\delta_B = \left(138^{+35}_{-46}\right)^\circ$ and $\gamma = \left(45^{+43}_{-38}\right)^\circ$.

Table 6.4: Fit results for $K^0_S\pi^+\pi^-$ data alone and when combined with $K^0_S K^+K^-$ data. For each observable, the first uncertainty is statistical. The second and third are systematic and arise from the LHCb sources of systematic uncertainty and from the propagation of uncertainties on the CLEO-c inputs, respectively.

	$K^0_S\pi^+\pi^-$ alone ($\times 10^{-2}$)	$K^0_S\pi^+\pi^-$ and $K^0_S K^+K^-$ ($\times 10^{-2}$)
x_+	$-8.6 \pm 5.4 \pm 1.7 \pm 1.6$	$-10.3 \pm 4.5 \pm 1.8 \pm 1.4$
x_-	$1.6 \pm 4.8 \pm 1.4 \pm 0.8$	$0.1 \pm 4.3 \pm 1.5 \pm 0.6$
y_+	$-0.3 \pm 3.7 \pm 0.9 \pm 2.7$	$-0.9 \pm 3.7 \pm 0.8 \pm 3.0$
y_-	$1.4 \pm 5.4 \pm 0.8 \pm 2.4$	$2.7 \pm 5.2 \pm 0.9 \pm 2.3$

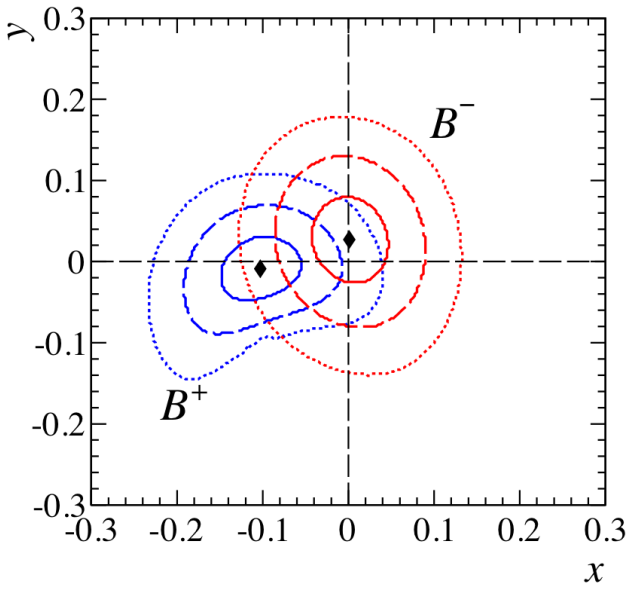

Figure 6.1: Likelihood scans for the B^+ (blue lines) and B^- (red lines) observables with the one (solid), two (dashed) and three (dotted) standard deviation contours shown, superimposed on the same plane for the analysis presented in this thesis.

This measurement of CP violation in the charged B meson system is the first LHCb $B^\pm \to \tilde{D}K^\pm$ analysis making use of a D final state containing more than two particles and is the first to place constraints on γ. Furthermore, it is the first model-independent $B^\pm \to \tilde{D}K^\pm$ analysis to make use of the $K^0_S K^+K^-$ final state. The results are compatible

with the current world average for γ using $B^{\pm} \to \tilde{D^{(*)}}K^{(*)\pm}$ decays, $\gamma = (66 \pm 12)^{\circ}$ [16]. As discussed in Chapter 1, it is of interest to compare the measurement of γ made directly, using tree-level decays, with that made indirectly through a global fit to the UT constraints. The latter gives $\gamma = (67.2^{+4.4}_{-4.6})^{\circ}$ [16], again in agreement with the measurement made in this thesis.

6.2.1 Comparison to results from the B-factories

Both the *BABAR* and Belle collaborations have reported measurements of CP violation in $B^{\pm} \to [K^0_S h^+ h^-]_D K^{\pm}$ decays.

Belle model-independent analysis [99]

The Belle collaboration has released both model-dependent and independent analyses of $B^{\pm} \to [K^0_S h^+ h^-]_D K^{\pm}$ decays, but only the latter is discussed here since the technique is very similar to that presented in this thesis. The analysis exploited the full 770 fb^{-1} Belle data set corresponding to the decays of 772 million $B\bar{B}$ pairs produced at the $\Upsilon(4S)$ resonance, and only considered $B^{\pm} \to [K^0_S \pi^+ \pi^-]_D K^{\pm}$ decays [104].

The measurements of the $x_{\pm}$ and $y_{\pm}$ observables are given in Table 6.5. The statistical uncertainties are very similar (c.f. Table 6.4) even though Belle observed 1177 ± 43 $B^{\pm} \to [K^0_S \pi^+ \pi^-]_D K^{\pm}$ candidates compared to the 756 ± 29 $B^{\pm} \to [K^0_S h^+ h^-]_D K^{\pm}$ candidates observed at LHCb. This similar statistical performance can be understood by considering the purity of the samples fitted which, for the LHCb sample, was around 87% around the signal peak but, in the Belle analysis, was considerably lower, around 60%. The statistical precision in extraction of the $x_{\pm}$ and $y_{\pm}$ parameters is enhanced by a sample with lower backgrounds.

The LHCb and Belle experimental systematic uncertainties are of a similar magnitude in both sets of results in Table 6.5.

The uncertainty arising from the CLEO-c input parameters is significantly larger on the

$y_\pm$ parameters than the $x_\pm$ parameters for the results from both experiments, an effect which results from the fact that the c_i input values which multiply $x_\pm$ are more precisely known than the s_i parameters which multiply $y_\pm$ (see Table 4.3). The systematic uncertainties on the LHCb results from this source are, in general, the same or larger than those on the Belle results. This is because the LHCb sample is smaller and because the c_i, s_i systematic uncertainty is sensitive to the sample size, as demonstrated in Section 5.5.1.

Table 6.5: Results of Belle model-independent analysis [99], where the first uncertainty is statistical, the second arises from Belle experimental systematic uncertainties and the third from the use of the CLEO-c input parameters.

	Belle measurement ($\times 10^{-2}$)
x_+	$-11.0 \pm 4.3 \pm 1.4 \pm 0.7$
x_-	$9.5 \pm 4.5 \pm 1.4 \pm 1.0$
y_+	$-5.0\ ^{+5.2}_{-5.5} \pm 1.1 \pm 1.7$
y_-	$13.7\ ^{+5.3}_{-5.7} \pm 1.5 \pm 2.3$

The likelihood contours for the Belle statistical uncertainties are given in Figure 6.2 where the axes are the same as in Figure 6.1. By comparison to Figure 6.1, the similar sensitivity between the measurements of $x_\pm$ and $y_\pm$ is evident.

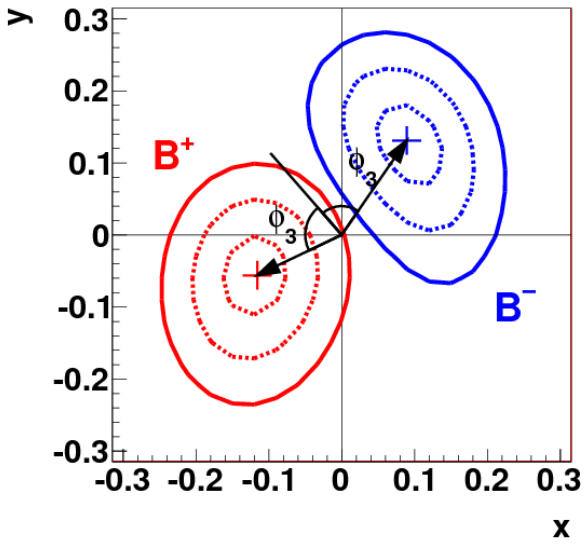

Figure 6.2: Likelihood scans for the B^+ (red lines) and B^- (blue lines) observables in the $(x_\pm, y_\pm)$ planes for the Belle model-independent $K^0_S\pi^+\pi^-$ results [104].

***BABAR* model-dependent analysis [93]**

The *BABAR* collaboration performed an analysis of CP violation in $B^{\pm} \to [K^0_S h^+ h^-]_D K^{\pm}$ decays using a model-dependent technique, where the D strong-phase information was taken from amplitude models for $D^0 \to K^0_S h^+ h^-$ decays. The most recent constraints on γ published by *BABAR* are based on the analysis of 470 million $B\bar{B}$ pairs in a data set corresponding to an integrated luminosity of approximately $430\,\text{fb}^{-1}$. The channels studied were $B^{\pm} \to \tilde{D}K^{\pm}$, $B^{\pm} \to \tilde{D}^* K^{\pm}$ ($D^* \to D\pi^0 / D^* \to D\gamma$) and $B^{\pm} \to \tilde{D}K^{*\pm}$. The analysis combined results from not only the $K^0_S \pi^+ \pi^-$ final state but the $K^0_S K^+ K^-$ final state as well. The most recent version of the analysis was published in 2010 [93] using the models presented in [35] which contain ten contributing $D^0 \to K^0_S \pi^+ \pi^-$ components and eight $D^0 \to K^0_S K^+ K^-$ components.

The measurements of $x_{\pm}$ and $y_{\pm}$ in the $B^{\pm} \to [K^0_S h^+ h^-]_D K^{\pm}$ system only are presented in Table 6.6. These statistical uncertainties are, for the $x_{\pm}$ parameters, considerably smaller than in the analysis presented in this thesis. For the $y_{\pm}$ parameters the statistical uncertainty on y_+ is considerably larger than in the LHCb measurement and that for y_- is comparable. The main explanation for the smaller uncertainties is the significantly larger sample size; the fit to the *BABAR* sample determined a $B^{\pm} \to \tilde{D}K^{\pm}$ yield which is around 40% larger than that presented in this thesis (1050 ± 38 $B^{\pm} \to [K^0_S h^+ h^-]_D K^{\pm}$ signal candidates compared to 756 ± 29). A second, less significant explanation is found in the expectation that the statistical uncertainty should be smaller in the model-dependent analysis since no loss in statistical sensitivity resulting from binning the data in the Dalitz plot is incurred, as discussed in Chapter 1.

The systematic error arising from uncertainties on the model parameters is, for all but the x_- parameter, between two and three times smaller than for the systematic uncertainty incurred in the LHCb analysis from the use of CLEO inputs. This modelling systematic uncertainty is not easy to define objectively, however, as seen by the much larger modelling systematic uncertainty found by the Belle collaboration in its version of the model-dependent analysis [104]. The measurements of γ have radically different modelling uncertainties; the

BABAR uncertainty corresponds to a 3° systematic uncertainty on γ whereas in the Belle analysis the uncertainty is 9°.

Table 6.6: Results of *BABAR* model-dependent analysis of $B^{\pm} \to [K^0_S h^+ h^-]_D K^{\pm}$ decays where the first uncertainty is statistical, the second arises from *BABAR* experimental systematic uncertainties and the third from the use of amplitude models for the D^0 meson decay [93].

	BABAR measurement ($\times 10^{-2}$)
x_+	$-10.3 \pm 3.7 \pm 0.6 \pm 0.7$
x_-	$6.0 \pm 3.9 \pm 0.7 \pm 0.6$
y_+	$-2.1 \pm 4.8 \pm 0.4 \pm 0.9$
y_-	$6.2 \pm 4.5 \pm 0.4 \pm 0.6$

6.2.2 Consequences for LHCb global γ measurement

The only $B^{\pm} \to \tilde{D}K^{\pm}$ analysis carried out by LHCb prior to that presented in this thesis was a study of $B^{\pm} \to [hh']K^{\pm}$ decays, published in 2012 [24]. The study was based on the same data set and yielded an observation of $B^{\pm}$ CP violation with 5.8σ significance as well as the first observation of the suppressed ADS mode, $B^{\pm} \to [K^{\mp}\pi^{\pm}]_D K^{\pm}$.

The analysis of $B^{\pm} \to [h^+h'^-]_D K^{\pm}$ using ADS and GLW techniques is made significantly more useful when combined with an analysis like that in the $K^0_S h^+ h^-$ final state which aids the resolution of a geometrical ambiguity remaining in the two body analysis. The effect of adding the $K^0_S h^+ h^-$ results can be seen in Figure 6.3 where, on addition, only the $\gamma \to \gamma + 180°$ ambiguity remains.

After the analysis in this thesis was published [1], a measurement of CP violation was made by LHCb in the $B^{\pm} \to [K^+\pi^-\pi^{\pm}\pi^{\mp}]_D K^{\pm}$ mode [28]. This, when combined with the $K^0_S h^+ h^-$ and hh' final states, led to an LHCb measurement of $\gamma = (70.5^{+14.9}_{-15.6})°$ in the $B^{\pm} \to \tilde{D}K^{\pm}$ system [98], where the uncertainty from LHCb measurements alone is approaching that of the world average.

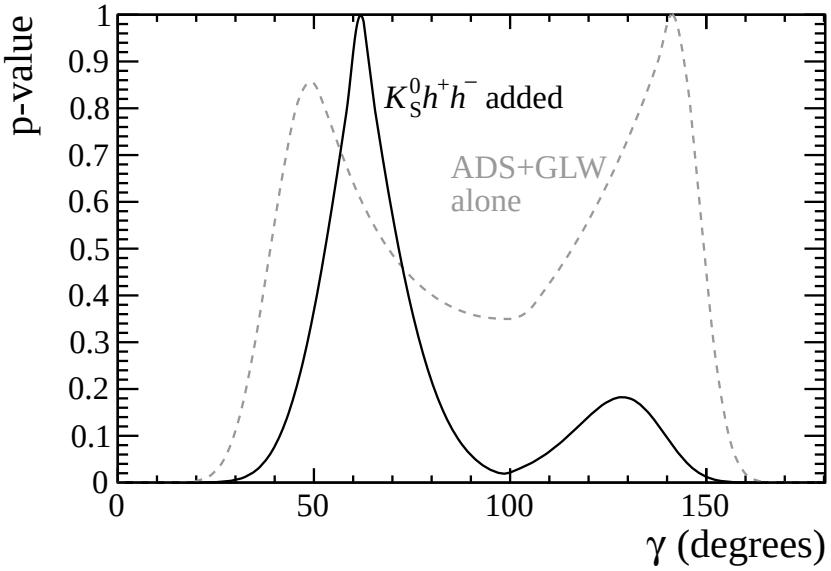

Figure 6.3: Likelihood distributions for γ showing the p-value of the fit (probability of finding a test-statistic equal to or more extreme than that observed) as a function of γ, where i) only ADS/GLW results [24] are included (grey hashed line) and ii) where the $B^\pm \to [K^0_S h^+ h^-]_D K^\pm$ results presented in this thesis are added (solid black line), reducing the ambiguity.

6.2.3 Future prospects for $B^\pm \to [K^0_S h^+ h^-]_D K^\pm$ analysis

The Belle $B^\pm \to [K^0_S h^+ h^-]_D K^\pm$ model-independent analysis resulted in a measurement of $\gamma = (68 \pm 14)^\circ$ [99]. Although the sensitivity to the $x_\pm$ and $y_\pm$ observables is the same in the analysis presented in this thesis, the constraints set on γ are much looser, $(45^{+43}_{-38})^\circ$, simply as a result of the low central value of $r_B = 0.07 \pm 0.04$ measured compared to $r_B = 0.15 \pm 0.03$ at Belle [99]. This effect is seen by the proximity of the red B^- contours to the origin in Figure 6.1. Extending the current analysis to include the $2\,\text{fb}^{-1}$ data set collected during 2012 will triple the size of the available sample and decrease the statistical uncertainties on the observables accordingly. Furthermore, the LHCb data set is set to increase to approximately $10\,\text{fb}^{-1}$ by the time of the so-called 'LS2' shutdown to prepare for the upgrade in 2018. Any increase in the central value of r_B in these analyses from its low value in this thesis will lead to an improved γ sensitivity.

The dominant source of systematic uncertainty in the LHCb analysis was the assumption that interference in the $B^\pm \to \tilde{D}\pi^\pm$ system could be neglected. The $B^\pm \to \tilde{D}\pi^\pm$

data are used in the analysis presented in this thesis to correct the $B^{\pm} \to \tilde{D}K^{\pm}$ yields for acceptance effects in the Dalitz plot and, as the statistical uncertainty on the efficiency corrections decreases with an increased data set, the systematic uncertainty arising from the no-interference assumption will become more and more significant. One way to avoid this would be to use another mode such as $B^- \to D^0\mu^-\bar{\nu}_\mu$ to provide a flavour-tagged D^0 sample with similar kinematics for efficiency corrections, where no interference effects are present between D^0 and $\bar{D}^0$ decay routes. Care would have to be taken to ensure the different trigger strategies employed are corrected for, and any kinematic differences taken into account.

The systematic uncertainty attached to the use of the CLEO-c c_i, s_i input values is very sensitive to fluctuations in the signal yields in the different Dalitz regions as discussed in Section 5.5.1 and the uncertainty should therefore diminish as the statistical fluctuations decrease. Improved measurements of the c_i and s_i parameters are expected from the analysis of BESIII data.

As the sensitivity to γ increases, it will become necessary to account for the effect of CP violation in the charm system on γ. It has been estimated that the systematic uncertainty on γ incurred by ignoring this effect is around 3° [105].

A final development of the analysis would be the replacement of the current selection by a multivariate one. Such a change of selection strategy has the potential to enhance the efficiency with which signal decay candidates are selected whilst maintaining the same sample purity.

6.2.4 Future prospects for γ analysis

Development continues apace with the goal of reducing the uncertainty on γ still further, with potential for an uncertainty below 10° using 2012 data. This would take the precision from LHCb alone to a level beyond that of the current world average. The accumulation of yet more data by LHCb and the addition of further D final states such as $K^0_S K^{\pm}\pi^{\mp}$ and the related $B^{\pm}$ final states $B^{\pm} \to \tilde{D^{(*)}}K^{(*)\pm}$, will allow even tighter constraints to be set in

the coming years. As progress continues as planned towards the $10\,\text{fb}^{-1}$ data set before the LHCb upgrade in 2018, the precision on γ in tree-level processes will allow a γ measurement with a precision of $(2-3)^\circ$ [106], surpassing that of current indirect measurements made through a global fit to the ensemble of Unitarity Triangle parameters. In the LHCb upgrade period after 2019, the accumulation of a $50\,\text{fb}^{-1}$ data set will allow still greater precision to be reached. The Unitarity Triangle, shown in its current form in Figure 6.4 [16], is set to face its sternest challenge yet.

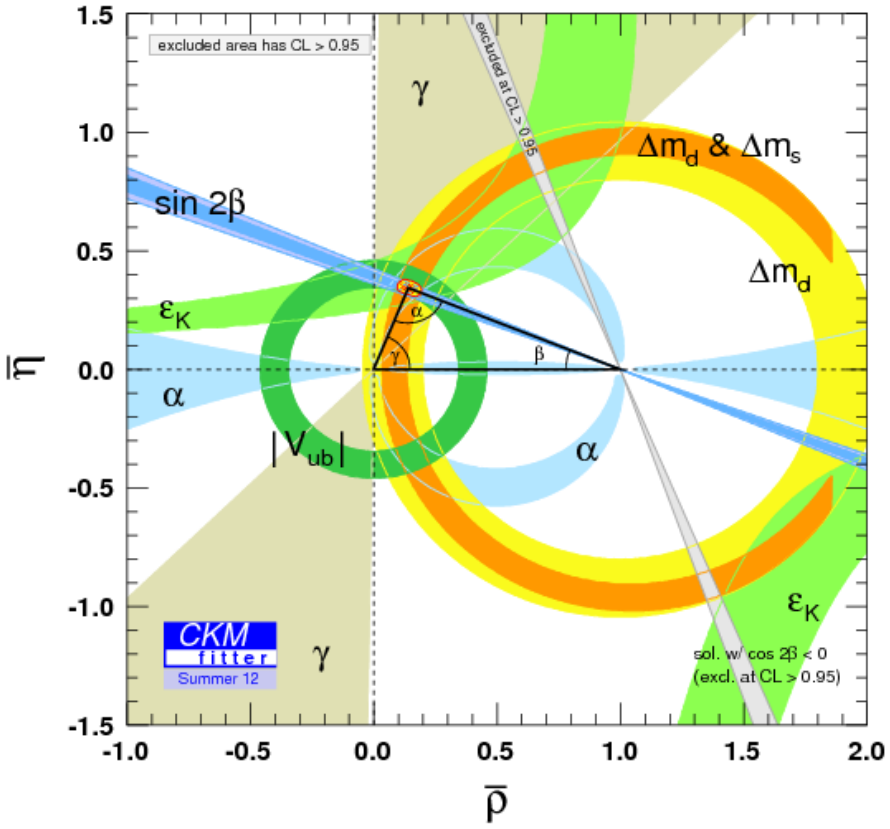

Figure 6.4: Current status of the CKMFitter UT constraints after the 2012 ICHEP conference [16].

A

Projections of fits to $B^{\pm}$ mass spectra in the Dalitz regions

The projections of the simultaneous fit to the $B^{\pm} \to [K^0_S\pi^+\pi^-]_D h^{\pm}$ and $B^{\pm} \to [K^0_S K^+ K^-]_D h^{\pm}$ data in all the Dalitz regions are given in Figures A.1 to A.4 for $K^0_S\pi^+\pi^-$ and Figures A.5 and A.6 for $K^0_S K^+ K^-$ where the simultaneous fits to the LL K^0_S and DD K^0_S samples are shown separately. Each row of figures forms a useful unit where the first pair of figures relate to the B^+ spectrum in a Dalitz region (e.g. bin 1) and the second pair relate to the B^- spectrum in the opposite Dalitz region (e.g. bin -1). CP violating effects would cause a difference between the pairs of plots. Within each pair, the left plot corresponds to the $B^{\pm} \to \tilde{D}K^{\pm}$ sample and the right to the $B^{\pm} \to \tilde{D}\pi^{\pm}$ sample.

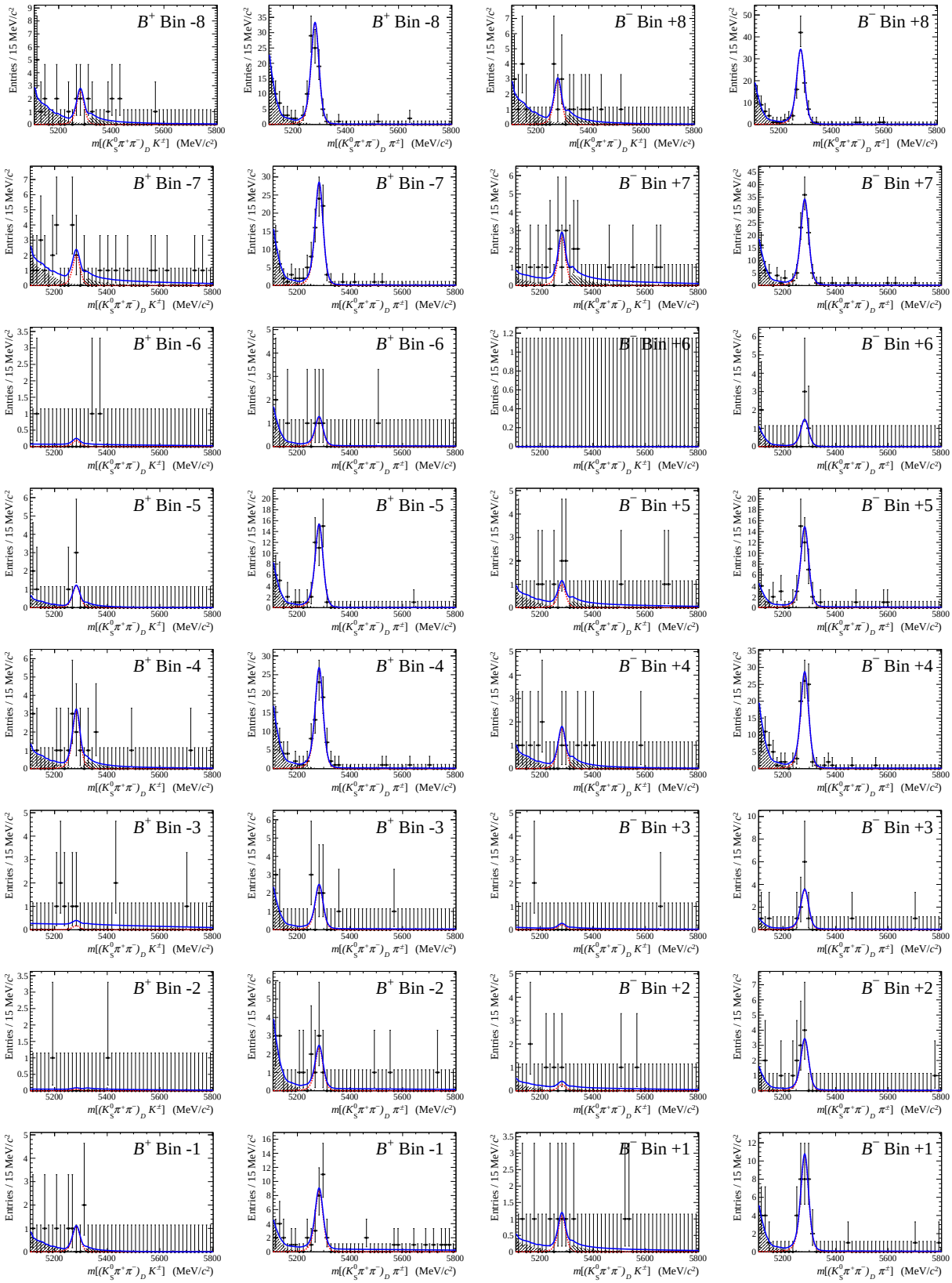

Figure A.1: Projections (LL K^0_S) for the fit to $K^0_S\pi^+\pi^-$ and $K^0_SK^+K^-$ data, $K^0_S\pi^+\pi^-$ bins -8 to -1. The PDF components are labelled in the same way as in Figure 4.14.

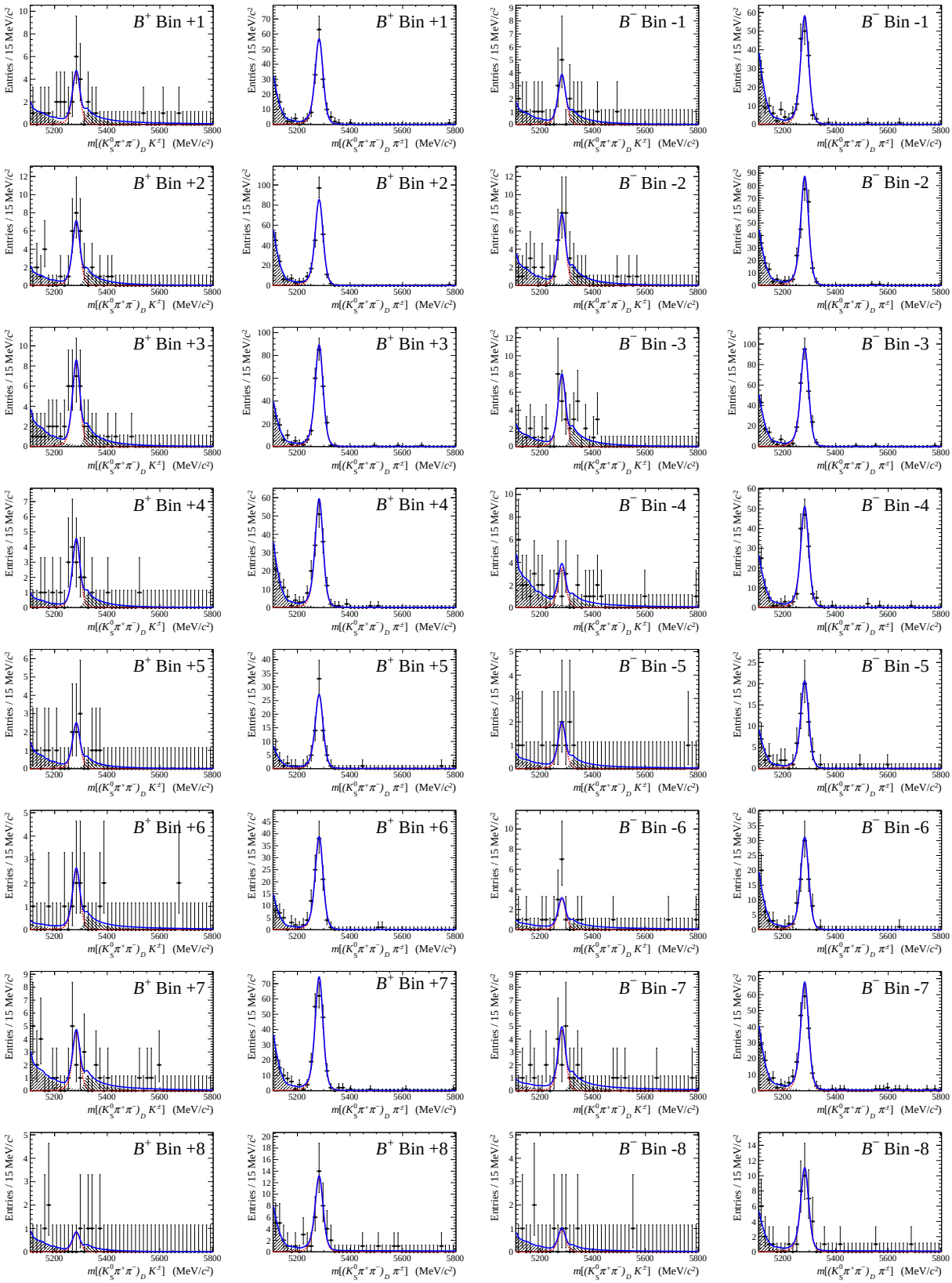

Figure A.2: Projections (LL K^0_S) for the fit to $K^0_S\pi^+\pi^-$ and $K^0_S K^+K^-$ data, $K^0_S\pi^+\pi^-$ bins 1 to 8. The PDF components are labelled in the same way as in Figure 4.14.

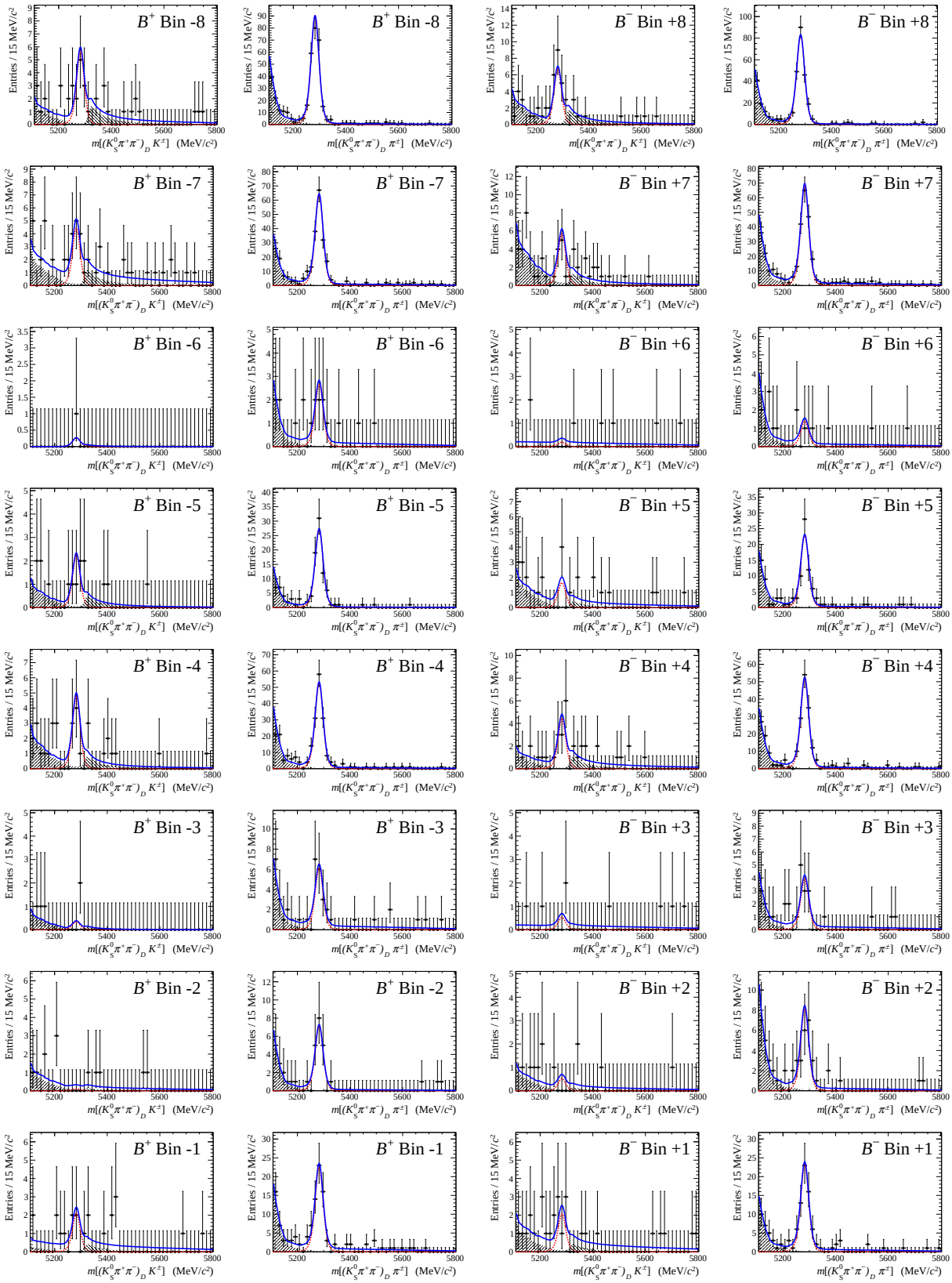

Figure A.3: Projections (DD K^0_S) for the fit to $K^0_S\pi^+\pi^-$ and $K^0_S K^+K^-$ data, $K^0_S\pi^+\pi^-$ bins -8 to -1. The PDF components are labelled in the same way as in Figure 4.14.

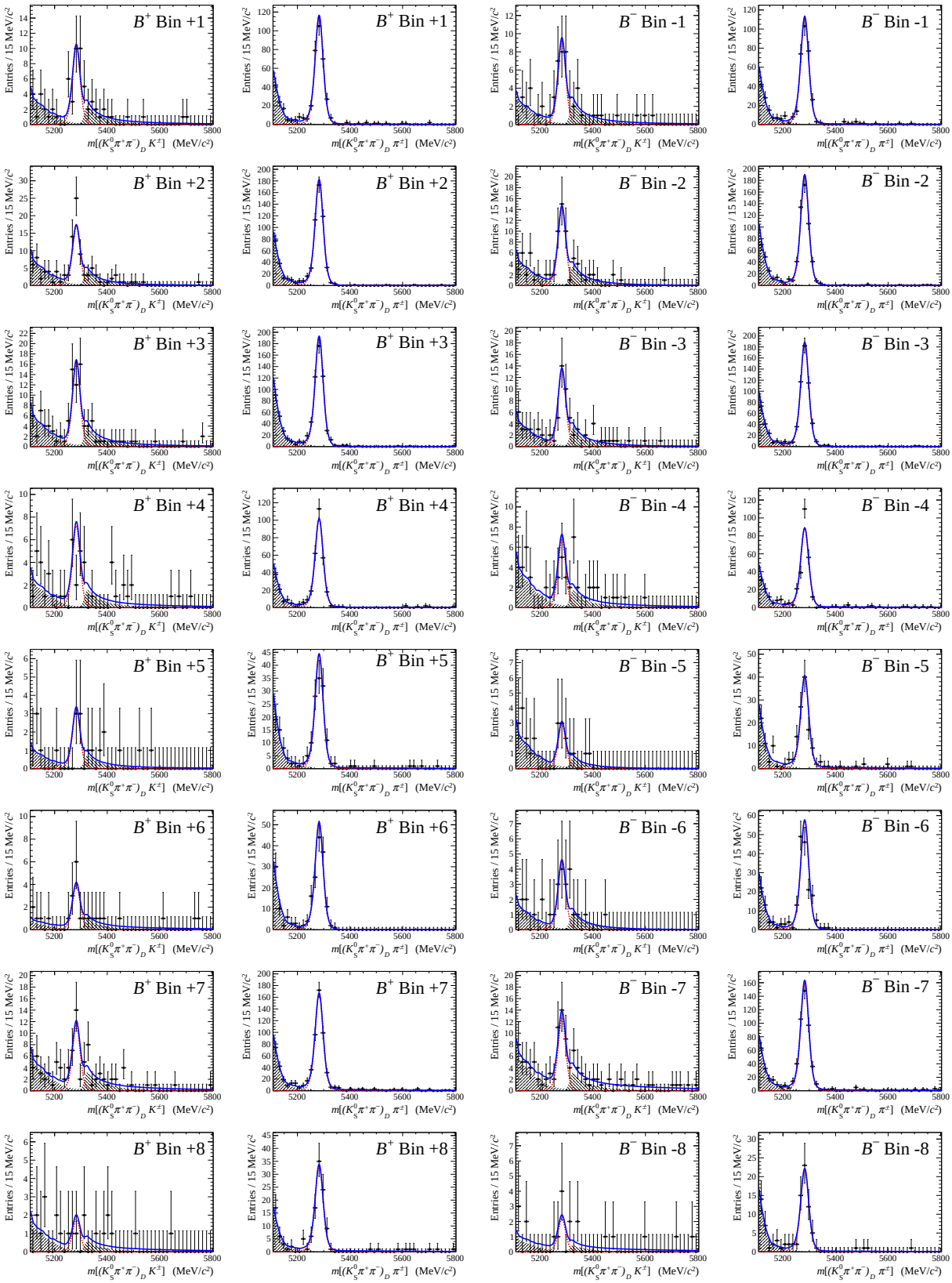

Figure A.4: Projections (DD K^0_S) for the fit to $K^0_S\pi^+\pi^-$ and $K^0_S K^+K^-$ data, $K^0_S\pi^+\pi^-$ bins 1 to 8. The PDF components are labelled in the same way as in Figure 4.14.

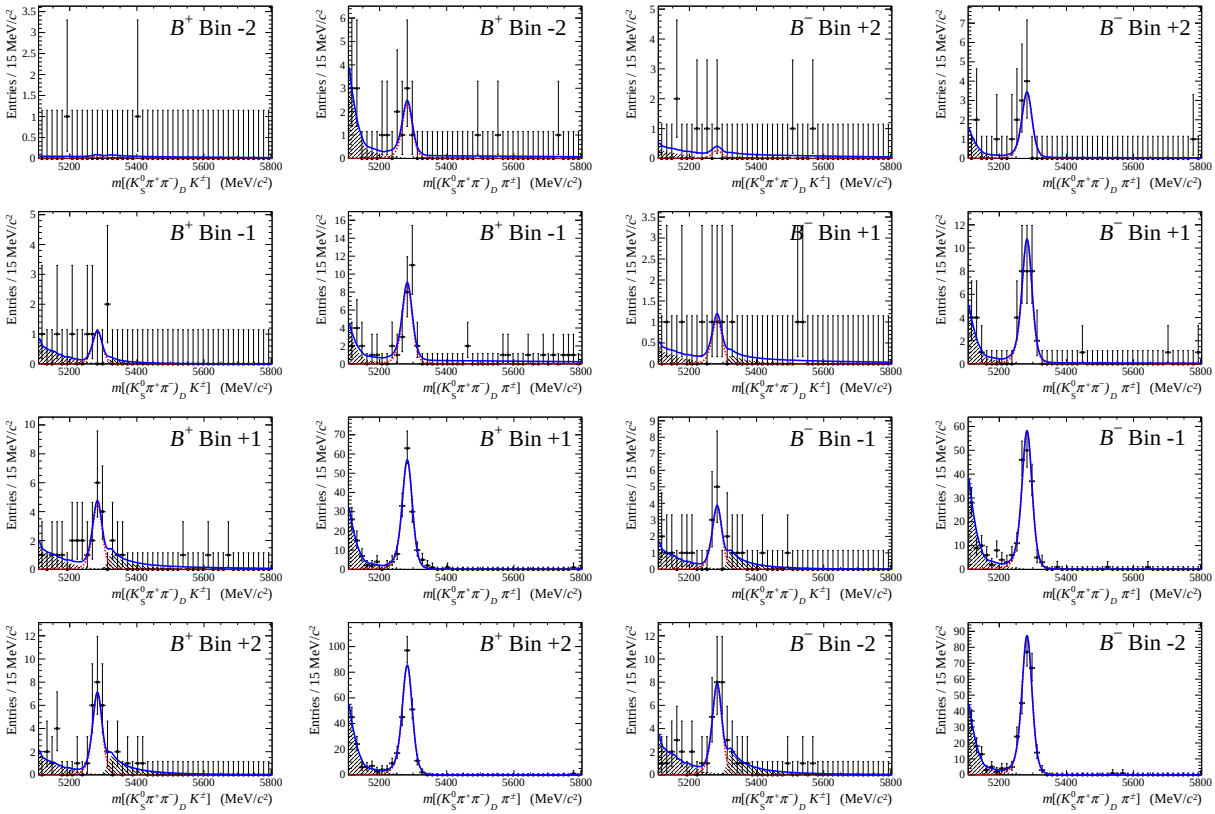

Figure A.5: Projections (LL K^0_S) for the fit to $K^0_S\pi^+\pi^-$ and $K^0_SK^+K^-$ data, $K^0_SK^+K^-$ bins -2 to 2. The PDF components are labelled in the same way as in Figure 4.14.

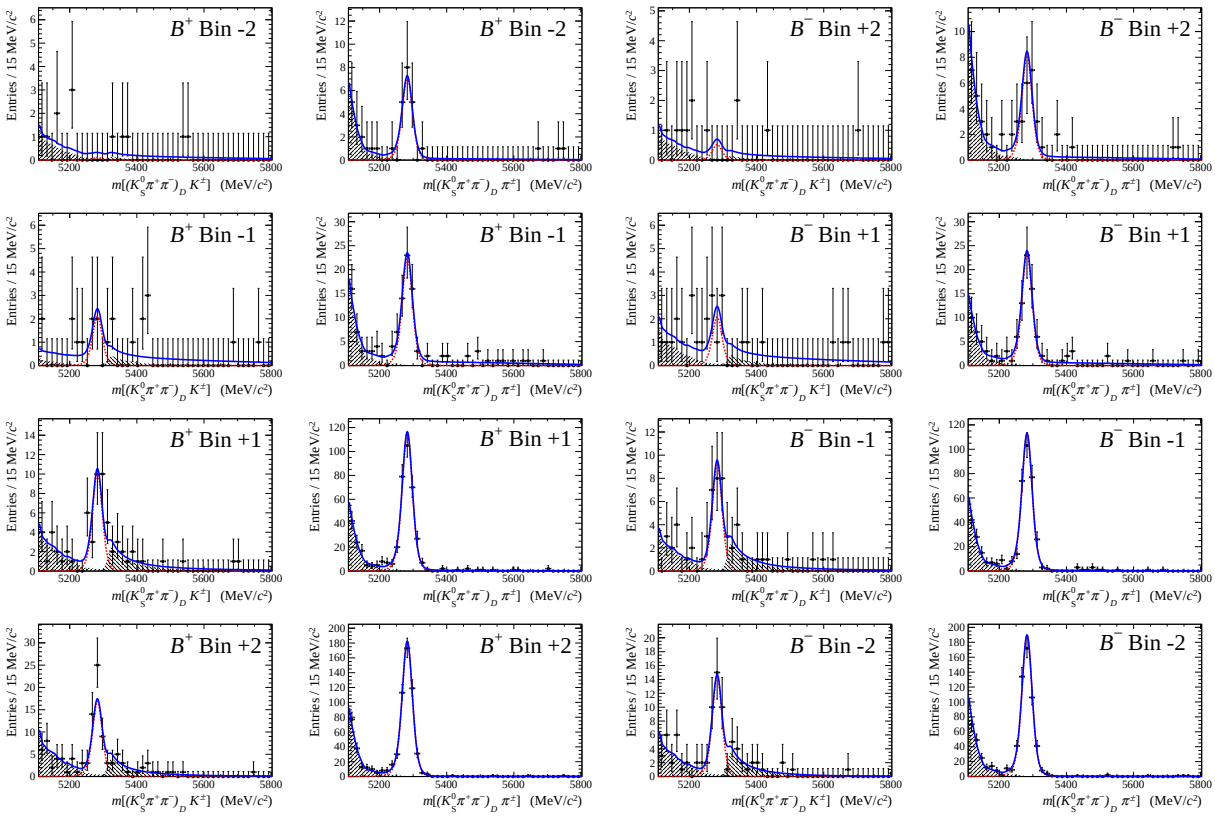

Figure A.6: Projections (DD K^0_S) for the fit to $K^0_S\pi^+\pi^-$ and $K^0_SK^+K^-$ data, $K^0_SK^+K^-$ bins -2 to 2. The PDF components are labelled in the same way as in Figure 4.14.

B

Measurement of γ in loop-level decays

As well as the technique for measuring γ in tree-level processes, described in Section 1.2.3, further techniques exist to measure γ at 'loop-level', where so-called 'penguin diagrams' containing loops make a contribution at a similar level to tree-level contributions [107]. One such decay is $B^0 \to \pi^+\pi^-$, which can take place according to the suppressed tree diagram shown in Figure B.1(a) or by the loop diagram in Figure B.1(b). The CKM element V_{ub} enters the first diagram with respect to the second and, since at leading order the only complex CKM element is V_{ub}, this leads to a weak phase of $\arg(V_{ub})$ between the processes. Considering the definition of $\gamma = \arg\left(-\frac{V_{ud}V_{ub}^*}{V_{cd}V_{cb}^*}\right)$, the phase difference between the diagrams in Figures B.1(a) and B.1(b) is simply $e^{-i\gamma}$. The two diagrams interfere, resulting in an overall decay rate for $B^0 \to \pi^+\pi^-$ which depends upon γ and further sensitivity through the effect of the interference on the B^0 oscillations. New physics effects may contribute through the entry of new particles in the Feynman loop and may therefore affect the level of CP violation observed, making it of great interest to compare processes such as this with measurements made using tree-level processes.

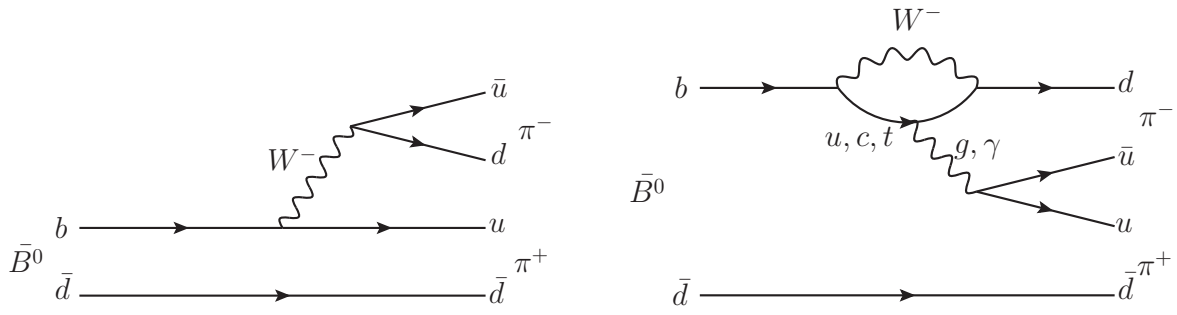

(a) Tree diagram

(b) Loop diagram

Figure B.1: Tree and loop diagrams for the decay $B^0 \to \pi^+\pi^-$. The weak phase difference between the diagrams is $e^{-i\gamma}$.

References

[1] LHCb collaboration, R. Aaij *et al.*, *A model-independent Dalitz plot analysis of $B^\pm \to DK^\pm$ with $D \to K^0_S h^+ h^-$ ($h = \pi, K$) decays and constraints on the CKM angle γ,* Phys. Lett. **B718** (2012) 43, arXiv:1209.5869.

[2] CLEO collaboration, J. Insler *et al.*, *Studies of the decays $D^0 \to K^0_S K^- \pi^+$ and $D^0 \to K^0_S K^+ \pi^-$,* Phys. Rev. **D85** (2012) 092016, arXiv:1203.3804.

[3] ATLAS collaboration, G. Aad *et al.*, *Observation of a new particle in the search for the Standard Model Higgs boson with the ATLAS detector at the LHC,* Phys. Lett. **B716** (2012) 1, arXiv:1207.7214.

[4] CMS collaboration, S. Chatrchyan *et al.*, *Observation of a new boson at a mass of 125 GeV with the CMS experiment at the LHC,* Phys. Lett. **B716** (2012) 30, arXiv:1207.7235.

[5] LHCb collaboration, R. Aaij *et al.*, *Observation of $D^0 - \overline{D}^0$ oscillations,* Phys. Rev. Lett. **110** (2013) 101802, arXiv:1211.1230.

[6] P. Maestro, *Observation of charm mixing at CDF,* arXiv:1305.7257.

[7] A. Sakharov, *Violation of CP invariance, c asymmetry, and baryon asymmetry of the Universe,* Pisma Zh. Eksp. Teor. Fiz. **5** (1967) 32.

[8] J. Christenson, J. Cronin, V. Fitch, and R. Turlay, *Evidence for the 2π decay of the K^0_2 Meson,* Phys. Rev. Lett. **13** (1964) 138.

[9] OPAL collaboration, K. Ackerstaff *et al.*, *Investigation of CP violation in $B^0 \to J/\psi K^0_S$ decays at LEP,* Eur. Phys. J. **C5** (1998) 379, arXiv:hep-ex/9801022.

[10] CDF Collaboration, T. Affolder *et al.*, *A measurement of $\sin(2\beta)$ from $B \to J/\psi K^0_S$ with the CDF detector,* Phys. Rev. **D61** (2000) 072005, arXiv:hep-ex/9909003.

[11] *BABAR* collaboration, B. Aubert *et al.*, *Observation of CP violation in the B^0 meson system,* Phys. Rev. Lett. **87** (2001) 091801, arXiv:hep-ex/0107013.

[12] Belle collaboration, K. Abe *et al.*, *Observation of large CP violation in the neutral B meson system,* Phys. Rev. Lett. **87** (2001) 091802, arXiv:hep-ex/0107061.

[13] L. Wolfenstein, *Parametrization of the Kobayashi-Maskawa Matrix,* Phys. Rev. Lett. **51** (1983) 1945.

[14] A. Somov, *Measurement of the CKM angle $\alpha(\phi_2)$ with $B \to \rho\rho$ decays at Belle and BABAR,* arXiv:hep-ex/0703025.

[15] BaBar collaboration, B. Aubert *et al.*, *Evidence for $B^0 \to \rho^0\rho^0$ decay and implications for the CKM angle α,* Phys. Rev. Lett. **98** (2007) 111801, arXiv:hep-ex/0612021.

[16] CKMfitter Group, J. Charles *et al.*, *CP violation and the CKM matrix: Assessing the impact of the asymmetric B factories. Updated results and plots available at: http://ckmfitter.in2p3.fr,* Eur. Phys. J. **C41** (2005) 1, arXiv:hep-ph/0406184.

[17] M. Gronau and D. London, *How to determine all the angles of the unitarity triangle from $B^0_d \to DK^0_S$ and $B^0_s \to D^0\phi$,* Phys. Lett. **B253** (1991) 483.

[18] M. Gronau and D. Wyler, *On determining a weak phase from CP asymmetries in charged B decays,* Phys. Lett. **B265** (1991) 172.

[19] D. Atwood, I. Dunietz, and A. Soni, *Enhanced CP violation with $B \to KD^0(\bar{D}0)$ modes and extraction of the CKM angle γ,* Phys. Rev. Lett. **78** (1997) 3257, arXiv:hep-ph/9612433.

[20] D. Atwood, I. Dunietz, and A. Soni, *Improved methods for observing CP violation in $B^\pm \to KD$ and measuring the CKM phase γ,* Phys. Rev. **D63** (2001) 036005, arXiv:hep-ph/0008090.

[21] *BABAR* collaboration, P. del Amo Sanchez *et al.*, *Measurement of CP observables in $B^\pm \to D_{CP}K^\pm$ decays and constraints on the CKM angle γ,* Phys. Rev. **D82** (2010) 072004, arXiv:1007.0504.

[22] Belle collaboration, K. Abe *et al.*, *Study of $B^\pm \to D_{CP}K^\pm$ and $D^*_{CP}K^\pm$ decays,* Phys. Rev. **D73** (2006) 051106, arXiv:hep-ex/0601032.

[23] CDF collaboration, T. Aaltonen *et al.*, *Measurements of branching fraction ratios and CP asymmetries in $B^\pm \to D_{CP}K^\pm$ decays in hadron collisions,* Phys. Rev. **D81** (2010) 031105, arXiv:0911.0425.

[24] LHCb collaboration, R. Aaij *et al.*, *Observation of CP violation in $B^+ \to DK^+$ decays,* Phys. Lett. **B712** (2012) 203, arXiv:1203.3662.

[25] Belle collaboration, Y. Horii *et al.*, *Evidence for the suppressed decay $B^- \to DK^-, D \to K^+\pi^-$,* Phys. Rev. Lett. **106** (2011) 231803, arXiv:1103.5951.

[26] *BABAR* collaboration, P. del Amo Sanchez *et al.*, *Search for $b \to u$ transitions in $B^- \to DK^-$ and D^*K^- decays,* Phys. Rev. **D82** (2010) 072006, arXiv:1006.4241.

[27] CDF collaboration, T. Aaltonen *et al.*, *Measurements of branching fraction ratios and CP-asymmetries in suppressed $B^- \to D(\to K^+\pi^-)K^-$ and $B^- \to D(\to K^+\pi^-)\pi^-$ decays,* Phys. Rev. **D84** (2011) 091504, arXiv:1108.5765.

[28] LHCb collaboration, R. Aaij *et al.*, *Observation of the suppressed ADS modes $B^\pm \to [\pi^\pm K^\mp \pi^+\pi^-]_D K^\pm$ and $B^\pm \to [\pi^\pm K^\mp \pi^+\pi^-]_D \pi^\pm$,* Physics Letters B **723** (2013) 44 , arXiv:1303.4646.

[29] A. Giri, Y. Grossman, A. Soffer, and J. Zupan, *Determining γ using $B^\pm \to DK^\pm$ with multibody D decays,* Phys. Rev. D **68** (2003) 054018.

[30] R. Dalitz, *On the analysis of tau-meson data and the nature of the tau-meson,* Phil. Mag. **44** (1953) 1068.

[31] CLEO collaboration, S. Kopp *et al.*, *Dalitz analysis of the decay $D^0 \to K^-\pi^+\pi^0$,* Phys. Rev. **D63** (2001) 092001, arXiv:hep-ex/0011065.

[32] S. M. Flatte, *Coupled-channel analysis of the $\pi\eta$ and $K\bar{K}$ systems near $K\bar{K}$ threshold,* Phys. Lett. **B63** (1976) 224.

[33] *BABAR* collaboration, B. Aubert *et al.*, *Dalitz plot analysis of $D^0 \to \bar{K}^0 K^+ K^-$,* Phys. Rev. **D72** (2005) 052008, arXiv:hep-ex/0507026.

[34] D. Aston *et al.*, *A study of $K^-\pi^+$ scattering in the reaction $K^- p \to K^-\pi^+ n$ at 11 GeV/c,* Nucl. Phys. **B296** (1988) 493.

[35] *BABAR* collaboration, P. del Amo Sanchez *et al.*, *Measurement of $D^0 - \bar{D}^0$ mixing parameters using $D^0 \to K^0_S\pi^+\pi^-$ and $D^0 \to K^0_S K^+ K^-$ decays,* Phys. Rev. Lett. **105** (2010) 081803, arXiv:1004.5053.

[36] H. M. Pilkuhn, *The interactions of hadrons, chapters 3-7.* North-Holland Publishing Company - Amsterdam, John Wiley & Sons, Inc. - New York, 1967.

[37] *LEPP website,* http://www.lepp.cornell.edu/. Accessed: 28-05-2013.

[38] CLEO collaboration, Y. Kubota *et al.*, *The CLEO-II detector,* Nucl. Instrum. Meth. **A320** (1992) 66.

[39] D. Peterson *et al.*, *The CLEO III drift chamber,* Nucl. Instrum. Meth. **A478** (2002) 142.

[40] R. Poling, *CLEO-c hot topics,* eConf **C060409** (2006) 005, arXiv:hep-ex/0606016.

[41] *Photographs courtesy of K. Ecklund,* http://www.lns.cornell.edu/ kme/zdphotos. Accessed: 28-05-2013.

[42] F. Halzen and A. D. Martin, *Quarks and leptons: an introductory course in modern particle physics.* John Wiley & Sons, Inc. - New York, 1984.

[43] M. Artuso *et al.*, *The CLEO RICH detector,* Nucl. Instrum. Meth. **A554** (2005) 147, arXiv:physics/0506132.

[44] CLEO collaboration, S. Kopp, *The CLEO III detector,* Nucl. Instrum. Meth. **A384** (1996) 61.

[45] CLEO collaboration, R. A. Briere *et al.*, *CLEO-c and CESR-c: a new frontier of weak and strong interactions,* 2001. CLNS-01-1742.

[46] P. Avery *et al.*, *QQ: The CLEO event generator (unpublished),* http://www.lns.cornell.edu/public/CLEO/soft/QQ. Accessed: 13-05-2013.

[47] D. J. Lange, *The EvtGen particle decay simulation package,* Nucl. Instrum. Meth. **A462** (2001) 152.

[48] GEANT4 collaboration, S. Agostinelli *et al.*, *GEANT4: A simulation toolkit,* Nucl. Instrum. Meth. **A506** (2003) 250.

[49] R. Aaij *et al.*, *The LHCb Trigger and its Performance in 2011,* JINST **8** (2013) P04022, arXiv:1211.3055.

[50] D. Fournier, *Performance of the LHC, ATLAS and CMS in 2011,* EPJ Web Conf. **28** (2012) 01003, arXiv:1201.4681.

[51] LHCb collaboration, J. Alves, A. Augusto *et al.*, *The LHCb detector at the LHC,* JINST **3** (2008) S08005.

[52] *LHCb website,* http://lhcb.web.cern.ch/. Accessed: 28-05-2013.

[53] LHCb-VELO collaboration, M. Alexander, *LHCb VELO tracking resolutions,* Nucl. Instrum. Meth. **A699** (2013) 184.

[54] P. R. Perez, *The LHCb Vertex Locator performance and Vertex Locator upgrade,* JINST **7** (2012) C12008, arXiv:1209.4845.

[55] A. Affolder *et al.*, *Radiation damage in the LHCb Vertex Locator,* arXiv:1302.5259.

[56] LHCb collaboration, P. Collins, *The LHCb upgrade,* arXiv:1108.1403.

[57] A. Jaeger, P. Seyfert, M. De Cian, J. van Tilburg, and S. Hansmann-Menzemer, *Measurement of the track finding efficiency,* Tech. Rep. LHCb-PUB-2011-025. CERN-LHCb-PUB-2011-025, CERN, Geneva, Apr, 2012.

[58] R. E. Kalman, *A new approach to linear filtering and prediction problems,* Transactions of the ASME Journal of Basic Engineering (1960), no. 82 (Series D) 35.

[59] R. Fruhwirth, *Application of Kalman filtering to track and vertex fitting,* Nucl. Instrum. Meth. **A262** (1987) 444.

[60] *LHCb magnet website,* http://lhcb-magnet.web.cern.ch/. Accessed: 28-05-2013.

[61] S. Eisenhardt, *Production and tests of Hybrid Photon Detectors for the LHCb RICH detectors,* Nucl. Instrum. Meth. **A595** (2008) 142.

[62] M. Adinolfi *et al.*, *Performance of the LHCb RICH detector at the LHC,* The European Physical Journal C **73** (2012), no. 5 1, arXiv:1211.6759.

[63] T. Gys, *Production of 500 pixel hybrid photon detectors for the RICH counters of LHCb,* Nucl. Instrum. Meth. **A567** (2006) 176.

[64] *LHCb Moore high level trigger software package,* http://lhcb-release-area.web.cern.ch/LHCb-release-area/DOC/moore/. Accessed: 28-05-2013.

[65] *LHCb Brunel reconstruction software package,* http://lhcb-release-area.web.cern.ch/LHCb-release-area/DOC/brunel/. Accessed: 28-05-2013.

[66] *LHCb DaVinci analysis software package,* http://lhcb-release-area.web.cern.ch/LHCb-release-area/DOC/davinci/. Accessed: 28-05-2013.

[67] *LHCb Gauss simulation software package,* http://lhcb-release-area.web.cern.ch/LHCb-release-area/DOC/gauss/. Accessed: 28-05-2013.

[68] I. Belyaev *et al.*, *Handling of the generation of primary events in Gauss, the LHCb simulation framework,* Nuclear Science Symposium Conference Record (NSS/MIC) **IEEE** (2010) 1155.

[69] T. Sjöstrand, S. Mrenna, and P. Skands, *PYTHIA 6.4 physics and manual,* JHEP **05** (2006) 026, arXiv:hep-ph/0603175.

[70] P. Golonka and Z. Was, *PHOTOS Monte Carlo: a precision tool for QED corrections in Z and W decays,* Eur. Phys. J. **C45** (2006) 97, arXiv:hep-ph/0506026.

[71] GEANT4 collaboration, J. Allison *et al.*, *Geant4 developments and applications,* IEEE Trans. Nucl. Sci. **53** (2006) 270.

[72] M. Clemencic *et al.*, *The LHCb simulation application, Gauss: design, evolution and experience,* J. of Phys: Conf. Ser. **331** (2011) 032023.

[73] *LHCb Boole digitisation software package,* http://lhcb-release-area.web.cern.ch/LHCb-release-area/DOC/boole/. Accessed: 28-05-2013.

[74] Particle Data Group, K. Nakamura *et al.*, *Review of particle physics,* J. Phys. **G37** (2010) 075021.

[75] B. Bhattacharya and J. L. Rosner, *Decays of charmed mesons to PV final states,* Phys. Rev. **D79** (2009) 034016, arXiv:0812.3167.

[76] CLEO collaboration, S. Dobbs *et al.*, *Measurement of absolute hadronic branching fractions of D mesons and $e^+e^- \to D\bar{D}$ cross-sections at the $\psi(3770)$,* Phys. Rev. **D76** (2007) 112001, arXiv:0709.3783.

[77] D. Johnson, S. Malde, J. Libby, C. Thomas, and G. Wilkinson, *A measurement of the coherence factor and strong phase difference of the $D^0 \to K^0_S K\pi$ decay,* Jan, 2011. CBX 2011-001.

[78] *BABAR* collaboration, B. Aubert *et al.*, *Amplitude analysis of the decay $D^0 \to K^-K^+\pi^0$,* Phys. Rev. **D76** (2007) 011102, arXiv:0704.3593.

[79] F. James and M. Roos, *Minuit - a system for function minimization and analysis of the parameter errors and correlations,* Computer Physics Communications **10** (1975), no. 6 343.

[80] J. Rademacker, *MINT,* http://www.phy.bris.ac.uk/people/rademacker_j/. Accessed: 24-04-2013.

[81] F. James, *MINUIT - Function minimization and error analysis - reference manual,* http://wwwasdoc.web.cern.ch/wwwasdoc/minuit/minmain.html, 2000.

[82] B. Bhattacharya and J. L. Rosner, *Flavor SU(3) tests from $D^0 \to K^0K^-\pi^+$ and $D^0 \to \bar{K}^0K^+\pi^-$ Dalitz plots,* Phys. Lett. **B714** (2012) 276, arXiv:1203.6014.

[83] CLEO Collaboration, P. Rubin *et al.*, *Search for CP Violation in the Dalitz-Plot Analysis of $D^\pm \to K^+K^-\pi^\pm$,* Phys. Rev. **D78** (2008) 072003, arXiv:0807.4545.

[84] E791 Collaboration, A. J. Schwartz, *Evidence for light scalar resonances in charm meson decays from Fermilab E791,* arXiv:hep-ex/0212057.

[85] D. Atwood and A. Soni, *Role of charm factory in extracting CKM phase information via $B \to DK$,* Phys. Rev. **D68** (2003) 033003, arXiv:hep-ph/0304085.

[86] CLEO collaboration, N. Lowrey *et al.*, *Determination of the $D^0 \to K^-\pi^+\pi^0$ and $D^0 \to K^-\pi^+\pi^+\pi^-$ coherence factors and average strong-phase differences using quantum-correlated measurements,* Phys. Rev. **D80** (2009) 031105, arXiv:0903.4853.

[87] CLEO collaboration, M. Artuso *et al.*, *Amplitude analysis of $D^0 \to K^+K^-\pi^+\pi^-$,* Phys. Rev. **D85** (2012) 122002, arXiv:1201.5716.

[88] S. Malde and G. Wilkinson, *$D^0 - \bar{D}^0$ mixing studies with the decays $D^0 \to K^0_S K^\mp \pi^\pm$,* Phys. Lett. **B701** (2011) 353, arXiv:1104.2731.

[89] A. Bondar and A. Poluektov, *The use of quantum-correlated D^0 decays for ϕ_3 measurement,* Eur. Phys. J. **C55** (2008) 51, arXiv:0801.0840.

[90] A. Bondar and A. Poluektov, *Feasibility study of model-independent approach to ϕ_3 measurement using Dalitz plot analysis,* Eur. Phys. J. **C47** (2006) 347, arXiv:hep-ph/0510246.

[91] CLEO collaboration, J. Libby *et al.*, *Model-independent determination of the strong-phase difference between D^0 and $\bar{D}^0 \to K^0_{S,L}h^+h^-$ ($h = \pi, K$) and its impact on the measurement of the CKM angle γ/ϕ_3,* Phys. Rev. **D82** (2010) 112006, arXiv:1010.2817.

[92] *BABAR* collaboration, B. Aubert *et al.*, *Improved measurement of the CKM angle γ in $B^\mp \to D^{(*)}K^{(*\mp)}$ decays with a Dalitz plot analysis of D decays to $K^0_S\pi^+\pi^-$ and $K^0_S K^+K^-$,* Phys. Rev. **D78** (2008) 034023, arXiv:0804.2089.

[93] *BABAR* collaboration, P. del Amo Sanchez *et al.*, *Evidence for direct CP violation in the measurement of the Cabibbo-Kobayashi-Maskawa angle γ with $B^{\mp} \to D^{(*)}K^{(*)\mp}$ decays,* Phys. Rev. Lett. **105** (2010) 121801, arXiv:1005.1096.

[94] T. Skwarnicki, *A study of the radiative cascade transitions between the upsilon-prime and upsilon resonances.* PhD thesis, Institute of Nuclear Physics, Krakow, 1986.

[95] Heavy Flavor Averaging Group, D. Asner *et al.*, *Averages of b-hadron, c-hadron, and tau-lepton properties as of 2010,* arXiv:1010.1589, online updates are available at http://www.slac.stanford.edu/xorg/hfag/osc/PDG_2010.

[96] K. S. Cranmer, *Kernel estimation in high-energy physics,* Comput. Phys. Commun. **136** (2001) 198, arXiv:hep-ex/0011057.

[97] J. E. Gentle, *Numerical linear algebra with applications in statistics.* Statistics and Computing. Springer, Berlin, 1998.

[98] LHCb collaboration, R. Aaij *et al.*, *Measurement of the CKM angle γ from a combination of $B \to Dh$ analyses,* arXiv:1305.2050.

[99] Belle collaboration, H. Aihara *et al.*, *First measurement of ϕ_3 with a model-independent Dalitz plot analysis of $B \to DK, D \to K^0_S\pi\pi$ decay,* Phys. Rev. **D85** (2012) 112014, arXiv:1204.6561.

[100] G. J. Feldman and R. D. Cousins, *A Unified approach to the classical statistical analysis of small signals,* Phys. Rev. **D57** (1998) 3873, arXiv:physics/9711021.

[101] *Belle FORTRAN code,* The code used in the Belle analysis for extraction of γ, r_B and δ_B from measurements of $x_\pm$ and $y_\pm$ was kindly provided by A. Poluektov.

[102] *BABAR* collaboration, B. Aubert *et al.*, *Dalitz plot analysis of D^0 hadronic decays $D^0 \to K^0K^-\pi^+$, $D^0 \to \bar{K}^0K^+\pi^-$ and $D^0 \to \bar{K}^0K^+K^-$,* arXiv:hep-ex/0207089.

[103] LHCb collaboration, R. Aaij *et al.*, *Observation of $D^0 - \overline{D}^0$ oscillations,* Phys. Rev. Lett. **110** (2013) 101802, arXiv:1211.1230.

[104] Belle collaboration, A. Poluektov *et al.*, *Evidence for direct CP violation in the decay $B \to D^{(*)}K, D \to K^0_S\pi^+\pi^-$ and measurement of the CKM phase ϕ_3,* Phys. Rev. **D81** (2010) 112002, arXiv:1003.3360.

[105] A. Bondar, A. Dolgov, A. Poluektov, and V. Vorobiev, *Effect of direct CP violation in charm on γ extraction from $B \to DK, D \to K^0_S\pi^+\pi^-$ Dalitz plot analysis,* arXiv:1303.6305.

[106] LHCb Collaboration, B. Adeva *et al.*, *Roadmap for selected key measurements of LHCb,* arXiv:0912.4179.

[107] R. Fleischer, *$B_{s,d} \to \pi\pi, \pi K, KK$: status and prospects,* Eur. Phys. J. **C52** (2007) 267, arXiv:0705.1121.